Universität Zürich
Physik-Institut

www.physik.unizh.ch

Wissenschaftlicher Jahresbericht

April 2006 - März 2007

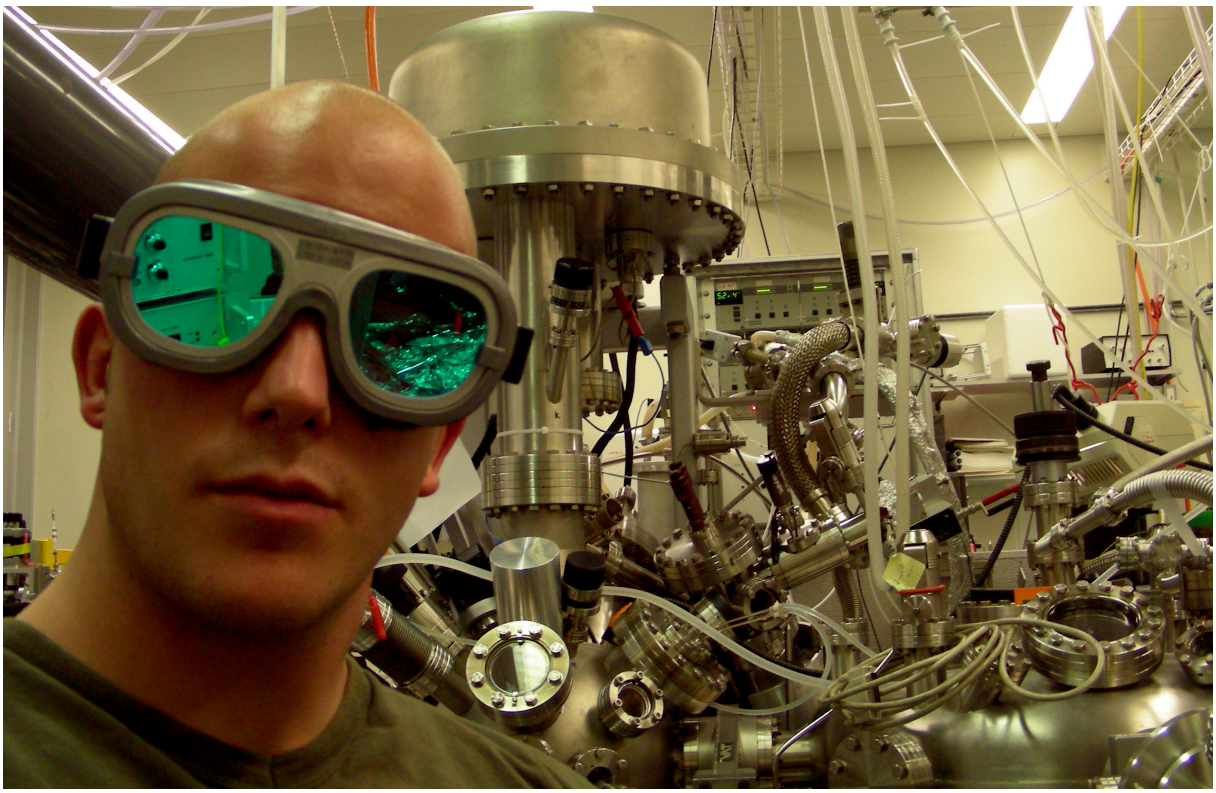

Winterthurerstrasse 190, CH-8057 Zürich/Schweiz

Universität Zürich
Physik-Institut

www.physik.unizh.ch

Wissenschaftlicher Jahresbericht

April 2006 - März 2007

Winterthurerstrasse 190, CH-8057 Zürich/Schweiz

The picture on the front shows Dominik Leuenberger of the Surface Physics group (Sec.10) protecting himself against the hazards of femtosecond laser beams. On the back of the cover a $H_2@C_{60}$ molecule is depicted, a buckminster fullerene containing a hydrogen molecule, which was studied by photoelectron spectroscopy.

Sekretariat	044 635 5721	secret@physik.uzh.ch
Prof. C. Amsler	044 635 5784 022 767 2914	amsler@cern.ch
Prof. H.-W. Fink	044 635 5801	hwfink@physik.uzh.ch
Prof. H. Keller	044 635 5748	keller@physik.uzh.ch
Prof. J. Osterwalder	044 635 5827	osterwal@physik.uzh.ch
Prof. A. Schilling	044 635 5791	schilling@physik.uzh.ch
Prof. U.D. Straumann	044 635 5768	strauman@physik.uzh.ch
Prof. P. Truöl	044 635 5777	truoel@physik.uzh.ch

The annual reports are available on the internet: http://www.physik.uzh.ch/reports.html.

Begleitwort

Die sieben Forschungsgruppen am Physik-Institut befassen sich mit verschiedenen aktuellen Forschungsthemen der modernen Physik - von der Untersuchung biologischer Systeme über die Oberflächenphysik und die Physik magnetischer und supraleitender Materialien bis hin zu fundamentalen Wechselwirkungen und Systemen in der Elementarteilchenphysik.

Die Forschungsgruppen am Physik-Institut sind vom Nationalfonds durch 21 Forschungsprojekte und von Beiträgen aus der *K. Alex Müller Stiftung*, der *Gebert-Rüf Stiftung*, sowie durch Drittmittelbeiträge des *Paul Scherrer Instituts* und des *IBM Forschungslaboratoriums Rüschlikon* unterstützt worden. Das Physik-Institut ist unter anderem am Nationalen Forschungskompetenzzentrum (NCCR) MaNEP (*Materials with Novel Electronic Properties*, Profs. H. Keller, A. Schilling) beteiligt und gehört zu den Mitgründern des *Swiss Institute of Particle Physics* (CHIPP) (Profs. C. Amsler, U. Straumann, P. Truöl).

Drei Forschungsgruppen des Physik-Instituts sind an EU Projekten beteiligt. Die Oberflächenphysik-Gruppe von Prof. J. Osterwalder koordiniert ein dreijähriges EU Projekt auf dem Gebiet der Nanowissenschaften (*Nanomesh) Boron Nitride Nanomesh as a Scaffold for Nanocatalysts, Nanomagnets and Functional Surfaces*) mit insgesamt acht Partnerinstitutionen. Prof. Fink leitet das EU Projekt *Obtaining Atomically Resolved Structural Information on Individual Bio-Molecules using Electron Holography* mit fünf Partnerinstitutionen, und Prof. Keller ist Partner im dreijährigen EU Projekt *Controlling Mesoscopic Phase Separation* (CoMePhS), welches von der Technischen Universität Athen geleitet wird und zwölf Partnerinstitutionen umfasst.

Einige wichtige Entwicklungen bei den Projekten der *Physics of Fundamental Interactions and Particles* seien hier kurz erwähnt: Die Gruppe Amsler hat die Entwicklungen zum Silizium-Pixeldetektor des CMS Experimentes am Large Hadron Collider fortgeführt. Die Detektor-Mechanik und die Kontrollelektronik wurden in den mechanischen und elektronischen Werkstätten des Instituts hergestellt. Ebenfalls am CERN sucht die Gruppe nach Kπ-Atomen mit dem DIRAC-Experiment und hat dazu einen neuartigen Cerenkov-Detektor bereitgestellt. Die Vorbereitungen des Flüssig-Argon-Detektors zum Nachweis der dunklen Materie wurden in Zusammenarbeit mit der ETHZ fortgesetzt.

Im Laufe des Jahres 2006 wurde nach ca. 6 Jahren Entwicklungszeit der Siliziumstreifendetektor für LHCb in unserer Werkstatt fertiggestellt. Im Dezember 2006 wurden vorerst dessen mechanische Teile am CERN eingebaut.

Die Messungen zum Zürcher Experiment zur Bestimmung der Gravitationskonstanten wurden im Jahre 2002 abgeschlossen. Die aus diesem Experiment stammenden Daten wurden in mehr als dreijähriger Arbeit sorgfältig analysiert und die systematischen Messfehler genau bestimmt. Die Hauptarbeit dafür leistete unser pensioniertes Institutsmitglied Dr. R.E. Pixley. Das endgültige Resultat wurde im Herbst 2006 in der Zeitschrift Phys. Rev. D publiziert. Der Zürcher Wert der Gravitationskonstanten führte zu einer wesentlichen Verbesserung des momentanen *world average* dieser Naturkonstanten, da er im Vergleich zu den anderen modernen Gravitationsexperimenten im 20 ppm Bereich durch ein anderes Messprinzip erhalten wurde.

Im Forschungsbereich *Condensed Matter Physics* sind unter anderem folgende Fortschritte erzielt worden: Bei der Rekonstruktion eines Objektes aus einem Hologramm entsteht ausser dem eigentlichen, gesuchten Bild des Objekts, auch noch ein konjugiertes Bild. Letzteres ist

dem gesuchten Bild überlagert und stört dessen Strukturaufklärung. Diese Schwierigkeit ist seit der Erfindung der Holografie mit dem Begriff *Twin-Image Problem* versehen worden und galt als ein intrinsisches, nur korrigierbares, nicht aber eliminierbares Artefakt der Holografie. Dieses mehr als 50 Jahre alte Problem der kohärenten Optik ist nun im vergangenen Jahr durch die Arbeiten von Dr. Tatiana Latychevskaia aus der Biophysik-Gruppe gelöst und erfolgreich auf experimentelle Hologramme angewandt worden.

Mit Hilfe von detaillierten Untersuchungen der magnetischen Eindringtiefe in der Vortex-Phase in einkristallinen Proben von Kuprat-Supraleitern ist es der Gruppe Supraleitung und Magnetismus im vergangenen Jahr gelungen zu zeigen, dass in Kuprat-Supraleitern zwei supraleitende Energielücken mit s- und d-Wellen-Symmetrie vorliegen. Diese Erkenntnis ist ein wichtiger Schritt hin zum Verständnis der Hochtemperatur-Supraleitung.

Mitglieder des Physik-Institutes haben im Berichtsjahr zwei bedeutende Konferenzen organisiert: Im August 2006 fand an unserem Institut ein sehr gut besuchter Workshop der Schweizerischen Hochenergiephysiker statt, wo über die kurz- und mittelfristigen Projekte am CERN und anderswo diskutiert wurde. Im Rahmen dieser Veranstaltung wurden auch Einzelheiten zum Aufbau und Betrieb des Hochleistungsrechners der Schweizerischen Teilchenphysikvereinigung (CHIPP) am CSCS in Manno beschlossen.

Die Oberflächenphysik-Gruppe organisierte im September einen internationalen Workshop in Braunwald mit 60 Teilnehmern, wo im Rahmen des von ihr koordinierten Europäischen Forschungsprojektes *NanoMesh* die neuesten Resultate und Ausblicke für mögliche Anwendungen der von der Gruppe kürzlich entdeckten Bornitrid-Nanostruktur präsentiert wurden. Die Bestimmung der genauen Geometrie dieser netzartigen atomaren Monolage mit zwei Nanometer weiten Poren, sowie die Tatsache dass diese Struktur an Luft und in Wasser stabil ist, fanden grosse Beachtung.

Die Forschungsprojekte des Physik-Instituts findet man auf den Websites der Forschungsdatenbank der Universität Zürich [1]. Der wissenschaftliche Jahresbericht des Physik-Instituts wurde wie immer in englischer Sprache abgefasst, um unsere Forschungstätigkeit einem internationalen Publikum besser zugänglich zu machen. Der vollständige Jahresbericht wie auch die Jahresberichte früherer Jahre können auf der Website des Physik-Instituts eingesehen werden [2].

Zürich, im Mai
Prof. Dr. Hugo Keller

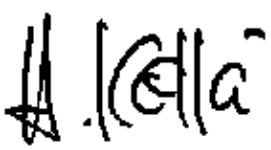

[1] http://www.research-projects.uzh.ch/math/unit71600/index.htm
[2] http://www.physik.uzh.ch/reports.html

Rücktritt

Prof. Dr. Peter Truöl

Ende August 2006 trat Prof. Peter Truöl nach 35 Jahren akademischer Lehr- und Forschungstätigkeit an der Universität Zürich in den Ruhestand. Ausgerüstet mit einer klassischen gymnasialen Bildung aus Bremen studierte er zuerst in Göttingen und ab 1958 an der Universität Zürich Mathematik, Chemie und Physik. Er promovierte an unserer Fakultät in Kernphysik bei Hans Staub und Verena Meyer, wobei er in seiner Dissertation mit Hilfe des van de Graaf Generators im damaligen Physik-Institut an der Schönberggasse die Eigenschaften des ^{10}B - Kernes durch Streuung von α - Teilchen am ^{6}Li untersuchte. Ein zweijähriges Forschungsstipendium der ETH Zürich erlaubte es ihm anschliessend in der Forschungsgruppe von Ken Crowe in Berkeley am Bevatron und am 184" Zyklotron mit Pionstrahlen zu experimentieren. In 1969, im Alter von nur 30 Jahren, wurde er Assistenzprofessor an der University of California in Los Angeles.

Zusammen mit seiner jungen Familie kehrte er später nach Zürich zurück, wo er vorerst am CERN und ab 1974 am neu erstellten Schweizerischen Institut für Nuklearforschung (heute PSI-West) mit seinen präzisen Pionstrahlen experimentierte. In Zusammenarbeit mit Gruppen der Universitäten Lausanne und München initiierte er wichtige Experimente zur Untersuchung von Kernresonanzen, zur Messung der Neutronenstreulänge und wichtiger Reaktionen in dem Gebiet, welches wir heute als Niederenergie-Teilchenphysik bezeichnen. Dabei kam meist das von ihm mitentwickelte grosse Paarspektrometer zum Einsatz, das über eine genaue Energiemessung der in den Reaktionen produzierten Photonen erlaubte, Kernzustände zu studieren. Einige Resultate von Peters Experimenten spielten später im Zusammenhang mit der *chiralen Störungsrechnung* der starken Wechselwirkung eine wesentliche Rolle.

Sein nächstes Engagement führte Peter Truöl 1979 ans CERN, wo am LEAR grosse Raten von Antiprotonen erzeugt werden konnten. Im Asterix-Experiment ging es wieder um die starke Wechselwirkung, diesmal im Proton-Antiproton System. Unter seiner Leitung wurden an unserem Institut zum ersten Mal grosse Vieldrahtproportionalkammern gebaut. Die Detektoren besassen eine sechseckige Geometrie mit einem Duchmesser von über einem Meter und bestanden aus drei aktiven Lagen, wobei zwischen der ersten und zweiten Lage ein Bleikonverter zur Detektion von Photonen eingebaut wurde.

1985 leitete Peter Truöl mit dem Beitritt zur H1 - Kollaboration am DESY in Hamburg eine neue Ära an unserem Institut ein. Es handelte sich bei diesem Experiment über tiefinelastische Streuung am ep - *Collider* HERA um die erste Hochenergieaktivität an unserem Institut. Hoch war nicht nur die Energie, bei der die durch die starke Wechselwirkung bestimmte Struktur der Protonen untersucht werden sollte, hoch war auch die Zahl der über 200 Physiker aus aller Welt, die am Experiment beteiligt waren. Unter seiner Leitung entwickelte unser Institut ein Triggerkonzept für dieses Experiment und baute die dafür notwendigen zylindrischen Propor-

tionalkammern, sowie eine Driftkammer. Dank Peter Truöls unermüdlichem Einsatz in engem Kontakt mit dem zuständigen Regierungsrat Dr. A. Gilgen flossen erhebliche finanzielle Mittel des Kantons Zürich in dieses Projekt. Daneben koordinierte er die Zusammenarbeit von PSI, ETH und der schweizerischen Industrie zum Bau eines supraleitenden Kompensationsmagneten für den HERA - Beschleuniger. Die Zürcher Beteiligung an H1 wurde später mit einer Zusammenarbeit mit der ETHZ und dem PSI ergänzt und trägt auch heute noch viel zum experimentellen Betrieb und der Publikationstätigkeit bei. HERA brachte neue Erkenntnisse in vielen Gebieten; besonders zu erwähnen wäre wohl die Bestätigung der Beschreibung der starken Wechselwirkung durch die Quantenchromodynamik in einem viel grösseren kinematischen Bereich mit hoher Genauigkeit.

Die nächste Station seiner Forschungstätigkeit führte Peter nach Brookhaven. Hier beteiligte er sich an verschiedenen Messungen zur Untersuchung seltener Kaonzerfälle, deren wichtigstes Resultat die Klärung der Stärke der Kopplung der *strange Quarks* an die schwache Wechselwirkung war. Auch für dieses Experiment baute er mit Hilfe der Werkstätten an unserem Institut grosse Vieldraht-Proportionalkammern.

Gesamthaft hat Peter Truöl in seiner 40 Jahre umfassenden aktiven Forschungszeit nicht weniger als 334 wissenschaftliche Arbeiten publiziert. Sie sind nicht nur wissenschaftlich interessant, besonderen Wert legte er auf die sprachliche Qualität. Auch in dieser Hinsicht diente er seinen Doktoranden als Vorbild.

Peter Truöl unterrichtete viele Jahre lang die Physik - Studierenden in Teilchenphysik und hielt unzählige Male die Grundvorlesungen für angehende Mediziner und Biologen. Dabei gelang es ihm, den Studierenden die Faszination an der Erforschung fundamentaler physikalischer Fragen zu vermitteln, und die Physik als Grundlagenfach den angehenden Naturwissenschaftern plausibel zu machen.

Peter Truöl ist nun ein halbes Jahrhundert lang mit dem Schicksal der Physik an unserer Universität verbunden. In dieser Zeit veränderte sich die Struktur und die Funktionsweise der Universität vollständig, parallel dazu nahm die Zahl aller Studierenden um mehr als einen Faktor 10 zu. Peter erlebte dabei drei Generationen von Physikprofessoren in ihrem Amt und überblickt so deren Einfluss auf die Entwicklung des Physik-Institutes.

Ein wichtiger und sehr nachhaltiger Beitrag von Peter Truöl zur Entwicklung der Experimental-Physik an unserer Universität war zweifellos seine mutige Initiative, grossen Hochenergiekollaborationen beizutreten, und komplexe Detektorsysteme dafür zu konstruieren. Deren Herausforderungen, besonders die verlangte mechanische Präzision und die Verwendung immer neuer Materialien und Produktionsmethoden, stimulierten die Entwicklung der technischen Infrastruktur des Physik-Institutes, vor allem der feinmechanischen Werkstatt, die sich so für ihre Qualitätsarbeit einen hervorragenden internationalen Ruf aufbauen konnte und von der mittlerweile auch viele andere Forschungsaktivitäten an unserer Universität profitieren dürfen.

Von 1993 bis 2000 leitete Peter Truöl am Paul-Scherrer-Institut das *Program Review Committee* für Kern- und Teilchenphysik, wo seine breite physikalische Erfahrung manchem möglichen und wohl auch unmöglichen Experiment zu Gute kam. Von 2001 bis 2004 war er Direktor des Physik-Institutes, anschliessend bis zu seinem Rücktritt Dekan der mathematisch-naturwissenschaftlichen Fakultät unserer Universität. Seit seinem Rücktritt fand er wieder mehr Zeit, sich der Forschung im Rahmen der H1 - Kollaboration zu widmen; wir freuen uns darüber, weiter mit ihm zusammenarbeiten zu können.

Mitarbeiter

Wissenschaftliches Personal

Enver	Alagöz	CMS
Milan	Allan	Oberflächenphysik
Yves	Allkofer	Dirac
Prof. Claude	Amsler	Dark Matter, Dirac, CMS
Holger	Bartolf	PTM
Simon	Berner	Oberflächenphysik
Dr. Roland	Bernet	LHCb
Dr. Ralf Patrick	Bernhard	DØ, LHCb
Ueli	Bieler	LHCb
Vittorio	Boccone	Dark Matter
Louis	Brandenberger	Oberflächenphysik
Thomas	Brugger	Oberflächenphysik
Angela	Büchler	LHCb
Dr. Vincenzo	Chiochia	CMS
Nicola	Chiapolini	LHCb
Claudio	Cirelli	Oberflächenphysik
Martina	Corso	Oberflächenphysik
Raffaele	Dell'Amore	PTM
Jan-Hugo	Dil	Oberflächenphysik
Andrei	Dolocan	Oberflächenphysik
Dr. Andreas	Engel	PTM
Conrad	Escher	Bio-Physik
Dr. Dmitry	Eshchenko	Supraleitung & Magnetismus
Prof. Hans-Werner	Fink	Bio-Physik
Dr. Carine	Galli Marxer	Oberflächenphysik
Dr. Johannes	Gassner	LHCb
Prof. Thomas	Greber	Oberflächenphysik
Dr. Petra S.	Häfliger	Supraleitung & Magnetismus
Viktor	Hangartner	LHCb
Dr. Matthias	Hengsberger	Oberflächenphysik
Stefan	Heule	UCN
Sosuke	Horikawa	Dark Matter, Dirac
Christoph	Hörmann	CMS
Dr. Ian	Johnson	Dark Matter
Prof. Hugo	Keller	Supraleitung & Magnetismus
Dr. Rustem	Khasanov	Supraleitung & Magnetismus
Andreas	Knecht	UCN
Dr. Michael	Krüger	Bio-Physik
Fabio	La Mattina	Supraleitung & Magnetismus
Dr. Igor	Landau	Supraleitung & Magnetismus
Dr. Tatiana	Latychevskaia	Bio-Physik
Dr. Frank	Lehner	DØ, LHCb
Dominik	Leuenberger	Oberflächenphysik

Wissenschaftliches Personal (cont)

Linus	Lindfeld	H1
Dr. Jorge	Lobo-Checa	Oberflächenphysik
Alexander	Maisuradze	Supraleitung & Magnetismus
Dr. Mihael	Mali	Supraleitung & Magnetismus
Thomas	Mattle	Oberflächenphysik
Martin	Morscher	Oberflächenphysik
Prof. K. Alex	Müller	Supraleitung & Magnetismus
Dr. Katharina	Müller	H1
Krzysztof	Nowak	H1
Dr. Hiroshi	Okamoto	Bio-Physik
Dr. Taichi	Okuda	Oberflächenphysik
Prof. Jürg	Osterwalder	Oberflächenphysik
Dr. Ralph E.	Pixley	G
Dr. Kirill	Prokofiev	CMS
Dr. Christian	Regenfus	CMS, Dark Matter, Dirac
Mark	Reibelt	PTM
Dr. Peter	Robmann	CMS, H1, $\pi \to e\nu$
Tanja	Rommerskirchen	CMS
Dr. Josef	Roos	Supraleitung & Magnetismus
Rosmarie	Rössel	Studienberatung
Dr. Tariel	Sakhelashvili	LHCb, $\pi \to e\nu$
Christophe	Salzmann	DØ,LHCb
Dr. Andries	van der Schaaf	$\pi \to e\nu$
Simon	Scheu	$\pi \to e\nu$
Prof. Andreas	Schilling	PTM
Dr. Richard	Schillinger	Oberflächenphysik
Carsten	Schmitz	H1
Prof. Toni	Schneider	Supraleitung & Magnetismus
Stefan	Siegrist	PTM
Dr. Thomas	Speer	CMS
Dr. Olaf	Steinkamp	LHCb
Elvira	Steinwand	Bio-Physik
Gregory	Stevens	Bio-Physik
Simon	Strässle	Supraleitung & Magnetismus
Prof. Ulrich	Straumann	H1, LHCb, $\pi \to e\nu$, UCN
Dr. Jeroen	van Tilburg	LHCb
Prof. Peter	Truöl	H1, $\pi \to e\nu$
Dr. Achim	Vollhardt	LHCb
Dimitro	Volyanskyy	LHCb
Tobias	Wassmann	Oberflächenphysik
Andreas	Wenger	DØ, LHCb
Stephen	Weyeneth	Supraleitung & Magnetismus
Lotte	Wilke	CMS
Bastian M.	Wojek	Supraleitung & Magnetismus
Dr. Stefania	Xella Hansen	H1

Technisches und administratives Personal

Cornel	Andreoli	Bio-Physik
Eva	Baby	Sekretariat
Kurt	Bösiger	Werkstatt
Tiziano	Crudeli	Zeichnen
Walter	Fässler	Dokumentation, Elektronik
Omid	Fardin	Werkstatt
Ruth	Halter	Sekretariat
Martin	Klöckner	Oberflächenphysik
Bruno	Lussi	Werkstatt
Reto	Maier	Werkstatt
Hanspeter	Meyer	Elektronik
Lucien	Pauli	Vorlesungsbetrieb
Rolf	Reichen	Werkstatt
Jacky	Rochet	CMS, Dark Matter, Dirac
Monika	Röllin	Sekretariat
Marcel	Schaffner	Werkstatt
Jacqueline	Schenk	Sekretariat
Silvio	Scherr	Werkstatt
Jürg	Seiler	Vorlesungsbetrieb
Peter	Soland	Elektronik
Stefan	Steiner	CAD, CMS, LHCb
Karoly	Szeker	Elektronik

Contents

Physics of Fundamental Interactions and Particles 1

1 Determination of Newton's Gravitational Constant 1

2 Towards a dark matter experiment 3

2.1 Photomutiplier operation at low temperature 4

2.2 Light yield in argon 5

3 A precision determination of the $\pi^+ \to e^+ \nu$ branching ratio 9

3.1 Lepton universality 9

3.2 $\Gamma_{\pi \to e\overline{\nu}}/\Gamma_{\pi \to \mu\overline{\nu}}$ 9

3.3 Measurement principles 10

3.4 Status of PEN 11

4 Search for $K\pi$-atoms 13

4.1 Aerogel Čerenkov-detector 14

4.2 Heavy gas system 16

4.3 Outlook 17

5 Particle Physics at DESY/HERA (H1) 19

5.1 Electron-proton collisions at a centre of mass energy of 320 GeV - summary 19

5.2 Technical status of the H1 experiment 20

5.3 Low energy run 22

5.4 Results from recent analyses 23

6 High-precision CP-violation Physics at LHCb 31

6.1 LHCb detector 31

6.2 Silicon tracker 32

6.3 Trigger tracker 32

6.4 Readout system . . . 34
6.5 Detector simulation and reconstruction software . . . 34
6.6 Physics studies . . . 35
6.7 Summary and outlook . . . 35

7 Particle Physics with CMS **36**
7.1 Reconstruction software . . . 37
7.2 $B_s \to (J/\psi)\phi$ . . . 37
7.3 $h \to b\bar{b}$ in SUSY cascades . . . 39
7.4 Pixel sensors and associated software . . . 39
7.5 Pixel efficiency . . . 42
7.6 Detector support structure and service tubes . . . 43

Condensed Matter Physics **46**

8 Superconductivity and Magnetism **46**
8.1 Studies of oxygen isotope effects in novel superconductors . . . 46
8.2 Studies of pressure effects in novel superconductors . . . 48
8.3 Spectroscopic studies of novel electronic materials . . . 49
8.4 Magnetic properties of novel electronic materials . . . 55
8.5 Electric field effects in perovskites . . . 58
8.6 New developments in instrumentation and data handling . . . 59

9 Phase transitions, new materials and superconducting γ detectors **62**
9.1 Physics of superconducting thin-film nanostructures and possible applications as fast single-photon detectors . . . 62
9.2 A history dependent first-order like phase transition feature near H_{c2} in V_3Si . . . 65
9.3 Search for resonance phenomena in $TlCuCl_3$ in the MHz range . . . 67
9.4 Cation and anion substitution in $LaSrNiO_4$ and $LaBaNiO_{4-\delta}$ . . . 69

10 Surface Physics **71**

10.1 A new surface state on Ni(111) 73

10.2 Boron nitride nanomesh: a corrugated monolayer 74

10.3 Trapping molecules in the nanomesh pores 76

10.4 Using the nanomesh as a template for magnetic cluster growth 77

10.5 The unoccupied band structure of h-BN on Ni(111). 78

10.6 Two-photon photoemission from h-BN on Ni(111) across the ferromagnetic phase transition 80

10.7 Hydrogen in C_{60} 82

10.8 Test of a new electron detection scheme for Mott polarimeters 83

11 Physics of Biological Systems **85**

11.1 Holography of single molecules 85

11.2 Activation barrier for single DNA diffusion 92

11.3 Coherent low-energy electron diffraction microscopy of single biomolecules . . . 93

11.4 Bachelor studies 97

11.5 Education 97

Infrastructure and Publications **98**

12 Mechanical Workshop **98**

13 Electronics Workshop **103**

14 Publications **105**

1 Determination of Newton's Gravitational Constant

R.E. Pixley and U. Straumann

in collaboration with: St. Schlamminger, University of Washington, Seattle, USA.

The measurement of Newton's gravitational constant G has been an on-going project at our institute since 1994. Walter Kündig directed the gravitation group up until the time of his death in May 2005. Initial interest in this field was motivated by measurements indicating the possibility of a "fifth" force. This prompted measurements at the storage lake in Gigerwald in which the water level varied by 44 m. The experiment involved weighing two test masses (TM's) suspended next to the lake at different heights. No evidence was found (1) for the proposed "fifth" force. But, considering the large distances involved, a reasonably accurate value for Newton's gravitational constant G was obtained with an uncertainty of 750 ppm.

It was realized that the same type of measurement could be made in the laboratory with much better accuracy with the lake being replaced by the well defined geometry of a vessel containing a dense liquid such as mercury. Equipment for this purpose was designed and constructed in which two 1.1 kg TM's were alternately weighed in the presence of two moveable field masses (FM's) each with a mass of 7.5 tons. The experiment was installed in a quiet area at the Paul-Scherrer-Institut (PSI). A first series of measurements of G with this equipment resulted in an uncertainty of 220 ppm (2), dominated by the unknown nonlinearity of the balance response function.

In a second series of measurements, a system of auxiliary masses was introduced which allowed a systematic variation of the balance loading thereby making possible an estimate of slight nonlinearities in the response function of the balance. A brief report of these measurements has been given in (3) and a more detailed description in a thesis (4).

Since terminating the measurements, the last three years have been spent in improving the analysis and checking for possible systematic errors. The final analysis results in (5):

$$G = 6.67425(12) \times 10^{-11}\ \mathrm{m^3\ kg^{-1}\ s^{-2}}$$

with a relative uncertainty of 18 ppm. The value is in reasonable agreement with our previously published value (3) which had an uncertainty of 33 ppm. The improvements in the analysis are due to

- a more restrictive selection of data,
- a curvature correction for the zero-point drift of the balance,
- a better determination of the response function of the balance and
- the use of the measured mercury density, together with the mass and the volume of the FM's to constrain the mass-integration constant.

The smaller uncertainty obtained for G was due mainly to an 18 ppm to 6.1 ppm decrease in the relative uncertainty of the response function and a 20 ppm to 6.7 ppm decrease in the relative uncertainty of the mass-integration constant.

In Fig. 1.1, the values of G obtained in the most accurate torsion balance measurements are compared to that obtained in our beam balance measurement. Due to previous discrepancies in the reported values of G, all of which were measured with torsion balances, our measurement made with an entirely differ-

ent method is a valuable contribution to the current debate over the true value of G.

The experiment could not have been carried out without the close support of the Mettler-Toledo company which donated the balance used in this measurement and made their laboratory available for our use. Also, the Swiss Metrological Institute and the Physikalisch-Technische Bundesanstalt, Braunschweig, Germany made a number of certified precision measurements which were very important for this experiment.

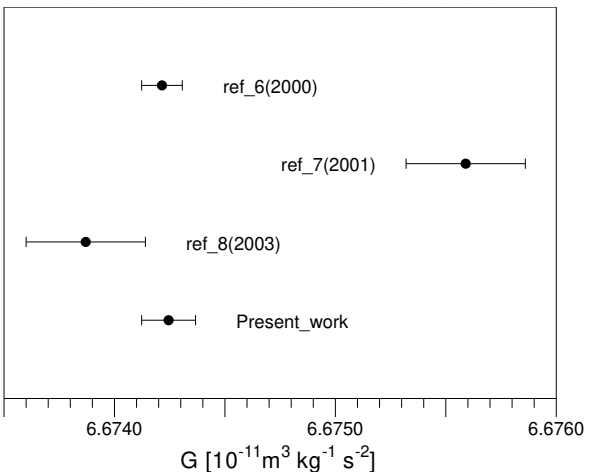

Figure 1.1:
Recent measurements of G with relative errors less than 50 ppm. The labels refer to the experiments described in ref. [6], [7] and [8], respectively.

[1] B. Hubler et al., Phys. Rev. **D51**, 4005 (1995).

[2] F. Nolting et al., Meas. Sci. Technol. **10**, 439 (1999).
F. Nolting, Dissertation, Universität Zürich (1998).
J. Schurr et al., Phys. Rev. Lett. **80**, 1142 (1998).
J. Schurr et al., Phys. Lett. **A 248**, 295 (1998).

[3] St. Schlamminger, E. Holzschuh and W. Kündig, Phys. Rev. Lett. **89**, 161102-1 (2002).
See also "Wissenschaftlicher Jahresbericht 2002/3", Physik-Institut Universität Zürich, page 1
http://www.physik.unizh.ch/reports/jb/2003/jb2003.pdf

[4] St. Schlamminger, Dissertation, Universität Zürich (2002).

[5] St. Schlamminger, E. Holzschuh, W. Kundig, F. Nolting, R. E. Pixley, J. Schurr and U. Straumann, Phys. Rev. D **74**, 082001 (2006).

[6] J. H. Gundlach and S. M. Merkowitz, Phys. Rev. Lett. **85**, 2869 (2000).

[7] T. J. Quinn, C. C. Speake, S. J. Richman, R. S. Davis and A. Picard, Phys. Rev. Lett. **87**, 111101-4(2001).

[8] T. R. Armstrong and M. P. Fitzgerald, Phys. Rev. Lett. **91**, 201101-4(2003).

2 Towards a dark matter experiment

C. Amsler, V. Boccone, H. Cabrera, S. Horikawa, P. Lightfoot[3], C. Regenfus, and J. Rochet

in collaboration with:
CIEMAT, ETHZ, Soltan Institute (Warsaw), Universities of Granada and Sheffield

(ArDM Collaboration)

In 2006 we continued the development of the light readout system for the ArDM dark matter experiment. We plan to use a one ton liquid argon time projection chamber to detect recoil nuclei from the scattering of Weak Interacting Massive Particles. WIMPs are among the favorite candidates for the missing non-baryonic matter in the universe, and the prominent candidate is the lightest supersymmetric (SUSY) particle, the neutralino, with a mass of at least 40 GeV. The experimental upper limit for the cross-section of WIMPs with nucleons is about 10^{-6} pb, a cross section that would lead to 100 events per day in the ArDM detector, assuming a detection threshold of 30 keV for recoil argon nuclei.

Details on the experiment can be found in our previous annual report and in ref. (1). The drifting electron charge from ionizing recoils and the VUV scintillation light (128 nm) will be recorded with high efficiency to suppress the electron background from the radioactive β-emitter ^{39}Ar. Its activity in natural ^{40}Ar argon has been measured to be about 1 Bq/kg (2), therefore inducing a background rate of about 1 kHz in a one ton detector. The rejection of the γ- and β-background will be achieved through the combined measurement of the charge-to-light ratio, the time structure of the light signal, and the determination of the interaction point on an event-by-event basis.

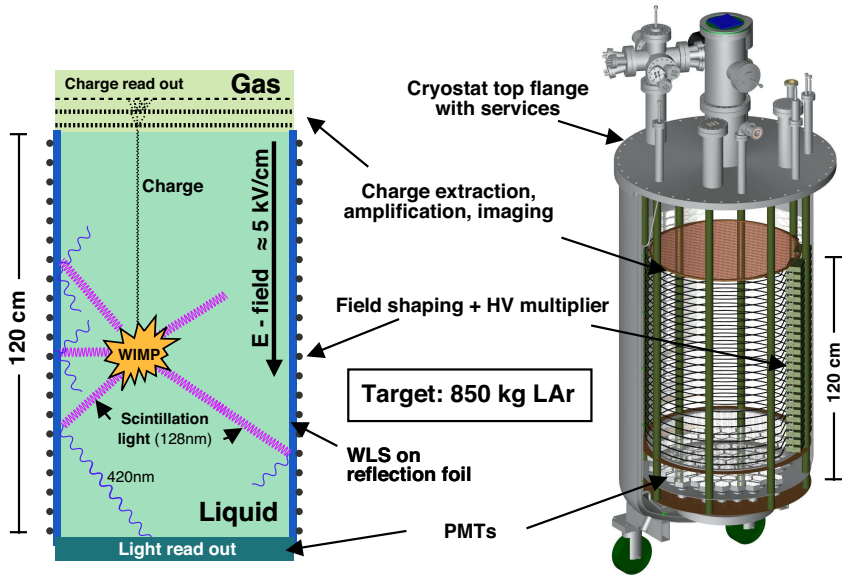

Figure 2.1: Detection principle and 3D-drawing of the ArDM detector.

[3]Visitor from the University of Sheffield

The ratio of primary scintillation light to ionization charge collected after a given drift time in an external electric field is different for nuclear recoils and minimum ionizing particles, being very high for the former, due to quenching. This provides the main discrimination between WIMPs and background. On the other hand, the VUV photons are produced from the spin singlet and triplet states of the excited dimer A_2^*, following ionization, which have different lifetimes (τ = 7 ns, resp. 1.6 μs in liquid (3)). These states are populated differently according to the excitation process: for heavy ionization (such as nuclear recoils) the singlet dominates, while for minimum ionizing particles (such as electrons) the triplet dominates (3). Hence the discrimination of decay time allows a further separation between WIMP induced recoils and background from γ or electrons.

The working principle of the two-phase detector is shown in Fig. 2.1 (left). A WIMP interaction leading to 30 keV recoils produces about 400 VUV photons, together with a few free electrons. The strong vertical electric field (5 kV/cm) sweeps the electrons to the top surface of the liquid and extracts them into the gas phase. After multiplication ($\approx 10^5$) in a two stage Large Electron Multiplier (LEM) the charges are collected by a segmented anode. The VUV light is emitted isotropically from the interaction point and converted to blue light by a wavelength shifter (WLS) on the side walls. The shifted and reflected light is collected at the bottom of the cryostat by 14 phototubes (8") immersed in the liquid. The 3D-CAD sketch (Fig. 2.1, right) shows the mechanical design of the prototype detector and the cryostat. Not shown is the (non-conductive) wavelength shifting foil inside the field shapers.

2.1 Photomutiplier operation at low temperature

Low temperature photomultipliers (PMTs) covering a surface of ≈1.5 m^2 and immersed in liquid argon will be used in the ArDM experiment. A bialkali photocathode has a quantum efficiency of typically 30% at room temperature, but becomes insulant at liquid argon temperatures (≈ 88K). A platinum (Pt) underlay under the photocathode is necessary to restore the electron population in the photocathode. Unfortunately, this solution also reduces the quantum efficiency to ≈15%.

We have investigated two 3" PMTs for their functionality and quantum efficiency at low temperature. The best result was obtained with a square 8-dynode tube from Hamamatsu (R6237-MOD) manufactured with Pt-underlay. The dark current (thermal emission rate × gain) and the response to light (gain) were measured. Figure 2.2 shows the expected decrease of dark current for the Hamamatsu tube at low temperature, while the light response remains constant (the slight increase in Fig. 2.3 is attributed to a gain fluctuation).

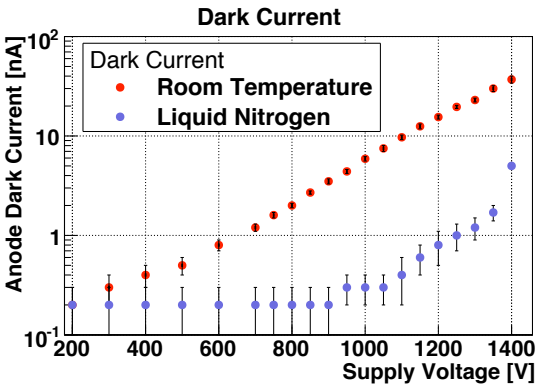

Figure 2.2: Dark current vs. bias voltage for room and liquid N_2 temperature.

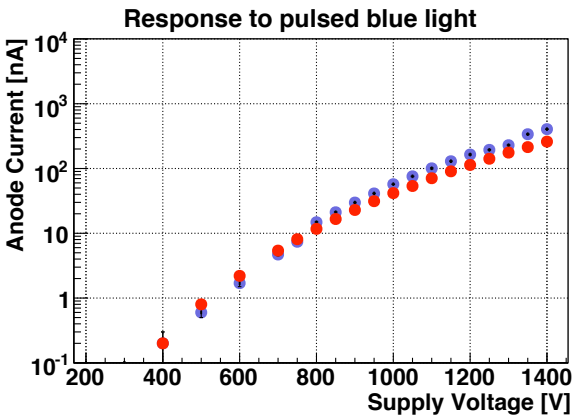

Figure 2.3: Response to blue light of the Hamamatsu PMT vs. bias for room (red dots) and liquid N_2 (blue dots) temperature.

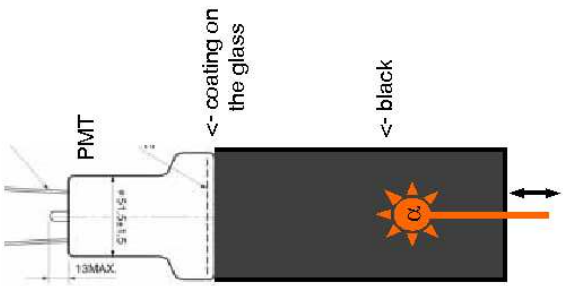

Figure 2.4: Experimental setup.

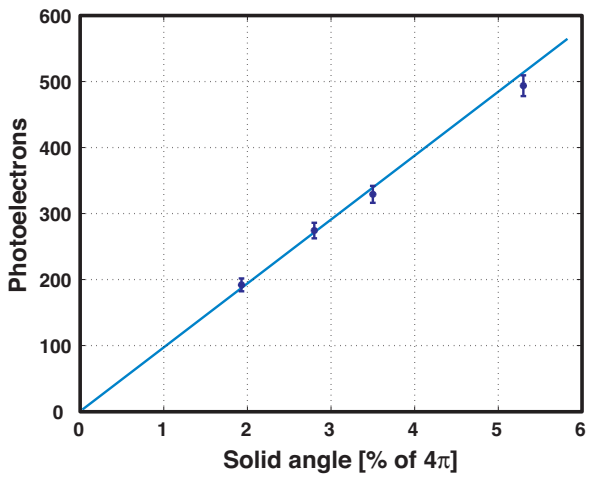

Figure 2.5: Number of photoelectrons from the 5.3 MeV α-source as a function of the solid angle subtended by the Hamamatsu R6237-MOD PMT in argon gas.

To optimize the light collection efficiency we performed various measurements with different setups, reflectors material and WLS. For example, the glass window of PMTs can be coated with a WLS within a matrix of paraloid or polystyrene (4), giving thin transparent wavelength shifting layers. Light emitted from the WLS in the (optically dense) matrix is trapped and efficiently produces photoelectrons at the photocathode. Efficient conversion of VUV light was observed by coating the PMT glass surface with tetraphenyl-butadiene (TPB) dissolved in paraloid or polystyrene (PS). The layer (1 μm thickness) was deposited by dissolving TPB/PS in chloroform and dipping the PMT in the solution. A black box filled with argon gas and a 5.3 MeV movable α-source were used (Fig. 2.4). The number of photoelectrons was measured for different distances between the PMT and the α-source. As expected, the data expressed as a function of solid angle is compatible with a straight line. We obtained 480 photoelectrons for a 5% solid angle, which corresponds to a quantum efficiency of about 12%.

2.2 Light yield in argon

We have determined the light yield in gaseous and liquid argon and established the ratio of singlet to triplet contributions. Our measurements in gas with a 5ℓ vacuum chamber showed that the number of photoelectrons depends crucially on the purity of argon, the contribution from the slow component and its decay time increasing with purity (see our previous annual report). The two decay components were clearly observed with a mean life of 15.7 $\pm$ 4.0 ns for the fast (singlet) and 3.12 $\pm$ 0.08 μs for the slow (triplet) component (5). The latter is in good agreement with literature, 3.2 $\pm$ 0.3 μs (6). A first attempt to measure the singlet to triplet population ratio in liquid is shown in Fig. 2.6. The plots show the ratio R of fast ($<$ 50 ns) to total light output vs. total amplitude for the Po α-source (left) and with

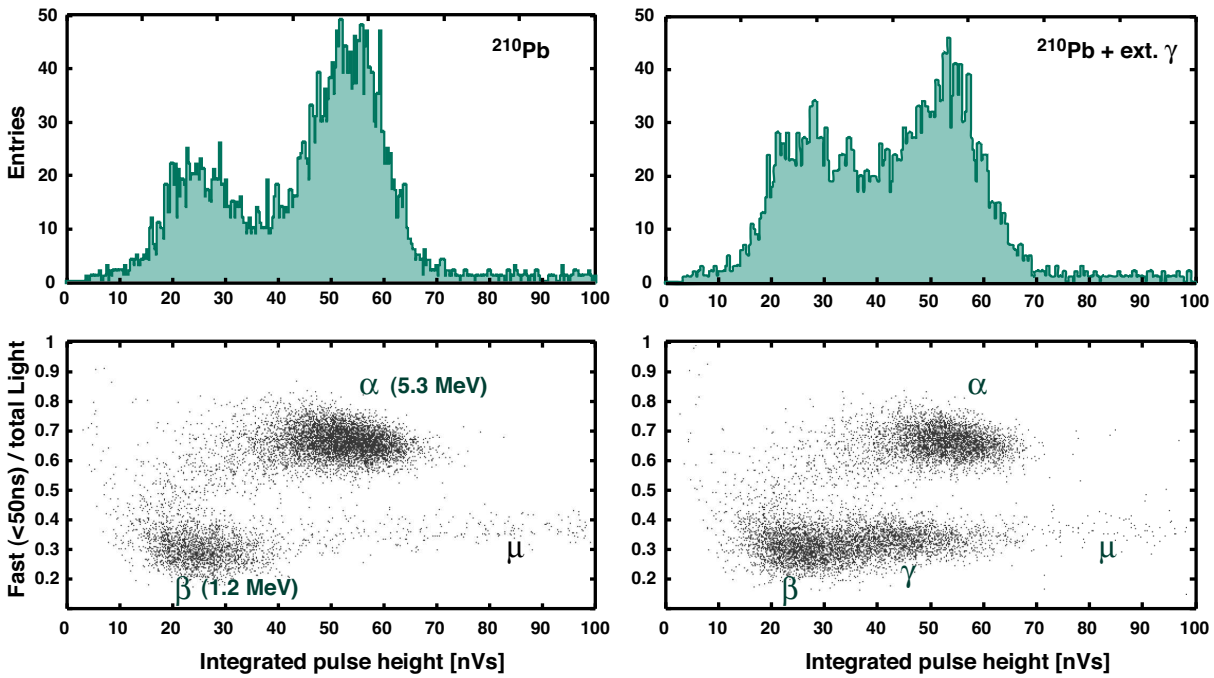

Figure 2.6: Ratio R of fast to total light output vs. time integrated amplitude with (left) and without (right) external γ source.

an additional external γ-source (right). One observes a clear separation between heavily ionizing projectiles and electrons.

Figures 2.7 and 2.8 show the improved apparatus built in 2006. Two Hamamatsu (R6237-MOD) PMTs face one another. The cell volume is roughly 1ℓ and an α-source is located in the center. The PMT glass surfaces are coated with a transparent TPB/paraloid layer. The side walls consist of 10×10 cm^2 foils with evaporated TPB. The analogue signal from the PMT is sampled by a 1 GHz digital oscilloscope, stored to hard disk and analysed offline.

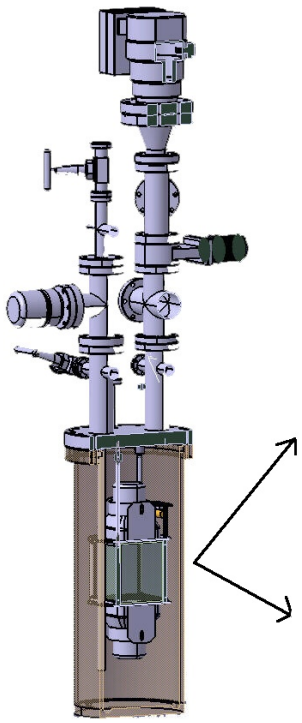

Figure 2.7: 2006 setup.

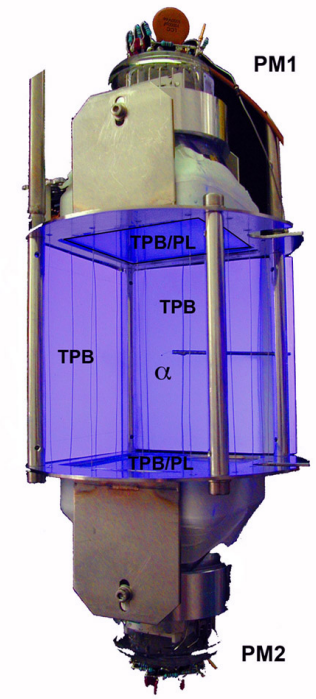

Figure 2.8: Enhanced view of the liquid argon cell cell under UV illumination.

A baseline correction is performed with the portion of the signal before trigger time. The noise is determined by the amplifier. The number of detected photons is calculated as usual by dividing the integrated charge by the average single photon charge, which we find from distributions of dark counts and LED light pulses.

From several measurements with the old and the new setup we find an average value for the triplet to singlet ratio of 6.0 $\pm$ 1.8 for 5.3 MeV α in argon gas at NTP. The error was estimated from fluctuations among the data sets. The largest measured value for the triplet decay time τ_2 = 3.12 μs, mentioned above, was found for the purest argon gas. Impurities in argon gas were found to reduce the scintillation light by shortening the decay time τ_2. This effect was studied in detail by mixing argon gas with air at partial pressures between 1 and 10^{-6} mbar (5). For the various partial air pressures the averaged α-signals were fitted and analysed, as described above. Figure 2.9 shows the yields obtained for the fast and slow components vs. τ_2. The contribution from the slow component increases linearly with τ_2, reaching to 3.2 μs in gas at NTP, while the fast component remains constant. This behaviour can be explained as due to the non-radiative destruction of the triplet excimer states by gas impurities. This is presumably due to residual water, since cooling improves on the light yield (and τ_2).

Figure 2.10 shows measurements done with different coatings and reflectors. From the known yield of VUV photons (78 k / α-particle (7)), we find the detection efficiencies (defined as the ratio of detected photoelectrons to emitted UV photons) for the different designs by extrapolating to τ_2 = 3.2 μs. The best result (1% detection efficiency) was achieved with TPB evaporated on 3M reflective foils.

Evaporation leads to a much more uniform coating than spraying (Fig. 2.11). We have de-

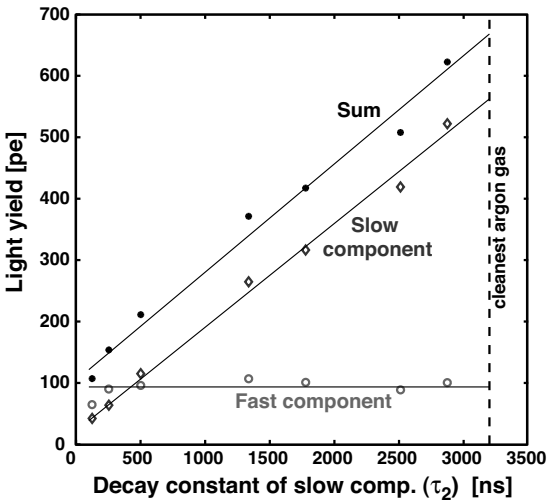

Figure 2.9:
Light yield (number of photoelectrons) in gaseous argon (NTP) as a function of τ_2. The measurements correspond to different partial air pressures.

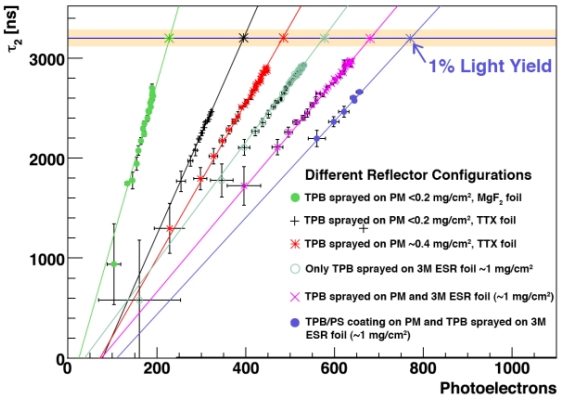

Figure 2.10: τ_2 vs. number of photoelectrons for various coatings and reflectors.

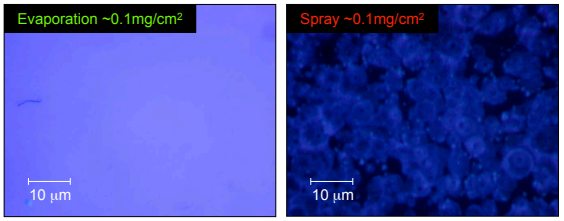

Figure 2.11: Microscope comparison between evaporated and sprayed TPB, illuminated by UV light.

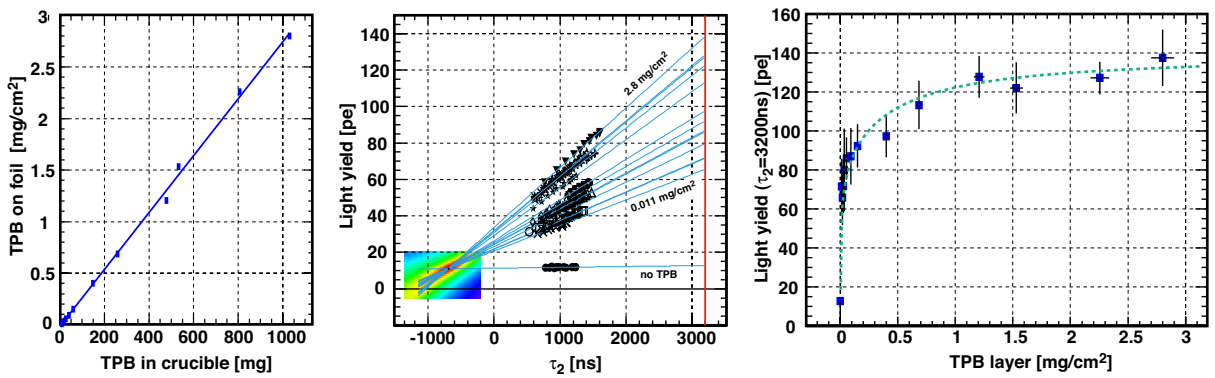

Figure 2.12: Left: TPB thickness vs. mass in crucible. Middle: number of photoelectrons vs. τ_2. Right: number of photoelectrons vs. TPB thickness. The dashed line is drawn to guide the eye.

termined the optimum thickness of TPB wavelength shifter to be evaporated on the 3M reflector by using the black box setup shown in Fig. 2.4. A small glass exsicator was modified to include a heated crucible. The layer thickness of TPB was calculated by weighing the foil before and after vacuum evaporation. Figure 2.12 (left) shows the expected linear correlation between the deposited thickness and the mass of TPB prepared in the crucible, which demonstrates the reliability of the procedure. Figure 2.12 (middle) shows the light yield as a function of τ_2 (hence gas purity) for various TPB thicknesses. The straight lines are fits to a common intersection point. Extrapolation to τ_2 = 3.2 μs lead to the expected light yield for 100% argon purity. The latter is shown as a function of TPB thickness in Fig. 2.12 (right). Saturation is observed above 1 mg/cm^2 which corresponds to a film of about 10 μm thickness.

A similar correlation between light yield and τ_2 seems to be observed in liquid argon and is the subject of our present investigations. The goal is to collect enough light in liquid to distinguish between nuclear recoils and electrons and to measure the suppression factor for ^{39}Ar background events. In liquid the light output from the α-emitter is quenched by the strong dE/dx and one expects about 15 photons / keV (or 450 photons from a recoiling nucleus of 30 keV), while a minimum ionizing particle leads to 40 photons / keV in the absence of electric field (8).

Our R&D developments for the VUV light yield are encouraging for a large detector volume, the goal being to reach 2%, while 1% has already been achieved. We will therefore proceed with the construction of the one ton prototype in 2007.

[1] C. Regenfus, Proc. 6th Int. Workshop on the Identification of Dark Matter (IDM06), Rhode Island, World Scientific, 2006.

[2] P. Benetti et al. (WARP Collaboration), preprint astro-ph/0603131 (2006).

[3] A. Hitachi et al., Phys. Rev. **B 27** (1983) 5279.

[4] G. Eigen, E. Lorenz, Nucl. Instr. Meth. **166** (1979) 165.

[5] A. Büchler, Bachelor Thesis, Universität Zürich (2006).

[6] J. Keto et al., Phys. Rev. Lett. **33** (1974) 1365.

[7] R. Chandrasekharan et al., Nucl. Instr. Meth. in Phys. Res. **A 546** (2005) 426.

[8] P. Cennini et al., Nucl. Instr. Meth. in Phys. Res. **A 432** (1999) 240.

3 A precision determination of the $\pi^+ \to e^+\nu$ branching ratio

P. Robmann, T. Sakhelashvili, A. van der Schaaf, S. Scheu, and U. Straumann

in collaboration with: Department of Physics, University of Virginia, Charlottesville, USA; Institute for Nuclear Studies, Swierk, Poland; JINR, Dubna, Russia; Paul Scherrer Institut, Villigen, Switzerland and Rudjer Bošković Intitute, Zagreb, Croatia

(PEN Collaboration)

3.1 Lepton universality

Lepton universality postulates that the interactions of leptons do not explicitely depend on lepton family number other than through their different masses and mixings. The concept can be generalized to include the quarks. Whereas there is little doubt about the universality of electric charge (*i.e.* the coupling strength to photons) there are scenarios outside the Standard Model (SM) in which lepton universality is violated in the interactions with W and Z bosons.

Allowing for universality violations one can generalize the $V-A$ charged current weak interaction of leptons to [4]:

$$\mathcal{L} = \sum_{l=e,\mu,\tau} \frac{g_l}{\sqrt{2}} W_\mu \overline{\nu}_l \gamma^\mu (\frac{1-\gamma_5}{2}) l + \text{h.c.} \qquad (3.1)$$

Violations may also have their origin in non-SM contributions to the transition amplitudes. Such apparent violations of lepton universality have been discussed in the literature for various particle decays:

- in W, Z and π decay resulting from R-parity violating extensions to the MSSM (1; 2),
- in W decay resulting from charged Higgs bosons (3),
- in π decay resulting from box diagrams involving non-degenerate sleptons (4),
- in K decay resulting from LFV contributions in SUSY (5),
- in Υ decay resulting from a light Higgs boson (6),
- in π and K decay from scalar interactions (7), enhanced by the strong chiral suppression of the SM amplitude for decays into $e\overline{\nu}_e$. Since these contributions result in interference terms with the SM amplitude the deviations scale with the mass M of the exchange particle like $1/M^2$ rather than $1/M^4$ as may be expected naively.

Experimental limits have recently been compiled by Loinaz *et al.* (8). Results are shown in Table 3.1.

3.2 $\Gamma_{\pi\to e\overline{\nu}}/\Gamma_{\pi\to\mu\overline{\nu}}$

In lowest order (tree level) the decay width of $\pi \to l\overline{\nu}_l$ ($l = e, \mu$) is given by:

$$\Gamma^{\text{tree}}_{\pi\to l\overline{\nu}_l} = \frac{g_l^2 g_{ud}^2 V_{ud}^2}{256\pi} \frac{f_\pi^2}{M_W^4} m_l^2 m_\pi (1-\frac{m_l^2}{m_\pi^2})^2 \ . \quad (3.2)$$

By taking the branching ratio $R_{e/\mu} \equiv \Gamma_{\pi\to e\overline{\nu}}/\Gamma_{\pi\to\mu\overline{\nu}}$ the factors affected by hadronic uncertainties cancel. Radiative corrections lower the result by 3.74(3)% (9) when assuming that final states with additional photons are included.

[4] Still more general violations lead to deviations from the $1-\gamma_5$ structure of the weak interaction.

Table 3.1:Limits on lepton universality from various processes. Violations may affect the various tests differently so which constraint is best depends on the mechanism. Hypothetical non V-A contributions, for example, would lead to larger effects in decay modes with stronger helicity suppression such as $\pi \to e\nu$ and $K \to e\nu$. Adapted from Ref. [8].

decay mode			constraint	
W	$\to$	$e\,\overline{\nu}_e$	$(g_\mu/g_e)_W = 0.999$	$\pm\,0.011$
W	$\to$	$\mu\,\overline{\nu}_\mu$	$(g_\tau/g_e)_W = 1.029$	$\pm\,0.014$
W	$\to$	$\tau\,\overline{\nu}_\tau$		
μ	$\to$	$e\,\overline{\nu}_e\,\nu_\mu$	$(g_\mu/g_e)_\tau = 0.9999$	$\pm\,0.0021$
τ	$\to$	$e\,\overline{\nu}_e\,\nu_\tau$	$(g_\tau/g_e)_{\tau\mu} = 1.0004$	$\pm\,0.0022$
τ	$\to$	$\mu\,\overline{\nu}_\mu\,\nu_\tau$		
π	$\to$	$e\,\overline{\nu}_e$	$(g_\mu/g_e)_\pi = 1.0021$	$\pm\,0.0016$
π	$\to$	$\mu\,\overline{\nu}_\mu$	$(g_\tau/g_e)_{\tau\pi} = 1.0030$	$\pm\,0.0034$
τ	$\to$	$\pi\,\nu_\tau$		
K	$\to$	$e\,\overline{\nu}_e$	$(g_\mu/g_e)_K = 1.024$	$\pm\,0.020$
K	$\to$	$\mu\,\overline{\nu}_\mu$	$(g_\tau/g_\mu)_{K\tau} = 0.979$	$\pm\,0.017$
τ	$\to$	$K\,\overline{\nu}_\tau$		

This leads to the theoretical prediction:

$$R_{e/\mu}^{theor.} = (g_e/g_\mu)^2 \times 1.2354(2) \cdot 10^{-4} \quad . \qquad (3.3)$$

Two experiments (10; 11) contribute to the present world average for the measured value:

$$R_{e/\mu}^{exp.} = 1.231(4) \times 10^{-4} \quad . \qquad (3.4)$$

As a result μe universality has been tested at the level: $(g_\mu/g_e)_\pi$=1.0021(16) (see Table 3.1).

3.3 Measurement principles

Measurements of $R_{e/\mu}$ are based on the analysis of e^+ energy and time delay with respect to the stopping π^+. The decay $\pi \to e\nu$ is characterized by $E_{e^+} = 0.5 m_\pi c^2 = 69.8$ MeV and an exponential time distribution following the pion life time τ_π=26 ns. In the case of the $\pi \to \mu\nu$ decay the 4 MeV muons which have a range of about 1.4 mm in plastic scintillator can be kept inside the target and are monitored by the observation of the subsequent decay $\mu \to e\nu\overline{\nu}$ which is characterized by $E_{e^+} < 0.5 m_\mu c^2 = 52.8$ MeV and a time distribution which first grows according to the pion life time and then falls with the muon life time.

A major systematic error is introduced by uncertainties in the low-energy tail of the $\pi \to e\nu(\gamma)$ energy spectrum in the region below $0.5 m_\mu c^2$. This tail fraction typically amounts to $\approx$1 % . The low-energy tail can be studied by suppressing the $\pi \to \mu \to e$ chain by the selection of early decays and by vetoing events in which the muon is observed in the target signal. Suppression factors of typically 10^{-5} have been obtained. A study of this region is also interesting since it might reveal the signal from a heavy sterile neutrino (12).

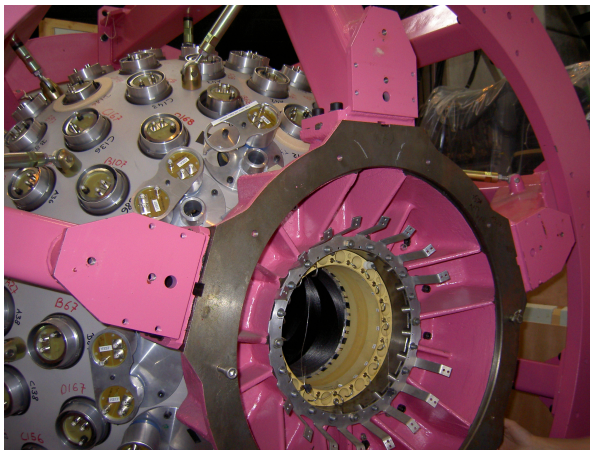

Figure 3.1: The PEN CsI calorimeter before installation of the cylindrical tracking detectors and beam counters shown in Fig. 3.2.

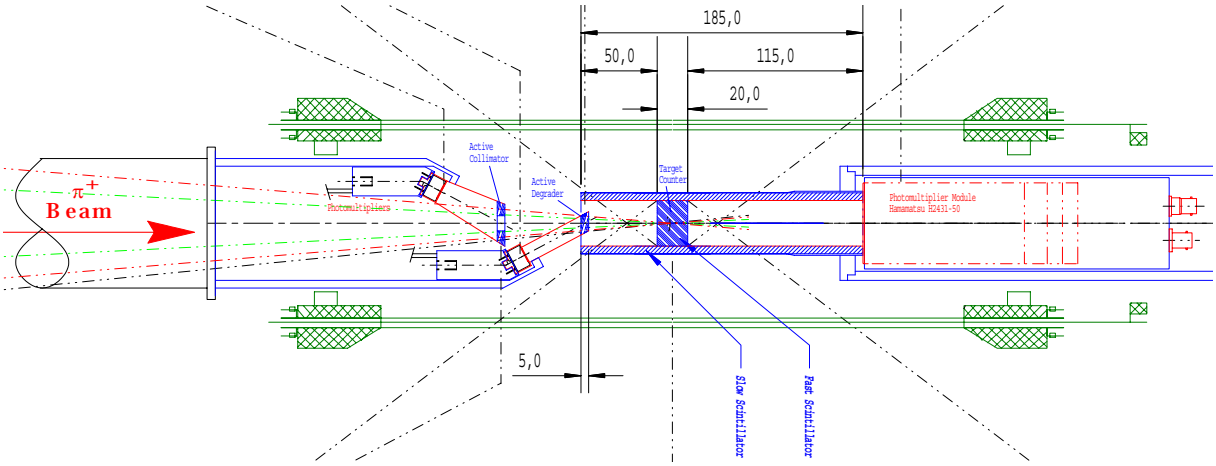

Figure 3.2: y - z view of the innermost MWPC (in green) and three of the four beam counters (in blue). A fourth detector situated in an intermediate focus a few meters upstream is used to measure particle velocities which helps to suppress muons in the beam and to calculate the pion momentum on an event-by-event basis.

3.4 Status of PEN

Both at PSI (13) and at TRIUMF (16) proposals for new $R_{e/\mu}$ measurements have been accepted. At PSI the 3π sr CsI calorimeter built for a determination of the $\pi^+ \to \pi^0 e^+ \nu$ branching ratio (see Fig. 3.1) is being used. The setup was also used for the most complete studies of the radiative decays $\pi \to e\nu\gamma$ (14) and $\mu \to e\nu\bar{\nu}\gamma$ (15) done so far.

Large samples of $\pi \to e\nu$ decays have been recorded parasitically in the past which were used as normalization for $\pi^+ \to \pi^0 e^+ \nu$ with an accuracy of $< 0.3\%$, *i.e.* the level of the present experimental uncertainty of $R_{e/\mu}$. Based on this experience an improvement in precision for $R_{e/\mu}$ by almost an order of magnitude is expected.

Our institute supplied new beam counters optimized for the specific requirements of these measurements (Fig. 3.2) *i.e.* optimal time, energy and double-pulse resolutions. The signals from these fast scintillating detectors are recorded with wave-form digitizers allowing for optimal off-line reconstruction of the complex target information containing two or three overlapping signals (see Fig. 3.3).

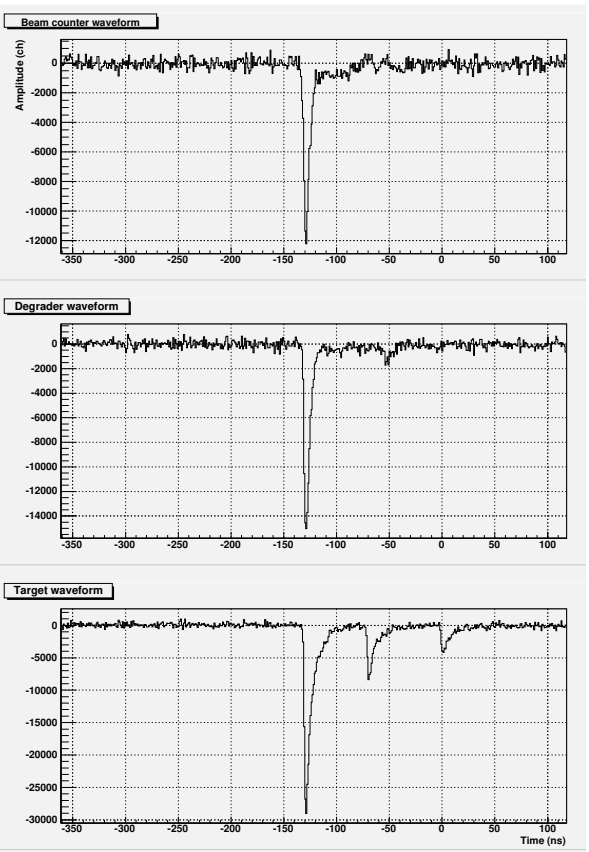

Figure 3.3: Beam-counter wave forms for the event of a π^+ stopping in the active target followed by the decay sequence $\pi \to \mu\bar{\nu}$, $\mu \to e\nu\bar{\nu}$. The sampling frequency is 2 GHz.

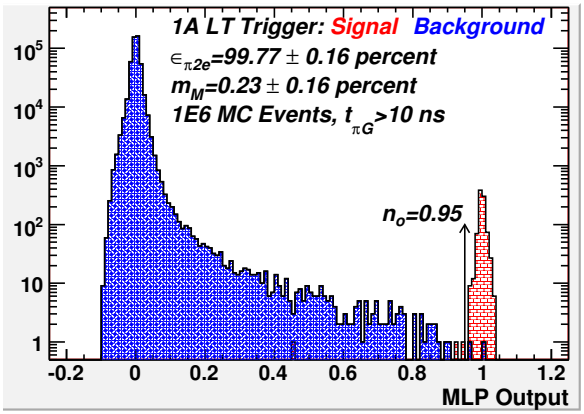

Figure 3.4: Separation of $\pi \to e\bar{\nu}$ and $\pi \to \mu\bar{\nu}$ events using a multi-layer perceptron (MLP) artificial neural network.

As mentioned above the separation of $\pi \to e\nu(\gamma)$ from $\pi \to \mu\nu(\gamma)$ is based on the analysis of many pieces of information. As discussed in some detail in Sec. 5 for the separation of single photons from π^0 decays various methods are available. Figure 3.4 shows as an example the separation obtained with an artificial neural network.

Presently we are replacing the plastic hodoscope situated between the tracking detectors detectors and the CsI calorimeter. First tests have shown that the light yield will increase by more than an order of magnitude which will guarantee both the very high positron detection efficiency and the subnanosecond time resolution required for this experiment. Starting early September we hope to take data which should lead to a first significant improvement in $R_{e/\mu}$.

[1] O. Lebedev, W. Loinaz and T. Takeuchi, Phys. Rev. D **61** (2000) 115005.

[2] M. J. Ramsey-Musolf, Phys. Rev. D **62** (2000).

[3] J. h. Park, JHEP **0610** (2006) 077.

[4] M. J. Ramsey-Musolf and S. Su, "Low energy precision test of supersymmetry," arXiv:hep-ph/0612057.

[5] A. Masiero, P. Paradisi and R. Petronzio, Phys. Rev. D **74** (2006) 011701.

[6] M. A. Sanchis-Lozano, Contributed paper to the Workshop on B-Factories and New Measurements, September 13-14, 2006, KEK, arXiv:hep-ph/0610046.

[7] B.A. Campbell and D.W. Maybury, Nucl. Phys .B709, 419 (2005).

[8] W. Loinaz, N. Okamura, S. Rayyan, T. Takeuchi and L. C. R. Wijewardhana, Phys. Rev. D **70** (2004) 113004.

[9] M. Finkemeier, Phys. Lett. B **387** (1996) 391.

[10] G. Czapek et al., Phys. Rev. Lett. **70** (1993) 17.

[11] D. I. Britton et al., Phys. Rev. Lett. **68** (1992) 3000.

[12] Smirnov, and R. Funchal, Phys.Rev.D74:013001 (2006).

[13] PEN Collaboration, PSI experiment R-05-01, D. Pocanic and A. van der Schaaf, spokespersons.

[14] M. A. Bychkov, Ph.D. thesis, University of Virginia, (2005), unpublished.

[15] B. A. VanDevender, Ph.D. thesis, University of Virginia,(2005), unpublished.

[16] PIENU Collaboration, TRIUMF experiment 1072, D. Bryman and T. Numao, spokespersons.

4 Search for $K\pi$-atoms

Y. Allkofer, C. Amsler, A. Benelli[5], S. Horikawa, C. Regenfus, and J. Rochet

In collaboration with: Basel, Bern, Bucarest, CERN, Dubna, Frascati, IHEP-Protvino, KEK, Kyoto, Moscow, Prague, Santiago, Tokyo and Trieste

(DIRAC-II Collaboration)

The $K^+\pi^-$-atom is a hydrogen-like non-relativistic system of a K^+ and a π^- bound by the Coulomb force. The binding energy of the 1s level is 2.9 keV. The atomic level is broadened and shifted by the overlap of the pion and kaon wave functions. The atom is unstable and decays into $K^0\pi^0$. Such atoms have not been observed so far, but $\pi^+\pi^-$ atoms were studied by the DIRAC Collaboration at CERN (1). The lifetime of the 1s level is related to the difference $|a_1 - a_3|$ between the $K\pi$ S-wave scattering lengths a_1 and a_3 corresponding to the isospin 1/2 and 3/2 states, respectively.

A measurement of the scattering lengths is important for chiral perturbation theories (ChPT). In contrast to $\pi^+\pi^-$-atoms, the $K\pi$-scattering length probes ChPT extended to s-quarks in the limit where the masses of the u-, d- and s-quarks vanish. The scattering lengths can be obtained by extrapolation to zero energy from the isospin 1/2 and 3/2 S-wave phase shifts, however with substantial uncertainties due to the lack of good low energy $K\pi$-scattering data. The extrapolations from the various scattering measurements disagree by large factors: measurements of a_1 vary between 0.17 and 0.34 m_π^{-1}, those of a_3 between –0.07 and –0.14 m_π^{-1}. The scattering lengths were also computed from dispersion relations using scattering data, assuming analytical continuation, unitarity and crossing symmetry (2):

$$a_1 = \quad 0.224 \pm 0.022 \quad \mathrm{m}_\pi^{-1}$$
$$a_3 = -0.0448 \pm 0.0077 \quad \mathrm{m}_\pi^{-1}.$$

However, there are inconsistencies below 1 GeV/c (2). Assuming the above values one predicts a mean life $\tau \sim 3.7$ fs for the $K\pi$-atom. Note that a 20% measurement error in the lifetime leads to a 10% error in $|a_1 - a_3|$. Details on the physics motivations can be found in our 2005 annual report.

In DIRAC-II (3) our group provides the aerogel Čerenkov counters and the heavy gas system for kaon detection. Kaons and pions are produced by the 24 GeV/c PS proton beam on target, typically a 100 μm thick nickel foil (4). The emerging particles are analyzed in a double-arm magnetic spectrometer measuring the momentum vectors of two oppositely charged hadrons (Fig. 4.1). The dissociated kaon and pion from $K\pi$-atoms emerge behind the target with a very small relative momentum $Q < 3$ MeV/c. $K^+\pi^-$-atoms, once produced, move forward and annihilate into $K^0\pi^0$, are being excited or ionize in the target. Since annihilation, excitation and ionization are competing processes, one can determine the mean life by measuring the (calculable) breakup probability in the target.

Detecting Čerenkov radiation from kaons in the DIRAC-II momentum range between 4 and 8 GeV/c requires a transparent medium with a refractive index of typically $n = 1.015$. This can be achieved with aerogel. However, the suppression of fast protons at small angles with respect to the primary beam line requires an even smaller refractive index of typically 1.008. Unfortunately the light yield decreases rapidly with refractive index, and hence

[5]Visitor from the University of Basel

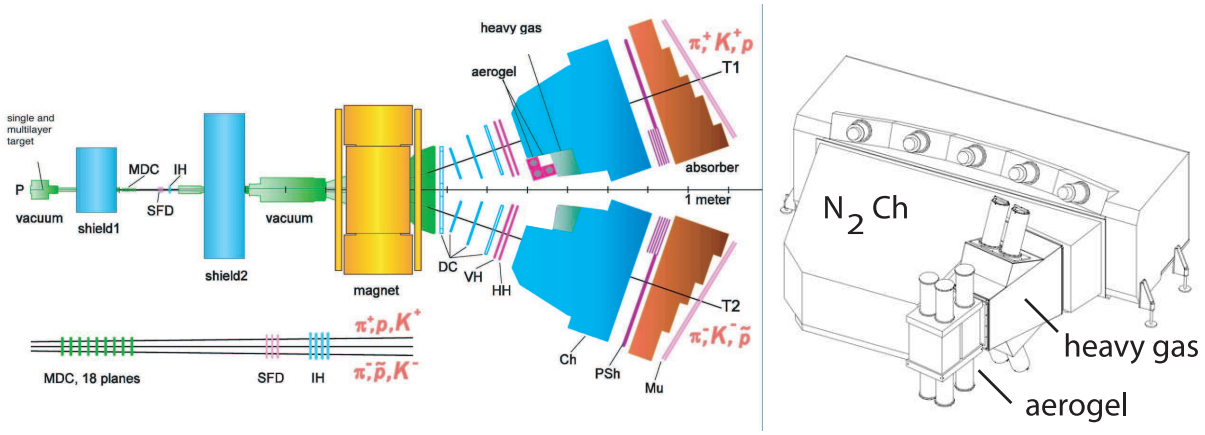

Figure 4.1: Sketch of the updated DIRAC-II spectrometer showing the locations of the Čerenkov counters to identify electrons, pions and kaons. MDC = microdrift chambers, SFD = scintillator fibre detector, IH = ionization hodoscope, DC = drift chambers, VH, HH = scintillation hodoscopes, Ch = N_2-Čerenkov counter, PSh = preshower, Mu = muon counters. Right: aerogel, heavy gas and N_2-Čerenkov counters.

R&D developments were required to achieve a reasonable light collection efficiency.

On the other hand, the faster pions and the beam contaminating electrons will also be detected by our aerogel counters. The latter are vetoed by an N_2-Cerenkov counter and the former by a heavy gas Čerenkov detector (see Fig. 4.1) for which we developed the gas distribution system. Positive kaons are detected in the left arm with the aerogel counter which also suppresses the overwhelming background from scattered protons. On the other hand, the background from antiprotons in the right arm is small so that negative kaons from $K^-\pi^+$-atoms do not need to be detected directly with an aerogel counter.

4.1 Aerogel Čerenkov-detector

In 2006 the design of the aerogel Čerenkov-counter for kaon-proton separation was finalized, the detector constructed and installed in the DIRAC-II experiment. The final detector consists of three independent modules (Fig. 4.2). Two of them have aerogel with the refractive index $n = 1.015$ for kaon-proton separation between 4 and 5.5 GeV/c (24ℓ supplied by Panasonic) and the third one has the lower index n = 1.008 for 5.5 to 8 GeV/c kaons (13ℓ purchased from the BINP/BIC Institutes in Novosibirsk).

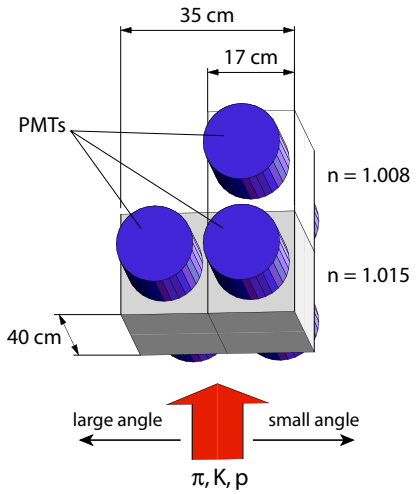

Figure 4.2: Sketch of the three aerogel counters, each read out by two (5") Photonis XP4570B photomultipliers (PMT) with UV window. Fast protons populate the small angle region with respect to the primary beam axis and are vetoed with the n = 1.008 aerogel module.

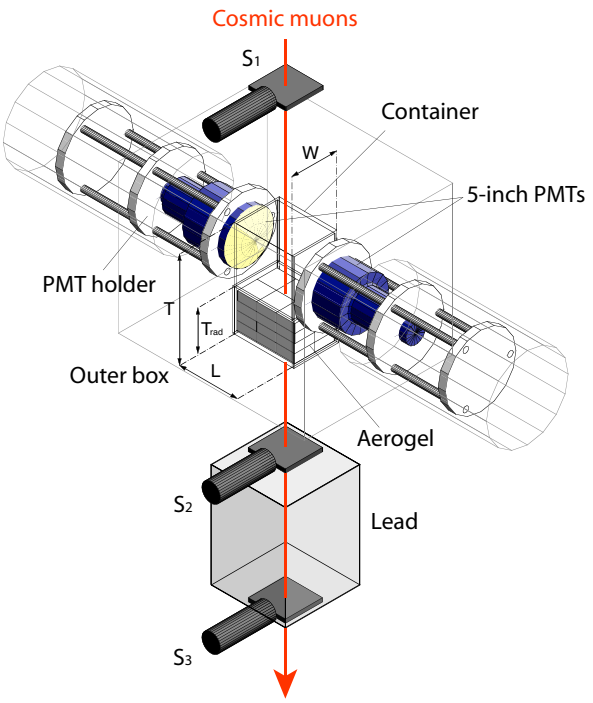

Figure 4.3: Apparatus used to measure the light yield of aerogel and the detection efficiency of Čerenkov light with cosmic rays. High energy muons are selected with the lead absorber between the scintillation counters S_2 and S_3.

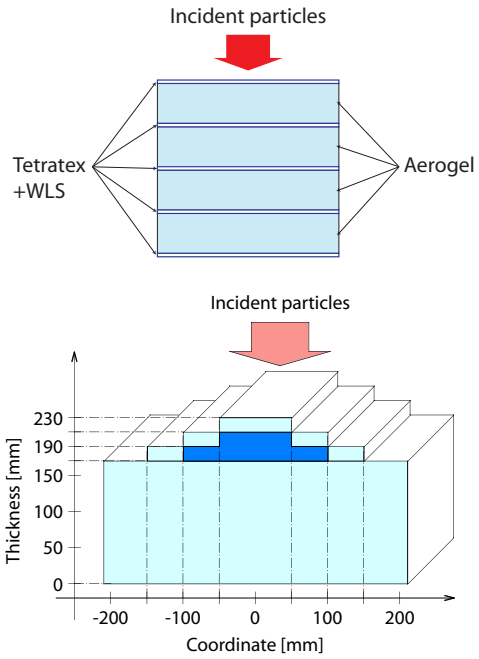

Figure 4.4: Principle of the aerogel sandwich counter (top) and pyramidal structure (bottom).

The light yield is proportional to the factor $1 - 1/\beta^2 n^2$ (where β is the kaon velocity) and therefore becomes very small for low refractive indices. On the other hand, the Čerenkov light intensity is inversely proportional to the wavelength and hence concentrated in the UV-region. We have determined the light yield for kaons using a test setup, cosmic rays and simulation (Fig. 4.3).

The light detection efficiency for kaons traversing the aerogel at equal distance (20 cm) from the two PMTs is reduced by roughly 50% compared to kaons passing near one of the photocathodes. For a 17 cm thick aerogel detector with refractive index n = 1.008 we expect between 4 and 7 photoelectrons from kaons at 7 GeV/c, depending on the impact position. However, the light absorption length depends strongly on wavelength and increases rapidly from about 10 cm at 270 nm to 3 m at 350 nm. The loss due to absorption can be compensated by using a wavelength shifter and also by increasing the radiator thickness at the center of the detector.

To compensate for the low Čerenkov light yield in the 1.008 counter and to increase the absorption length we have developed a novel sandwich design consisting of aerogel tiles interleaved with a wavelength shifter (WLS) coated reflector (such as Tetratex), as illustrated in Fig. 4.4 (top). The goal was to shift the Čerenkov UV towards blue light, thereby increasing the absorption length by two orders of magnitude, and also matching the photocathode sensitivity of the PMT. The best results were obtained with Tetratex as reflector immersed in a solution of p-terphenyl dissolved in chloroform for the WLS. This technique increased the light detection efficiency by 50%. Details on these developments can be found in our 2005 annual report and in a recent publication (5). On the other hand, the pyramidal shape compensates for the stronger absorption in the center (Fig. 4.4, bottom). The thickness of the 1.008 aerogel radiator varies from 16 to 23 cm, the thickness of

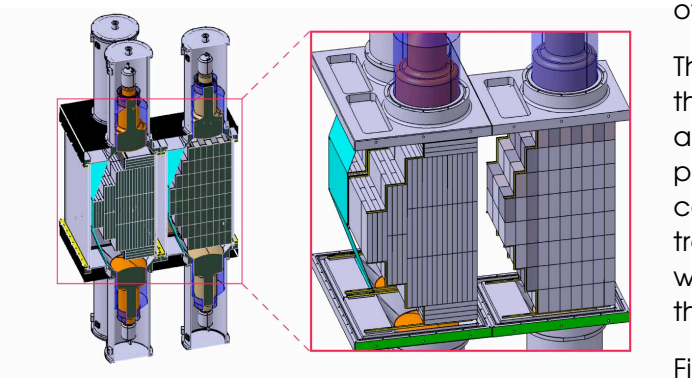

Figure 4.5:
Drawing of the final setup. The aerogel tiles are arranged in a pyramidal geometry in a steel box that also supports the housing of the PMTs and their mu-metal shields. The steel box is shielding the PMTs from the fringe field of the DIRAC dipole magnet.

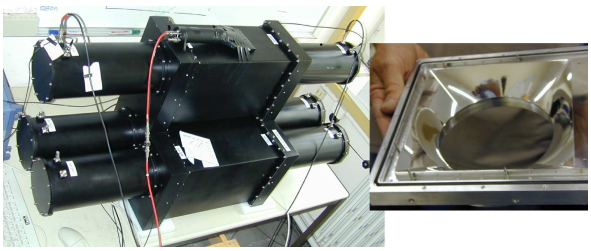

Figure 4.6:
Left: completed left arm detector.
Right: spherical mirrors to focus the light on the PMT photocathodes.

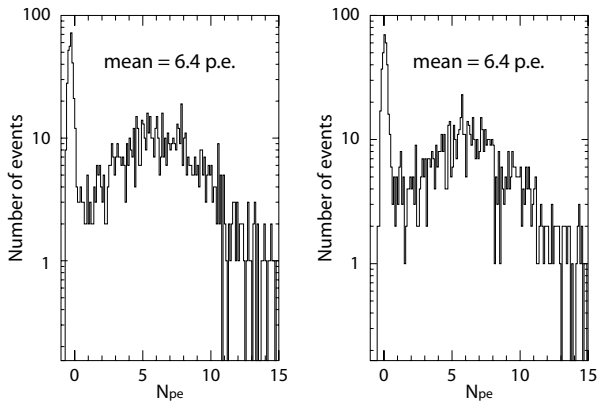

Figure 4.7:
Amplitude distribution (number of photoelectrons) for the 1.015 modules from cosmic muons passing near the PMT (left) and in the middle of the counter (right).

the 1.015 radiator from 11 to 23 cm. A drawing of the final detector is presented in Fig. 4.5.

The inner container surfaces are covered with three layers of Tetratex. The aerogel tiles are held by a steel frame covered with TiO_2 paint as diffuse reflector. The 1.008 pyramid contains 236 and the 1.015 pyramids 124 extremely fragile aerogel tiles which are held with a coarse mesh made of 250 μm thick threads.

Figure 4.6 shows the completed apparatus in our laboratory, ready for tests with cosmic ray muons, since test beams were unfortunately not available at CERN in 2005 and early 2006. The aluminium coated spherical mirrors are covered with an MgF_2 layer for which the thickness was optimized to the emission spectrum of the WLS. Apart from the mirrors most of the mechanical structure was built in the Institute's workshop. The cosmic ray test showed that the light yield did not depend significantly on the impact position (Fig. 4.7). For the 1.015 detector we obtained about 6.4 photoelectrons for cosmic muons, implying $\sim$5 photoelectrons for 4 GeV/c kaons. The performance of the 1.008 counter could not be tested with cosmic rays.

4.2 Heavy gas system

The Zurich group has also designed and built a gas recirculation system for the heavy gas Čerenkov counter. We are using C_4F_{10} (perfluorobutane) with a refractive index of 1.00137 (at 300 nm and 1 bar) to detect pions in the range 4 – 9 GeV/c, while suppressing kaons. The system (Fig. 4.8) is inspired by RICH counters used in other experiments (such as COMPASS). We purchased 30 kg of C_4F_{10} liquid from F2 Chemicals (6) Ltd., enough for four years of measurements, taking into account the unavoidable losses. C_4F_{10} liquid is first transferred from the gas bottle to the gas-liquid separation tank in the freezer (-18°C) shown in Fig. 4.9. The inner pressure is raised to $\sim$2 bar

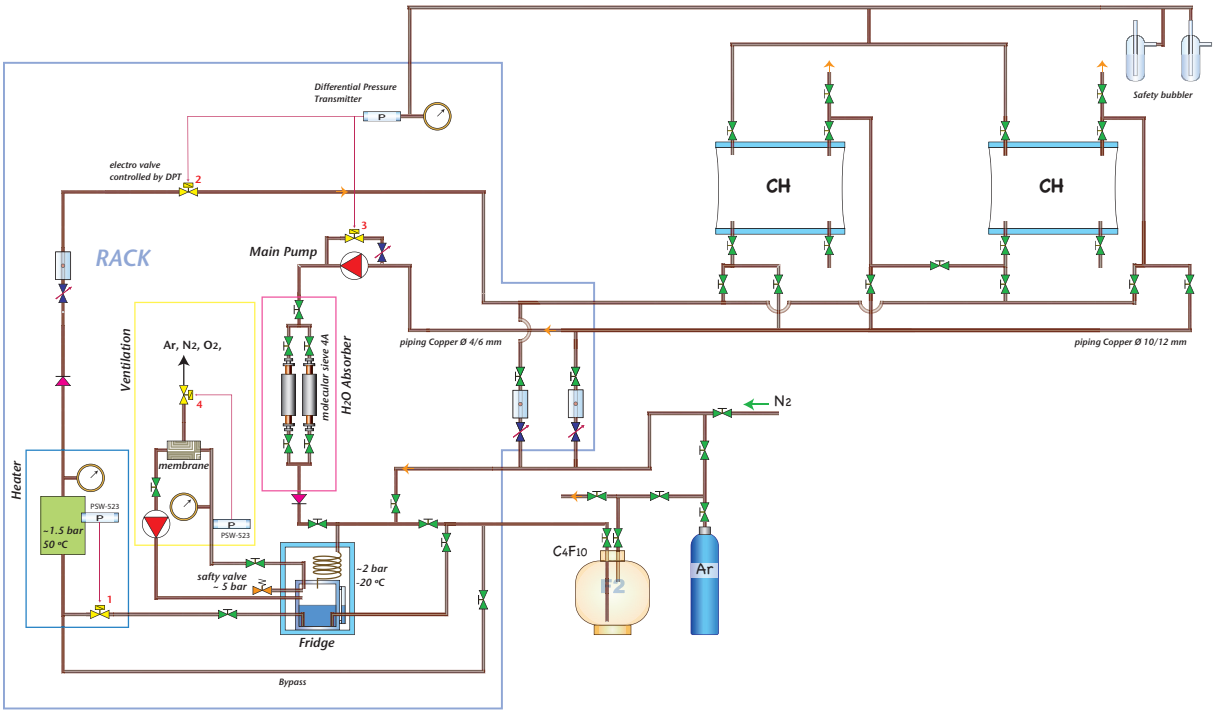

Figure 4.8: C_4F_{10} gas recirculation system. Important functions such as gas purification, pressure regulation and main circulation pump are integrated in the gas rack on the left. Valves near the two detector vessels (left and right arms of DIRAC-II) allow various circulation and recovering modes.

by the main pump to liquefy the gas, while contaminants such as nitrogen, oxygen or argon remain gaseous. This gas mixture is circulated through a hollow-fiber membrane module (7) transparent to smaller molecules.

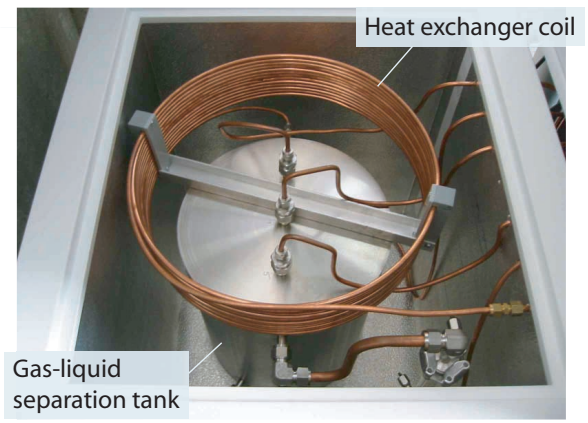

Figure 4.9: Inside the freezer: the C_4F_{10} gas returning from the detector flows through a heat exchanger coil and is liquefied before being restored in the gas-liquid separation tank.

These contaminants are thus vented to the air. The purified liquid is then transferred to the gas buffer which is heated up to 50°C. The gas returning from the detector flows through molecular sieves (4 Å) which absorb water vapor. The pressures in the separation tank and in the gas buffer are regulated using small mechanical pressure switches and electrovalves to ensure a constant flow. The tank, the buffer and the molecular sieve cylinders were constructed in our Institute's workshop.

4.3 Outlook

The aerogel detector was installed in the DIRAC-II beam line in summer 2006. The beam was turned on in late August but was soon interrupted by repeated failures of a switching magnet in the CERN primary proton beam line. This unfortunately led to the cancella-

tion of data taking in 2006. A replacement magnet will be provided for the 2007 runs. The C_4F_{10}-Čerenkov counter was built and installed with the help of our Russian collaborators in October 2006 and the assembly of the gas system was completed the following month.

Meanwhile we are developing the analysis programs. The software is being tested with data taken in 2001 to determine the lifetime of $\pi^+\pi^-$-atoms. So far some 12'000 $\pi^+\pi^-$-atoms have been observed by DIRAC. We plan to use only the detectors downstream of the dipole magnet (see Fig. 4.1). This would increase the available data sample by about a factor of 2 – 3, but presumably also increase systematic errors.

The yield of $K\pi$- atoms is expected to be about 25 $\times$ lower than for $\pi^+\pi^-$-atoms. Assuming equal acceptances and the increase in beam flux by a factor of two, this should lead to about 1'000 reconstructed $K^+\pi^-$- (and $K^-\pi^+$-) atoms during three months of data taking.

[1] B. Adeva et al. (DIRAC Collaboration), Phys. Lett. **B 619** (2005) 50.

[2] P. Büttiker, S. Descotes-Genon, B. Moussallam, Eur. Phys. J. **C 33** (2004) 409.

[3] B. Adeva et al., Addendum to DIRAC proposal, CERN - SPSC - 2004 - 009.

[4] B. Adeva et al., Nucl. Instr. and Meth. in Phys. Res. **A 515** (2003) 467.

[5] Y. Allkofer et al., submitted to Nucl. Instr. and Meth. in Phys. Res. **A**.

[6] F2 Chemicals Ltd., HTTP://WWW.FLUOROS.CO.UK/.

[7] O. Ullaland, Nucl. Instr. and Meth. in Phys. Res. **A 553** (2005) 107. [6]

5 Particle Physics at DESY/HERA (H1)

L. Lindfeld (until December 2006), Katharina Müller, K. Nowak, P. Robmann, C. Schmitz, U. Straumann, P. Truöl, and Stefania Xella Hansen (until May 2006)

in collaboration with: N. Berger, M. Del Degan, C. Grab, G. Leibenguth, M. Sauter, A. Schöning, and T. Zimmermann, Institut für Teilchenphysik der ETH, Zürich; S. Egli, R. Eichler, M. Hildebrandt, and R. Horisberger, Paul–Scherrer–Institut, Villigen, and 37 institutes outside Switzerland

(H1 - Collaboration)

5.1 Electron-proton collisions at a centre of mass energy of 320 GeV - summary

On March 20, 2007 the last data were taken by the H1-collaboration from collisions of 27.4 GeV electrons and positrons with 920 GeV protons. For the remaining months until the end of the experimental phase on June 30, 2007 the HERA storage ring will run with protons at a reduced energy of 460 GeV. The H1-detector will then record events with triggers optimized for a measurement of the longitudinal structure function $F_L(x, Q^2)$ at high electron inelasticity. The integrated luminosity for the post-upgrade HERA-II phase (2004-2007) amounts to 238 pb^{-1} taken with electron and 219 pb^{-1} taken with positron beams, compared to 118 pb^{-1} in total for the HERA-I phase (1993-2000). During the last, low energy phase both left- and right-handed longitudinally polarized beams will be available with polarisations exceeding slightly those obtained during all of the HERA-II running. All runs up to the end are already included in the searches for beyond the Standard Model physics most readily accessible through the multi-lepton (electron or muon), high transverse momentum analysis (see Sec. 5.4.1 below).

As in the past both the H1- and the ZEUS-collaboration continued their efforts dedicated to the exploration of proton structure and tests of quantum chromodynamics (QCD) predictions, evidenced by a nearly constant publication rate over the years. This program entails the precise determination of the neutral and charged electroweak current cross sections at high momentum transfer leading to parton density functions in pre-HERA inaccessible domains of Bjorken x and momentum transfer Q^2, diffractively produced final states, hidden and open charm and beauty production as well as the already mentioned searches for states outside the Standard Model.

Our analysis effort concentrated on events with isolated photons produced in either photoproduction ($Q^2 \approx 0$) or deep inelastic scattering (DIS, $Q^2 > 4$ GeV^2) and search for lepton flavor violation. The thesis of Linus Lindfeld resulting from the latter project has been concluded (1) and a publication has been submitted (2). This work was described in last years annual report (3) in greater detail. The DIS part of isolated photon production, the thesis project of Carsten Schmitz supervised by Katharina Müller, is also concluded. Results have been presented at conferences, and the internal H1-reviewing process for the publication is nearly finished. Higher statistics and an extended kinematical range compared to earlier work allows a clear distinction of the radiation originating from the initial or final state leptons and the struck quarks and thus a test of QCD calculations carried out at the Institute of Theoretical Physics (UZH) (4). This is discussed in Sec. 5.4.2 below in more detail. Noteworthy is also the fact, that this will be

the first H1-publication using a major fraction of the HERA-II data, 227 pb^{-1} in total, about twice the hitherto largest published sample in any of the collaboration papers. First results of the photoproduction analysis, the thesis project of Krzysztof Nowak, are available, too. A short account of this work is also given below (Sec. 5.4.2).

Other analyses of HERA-I data lead to fourteen additional publications (5)-(18), of which three still being reviewed. As usual the preliminary results of ongoing analyses were presented at the summer 2006 high-energy physics conference ICHEP06 in Moscow (19) ((20)-(37)). The following subjects have been covered:

- searches for states and interactions outside the Standard Model like lepton flavor violation (1; 2), excited neutrinos (35), leptoquarks (36), multi-lepton events (33) and events with isolated leptons and missing transverse momentum (32; 35; 37) (see also Sec. 5.4.1 below), single top production (16), doubly charged Higgs bosons (9);

- searches for exotic baryons like strange pentaquarks (11), or decaying to $\Xi\pi$ (30);

- charged and neutral current interactions with longitudinally polarized electrons and positrons (28; 29), discussed in last years annual report (3);

- various aspects of diffraction like parton densities determined from dijet production and F_2^D (13; 18; 24; 25), DIS with the leading proton observed (12), charm in DIS and photoproduction (15; 31), elastic J/ψ production (5), and ρ_0 photoproduction (7; 27);

- final states involving heavy quarks like inclusive charm ($D^{*\pm}$) and beauty dijet production in DIS or at $Q^2 \approx 0$ (10; 14; 17);

- testing specific aspects of QCD based model calculations like isolated photon production (23), which was already mentioned, deeply virtual Compton scattering (26), dijet and threejet production (6; 14; 20) as well as correlations (21), and scaled charged particle momentum distributions (22).

5.2 Technical status of the H1 experiment

Over the long running period of the H1-experiment and despite decreasing manpower in recent years the overall performance of the set-up has been continuously improved. For example the running efficiency from January to March 2007 reached 84 %. The HERA accounting starts with the luminosity tuning phase when both rings have been filled, the beams are at full energy and are brought into collision (62.3 pb^{-1} for this period). H1 starts to take data and tries to turn the tracking chambers on, when tuning is finished (59.7 pb^{-1} or 96 % remaining). This step depends critically on background conditions, which may vary from fill to fill, and apart from dead-time induced by readout, on-line analysis and data storage it accounts for most of the losses (53.5 pb^{-1} or 86 % left). Finally only 2% of the delivered luminosity is lost due to malfunctioning of the data acquisition, hardware components and errors of the shift crew, which was reduced to two persons from initially four. Many monitoring and operational tasks were automated over the years, e.g. the tracker turn on and trip recovery procedure (mostly caused by spikes in the beam, ageing effects have minor influence) and trigger prescale adjustment.

Benchmarks of HERA-II running are peak (average) luminosities of 37.5 (17.2) μb^{-2}s^{-1} and specific luminosities 1.79 (1.29) μb^{-2}s^{-1}mA^{-2} with maximum (average) proton and electron/positron currents of I_p=113 (93) mA and I_e=43 (27) mA, respectively. In 2006/7 (HERA-

II) thus 0.59 pb^{-1} per day (excluding the annual shutdown period) were collected by H1 compared to 0.26 pb^{-1} per day in 1999/2000 (HERA-I). One has to admit that the original goal of the upgrade program calling for a factor of seven increase in peak luminosity with 74 μb^{-2}s^{-1} expected has been missed, and that the time which was needed to reach routine operation after the end of HERA-I (2000-2003) was considerably underestimated.

Our group built a five-layer inner multiwire proportional chamber (CIP2000) for the upgraded H1-detector, which has finer granularity and increased redundancy, is equipped with state of the art electronics and an optical readout delivering signals for a sophisticated z-vertex trigger. It functioned without problems, and hence remained to be an essential ingredient of nearly all trigger elements. A technical description of the system and its performance has been submitted for publication (38). Other hardware improvements entered production modes in the last year: the liquid argon based jet trigger enhances the first-level trigger efficiency for low positron inelasticity, the match of this trigger with the fast track trigger derived from the central jet chamber enhances the sensitivity to $b-$quark physics at the third trigger level, and lastly a topological trigger derived from the backward electromagnetic calorimeter (SpaCal) which receives input also from the CIP2000 and the backward silicon tracker (BST) was implemented successfully. The latter will be useful for the low energy run (see Sec. 5.3).

In our annual report 2000/2001 at the end of the HERA-I period (3) we referred to the major effort of improving the calibration and alignment of all components of the tracker. The significant progress then achieved was based on the program *Millipede* (39; 40) developed by Volker Blobel of Hamburg University. It allows the determination of a large number of global detector parameters from a simultaneous linear least square fit of an arbitrary number of tracks accounting for the

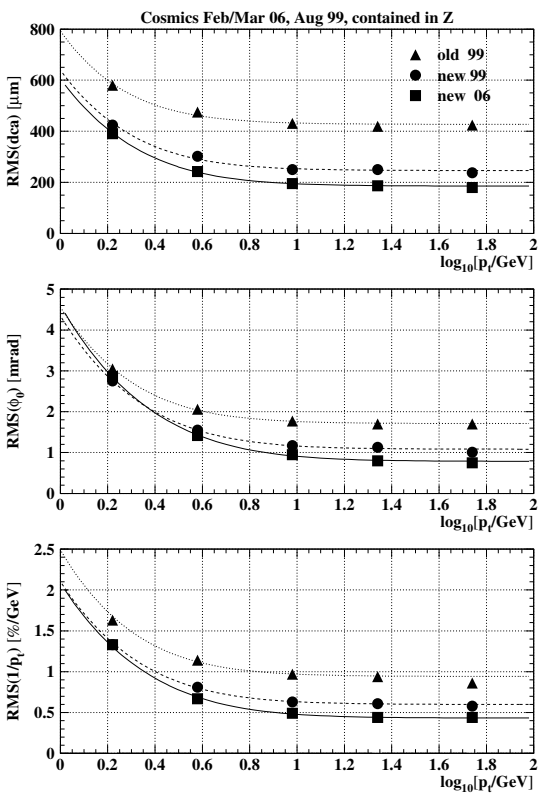

Figure 5.1: Track parameter resolution in the transverse plane obtained with the central jet chamber by comparing two halves of cosmic muon tracks traversing the central tracker. Shown as a function of the transverse momentum are the distance to the interaction point (dca), the azimuth (ϕ_0) and the curvature (1/p$_t$) in the 1999-data (HERA-I) before and after improvement of the code, and in the 2006-data (HERA-II) (from ref. [41]).

correlations with the local track parameters. This effort has continued and further improvements have been made for the HERA-II data. For example the radial and longitudinal variations of the electric and magnetic field in the central jet chamber (CJC), which influence drift velocity and Lorentz angle were implemented. The new elliptical shape of the central silicon tracker (CST) needed adjustments in the program apart from re-calibration, the $z-$information is now derived from CST and the central outer $z-$chamber (COZ) instead from the central inner $z-$chamber (CIZ) and

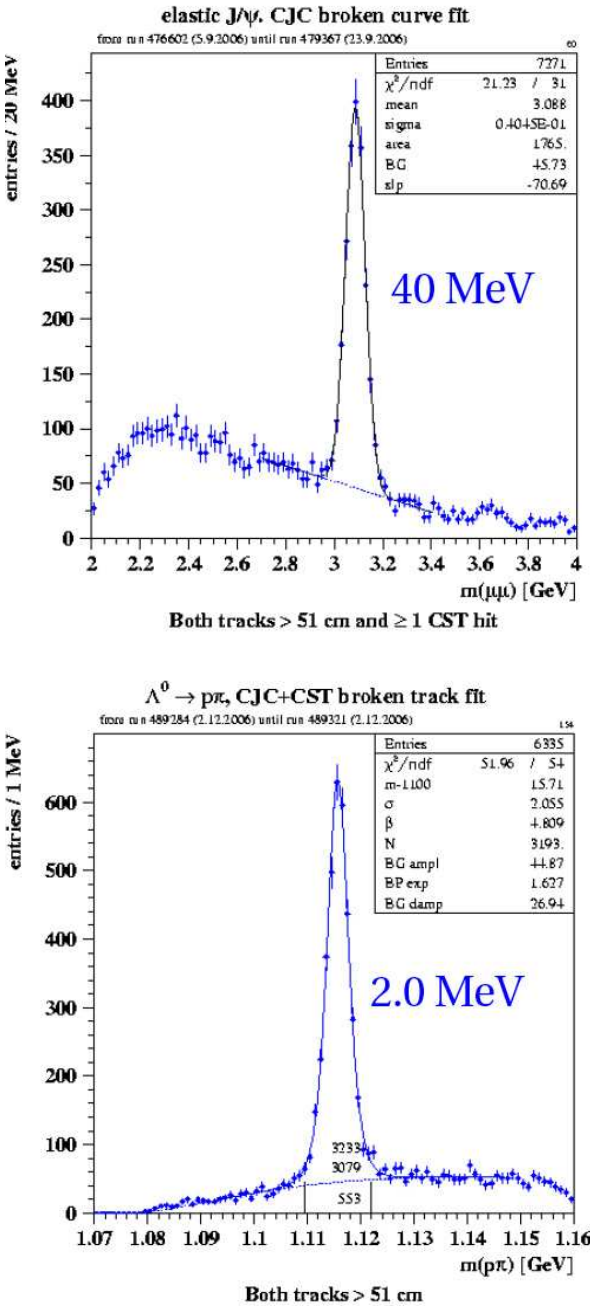

Figure 5.2:
Examples of the mass resolution obtained with the H1 central tracker after implementing the new broken-curve fit.
Top: J/Ψ decaying into a muon pair and bottom: Λ decaying into πp.
The r.m.s. widths of the peaks are indicated. Long tracks in the central jet chamber are required.

COZ, and charge division at both ends of the CJC wires. Figure 5.1, taken from a report at a recent LHC-workshop (41), summarizes the tracker performance in the transverse $R\varphi$ plane deduced from comparing the two halves of cosmic muon tracks traversing the central tracker. For momenta above 10 GeV/c, where the contribution from multiple scattering can be neglected a resolution for the distance of closest approach of 185 μm, for the track angle at the interaction vertex of 0.79 mrad and for the curvature ($1/p_t$) of 0.43%/GeV has been measured. The standard track fit does not allow for multiple scattering, it only corrects for the mean energy loss. The new fast track-fit algorithm based on broken lines (42) corrects for this, and leads to higher precision, as demonstrated by the r.m.s. width of the Λ and J/Ψ mass peaks shown in Fig. 5.2, which reduced from 2.5 to 2.0 MeV and from 43 to 40 MeV, respectively.

5.3 Low energy run

The H1 and the ZEUS collaboration expressed interest in low energy run with the HERA storage ring in September 2005. Considering the amount of e^+p-data taken since summer 2006, the observed evolution of the significance of the excess of observed high transverse momentum lepton events (see Sec. 5.4.1), the success of low energy machine studies earlier on, and the success of understanding high inelasticity data from standard running, the H1-collaboration requested a low energy run to start on March 21, 2007. This run has now successfully started. At a proton energy of 460 GeV a peak luminosity of 7.5 $\mu b^{-2}s^{-1}$ and a specific luminosities 0.46 $\mu b^{-2}s^{-1}mA^{-2}$ with 99 mA protons and 36 mA positrons have been reached, allowing for 0.1 to 0.2 pb^{-1} per fill.

The primary goal of the low energy run is the determination of the longitudinal structure function appearing in the inclusive deep

inelastic cross section as

$$\frac{d^2\sigma}{dxdQ^2} = \frac{2\pi\alpha^2 Y_+}{Q^4 x}\left[F_2(x,Q^2) - f(y)\cdot F_L(x,Q^2)\right] ,$$

with $y = Q^2/sx$, $Y_+ = 1+(1-y)^2$ and $f(y) = y^2/Y_+$. The two structure functions F_2 and F_L have so far not been properly disentangled at HERA. The measured cross sections have been interpreted in terms of F_2 with some reasonable assumptions on F_L, except at large y where the treatment was reversed (43). The two functions correspond to the transverse and longitudinal polarisation state of the exchanged virtual photon probing the proton structure, i.e. $F_T = F_2 - F_L$ and F_L, respectively. In the quark-parton model F_L is zero since longitudinally polarised photons do not couple to spin $1/2$ quarks (44). In the DGLAP approximation of perturbative QCD, to lowest order, the longitudinal structure function is given by (47)

$$F_L(x) = \frac{\alpha_s}{4\pi}x^2\int_x^1 \frac{dz}{z^3}\left[\frac{16}{3}F_2(z) + 8\sum e_q^2(1-\frac{x}{z})zg(z)\right]$$

with contributions from quarks and from gluons. At low x, $F_L(x,Q^2)$ essentially determines the gluon distribution $xg(x,Q^2)$ ($\approx 8.3F_L(0.4x)/\alpha_s$ numerically). Presently the gluon distribution at low x is constrained indirectly by the Q^2 evolution of $F_2(x,Q^2)$. This assumes the validity of the DGLAP theory, which becomes questionable at low x.

It is possible to extract the longitudinal structure function directly from two or more cross section measurements at fixed x and Q^2 by varying y, which is possible by changing s. Since $s = 4E_eE_p$ one may vary the electron or proton beam energy or both. The sensitivity to F_L is proportional to y^2. As at large y and low Q^2 the inelasticity is given by $y \approx 1 - E'_e/E_e$, reducing the electron beam energy would require to lower the scattered electron energy below the 2 GeV trigger threshold. Moreover, a reduction of the electron beam energy affects the scattered electron angle stronger than a reduction of the proton beam energy would do. It has therefore been decided to opt for lowering E_p. Estimates for a successful determination of F_L to at least 5 standard deviations are based on the assumption, that 10 pb^{-1} can be collected at 460 GeV until the end of June 2007. At large y and low Q^2 the scattering kinematics at HERA resemble those of a fixed target scattering experiment: the electron scattered off quarks at very low x is scattered through a small angle. It is accompanied by part of the hadronic final state which is related to the struck quark. Since high inelasticities y demand to identify scattered electrons down to a few GeV of energy, there is a considerable background from hadrons or photons, e.g. from π^0 decay, usually from photoproduction with the scattered electron escaping unobserved through the beam pipe. Removal of this background is possible by requiring a track to be associated to the energy cluster in the SPACAL, which rejects photons, and by measuring its charge, which on a statistical basis allows the remaining part of the background to be removed, as was demonstrated with the BST and the CJC (43).

5.4 Results from recent analyses

5.4.1 High transverse momentum phenomena

Examining the data that H1 collected during the period 1994-2000, eighteen events were identified which contain an isolated electron or muon and show missing transverse momentum. The Standard Model (SM) predicted 12.4±1.7 events of this kind, the majority coming from the decays of W bosons. Whilst these numbers were broadly in agreement with each other, the comparison became more interesting when the selection was restricted to those events which have a particularly powerful jet. When this jet punched side-

Table 5.1: **Summary of the H1 searches for events with isolated electrons or muons of either charge with missing transverse momentum for all data sets taken up to February 2007, comprising 95% of the total integrated luminosity. The signal component of the Standard Model expectation, dominated by W production is indicated as well.**

H1-preliminary (Feb. 2007)		Electron obs.	Electron expected	Electron signal	Muon obs.	Muon expected	Muon signal	Combined obs.	Combined expected	Combined signal
94-07 e^+p	Full sample	25	24.2±3.3	71%	13	6.3 ±1.0	85%	38	30.5±4.2	75%
258 pb^{-1}	$P_T^X > 25$ GeV	10	4.1 ±0.8	75%	8	3.7 ±0.6	85%	18	7.8 ±1.3	80%
98-06 e^-p	Full sample	16	19.4±2.7	65%	2	5.1 ±0.7	78%	18	24.4±3.4	68%
184 pb^{-1}	$P_T^X > 25$ GeV	3	3.8 ±0.6	61%	0	3.1 ±0.5	74%	3	6.9 ±1.0	67%
94-07 $e^\pm p$	Full sample	41	43.6±6.0	68%	15	11.4 ±1.7	82%	56	55.0±7.6	71%
442 pb^{-1}	$P_T^X > 25$ GeV	13	7.9 ±1.4	67%	8	6.8 ±1.1	79%	21	14.7±2.3	72%

ways (transversely) into the detector with a momentum of more than 25 GeV, ten events were found compared to a SM expectation of 2.9±0.5. The chance of a statistical fluctuation producing this number of observed events was around 0.15% (45). This exciting observation lead to the establishment of a hot line for events of this type, and allowed a continuous updating of the status. Table 5.1 summarizes the situation as it stood at the end of January 2007, an update of what was reported at the ICHEP2006 conference (32; 33). The statement *seemingly the HERA-II data are more SM like than the HERA-I data* captures the disappointing fact. The slight excess in the positron data is well compensated by the electron data (see also Fig. 5.3). A working group has been formed, which will combine the H1- and ZEUS data, which differ in their accepted kinematic range, but unfortunately also seem to hold no surprises either.

The general search for non-SM events following the method outlined in our 2004 publication (46) has been extended to the HERA-II data, too (37). All event topologies involving isolated electrons, photons, muons, neutrinos and jets with high transverse momenta are investigated in a single analysis. Events are assigned to exclusive classes according to their final state. A statistical algorithm is applied to search for deviations from the

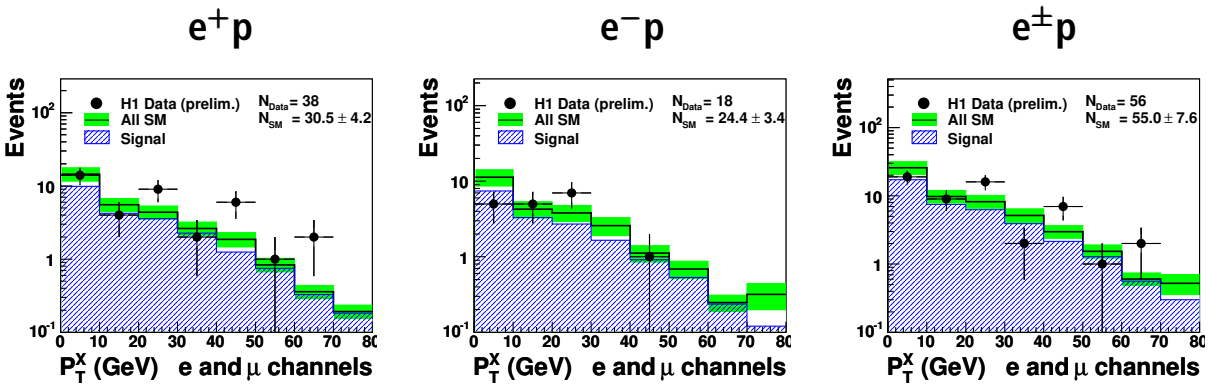

Figure 5.3: **The hadronic transverse momentum distribution in the combined electron and muon channels is compared to the Standard Model expectation (open histogram). The hatched histogram indicates the contribution of real W production which dominates the signal. The total number of observed and expected events are given by N_{Data} and N_{SM}, respectively. From left to right: e^+p, e^-p and combined data.**

Standard Model in the distributions of the scalar sum of transverse momenta or invariant mass of final state particles and to quantify their significance. No significant deviations from SM expectations have been found.

5.4.2 Isolated photons in photoproduction and deep inelastic scattering

Two thesis projects of Zürich graduate students concern the reaction $e^{\pm}p \to e^{\pm}\gamma X$ either with the exchanged virtual photon (Fig. 5.4) nearly on shell ($Q^2 \approx 0$, photoproduction (PP), thesis Krzysztof Nowak) or at higher momentum transfer ($Q^2 > 0$, deep inelastic scattering (DIS), thesis Carsten Schmitz). Common to both analyses is that the observed photon is isolated and has high transverse momentum (energy) E_T. In DIS the scattered electron is observed in the backward electromagnetic calorimeter of H1 (SpaCal), while in PP it escapes mostly unobserved through the beam pipe.

The reaction receives contributions from wide angle bremsstrahlung of the initial and final state electron or positron (LL) and from the radiation of the struck quark (QQ), and from their interference (LQ). The leading order diagrams are depicted in Fig. 5.4. In the QCD calculation of Gehrmann-de Ridder *et al* (4) pertaining to DIS the parton-level lepton-quark cross section $\hat{\sigma}(eq \to e\gamma q)$ is convoluted with the parton densities in the proton to obtain the $\sigma(ep \to e\gamma X)$ cross section. The most interesting QQ contribution is dominated by the direct radiation from the struck quark, but contains also the contribution from quark fragmentation to a photon. This part can not be calculated in perturbation theory (pQCD). A phenomenological process-independent quark-to-photon fragmentation function $D_{q\to\gamma}(z)$

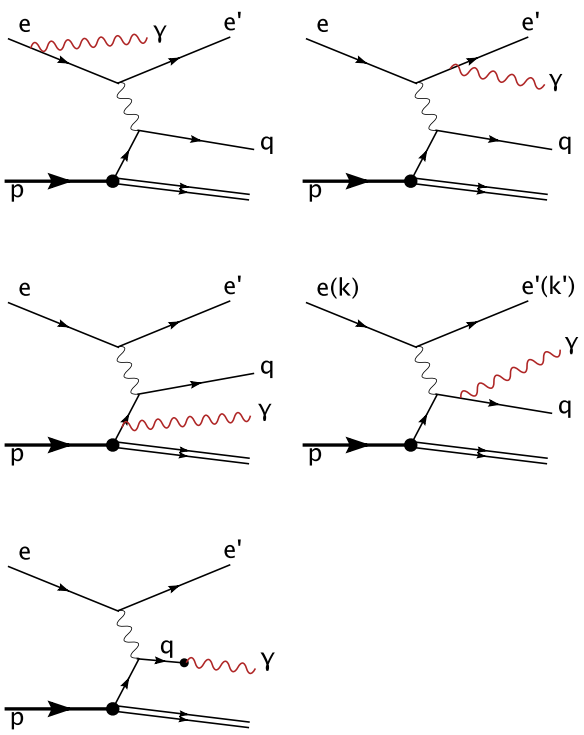

Figure 5.4: Leading order contributions to isolated photon production at $Q^2 \approx 0$ (photoproduction, PP) and for larger Q^2 (deep inelastic scattering, DIS). Top: initial and final state lepton bremsstrahlung in DIS; middle: radiation from the struck quark present in both DIS and PP; bottom: diagram illustrating the contribution from quark-to-photon fragmentation.

($z \equiv$ fraction of the quark momentum carried by the photon) is needed, for which data from LEP-experiments exist. Even at leading order, the parton-level cross section contains a collinear quark-photon divergence, which is absorbed into the fragmentation function. The reconstruction of the photon and the electron in different parts of the detector ensures sufficient separation to avoid collinear singularities in the LL QED-contribution. The interference term (LQ), which differs in sign for e^+p and e^-p scattering contributes less than 3 % to the cross section. The commonly used RAPGAP Monte Carlo generator (48) can also be used to predict the LL contribution, while for the QQ process the PYTHIA Monte Carlo generator (49) is available which, however,

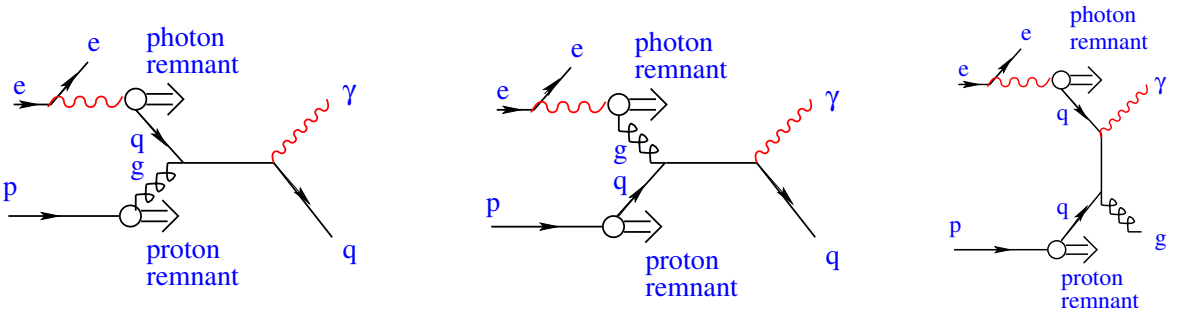

Figure 5.5: Resolved photon contribution to isolated photon production at $Q^2 \approx 0$.

does not contain the contribution from fragmentation, nor is the LQ-interference calculable in this way.

In photoproduction the direct QQ contribution described above is supplemented by the resolved photon contribution, where the photon converts itself into partons before it interacts (see Fig. 5.5). This contribution is available through PYTHIA, too.

Experimentally the DIS (PP) data are confined to the kinematic range in photon transverse energy: $3 < E_T^\gamma < 10$ GeV ($5 < E_T^\gamma < 10$ GeV), in pseudorapidity $\eta^\gamma \equiv -\ln\tan\theta^\gamma/2$: -1.2 $< \eta^\gamma <$ 1.8 (-1.0 $< \eta^\gamma <$ 0.9), in momentum transfer: $4 < Q^2 < 150$ GeV^2 ($Q^2 < 0.1$ GeV^2), in electron inelasticity: $0.05 < y < 0.9$ ($0.2 < y < 0.7$) and in the invariant mass of the hadronic system $W > 50$ GeV to exclude elastic Compton scattering. A typical DIS event is shown in Fig. 5.6. To ease the comparison with pQCD calculations an infrared-safe definition of the isolation criterion requires the fraction z of the jet energy carried by the photon to be larger than 0.9. In DIS the sample is divided further into subsamples without and with further jets.

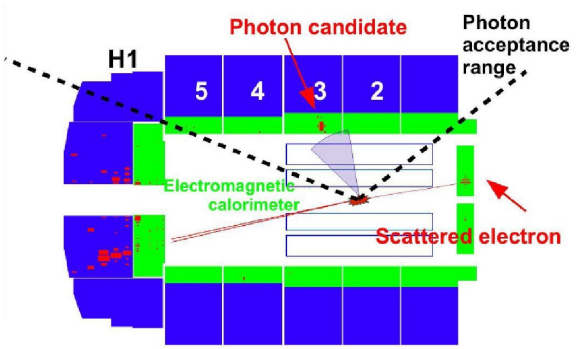

Figure 5.6:
An isolated high transverse momentum photon in a deep inelastic scattering event observed in the H1-detector. The kinematical acceptance is indicated.

The major challenge of the analysis is the discrimination of the photons, detected in the electromagnetic part of the liquid argon calorimeter, against π^0 and other mesons decaying into photons. The isolation criterion helps, since most π^0 appear as content of jets. But even after applying it, the background amounts to 70 % of the total sample. A multivariate analysis using six variables describing the spatial extent and symmetry of the shower in three dimensions is therefore used in the final discrimination step. This procedure was described in detail in last years annual report (3). As an example the signal extraction in the photoproduction data is shown in Fig. 5.7.

An excerpt of the preliminary photoproduction data is shown Fig. 5.8. Considering, that systematic errors have not been evaluated and not all cross checks have been done reasonable overall agreement with published, lower statistics results for the transverse energy dependence of the inclusive cross section is observed. The same holds for the comparison with theoretical predictions. Results for the η dependence and the photon plus jet cross section are available, too.

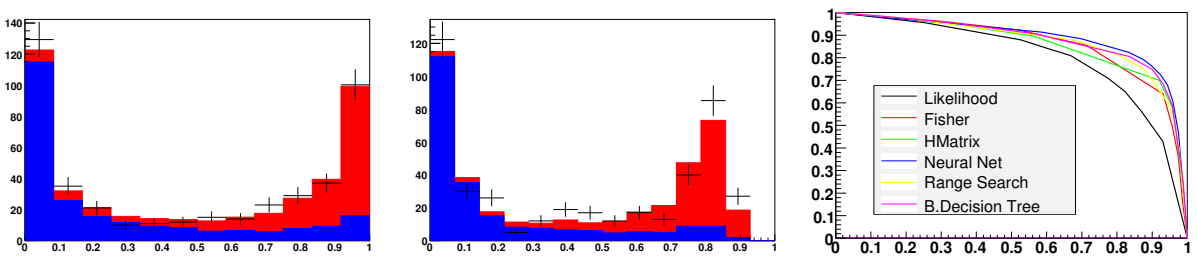

Figure 5.7: Photon signal extraction based on the analysis of shower shapes. The six electromagnetic cluster variables are either fed to a likelihood analysis (left), a neural network (middle) or four other commonly used multi-variate analysis methods (not shown). The background is represented by the blue histograms, the signal by the red histograms, the horizontal axis corresponds to the normalized discrimination variable. The signal selection efficiency (vertical axis) versus background rejection (horizontal axis) for all methods is shown on the right.

Examples of the measured DIS cross sections are shown in Figures 5.9 and 5.10. The difference in the angular distributions of the LL and the QQ radiation allows to disentangle the two contributions. Radiation from the electron is negligible for $\eta^{\gamma} > -0.6$. The leading order calculation (4) underestimates the inclusive cross section by 45 % most significantly at low Q^2. The same holds for the PYTHIA plus RAPGAP prediction, which lies 48 % lower. For $Q^2 > 40$ GeV^2 the leading order calculation is closer to the data (low by 25 %) and the shape is described well. Exclusive measurements of the cross section with and without additional jets are available for the first time, too. Radiation from the electron is largely suppressed for photon plus no jet. This separation has not been previously available. Both exclusive cross sections are underestimated by the leading order calculation, too, indicating the need for higher order calculation. The only previous measurement at HERA from the ZEUS-collaboration (51) only starts at $Q^2 \approx 35$ GeV^2, has a higher E_T-cut and considerably less statistics.

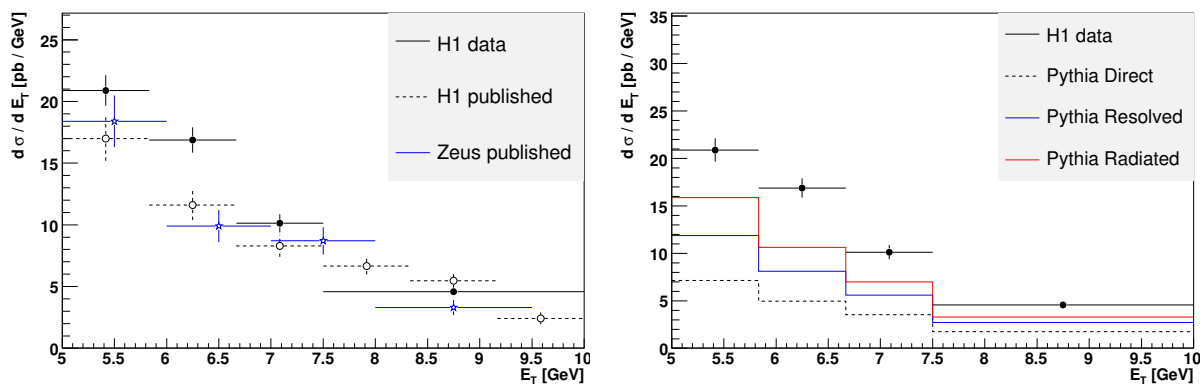

Figure 5.8: Preliminary results for the transverse momentum (energy) dependence of the inclusive cross section for isolated photon production compared to previous H1 and ZEUS photoproduction data (left) and to predictions using the PYTHIA Monte Carlo generator (right).

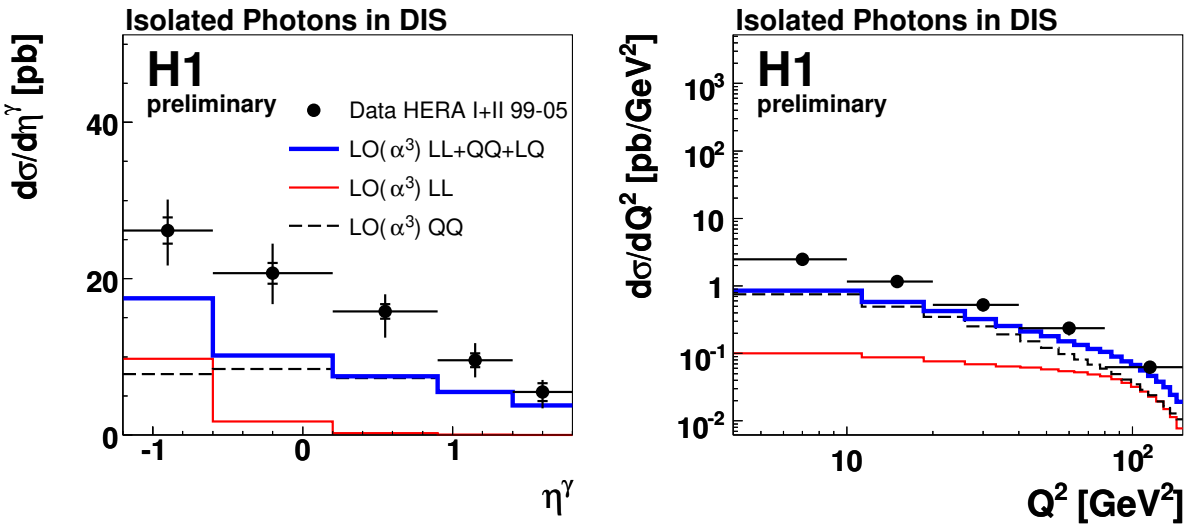

Figure 5.9: Inclusive differential cross sections $d\sigma/d\eta^\gamma$ and $d\sigma/dQ^2$ for isolated photons in DIS. The cross sections are shown together with a leading order $\mathcal{O}(\alpha^3\alpha_s^0)$ calculation [4] corrected for hadronisation effects, LL corresponding to radiation from the electron and QQ to radiation from the quark. LL is negligible for η^γ>0.6 . The calculation is low by 45% most significantly at low Q^2.

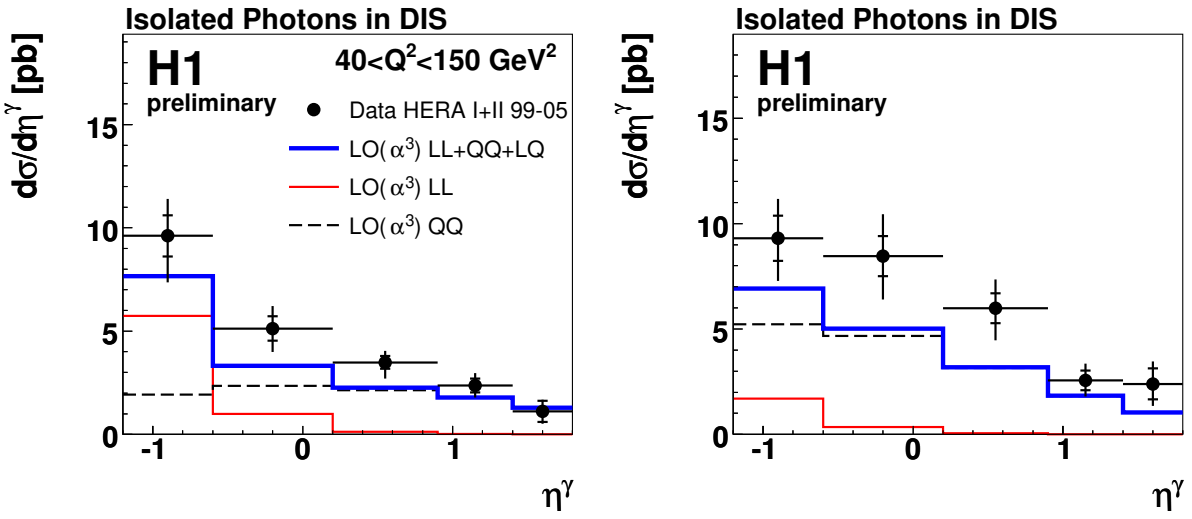

Figure 5.10: Differential cross sections $d\sigma/d\eta^\gamma$ for Q^2>40 GeV^2 (left) for the inclusive measurement and the exclusive measurement for photon plus no-jets with Q^2>4 GeV^2 (right). At high Q^2 there is much better agreement between calculation and measured data in shape and in magnitude. Exclusive sample: photon plus no jet: LO below the data but - compared to the inclusive sample - the radiation from the electron (LL) is suppressed, mainly by the W cut.

[1] **Search for Lepton Flavour Violation with the H1 Experiment at HERA**,
Linus Lindfeld, PhD Thesis, University of Zürich (2006).

[2] **Search for Lepton Flavour Violation in ep Collisions**,
H1-Coll., A. Aktas et al., DESY 07 – 007,
hep-ex/0703004, submitted to Eur.Phys.J.**C** (2007).

[3] Physik-Institut, University of Zürich,
Annual Reports 1996/7 ff.; available at
www.physik.unizh.ch/reports.html.

[4] A. Gehrmann-De Ridder, T. Gehrmann, and E. Poulsen,
Phys.Rev.Lett.**96** (2006), 132002;
Eur.Phys.J.**C47** (2006), 395.

[5] **Elastic J/ψ Production at HERA**,
H1-Coll., A. Aktas et al., DESY 05 – 161,
hep-ex/0510016, Eur.Phys.J.**C46** (2006), 585 - 603.

[6] **Photoproduction of Dijets with High Transverse Momenta at HERA**,
H1-Coll., A. Aktas et al., DESY 06 – 020,
hep-ex/0603014, Phys.Lett.**B639** (2006), 21 - 31.

[7] **Diffractive Photoproduction of ρ Mesons with Large Momentum Transfer at HERA**,
H1-Coll., A. Aktas et al., DESY 06 – 023,
hep-ex/0603038, Phys.Lett.**B638** (2006), 422 - 431.

[8] **Tau Lepton Production in ep Collisions at HERA**,
H1-Coll., A. Aktas et al., DESY 06 – 029,
hep-ex/060422, Eur.Phys.J.**C48** (2006), 699 - 714.

[9] **Search for Doubly-Charged Higgs Boson Production at HERA**,
H1-Coll., A. Aktas et al., DESY 06 – 038,
hep-ex/0604027, Phys.Lett.**B638** (2006), 432 - 440.

[10] **Measurement of Charm and Beauty Dijet Cross Sections in Photoproduction using the H1 Vertex Detector at HERA**,
H1-Coll., A. Aktas et al., DESY 06 –039,
hep-ex/0605016, Eur.Phys.J.**C47** (2006), 597 - 610.

[11] **Search for a Narrow Baryonic Resonance in Decaying in $K^0_s p$ or $K^0_s \bar{p}$ in Deep Inelastic Scattering at HERA**,
H1-Coll., A. Aktas et al., DESY 06 – 044,
hep-ex/060456, Phys.Lett.**B639** (2006), 202 - 209.

[12] **Diffractive Deep Inelastic Scattering with a Leading Proton at HERA**,
H1-Coll., A. Aktas et al., DESY 06 – 048,
hep-ex/0606003, Eur.Phys.J.**C48** (2006), 749 - 766.

[13] **Measurement and QCD Analysis of the Diffractive Deep Inelastic Scattering Cross Section at HERA**,
H1-Coll., A. Aktas et al., DESY 06 – 049,
hep-ex/0606004, Eur.Phys.J.**C48** (2006), 715 - 748.

[14] **Inclusive $D^{*\pm}$-Meson and $D^{*\pm}$-Jet Correlations in Photoproduction at HERA**,
H1-Coll., A. Aktas et al., DESY 06 – 110,
hep-ex/0608042, Eur.Phys.J.**C50** (2007), 251 - 269.

[15] **Diffractive Open Charm Production in Deep Inelastic Scattering and Photoproduction at HERA**,
H1-Coll., A. Aktas et al., DESY 06 – 164,
hep-ex/0610076, Eur.Phys.J.**C50** (2007), 1-20.

[16] **Search for Single Top Production in ep Collisions at HERA**,
Stefania Xella, Proc. Int. Workshop on Top Quark Physics (TOP2006), Coimbra, Portugal, January 12 - 15, 2006; Proc. of Science **TOP 2006** (2006), 030.

[17] **Production of D^* Mesons with Dijets in Deep Inelastic Scattering**,
H1-Coll., A. Aktas et al., DESY 06 – 240,
hep-ex/0701023, submitted to Eur.Phys.J.**C** (2007).

[18] **Tests of Factorisation in the Diffractive Production of Dijets in Deep Inelastic Scattering and Photoproduction at HERA**,
H1-Coll., A. Aktas et al., DESY 07 – 018,
hep-ex/0703022, submitted to Eur.Phys.J.**C** (2007).

[19] Contributed papers by the H1-Coll. to ICHEP2006: 33^{th} Int. Conf. on High Energy Physics Moscow (Russia), July 26-August 2, 2006; only those papers are listed, which have not yet been submitted to journals.

[20] **Threejet Production in Deep Inelastic ep Scattering and Low x Parton Dynamics at HERA** [19].

[21] **Azimuthal Correlations in Dijet Events from Deep Inelastic Electron-Proton Scattering at HERA** [19].

[22] **Scaled Charged Particle Momentum Distributions at High Q^2 at HERA** [19].

[23] **Inclusive Prompt Photon Production in Deep Inelastic Scattering at HERA** [19].

[24] **Determination of Diffractive Parton Densities by a Combined Analysis of Diffractive Dijet Production and of the Inclusive Diffractive Structure**

Function F_2^D in Deep Inelastic Scattering [19].

[25] **Measurement and Interpretation of Diffractive Cross Sections at Medium Q^2** [19].

[26] **Measurement of Deeply Virtual Compton Scattering at HERA-II** [19].

[27] **A New Measurement of Exclusive ρ^0 Meson Photoproduction at HERA** [19].

[28] **Charged Current Interactions in ep Scattering at HERA with Longitudinally Polarised Electrons** [19].

[29] **Neutral Current Interactions in $e^{\pm}p$ Scattering with Longitudinally Polarised Leptons** [19].

[30] **Search for Baryonic States Decaying to $\Xi\pi$ in Deep Inelastic Scattering at HERA** [19].

[31] **Diffractive Charm Production at HERA** [19].

[32] **Search for Events with Isolated Leptons and Missing Transverse Momentum** [19]; available at www-h1.desy.de/psfiles/confpap/ICHEP2006/-H1prelim-06-162.ps.

[33] **Multilepton Events at HERA** [19].

[34] **Search for Excited Neutrinos in e^-p Collisions at HERA** [19]

[35] **Search for Events with Isolated Tau-Leptons and Missing Transverse Momentum at HERA** [19]

[36] **Search for Leptoquarks in e^-p Collisions at HERA** [19]

[37] **A General Search for New Phenomena in e^-p Scattering at HERA** [19]; available at www-h1.desy.de/psfiles/confpap/ICHEP2006/-H1prelim-06-161.ps.

[38] **A Vertex Trigger based on Cylindrical Multiwire Proportional Chambers**,
J. Becker, K. Bösiger, L. Lindfeld, K. Müller, P. Robmann, S. Schmitt, C. Schmitz, S. Steiner, U. Straumann, K. Szeker, P. Truöl, M. Urban, A. Vollhardt, N. Werner, D. Baumeister, S. Löchner, and M. Hildebrandt, physics/0701002, submitted to Nucl.Instr.Meth. A (2007).

[39] **A New Method for the High Precision Alignment of Track Detectors**,
Proc. Conf. on Advanced Statistical Techniques in Particle Physics, Durham, UK (Mar. 18-22, 2000), M.R. Walley and L. Lyons eds., p. 268; DESY 02 – 077, hep-ex/0208021.

[40] **Software Alignment for Tracking Detectors**,
Proc. Workshop on Tracking in High Multiplicity Environments (TIME05), Zürich (Oct. 3-7, 2005), Nucl.Instr.Meth. A**566** (2006), 5.

[41] **H1 Alignment Experiences**,
C. Kleinwort, Contr. to LHC-Detector Alignment workshop, CERN, Geneva (Sept. 4-6, 2006), to be published in CERN Yellow Reports.

[42] **A New Fast Track-Fit Algorithm Based on Broken Lines**,
Proc. Workshop on Tracking in High Multiplicity Environments (TIME05), Zürich (Oct. 3-7, 2005), Nucl.Instr.Meth. A**566** (2006), 14.

[43] **Measurement of Inclusive ep Scattering at Low and a Determination of α_s**,
H1-Coll., A. Adloff et al., Eur.Phys.J.**C21** (2001), 33; Rainer Wallny, PhD Thesis, University of Zürich (2001); see also H1-report H1prelim-03-043 available at www-h1.desy.de/general/home/intra_home.html

[44] G. Callan, and D. Gross, Phys.Rev.Lett.**22** (1969), 156.

[45] **Isolated Electrons and Muons in Events with Missing Transverse Momentum at HERA**,
H1-Coll.. V. Andreev et al., Phys.Lett.**B561** (2003), 241;
Observation of Events at Very High Q^2 in ep Collisions at HERA,
H1 Collab., C. Adloff et al., Z.Phys. **C74** (1997), 191.

[46] **A General Search for New Phenomena in ep Scattering at HERA**,
H1 Collab., A. Aktas et al., Phys.Lett.**B602** (2004), 14.

[47] G. Altarelli, and G. Martinelli, Phys.Lett.**B76** (1978), 89.

[48] H. Jung, Comp. Phys. Comm. **86** (1995), 147 (Version 3.1); see also www.desy.de/jung/rapgap.html

[49] T. Sjöstrand, L. Lönnblad, and S. Mrenna, PYTHIA 6.2: Physics and manual, Lund University rep. LU-TP-01-21 (2001); hep-ph/0108264.

[50] **Measurement of Prompt Photon Cross Sections in Photoproduction at HERA**,
H1-Coll., A. Aktas et al., Eur.Phys.J.**C38** (2005), 437.

[51] ZEUS-Coll.: S. Chekanov et al., Phys.Lett.**B595** (2004), 86; Eur.Phys.J.**C49** (2007), 511; J. Breitweg et al. Phys.Lett.**B472** (2000), 175.

6 High-precision CP-violation Physics at LHCb

R. Bernet, R.P. Bernhard, U. Bieler, A. Büchler, N. Chiapolini, J. Gassner, V. Hangartner, F. Lehner, T. Sakhelashvili, C. Salzmann, S. Steiner, O. Steinkamp, U. Straumann, J. van Tilburg, A. Vollhardt, D. Volyanskyy, A. Wenger

in collaboration with: The silicon tracking group of LHCb: University of Lausanne; Max Planck Institute, Heidelberg, Germany; University of Santiago de Compostela, Spain; and Ukrainian Academy of Sciences, Kiev, Ukraine.

The full LHCb collaboration consists of 48 institutes from Brazil, China, France, Germany, Italy, The Netherlands, Poland, Romania, Russia, Spain, Switzerland, Ukraine, the United Kingdom, and the United States of America.

(LHCb)

The main goal of the LHCb experiment (1; 2) is to perform high precision measurements of CP violating processes and rare decays in the B meson systems. The comparison of results from many different decay modes will permit to perform consistency tests of the Standard Model explanation of CP violation. Since CP violating asymmetries are generated through processes involving internal loops of virtual particles, they are very sensitive to contributions from possible new particles. Precision measurements of CP violating processes therefore provide a powerful tool to search for physics beyond the Standard Model, which is complementary to direct searches at the high energy frontier. Our group concentrates on the development, construction, operation and data analysis of the LHCb Silicon Tracker and on the preparation of physics analyses.

6.1 LHCb detector

The LHCb detector is currently being installed at the new 14 TeV proton-proton collider LHC at CERN. It is foreseen to receive first beams in autumn this year and to collect first physics-quality data in 2008. A vertical cut through the detector is shown in Fig. 6.1. Since the production of b quarks at the LHC is strongly peaked towards small polar angles with respect to the beam axis, the detector is layed out as a single-arm forward spectrometer.

The LHCb tracking system consists of a silicon-microstrip vertex detector (VELO) and four planar tracking stations (TT upstream of the LHCb dipole magnet and T1-T3 downstream of the magnet). The Silicon Tracker comprises two components of the tracking system: The Trigger Tracker (TT (2; 4)) is a 160 cm wide and 130 cm high four-layer tracking station which covers the full acceptance of

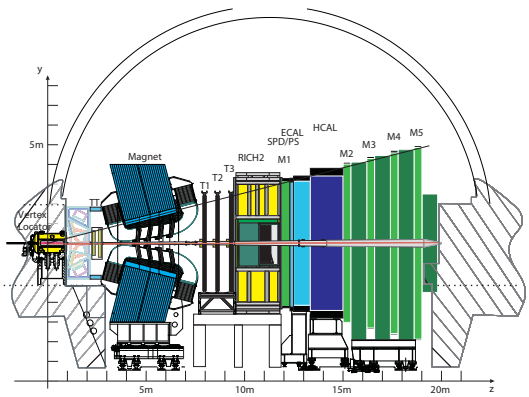

Figure 6.1:
Vertical cross section through the LHCb detector.

the experiment with long silicon micro-strip detectors. The Inner Tracker (IT (3)) also uses silicon micro-strip detectors and covers a 120 cm wide and 40 cm high region in the centre of T1-T3. The outer region of these stations is covered by straw drift-tubes. Other components of the LHCb detector are two ring-imaging Cerenkov (RICH) detectors, calorimeters (SPD,PS,ECAL,HCAL) and muon chambers (M1-M5).

6.2 Silicon tracker

Our group has taken the leading rôle in the development, production, commissioning and operation of the Silicon Tracker. The project is led by O. Steinkamp with U. Straumann as his deputy.

Within this project, the main responsibility of our group is the design and construction of the TT station. A large fraction of our efforts in 2006 was spent on the production and quality assurance (QA) of detector modules and on the assembly, testing and installation of the detector box and support frames. Both activities were completed in the beginning of 2007. Other responsibilities of our group include the design and procurement of the silicon sensors and the design and production of the optical digital readout link for both TT and IT. The last batch of silicon sensors was received and successfully tested early in 2006, whereas the production of the readout system components took place in autumn 2006.

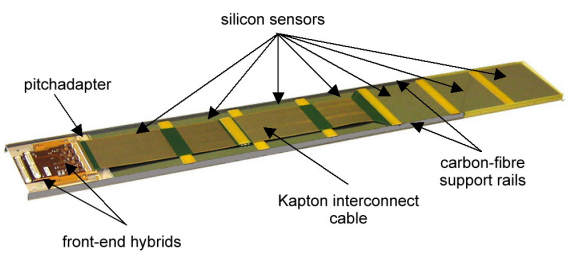

Figure 6.2: TT detector module.

6.3 Trigger tracker

A photograph of a TT detector module is shown in Fig. 6.2. The module consists of seven silicon sensors that are electronically organised into either two or three readout sectors. The front-end readout hybrids for all readout sectors are located at one end of the module, the "inner" readout sectors being connected to their readout electronics via approximately 39 cm, resp. 58 cm, long Kapton interconnect cables. The layout of a TT detection layer is illustrated in Fig. 6.3. Different readout sectors are indicated by different shadings. The areas above and below the beam pipe are each covered by a single detector module, the areas to the left and to the right of the beam pipe are covered by 14-sensor long super-modules that are formed by gluing two detector modules together end-to-end. The advantage of the chosen detector design is that it permits to keep all readout electronics and the associated dead material outside of the acceptance of the experiment.

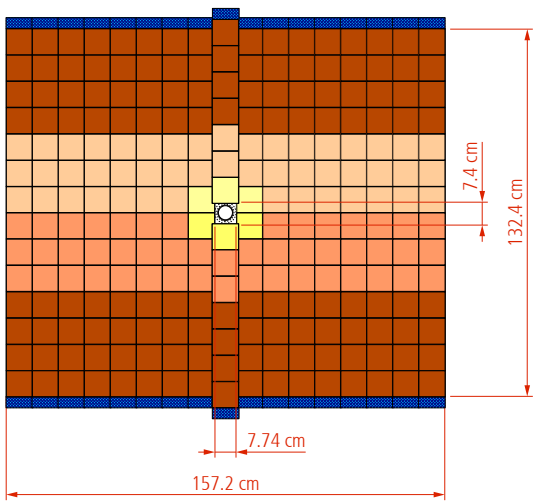

Figure 6.3: Layout of one detection layer of TT.

6.3.1 Module production and quality assurance

The series production of detector modules was launched in September 2005 and completed just before Christmas 2006. Including 15% spares, a total of 148 modules with about 165'000 readout channels has been produced. At all stages of the production, a rigorous QA programme was carried out to ensure that the modules fulfill our strict mechanical and electrical acceptance criteria (5). As part of this QA programme, each module went through at least two "burn-in" tests. These included 36h-long temperature cycling between room temperature and the foreseen operating temperature of 5°C, measurements of leakage currents as a function of temperature and applied bias voltage, of detector noise to identify faulty readout channels and readout chips, of signal pulse-shapes and of the charge collection efficiency. For the latter measurement, charge was generated at pre-defined locations in the silicon sensors using pulsed infra-red laser diodes. A total of 2 TByte of data were accumulated during these burn-in tests. They are stored in a central production data base that was set up for this purpose and permits easy access to the data and the main test results.

Figure 6.4: TT module production.

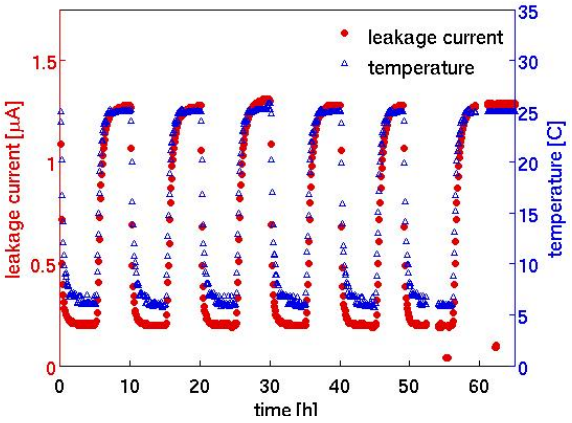

Figure 6.5: Operating temperature and leakage current as a function of time as measured during the burn-in of a TT detector module.

Based on the results of these tests, a quality grading has been established that permits to select the "best" modules for installation in the most important region of the detector close to the beam-pipe, and to assign the least good modules as spares. The module production was run by F. Lehner and T. Sakhelashvili with help from J. Gassner, the quality assurance programme was run by J. Gassner with help from D. Volyanskyy and A. Vollhardt. The production data base was set up by T. Müller and N. Chiapollini and a significant part of the data analysis was done by V. Hangartner. For the latter two, this work was part of their Bachelor theses (6; 7). A photograph from the module production and an example of one of the many measurements performed in the burn-in test are shown in Figs. 6.4 and Figs. 6.5.

6.3.2 Detector box and support rails

All detector modules will be housed in a common light-tight and thermally insulating box, which also provides electrical insulation to the environment (8). This detector box consists of two halves that are mounted onto precision rails and can be retracted from the beam pipe for detector maintenance and for bake-

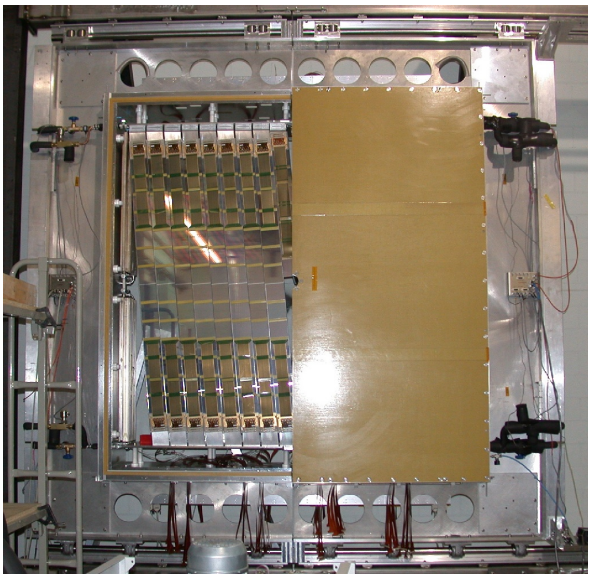

Figure 6.6: The test installation in Zürich.

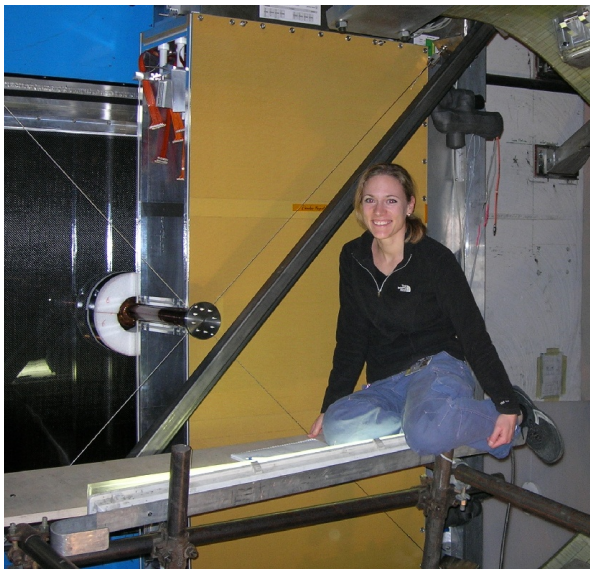

Figure 6.7: The installation in LHCb.

outs of the LHC beam pipe. To remove the heat generated by the front-end electronics and to obtain the desired ambient temperature of around 5°C inside the detector box, the box design incorporates several cooling plates through which C_6F_{14} is circulated as a cooling agent.

In summer 2006, the complete detector box including support rails was set up in our mechanical workshop and various mechanical and thermal tests were performed, including a test installation of several detector modules. The detector box was then disassembled and shipped to CERN where it was installed in the LHCb experiment in December 2006. The design and production of the station mechanics has been the responsibility of S. Steiner. The thermal tests were prepared, performed and documented by A. Büchler as part of her Master thesis (9). J. van Tilburg and S. Steiner played leading rôles in the installation of the detector box at CERN. Photographs from the test installation in Zürich and from the final installation at CERN are shown in Figs. 6.6 and 6.7.

6.4 Readout system

The analog detector signals from TT and IT are transmitted via short copper cables to so-called Service Boxes, where they are digitised, multiplexed and prepared for optical transmission to the LHCb electronics barrack. The Service Box crates and the "digitizer boards" on which the processing of the signals takes place have been produced and are currently being tested in the laboratory in Zürich. Their installation in the experiment is foreseen for spring 2007. The design, production, testing and commissioning of the readout link for TT and IT is the responsibility of A. Vollhardt.

6.5 Detector simulation and reconstruction software

In addition to the hardware activities described above, we continued our involvement in software activities on the Monte-Carlo simulation of the Silicon Tracker and on algorithms for track reconstruction and detector alignment. Main achievements were the implementation of a more robust algorithm for

track fitting and an upgrade of the track reconstruction software to be able to cope with mis-aligned detectors. J. van Tilburg has been a main contributor to these LHCb-wide activities.

6.6 Physics studies

Monte-Carlo simulation studies for the decay mode $B_s^0 \to J/\psi\,\eta'$ have been continued. The time-dependent measurement of the CP asymmetry in this decay can be used to determine the phase of $B_s^0\overline{B^0}_s$ oscillations (i.e. the CKM angle χ). Since this phase is predicted to be very small in the Standard Model, it provides a sensitive probe for contributions from "new" physics beyond the Standard Model (10).

The goal of our simulation study is to optimize event selection criteria and to estimate the sensitivity of the experiment to the underlying physics parameters. Selection cuts have been further optimised using a multi-variate grid search and larger samples of generated background events. The chosen set of cuts results in an estimated annual signal yield of about 4k reconstructed events and an upper limit on the background-to-signal ratio of around 0.4 at 90% confidence level. The results of this Monte-Carlo study have then been used to simulate a large number of toy experiments and estimate the expected sensitivity of LHCb to the CKM angle χ. For the statistics corresponding to one nominal year of data taking the sensitivity was found to be 0.04 rad (11). This physics study has been undertaken by D. Volyanskyy who is currently finishing his Ph.D. thesis under the guidance of J. van Tilburg and U. Straumann.

6.7 Summary and outlook

The series production of detector modules for the Trigger Tracker has been completed. An extensive quality assurance programme has been performed on all modules and the quality of the produced modules has been found to be excellent. The Trigger Tracker detector box has been assembled, tested and installed in the experiment. The readout electronics boards for Trigger Tracker and Inner Tracker have been produced, testing of these boards will be completed soon.

Software developments for detector simulation and reconstruction algorithms are ongoing as well as simulation studies in preparation for physics analyses.

[1] LHCb technical proposal, CERN/LHCC 98-004.

[2] LHCb Reoptimised Detector Technical Design Report, CERN/LHCC 2003-030.

[3] LHCb Inner Tracker Technical Design Report, CERN/LHCC 2002-029.

[4] Layout and expected performance of the LHCb TT station, J. Gassner, M. Needham, O. Steinkamp, LHCb note 2003-140.

[5] Design and Production of Detector Modules for the LHCb Silicon Tracker, O. Steinkamp et al., LHCb notes 2006-063 and 2007-009.

[6] The LHCb TT production database and an overview of quality characteristics of the detector modules, N. Chiapolini, Bachelor thesis, Universität Zürich (2007).

[7] LHCb TT module properties, V. Hangartner, Bachelor thesis, Universität Zürich (2007).

[8] The Mechanical Design of the LHCb Silicon Trigger Tracker, J. Gassner, F. Lehner, S. Steiner, LHCb note 2004-110.

[9] Thermal and mechanical characterisation of the TT detector for the LHCb experiment, A. Buechler, Master Thesis, Universität Zürich (2007).

[10] J.P. Silva and L. Wolfenstein, Phys. Rev. $\mathbf{D}\ \mathbf{55}$ (1997) 5331.

[11] Selection of the $B_s^0 \to J/\psi\,(\mu^+\mu^-)\,\eta'\,(\rho^0\gamma)$ decay at LHCb and its sensitivity to the B_s^0 mixing phase ϕ_s, J. van Tilburg and D. Volyanskyy, LHCb note 2007-027.

7 Particle Physics with CMS

E. Alagöz, C. Amsler, V. Chiochia, C. Hörmann[7], H. Meyer, C. Regenfus, P. Robmann, J. Rochet, T. Rommerskirchen, T. Speer, S. Steiner, D. Tsirigkas[8], and L. Wilke

In collaboration with:
ETH - Zürich, Paul Scherrer Institut (PSI) and the CMS Collaboration

The main goal of the CMS experiment is to search for the Higgs boson and for physics beyond the Standard Model (SM). The mass of the Higgs can be calculated from the t-quark mass and radiative corrections: M_H <186 GeV (95% CL) (1). A light Higgs (M_H <130 GeV), decays mainly to $b\bar{b}$, a heavy Higgs mainly to four leptons via W^+W^- or Z^0Z^0. However, for light Higgs the $gg \rightarrow b\bar{b}$ background dominates the $H \rightarrow b\bar{b}$ signal in an inclusive search.

The Minimal Supersymmetric Standard Model (MSSM) is the most popular extension of the SM which stabilizes the Higgs mass and achieves unification at high energies. In addition to SUSY particles the MSSM requires five spin zero fields, the neutral h, H, A and the charged $H^{\pm}$. Two parameters (M_A and tanβ) are needed to fix their masses.

At pp colliders and for small tanβ the h, H, A should be produced dominantly by two gluons through the b- and t-quark loops (Fig. 7.1a) supplemented by SUSY contributions. However, large value of tanβ (≥ 5) are favoured (2) in which case the main Higgs production mechanism is radiation off b-quarks (Fig. 7.1b).

The h lies below 130 GeV and decays dominantly into $b\bar{b}$. The A and H decay into $b\bar{b}$ (or $t\bar{t}$), the H into hh for small tanβ which also lead to b-quarks. Hence the detection of B-mesons is of *crucial importance* in Higgs physics. Several benchmark channels for MSSM Higgs searches have been studied in CMS (3). The Zurich group is preparing a

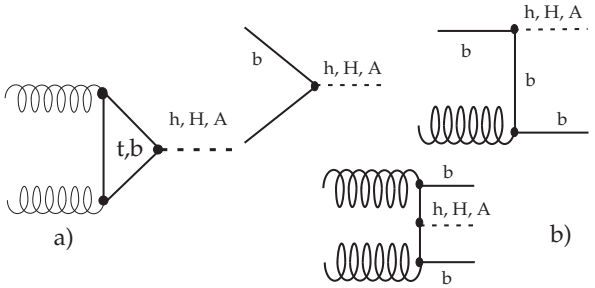

Figure 7.1: Main contribution to the MSSM Higgs production at the LHC for small tanβ (a). Higgs-strahlung becomes important for large tanβ (b).

search for the h associated with the decay of supersymmetric particles. However, during the first two years of LHC operation the luminosity will be well below the design value of 10^{34} cm^{-2}s^{-1} which makes an early discovery of the Higgs unlikely. Meanwhile tools (secondary vertex reconstruction, trigger, b-tagging) need to be developed or tuned with early data. We therefore plan to examine first b-physics issues, hence decays of B-mesons.

Many properties of the B_s, such as the differences between the masses and widths of the two weak eigenstates (B_S^H and B_S^L), can be studied with the decay $B_s \rightarrow (J/\psi)\phi$. A full reconstruction of the B_s can be achieved through the decays $J/\psi \rightarrow \mu^+\mu^-$ and $\phi \rightarrow K^+K^-$. First measurements of the mass difference Δm_s between B_S^H and B_S^L have recently been reported from the Tevatron (4). However, the difference between their widths, $\Delta\Gamma_s$, has not been measured with sufficient precision to be compared with the SM prediction ($\Delta\Gamma_s/\Gamma_s \sim 0.1$).

[7] Until June 2006
[8] CERN doctoral student

The $B_s \rightarrow (J/\psi)\phi$ decay also provides one of the best ways to determine the height of the unitarity triangle. One would measure the (CP-violating) asymmetry between $B_s \rightarrow (J/\psi)\phi$ and $\bar{B}_s \rightarrow (J/\psi)\phi$ which requires tagging the flavor of the B_s. An alternative method is to measure the angular distributions of the final state K's and μ's which are different for the CP-even and CP-odd components. This does not require tagging but large data samples which can be obtained at the LHC.

The Zurich group is contributing to the CMS experiment since 1995. We are involved in the reconstruction software, in particular track and vertex reconstruction (5; 6) and constraining kinematic fits (7). We are preparing the analysis of $B_s \rightarrow (J/\psi)\phi$ and a search for the MSSM Higgs bosons decaying into, or associated to, $\bar{b}b$ pairs. We are contributing to the innermost device, the barrel pixel detector, with which secondary vertices from B-decays can be determined. We have measured on CERN test beams the performance of pixel sensors before and after irradiation. Many details can be found in ref. (8). We have contributed to the development of the readout chip and of the power distribution system. We are constructing the mechanical support structure for the pixel detector and the service tubes which provide the coolant and power, and transfer the signals to and from the pixel detector.

7.1 Reconstruction software

In 2006 we ported the track and vertex algorithms (previously written in ORCA) to the new reconstruction environment (CMSSW) while maintaining the performance demonstrated in the Physics TDR (9). For the vertex reconstruction we had to rewrite the software and adapt the various fitters (Kalman, Gaussian-sum, and kinematic fits, see previous annual reports).

The CMS b-tagging working group, led by one of us (T.S.), is responsible for the development of b-tagging, offline vertex reconstruction algorithms and high level trigger (HLT) for b-decays. The main feature used to distinguish b-jets from light flavour jets is the long lifetime of B-hadrons. The simplest algorithm (used in the HLT) is based on the large impact parameter with respect to the primary vertex. More elaborate algorithms identify the b-decay vertex and select large decay lengths to reject the short-lived background. Further properties can be used, such as the large mass of the b-quark and the high (> 4) final state multiplicity.

The detection of an electron (or a muon) can be used, the semileptonic branching fraction of b-quarks to an electron being of the order of 10%. We are contributing to the reconstruction of electrons from semileptonic b-decays. Some b-jets contain electrons with follow curved trajectories in the magnetic field until they reach the electromagnetic calorimeter. Without tracker material the projection of the trajectories in the transverse plane would be circular, leading to energy deposits in the calorimeter extending over a small number of crystals. However, bremsstrahlung photons from the tracker material leads to azimuthal smearing of the energy deposits. We have improved on algorithms to disentangle energy deposits from different electrons and have included them in CMSSW.

7.2 $B_s \rightarrow (J/\psi)\phi$

This channel has been chosen a a benchmark channel by the CMS collaboration (3). In the offline analysis the decay $B_s \rightarrow (J/\psi)\phi \rightarrow \mu^+\mu^- K^+ K^-$ is reconstructed by combining a pair of $\mu^+\mu^-$ tracks with two additional tracks of opposite charges. As CMS does not possess a particle identification system all tracks have to be considered as possible kaon candidates. A kinematic fit is applied in which the

four tracks are constrained to a common vertex and the $\mu^+\mu^-$ invariant mass is constrained to the mass of the J/ψ.

A maximum likelihood fit of the decay angular distribution was performed on a sample of 14'000 simulated events, together with background events such as the dominant

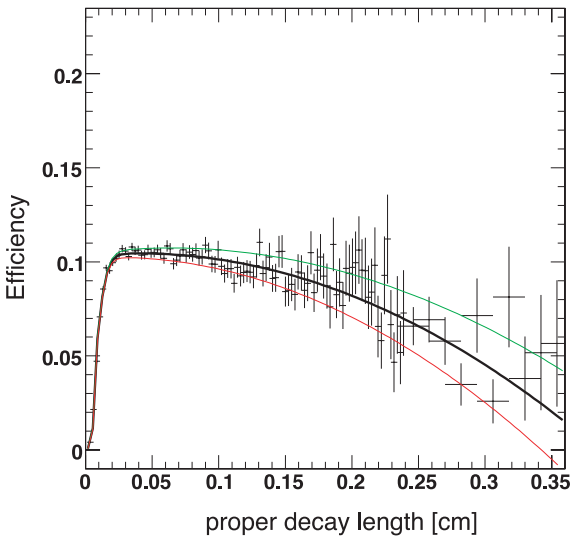

Figure 7.2: Distribution of the B_s-detection efficiency as a function of proper decay length with fit function and 1σ uncertainties.

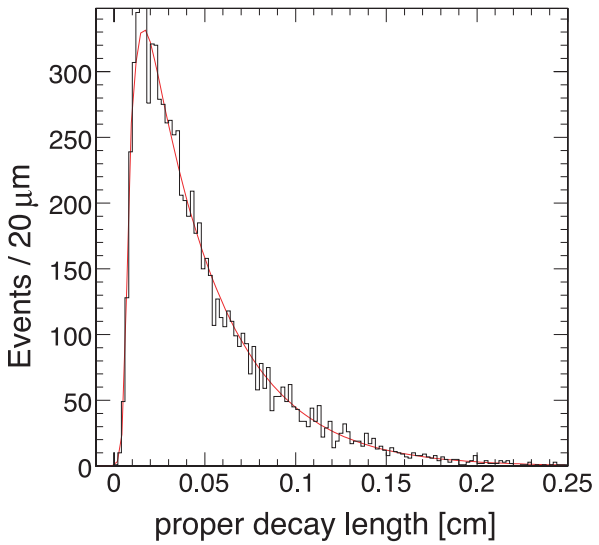

Figure 7.3:
B_s decay-length distribution with fit in red.

$B \to J/\psi X$. The decay $B_d \to J/\psi K^{*0} \to \mu^+\mu^- K^+\pi^-$ is of particular concern, since the pion can be confused with a kaon. This final state also displays a time-dependent angular distribution similar to that of B_s-decay. The modeling of the reconstruction efficiency for the decay length is delicate. Without appropriate correction the events at large decay lengths lead to shorter lifetime measurements (Fig. 7.2).

The analysis of $B_s \to (J/\psi)\phi$ assumes a HLT trigger to enrich the B_s-sample. (We are also developing a trigger for other b-channels such as $B_d \to J/\psi K^* \to \mu^+\mu^- K^+\pi^-$ or $B_s \to \mu^+\mu^-$). In a first step one searches for two muons in the CMS muon chambers with transverse momenta above 3 GeV/c. In the HLT b-candidates are identified through partial reconstruction of the decay products in restricted tracking regions. The muon tracks are then precisely reconstructed and the b-decay vertex determined. A minimum distance from the primary vertex is required and J/ψ events are selected by a cut on the 2μ-invariant mass. The efficiency of the trigger for $B_s \to (J/\psi)\phi \to \mu^+\mu^- K^+K^-$ events is 20%.

The resolution on the B_s-invariant mass after kinematic fit is 14 MeV and the resolution on the proper decay time 77 fs (7). The decay length distribution is shown in Fig. 7.3. The results show that we will be able to measure a value of say $\Delta\Gamma_s/\Gamma_s = 0.20$ with an uncertainty of 20%. To investigate the influence of $\Delta\Gamma_s$ on the measurement a simple Monte-Carlo simulation was developed which produces events according to the angular (time-dependent) distribution smeared with the experimental resolution. From these studies we conclude that the statistical error on $\Delta\Gamma_s/\Gamma_s$ will decrease to 5% for 110'000 events (corresponding to 10 fb^{-1}) at which point the systematic error will start to dominate.

7.3 $h \longrightarrow b\bar{b}$ in SUSY cascades

The lightest Higgs (h) can be produced in cascades between SUSY particle, e.g. $\tilde{\chi}_2^0 \rightarrow \tilde{\chi}_1^0 h$, $h \rightarrow b\bar{b}$, where $\tilde{\chi}_1^0$ is the lightest neutralino (possibly the WIMP of dark matter searches). These cascades start with the production of squarks and gluinos and can be identified through their comparatively large number of high energetic jets. In R-parity conserving supersymmetry the $\tilde{\chi}_1^0$ (with mass around 200 GeV) is stable. Since dark matter has survived until today, $\tilde{\chi}_1^0$ must be interacting only weakly with matter. Its signature in the CMS detector would therefore be a large missing energy. This signature offers a possibility to tag events for which the main decay mode $h \rightarrow b\bar{b}$ is otherwise hard to distinguish against QCD background. Previous studies showed that a 5σ discovery should be possible with 2 fb^{-1}(10) and thus a signal could be observed rather early at LHC. Efficient b-tagging algorithms are crucial to distinguish the b-jets in Higgs decay from those in other processes. Figure 7.4 shows an example of b-tagging efficiency based on PYTHIA and the CMSSW reconstruction software: as expected, efficient b-tagging also leads to a high background from lighter quarks.

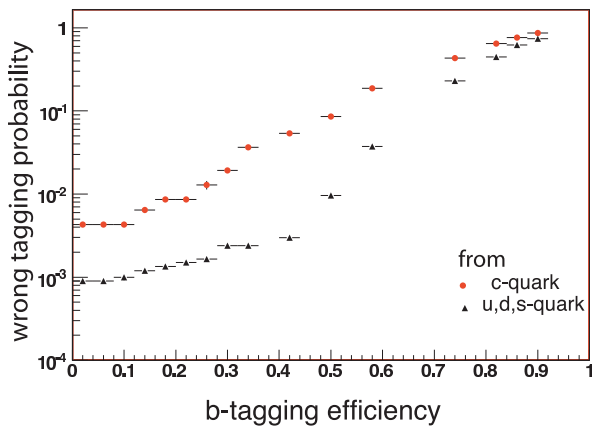

Figure 7.4: b-tagging efficiency vs. wrong tagging probability from c- or u-, d-, or s-jets.

7.4 Pixel sensors and associated software

The pixel barrel detector consists of three concentric cylindrical layers, 53 cm long, with radii of 4.4, 7.3 and 10.2 cm. The pixel sensors are made of n^+-structures on n-bulk silicon. They are mounted on segmented silicon plates connected by indium bump bonds to the readout chips. The analogue signals are read out to determine the coordinates more accurately, using charge sharing between pixels.

We have tested sensor prototypes with 105 – 225 GeV pions in the H2 beam line of the CERN SPS. Earlier results can be found e.g. in ref. (11) or in previous annual reports. In particular, we have demonstrated that the charge collection profiles measured in our beam tests and the expected trapping rates can be described by a two trap model producing a non-constant space charge density across the sensor bulk (12). This leads to electric field profiles with two maxima across the sensor bulk, one at each sensor edge. The model is supported by measurements of the electric field profile based on its dependence on the electron mobility. The measurements were obtained with a novel method using our test beam data (13). From these tests sensors with moderate p-spray isolation where chosen and the pixel size was fixed to 100×150 μm^2.

Our 2006 results on the position resolution are based on simulations relying on test beam data which were collected with pixels of dimensions 125×125 μm^2. The spatial resolution is improved after irradiation by applying so-called η-corrections to the charges collected on adjacent pixels (for details see our previous annual report). Figure 7.5 shows a simulation of the residual distribution (measured – predicted) for clusters of two pixels and tracks with an angle $\alpha = 20°$ with respect to the normal to the sensor surface. The sensor is assumed to have been irradiated with 5.9×10^{14}

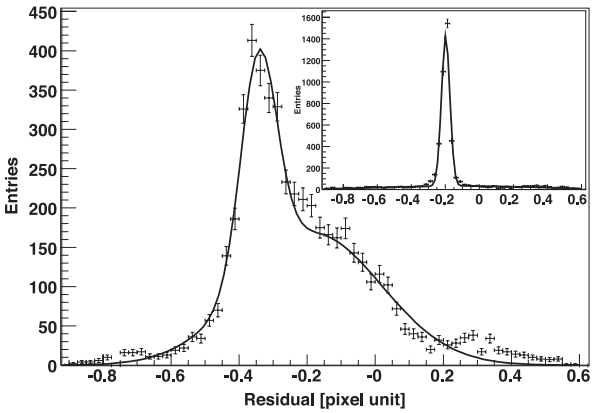

Figure 7.5: Distribution of residuals for incident tracks with α=20° and sensors irradiated to 5.9×10^{14} n$_{eq}$/cm^2. The continuous line is a double-Gaussian fit to the distribution. The inset shows the results with η-corrections. The residuals are not corrected for the Lorentz shift due to the magnetic field (from ref. [14]).

n$_{\rm eq}$/cm^2, which corresponds to the first four years of LHC operation for the innermost layer. The distribution before correction is not described by a single Gaussian and is affected by large systematic errors which depend on the inter-pixel hit position. The width can be largely reduced by applying η-corrections (inset in Fig. 7.5). A position resolution below 15 μm can be achieved for perpendicular tracks in the CMS transverse plane (14), even after heavy irradiation. Table 7.1 summarizes the expected spatial resolution for perpendicular tracks and different irradiation fluences.

Another beam test was performed at CERN in 2006 with the final pixel sizes (100 × 150 μm^2)

Table 7.1: Expected position resolution for perpendicular tracks at various irradiation fluences Φ and bias voltages V$_{bias}$.

Φ [$n_{\rm eq}$/cm^2]	V$_{bias}$ [V]	Resolution [μm]
0	200	9.0±0.1
2×10^{14}	200	12.1±0.2
6×10^{14}	300	12.9±0.1

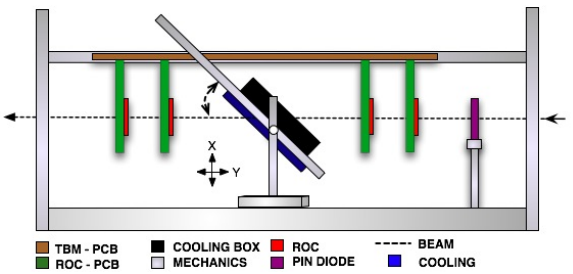

Figure 7.6: Setup used for our recent pixel test (see text).

and its front-end electronics in a 3 T magnetic field. Data were taken with irradiated and unirradiated pixel sensors with different chip calibration settings and bias voltages. The goal of this test was to study the position resolution of barrel pixel sensors before and after irradiation, with and without magnetic field, and to compare with expectations (Table 7.1).

The experimental setup (Fig. 7.6) consisted of a pixel sensor bump-bonded to a readout chip (ROC), a cooling device, a trigger system, a precise telescope to measure the direction of the incident pions, and a data acquisition system. The setup was located in a 3T Helmholtz coil with magnetic field perpendicular to the beam. The sensors (52 × 80 pixels)

Figure 7.7: PCB housing a pixel sensor bump-bonded to the ROC.

were bump-bonded to the ROC at PSI and irradiated at the CERN IRRAD1 facility with 24 GeV protons. The irradiation fluences varied from 0.37×10^{14} to $8.2 \times 10^{14} \mathrm{n_{eq}cm^{-2}}$. The irradiated samples were wire-bonded to a printed circuit board designed in our electronics workshop in Zurich (Fig. 7.7).

The beam telescope was made of four pixel sensor planes, bump-bonded to ROCs. Two of the planes were placed in front and two behind the test sensor. The beam telescope was used to determine accurately the hit position and incident angle on the test sensor. The planes were tilted by 20° to enhance charge sharing (and hence position resolution). The tested sensor was located in a cool box equipped with two cooling Peltier elements for operation at $-10^\circ\mathrm{C}$. The hot sides of the Peltier elements were cooled with water and nitrogen gas was flushed in the cooling box to avoid condensation. The cooling box could be rotated for measurements at different incident angles. A trigger signal was provided by a 2×6 mm^2 PID diode which was synchronized to the SPS beam clock (40 MHz). The analysis of these data is in progress. Preliminary results indicate that the measured charge distribution and cluster multiplicity agree with expectations.

In 2006 we also used our two-trap model to develop new reconstruction algorithms and calibration procedures for irradiated pixel sensors. The drifting electrons experience the Lorentz force in the 4T field of CMS and drift perpendicularly to the magnetic and biasing electric field. Figure 7.8 shows the average charge collected in a pixel cluster as a function of distance from the track entry point. The figure is produced assuming 10 GeV muons at a pseudo-rapidity $\eta \sim 2$ and using the full CMS detector simulation. The Lorentz angle Θ_L can be extracted from this figure using the relation $\tan\Theta_L = \frac{L}{T}\tan\phi$ where L is the cluster length along the track direction and $T = 285$ μm is the sensor thickness. Figure 7.9 shows the effect from test beam data for comparison.

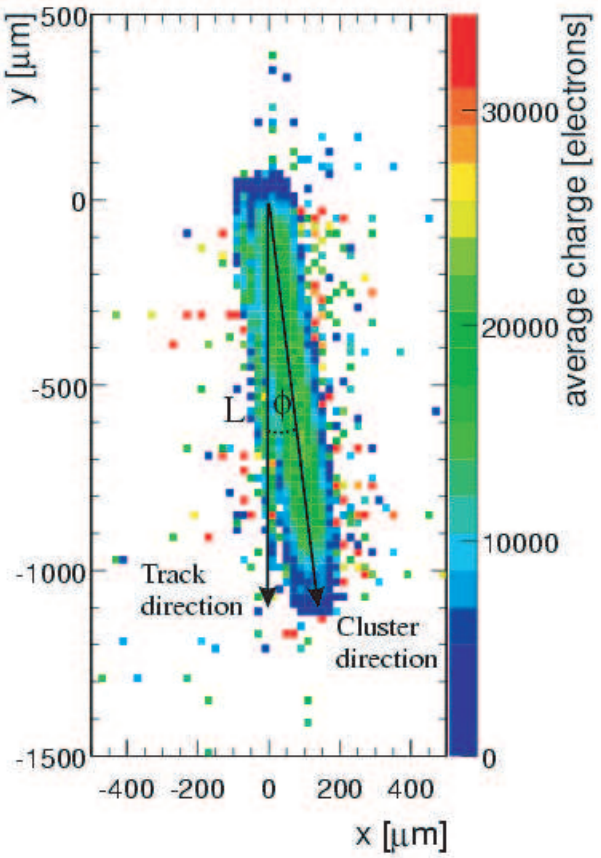

Figure 7.8: Average charge of clusters produced by 10 GeV muons in the first pixel barrel layer for η~2, as a function of distance from the track entry point (simulation). The y-coordinate is parallel to the beam direction. The collected charge is shifted along the x-coordinate due to the Lorentz effect.

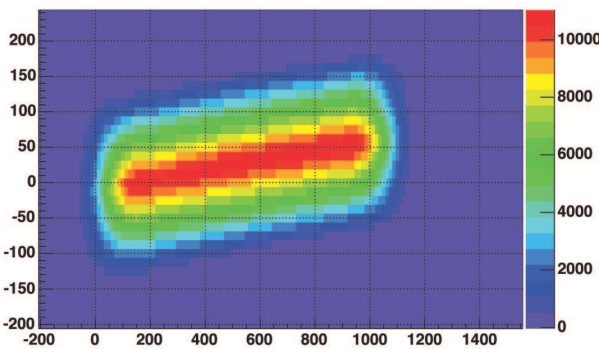

Figure 7.9: Real data from a beam test at 3 T.

Due to radiation damage the sensor response is expected to change during detector operation and several quantities have to be monitored to guarantee a precise determination of the hit positions. One of us (V.C.) is leading the pixel Data Quality Monitoring group (DQM). Data monitoring will be performed online and offline and includes raw hits, reconstruction of hit clusters and multiplicities, pixel track seeds, distribution of primary vertices from pixel tracks and impact parameters.

In particular, the Lorentz deflection leads to a shift of the hit coordinate (Fig. 7.5) which needs to be corrected. The correction (which can reach 120 μm) will change as a function of time and as a function of location due to radiation damages which modify the electric field distribution. The Lorentz angle will therefore be monitored in-situ. We wrote the software to extract the Lorentz deflection angle directly from CMS data. Since the three barrel layers will be exposed to different fluences, the Lorentz angle must be measured in each detector layer as a function of pseudo-rapidity. The shift can be determined for a given ionization depth in the sensor using a large number of well measured tracks (Fig. 7.10). The detector is subdivided into its

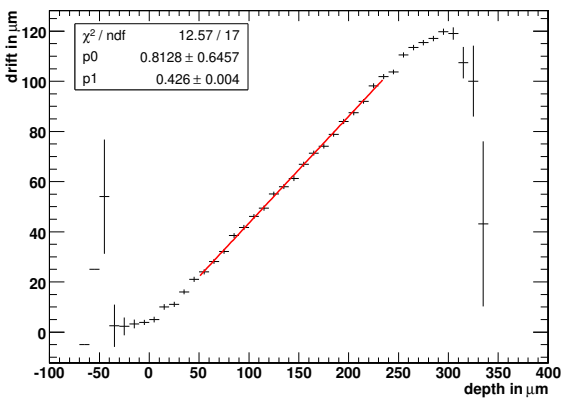

Figure 7.10: Shift of the hit coordinate due to the Lorentz drift as a function of depth at which the charge is produced in the sensor (simulation of non-irradiated sensors). The value for tan Θ_L is read from the slope of the fit (in red).

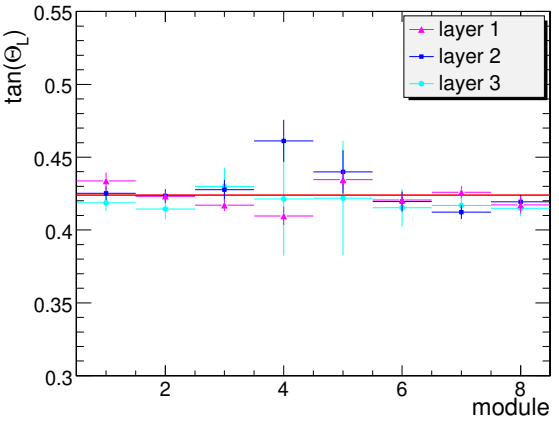

Figure 7.11: Reconstructed Lorentz angle angle for the 24 rings. The horizontal red line is the value assumed for the simulation.

three cylindrical layers with eight rings for various pseudo-rapidities. A separate fit is performed for each of the 24 rings. The reconstructed Lorentz angle from simulated $Z^0 \rightarrow \mu^+\mu^-$ events agrees with the assumed value in the simulation (Fig. 7.11).

We are currently developing applications for visualizing DQM histograms (web interface) and generate alarms. The DQM software will be tested with the pixel detector hardware during the integration phase planned for the first half of 2007.

7.5 Pixel efficiency

The performance of the barrel modules was studied in a recent PhD thesis (15). A module is made of 16 ROCs connected to the 66'560 pixels by the bump bonding technique. We measured the inefficiency under LHC conditions in a high rate pion beam at PSI and compared with simulations. The setup is shown in Figs. 7.12 and 7.12. The inefficiency is about 2% for the innermost layer (Fig. 7.14). Let us mention in particular the problem of Single Event Upsets (SEUs) which are due to the harsh radiation environment,

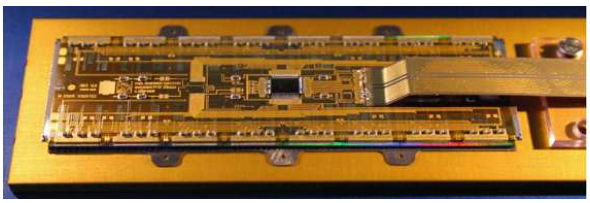

Figure 7.12: Pixel readout module.

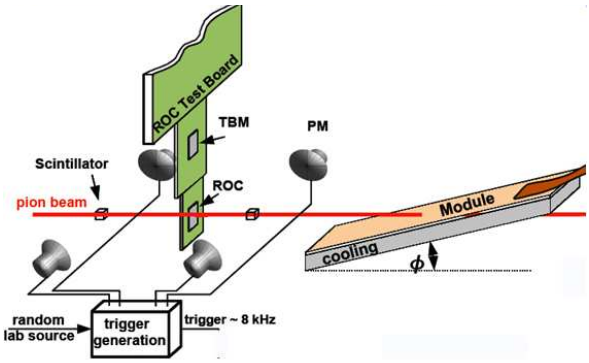

Figure 7.13: Beam setup to measure the inefficiency.

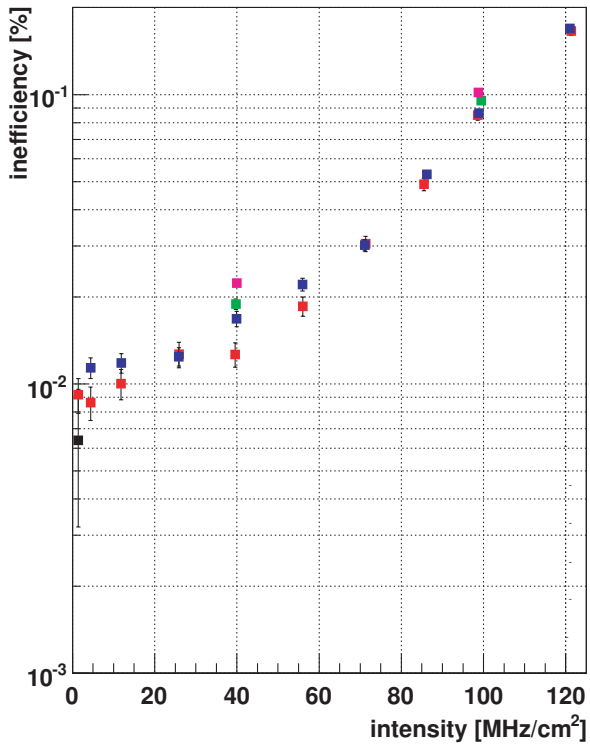

Figure 7.14: Inefficiency for different trigger rates (for details see ref. [15]). The flux at the innermost pixel layer in the LHC will be 60 MHz/cm^2.

causing corrupted memory cells. This was studied and alleviated with protection capacitors yielding about 1 SEU/s for the entire pixel barrel detector ($\sim 48 \times 10^6$ pixels) at full luminosity (15). This development is now completed and mass production is underway at PSI.

7.6 Detector support structure and service tubes

The support structure for the barrel pixel detector and the corresponding service tubes are currently under construction in the Institute's workshop. The 5m long assembly is made of two separated half shells containing the detector and two service half shells at each end (Fig. 7.15). The detector end-flanges were finalized in 2006 and adapted to the detector end-ring prints. The flanges consist of thin fibreglass frames (FR4) filled with foam (Airex) covered by carbon fibre blades. The end-flanges support the individual detector ladders of the three layers. The end-ring prints connect the detector modules mounted on the ladders to the readout electronics installed in the corresponding readout slots of the service tubes.

The various components, such as carbon fibre blades and cooling containers, were produced in 2006 and the assembly of the support structure has started. The power, the cooling fluid, the control and the optical signals are transferred through the service tubes to the pixel detector (Fig. 7.15). The massive cables are attached to the outer flange. The structure is supported by stainless steel tubes (wall thickness of 100 μm) connected to the stiffener rings and the inner and outer aluminium flanges. The tubes also supply the detector with the cooling fluid. The gaps are filled with Airex foam.

We have also designed the printed circuit supply boards (motherboards and readout elec-

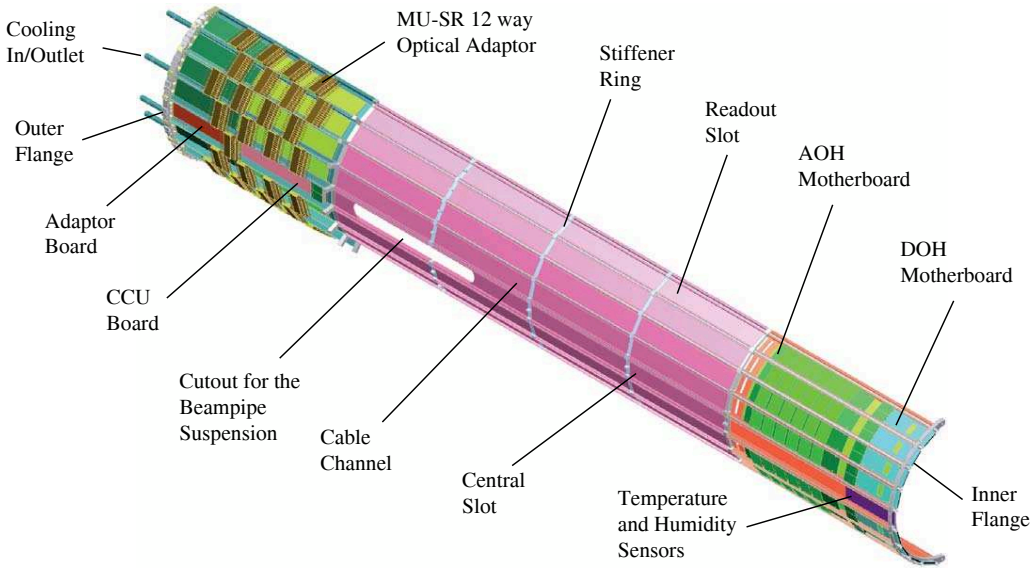

Figure 7.15: Overview of a supply tube half shell.

tronics). The motherboards which hold the optical hybrids for the analogue and digital control links are installed in eight readout slots near the detector on the integrated supply boards. The corresponding boards at the outer ends carry the power adaptor boards, which provide the detector power and the bias voltage. In the central slot the digital communication and control board (CCU) is installed which distributes the control signals to the individual readout boards of the eight readout sectors and collects the information on temperature, pressure and humidity. The optical fibres are loosely installed in the cable channels.

Our electronics workshop is involved in the pixel detector front-end control system. It consists of four CCUs, each controlling a quarter of the detector (eight barrel sectors). Figure 13.1 shows the block diagram of a CCU Board.

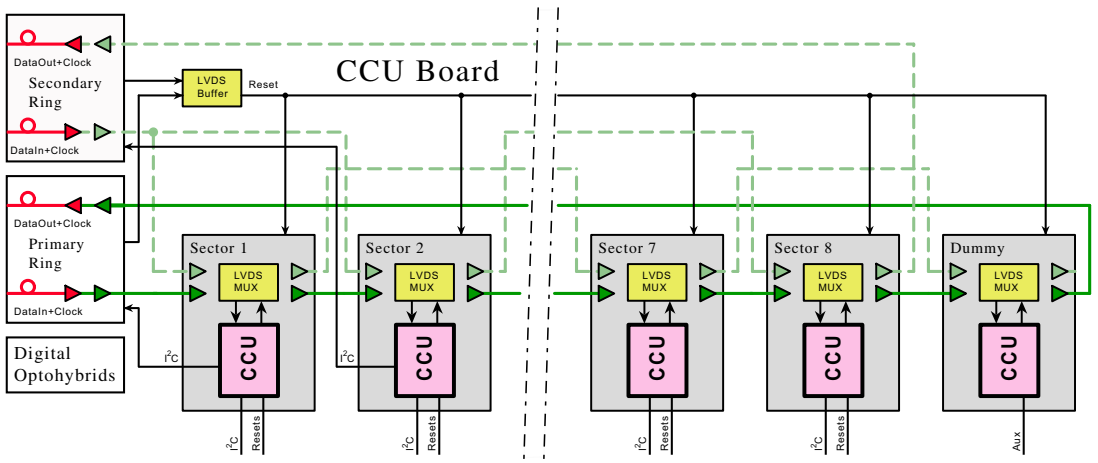

Figure 7.16: Block diagram of the Barrel Pixel control system. Only 5 of the 9 CCUs are shown for simplicity. One CCU board controls eight readout sectors of the barrel pixel detector.

Our group is also responsible for the design of the CMS pixel detector power distribution for the front end electronics (low voltage) and the pixel sensors (high voltage), and cabling. The power lines are integrated in the service tubes. The high and low DC voltages are generated with a commercial modular system manufactured by CAEN. The system has to cope with sudden (100 ns) current excursions of 2 A in 50 m long power lines.

The detector support structure for the three layers will be ready in August 2007 and the pixel detector will be installed in CMS in January 2008.

[1] LEP Electroweak working group (2005), http://lepewwg.web.cern.ch/LEPEWWG/ .

[2] For a brief summary, see C. Amsler, "SM and MSSM Higgs at the LHC", http://amsler.web.cern.ch/amsler/Higgs.pdf

[3] The CMS collaboration, "CMS Physics Technical Design Report Volume II: Physics Performance", CERN/LHCC 2006-021, CMS TDR 8.2, 2006.

[4] V.M. Abazov et al., Phys. Rev. Lett. **97** (2006) 021802; A. Abulencia et al., Phys. Rev. Lett. **97** (2006) 062003.

[5] R. Frühwirth and T. Speer, Nucl. Instr. and Meth. in Phys. Res. **A 534** (2004) 217.

[6] R. Frühwirth, K. Prokofiev, T. Speer, P. Vanlaer and W. Waltenberger, Nucl. Instr. Meth. in Phys. Res. **A 502** (2003) 699.

[7] K. Prokofiev, PhD Thesis, Universität Zürich (2005).

[8] Y. Allkofer et al., submitted to Nucl. Instr. Meth. in Phys. Res. **A**, prep. physics/0702092 (2007).

[9] The CMS collaboration, "CMS Physics Technical Design Report Volume I: Detector Performance and Software", CERN/LHCC 2006-001, CMS TDR 8.1, 2006.

[10] F. Moortgat, P. Olbrechts, L. Pape and A. Romeyer, CMS Note 2006/090.

[11] A. Dorokhov et al., Nucl. Instr. Meth. in Phys. Res. **A 530** (2004) 71.

[12] V. Chiochia et al., IEEE Trans. Nucl. Sci. **52** (2005) 1067; V. Chiochia et al., Nucl. Instr. Meth. in Phys. Res. **A 568** (2006) 51; M. Swartz et al., Nucl. Instr. Meth. in Phys. Res. **A 565** (2006) 212.

[13] A. Dorokhov et al., Nucl. Instr. Meth. in Phys. Res. **A 560** (2006) 112.

[14] E. Alagoz, V. Chiochia, M. Swartz, Nucl. Instr. Meth. in Phys. Res. **A 566** (2006) 149.

[15] C. Hörmann, PhD Thesis, Universität Zürich (2006).

8 Superconductivity and Magnetism

D.G. Eshchenko, P.S. Häfliger (April 2006 to March 2007), H. Keller, R. Khasanov, I. Landau (November till December 2006), F. La Mattina, A. Maisuradze, J. Roos, S. Strässle, St. Weyeneth, B.M. Wojek (since December 2006), R. Kuhn (Master student), C. Duttwyler (Master student)

Visiting scientists:
M.V. Eremin, B. Graneli, A. Ivanshin, B. Kochelaev, R. Pusniak, A. Shengelaya

Emeritus members:
Prof. K.A. Müller (Honorarprofessor), Prof. T. Schneider (Titularprofessor), Dr. M. Mali

in collaboration with: ETHZ (K. Conder, J. Karpinski), PSI (K. Conder, E. Morenzoni), Max-Planck-Institute for Solid State Research Stuttgart (A. Bussmann-Holder), IBM Rüschlikon Research Laboratory (J.G. Bednorz), University of Geneva (Ø. Fischer, J.M. Triscone), University of Birmingham (E.M. Forgan), University of Rome (D. Di Castro), Kazan State University (A. Dooglav, M.V. Eremin, V. Ivanshin, B.I. Kochelaev), Polish Academy of Sciences (R. Puzniak), University of Belgrade (I.M. Savić), Tbilisi University (A. Shengelaya), Kurchatov Institute (V.G. Storchak), University of Tokyo (T. Sasagawa, H. Takagi), UBC (J.H. Brewer), Iowa State University (A. Kaminski).

In 2006 we continued our research on magnetic and electronic properties of novel materials which we investigated by means of a combination of different complementary experimental techniques, including muon spin rotation (μSR), electron paramagnetic resonance (EPR), nuclear magnetic resonance (NMR), nuclear quadrupole resonance (NQR), as well as SQUID and torque magnetometry.

The main research topics were:

- Study of magnetic and electronic properties of novel superconductors: magnetic penetration depth in cuprate high-temperature superconductors and its signature of a two-gap behavior, local magnetic fields in cuprate multilayers studied by μSR, rare-earth ion relaxation in YBCO compounds by EPR, charge fluctuation effects in YBCO compounds by NMR/NQR, magnetic penetration depth studies in non-centrosymmetric superconductors $Li_2(Pd/Pt)_3B$ by μSR, magnetization studies of Al doped MgB_2.
- Investigation of the oxygen isotope effect and its field dependence in cuprate high-temperature superconductors.
- Pressure effect on the Ginzburg-Landau parameter in YB_6.
- Investigations of electric-field effects on the electronic structure of Cr-doped strontium titanate.
- Exploration of the microscopic magnetic properties of dilute magnetic semiconductor films by low-energy μSR.

8.1 Studies of oxygen isotope effects in novel superconductors

8.1.1 Oxygen isotope effect in optimally doped high-temperature superconductors

The observation of unusual isotope effects in cuprate high-temperature superconduc-

tors (HTS) on the transition temperature T_c (see e.g. (1; 2)) and on the zero temperature in-plane magnetic penetration depth $\lambda_{ab}(0)$ (see e.g. (3; 4; 5; 6; 7)) poses a challenge to the understanding of high temperature superconductivity. It was found that the oxygen isotope ($^{16}O/^{18}O$) effect (OIE) on both T_c and $\lambda_{ab}(0)$ have a tendency to increase with decreasing doping (3; 4; 5; 6; 7). In particular, for different families of cuprate HTS there is a *universal* correlation between the isotope shifts of these two quantities (5; 6; 7). Namely, in the under-doped region $\Delta T_c/T_c$ and $\Delta\lambda_{ab}(0)/\lambda_{ab}(0)$ scale linearly with respect to each other with $|\Delta T_c/T_c| \simeq |\Delta\lambda_{ab}(0)/\lambda_{ab}(0)|$. However, close to optimal doping the situation is not so clear. The Zürich group (5; 6) observed that in optimally doped $YBa_2Cu_3O_{7-\delta}$ the small OIE on T_c is associated with a rather large isotope shift of λ_{ab}, even comparable with that found in under-doped cuprates. In contrast, Tallon *et al.* (7) showed that in slightly over-doped $La_{2-x}Sr_xCu_{1-y}Zn_yO_4$ the OIE on $\lambda_{ab}(0)$ is zero while the OIE on T_c remains still substantial.

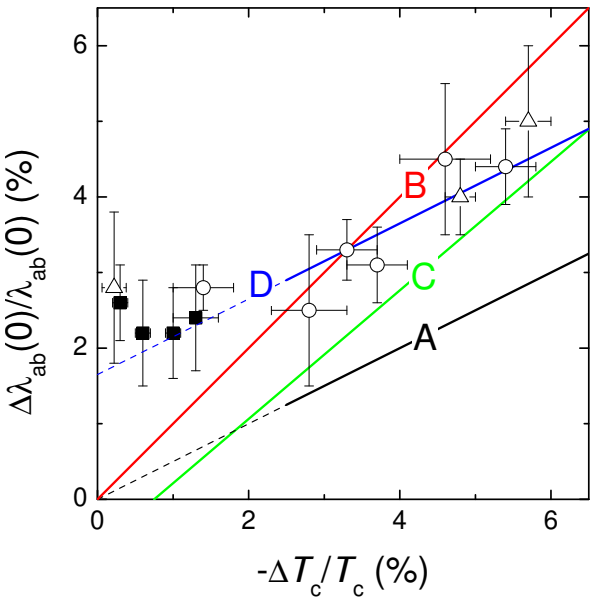

Figure 8.1: Plot of the isotope shift $\Delta\lambda_{ab}(0)/\lambda_{ab}(0)$ versus the isotope shift $-\Delta T_c/T_c$. Full squares are the μSR data obtained for $YBa_2CuO_{7-\delta}$, $Y_{0.8}Pr_{0.2}Ba_2Cu_3O_{7-\delta}$, $YBa_2Cu_4O_8$ and $La_{1.85}Sr_{0.15}CuO_4$. Circles are bulk μSR data for $Y_{1-x}Pr_xBa_2Cu_3O_{7-\delta}$ [5] and low-energy μSR data for optimally doped $YBa_2Cu_3O_{7-\delta}$ [5]. Triangles are torque magnetization and Meissner fraction data for $La_{2-x}Sr_xCuO_4$ [3; 4]. The lines correspond to the "differential Uemura" relation with $\Delta\lambda_{ab}(0)/\lambda_{ab}(0)=0.5|\Delta T_c/T_c|$ ("A"), $\Delta\lambda_{ab}(0)/\lambda_{ab}(0)=|\Delta T_c/T_c|$ ("B"), the "pseudo-gap" line from Ref. [7] ("C"), and the 2D-QSI relation given in Ref. [9] ("D"). The dashed lines indicate that the "differential Uemura" (line "A") and 2D-QSI (line "D") relations are strictly valid only in the under-doped regime (see Ref. [8]).

Recently, we performed an OIE study on T_c and $\lambda_{ab}(0)$ in optimally doped $La_{1.85}Sr_{0.15}CuO_4$ and $YBa_2CuO_{7-\delta}$, as well as in slightly under-doped $YBa_2Cu_4O_8$ and $Y_{0.8}Pr_{0.2}Ba_2Cu_3O_{7-\delta}$ by means of muon-spin rotation (μSR) (8). All the samples show a rather small OIE on T_c associated with a relatively large OIE on $\lambda_{ab}(0)$ as shown in Fig. 8.1. The fact that a substantial OIE on $\lambda_{ab}(0)$ is observed even in cuprates having a relatively small OIE on T_c suggests that lattice effects play an essential role in the occurrence of high-temperature superconductivity and have to be considered in any realistic model.

[1] J.P. Franck et al., Phys. Rev. B **44** 5318 (1991).

[2] D. Zech et al., Nature (London) **371**, 681 (1994).

[3] G.M. Zhao, M.B. Hunt, H. Keller, and K.A. Müller, Nature (London) **385**, 236 (1997).

[4] J. Hofer et al., Phys. Rev. Lett. **84**, 4192 (2000).

[5] R. Khasanov et al., J. Phys.: Condens. Matter **16**, S4439 (2004).

[6] H. Keller, in Superconductivity in Complex Systems, edited by K.A. Müller and A. Bussmann-Holder (Springer, Berlin 2005) p. 143.

[7] J.L. Tallon et al., Phys. Rev. Lett. **94**, 237002 (2005).

[8] R. Khasanov et al., Phys. Rev. B **74**, 064504 (2006).

[9] T. Schneider and H. Keller, New Journal of Physics **4**, 144 (2004).

8.1.2 Field dependence of oxygen isotope effects

The presence of nodes in the superconducting gap is probably one of the most significant features of cuprate HTS that has attracted considerable theoretical and experimental attention in recent years (see e.g., (1; 2)). The fourfold symmetric nature of the d-wave order parameter, together with the presence of gap nodes on the Fermi surface, open possibilities for novel effects to be observable in HTS. One of the most remarkable effect is the magnetic field dependence of the in-plane magnetic penetration depth λ_{ab} observed in various HTS in the mixed state. It was shown that the field dependent correction to λ_{ab} arises from the nonlocal and nonlinear response of a superconductor to an applied magnetic field (3; 4).

A simple analysis reveals that both the nonlinear and the nonlocal corrections to λ_{ab} are expected to depend on the mass of the in-plane charge carriers m^*_{ab} (5). A study of the field dependence of the isotope effect on λ_{ab} can serve as a direct test of this prediction. Indeed, several OIE studies of the in-plane penetration depth λ_{ab} in various cuprate families showed a pronounced oxygen-mass dependence of the in-plane supercarrier mass with ${}^{18}m^*_{ab} > {}^{16}m^*_{ab}$. Bearing in mind that within the simple London model $\lambda^2_{ab} \propto m^*_{ab}$ the in-plane magnetic penetration depth for the ^{16}O substituted sample would increase stronger with increasing magnetic field than for the ^{18}O substituted one.

We performed a study of the magnetic field dependence of the OIE on λ_{ab} in $YBa_2Cu_4O_8$ and $Y_{1-x}Pr_xBa_2Cu_3O_{7-\delta}$ (x=0.2, 0.3) by means of μSR. The following results were obtained: For each pair of the ^{16}O/^{18}O substituted samples $\lambda^{16}_{ab} < \lambda^{18}_{ab}$. The OIE on λ_{ab} decreases by more than a factor of 2 with increasing magnetic field from $\mu_0 H$=0.2 T to $\mu_0 H$=0.6 T. Both findings may be explained by the isotope dependence of the in-plane charge carrier mass m^*_{ab}.

[1] D.J. Scalapino, Phys. Rep. **250**, 329 (1995).

[2] C.C. Tsuei et al., Phys. Rev. Lett. **73**, 593 (1994).

[3] M.H.S. Amin, M. Franz, and I. Affleck, Phys. Rev. Lett. **84**, 5864 (2000).

[4] M.H.S. Amin, Ph.D. thesis, University of British Colombia, (1999); cond-mat/0011455.

[5] R. Khasanov et al., Phys. Rev. B **75**, 060505 (2007).

8.2 Studies of pressure effects in novel superconductors

8.2.1 Pressure effect on the Ginzburg-Landau parameter κ in YB_6

The Ginzburg-Landau parameter $\kappa = \lambda/\xi$ (λ is the magnetic penetration depth and ξ is the coherence length) is one of the fundamental parameters of a superconductor. The parameter κ defines the border between type-I ($\kappa < 1/\sqrt{2}$) and type-II ($\kappa > 1/\sqrt{2}$) superconductors. Remarkably, the two physical quantities (λ and ξ) entering κ depend on different properties of the superconducting material. A simple analysis (1) reveals that λ(T=0) is determined by the *normal* state properties only, whereas ξ(T=0) depends on the *normal* and the *superconducting* state properties of the material. This means that if one is able to affect only the superconducting (normal) state properties of a superconductor, the Ginzburg-Landau parameter κ would change. As a consequence, superconductors can be driven towards more type-I or more type-II behavior.

Experiments under pressure open a possibility to probe this phenomenon. It was shown (1) that the application of external pressure to an

$s-$wave BCS superconductor induces a large positive pressure effect (PE) on $\xi(0)$, together with a small positive effect on $\lambda(0)$, implying a strong negative pressure dependence of $\kappa(0)$. We studied the effect of pressure on the Ginzburg-Landau parameter κ in the single-band isotropic BCS superconductor YB_6 (1). With increasing pressure from 0 to 9.18 kbar we observed a decrease of $\kappa(0)$ by almost 8%. The pressure effects on the two quantities ($\lambda(0)$ and $\xi(0)$) entering $\kappa(0)$ were studied separately. It was found that the PE on $\kappa(0)$ arises mostly from the pressure dependence of the coherence length $\xi(0)$, while no PE on the magnetic penetration depth $\lambda(0)$ (within the experimental accuracy) was observed. It was also noticed that in BCS superconductors for which the relative pressure shift of T_c is much larger than $1/B$ (B is the bulk modulus), the pressure shifts of the superconducting quantities such as T_c, $\kappa(0)$, $\xi(0)$, $H_{c2}(0)$, $dH_{c2}/dT|_{T=T_c}$ are related to each other (see Fig. 8.2).

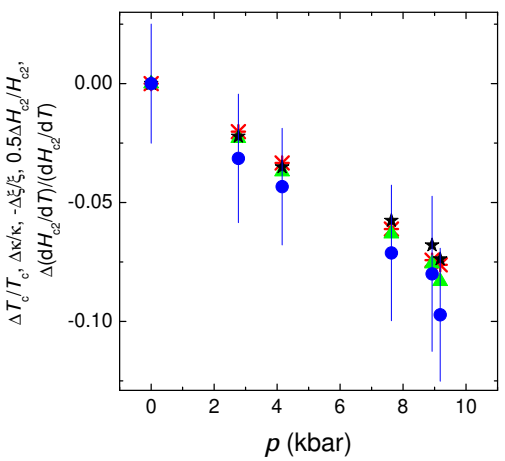

Figure 8.2: Pressure dependences of the relative pressure shifts $\Delta T_c/T_c$ (red stars), $\Delta\kappa(0)/\kappa(0)$ (green triangles), $1/2\Delta H_{c2}(0)/H_{c2}(0)$ (black stars), and $\Delta(dH_{c2}/dT|_{T=T_c})/(dH_{c2}/dT|_{T=T_c})$ (blue circles) of the YB_6 superconductor.

[1] R. Khasanov et al., Phys. Rev. Lett. **97**, 157002 (2006).

8.3 Spectroscopic studies of novel electronic materials

8.3.1 Charge effects in $LaBa_2Cu_3O_{7-\delta}$

We continued our search for charge effects in cuprates by means of ^{139}La NMR/NQR on oriented $LaBa_2Cu_3O_{7-\delta}$ powder samples (1). La is sensitive to charge effects, since its nucleus carries an electric quadrupole moment and due to its site symmetry the magnetic fields from the antiferromagnetically correlated Cu spin fluctuations are canceled. From NQR measurements we have determined the electric field gradient at the La site (quadrupole frequency and asymmetry parameter).

At the ^{139}La NMR central-line transition we determined the nuclear spin-lattice relaxation (NSLR) rate from 350 K down to 11 K. Above room temperature a thermally activated isotropic NSLR rate with an activation energy of the order of 2500 K was found. Below 270 K, however, a substantial rate anisotropy of 1.45 in the normal conducting phase was measured, which decreases below 200 K and becomes 1.3 below 150 K. By measuring the NSLR on corresponding satellite transitions at 100 K we found it to be independent of frequency, suggesting the interaction with conduction electrons as the main relaxation channel.

In the superconducting phase the NSLR rate for the field orientation parallel to the c axis of the crystal drops (see Fig. 8.3a) without showing the expected pronounced rate maximum due to vortex dynamics as observed e.g. in investigations of Y NSLR in $YBa_2Cu_4O_8$ (2). The ^{139}La nuclear spin-spin relaxation (NSSR) rate was measured by NMR at the central-line transition in the normal conducting phase. It is anisotropic in the whole investigated temperature range exhibiting pronounced steps and plateaus, which we confirmed in additional NQR NSSR measurements. To clarify the complex behavior of the measured

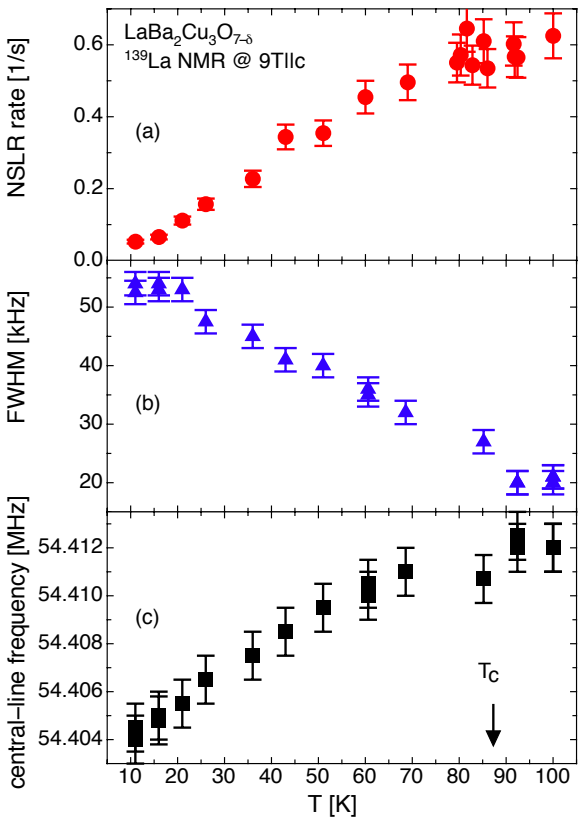

Figure 8.3:
Temperature dependence of the nuclear spin-lattice relaxation rate (a), of the full line width at half maximum (b), and of the frequency position (c) of the central-line transition of $LaBa_2Cu_3O_{7-\delta}$ in the superconducting phase at 9 T parallel to the c axis.

rates, further investigations are necessary. The ^{139}La NMR central line in the superconducting phase shows a substantial increase of the line width with decreasing temperature (see Fig. 8.3b), reflecting the temperature behavior of the magnetic field inhomogeneity caused by the rigid vortex lattice. Moreover, a decrease of the frequency of the central line was observed (see Fig. 8.3c). It is a consequence of the onset of diamagnetism and the decrease of the positive Knight shift below T_c.

[1] S. Strässle et al., in press (Physica C).

[2] M. Corti et al., Phys. Rev. B **54**, 9469 (1996).

8.3.2 NQR investigations of Fe substituted $YBa_2Cu_4O_8$

The substitution of Cu atoms by other transition metal atoms, such as Fe, Zn, Ni, Co, have proved to be a powerful way to investigate the superconducting and normal state properties of cuprate HTS. In general, with increasing substitution T_c is decreased progressively.

In case of the YBCO cuprate family the crystal structure has two different Cu sites: one in the chains (Cu1) with fourfold planar oxygen coordination, and the other (Cu2) in the CuO_2 planes with fivefold pyramidal coordination. It was observed that for Fe substitution in YBCO compounds the decrease of T_c with increasing Fe content is much stronger in the underdoped stoichiometric compound $YBa_2Cu_4O_8$ than in $YBa_2Cu_3O_{7-\delta}$ (1; 2). Since superconductivity is mainly taking place in the electronic system of the CuO_2 planes, a simple explanation for this different behavior of the two compounds could be that in $YBa_2Cu_4O_8$ Fe replaces Cu(2) in the planes, whereas in $YBa_2Cu_3O_{7-\delta}$ it occupies Cu(1) sites in the chains. In the later case Fe substitution of Cu(1) was verified by several studies using various structural techniques (see e.g., Ref. (3; 4). For $YBa_2Cu_4O_8$ the experimental situation remained unclear. From ^{57}Fe Mössbauer spectroscopy Bornemann et al. (2) and Boolchand et al. (3) found that Fe is replacing Cu(2) in the planes. In contradiction, Felner et al. (1) and Akachi et al. (5) using the same technique and additional X-ray-diffraction measurements observed Fe substituting Cu(1) in the chains.

In a new attempt to clarify this puzzling situation we performed Cu-NQR spectroscopy of $YBa_2(Cu_{1-x}Fe_x)_4O_{8+\delta}$ (x = 0, 0.00625, 0.0125, 0.01875, 0.025, 0.05) using samples from the same source as used in the study of Ref. (5). Similar to the findings of Matsumura et al. (4) we observed a decrease of the integrated spectral intensity for both Cu sites with increas-

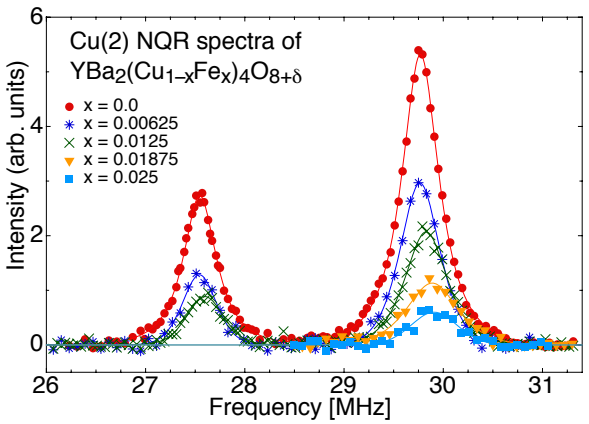

Figure 8.4: Wipe-out of spectral intensity at the plane copper site Cu(2) of $YBa_2(Cu_{1-x}Fe_x)_4O_{8+\delta}$.

ing x (wipe-out effect). The intensity from Cu nuclei that are neighbors (n, n.n or higher order n.n) to a Fe atom disappears from the observed spectra. Fig. 8.4 shows this fact for plane Cu(2). However, with growing x the intensity decrease is much stronger for Cu(2) than for Cu(1) in contrast to the case of Fe substituted $YBa_2Cu_3O_{7-\delta}$ (4). We performed various model calculations for a spectral wipe-out differing in site arrangements of Fe substitution and range of Cu neighbor order. The comparison with the observed x-dependent loss of spectral intensity for both Cu sites led us to the conclusion that Fe predominantly substitutes plane Cu sites especially for low Fe doping. We obtained additional strong support for these findings from the x-dependence of the spin-spin relaxation of the two Cu sites: whereas plane Cu(2) shows a remarkable growth of relaxation rate with increasing x, the relaxation of chain Cu(1) is independent of x. Furthermore, we observed in our investigation an influence of the extra oxygen introduced by Fe substitution on the long term microscopic structural stability of $YBa_2(Cu_{1-x}Fe_x)_4O_{8+\delta}$.

[1] I. Felner et al., Phys. Rev. B **43**, 8737 (1991).

[2] H.J. Bornemann et al., Physica C **199**, 130 (1992).

[3] P. Boolchand and D. McDaniel, in Studies on High-Temperature Superconductors, edited by Anant V. Narlikar (Nova Science, New Yoork, 1990, Vol. 4, p. 143.

[4] M. Masumura et al., Physica C **185-189**, 1135 (1991).

[5] T. Akachi et al., Physica C **301**, 315 (1998).

8.3.3 Study of charge transfer processes in Cr-doped $SrTiO_3$

During exposure to an electrical field (forming process), the resistance of Cr-doped $SrTiO_3$ is reduced by several orders of magnitude and a conductive state is reached. In this state electrical pulses of opposite polarity switch the resistance reversibly between a high- and a low-conductive state (1). We investigated the photocurrent induced at different wavelength in Cr-doped $SrTiO_3$. The illumination with photon-energy above 1.8 eV produces free electrons due to the ionization of Cr^{3+}. Such a valence state is possible in our crystals thanks to annealing in reducing atmosphere, and it explains why this charge transfer process is not visible in oxidized samples where the valence state of the Cr is 4^+ (2). The photon excitation of one electron to the conduction band was observed by EPR measurements, which show a decrease of the Cr^{3+} amount due to the light exposure. This process is fully reversible, and as shown in Fig.8.5(a), after 20 min in the dark the signal of Cr^{3+} recovers to the initial value.

A completely different effect is visible by applying a bias of 100 V (Fig.8.5(b)). Even after removing the bias voltage and the light, after 20 min the signal does not recover. This is a clear effect of the bulk change induced by the electric field, which modified the recovery process of Cr^{3+}. By combining EPR, with in-situ I-V measurements we found that the increase of the electrical current is correlated with the

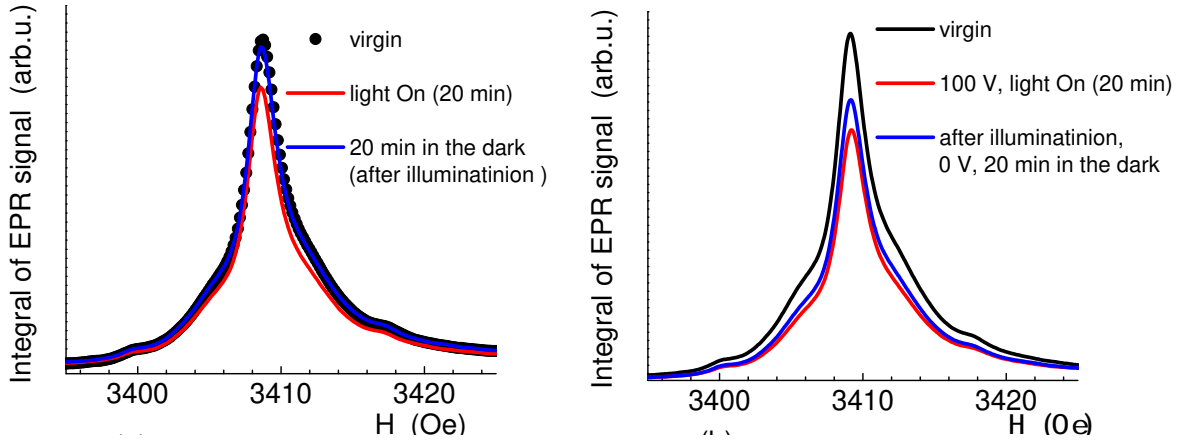

Figure 8.5: EPR signal of Cr^{3+} in Cr-doped $SrTiO_3$ at different photo-excitation (white light).

decrease of the Cr^{3+} EPR signal. The exposure to white light produces a photocurrent that decreases the forming time. One possible explanation is that the photo-ionization of the Cr^{3+} enhances the current which produces some avalanche processes leading to the insulator-to-metal transition.

8.3.4 Oxygen isotope effect of the spin-lattice relaxation of Yb^{3+} in Yb substituted $YBa_2Cu_3O_{7-\delta}$

Recently we performed a detailed study of the temperature dependence of Yb^{3+} relaxation in $YBa_2Cu_3O_x$ by measuring the Yb^{3+} EPR linewidth (1). It was found that both electronic and phononic processes contribute to Yb^{3+} relaxation. We were able to separate these processes and studied their relative contributions to relaxation as a function of oxygen doping. As expected, the electronic contribution decreases with decreasing oxygen doping, while the phonon contribution is practically doping independent. Note

[1] A. Beck et al., Appl. Phys. Lett. **77**, 139 (2000).
[2] S. A. Basun et al., Ferroelectrics **183**, 255 (1996).

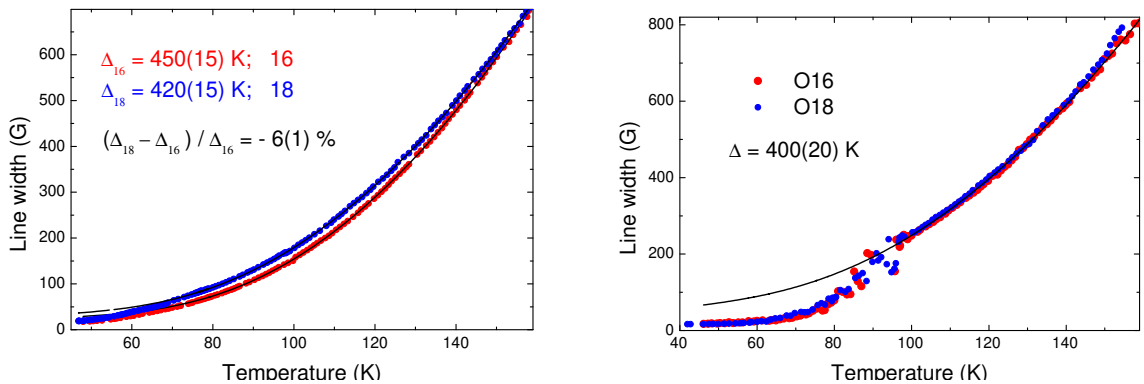

Figure 8.6: Temperature dependence of the Yb^{3+} EPR linewidth (relaxation rate) for ^{16}O and ^{18}O samples of underdoped $Y_{0.98}Yb_{0.02}Ba_2Cu_3O_{6.6}$ (left panel) and optimally doped $Y_{0.98}Yb_{0.02}Ba_2Cu_3O_{6.95}$ (right panel).

that traditional Raman and Orbach mechanisms involving acoustic phonons cannot explain the temperature dependence of the Yb^{3+} EPR linewidth. Instead, it appears that a Raman process via the coupling to high-energy ($\sim$ 500 K) optical phonons is responsible for the phononic part of Yb^{3+} relaxation in $YBa_2Cu_3O_x$. In this case one can expect an oxygen isotope effect (OIE) on Yb^{3+} relaxation. We checked this possibility by studying the Yb^{3+} EPR linewidth in $YBa_2Cu_3O_x$ with different oxygen isotopes (^{16}O and ^{18}O).

Two samples with different oxygen concentrations, x=6.6 (under-doped) and 6.95 (optimally doped) were studied. Figure 8.6 shows the temperature dependence of the EPR linewidth of these oxygen exchanged (^{16}O and ^{18}O) samples. In the under-doped sample there is a clear OIE on the EPR linewidth. On the other hand, no OIE is observed in the optimally doped sample. Surprisingly, the OIE on the Yb^{3+} EPR linewidth behaves very similar as the OIE on T_c, which is large in the under-doped regime and very small at optimal doping.

[1] Annual Report 2005/2006, www.physik.unizh.ch/reports.html.

8.3.5 μSR study of the non-centrosymmetric superconductors $Li_2(Pt, Pd)_3B$

Recently, the non-centrosymmetric superconductors Li_2Pd_3B and Li_2Pt_3B were discovered (1; 2). Some experiments indicate a parity-mixed superconducting state, in particular a significant spin-triplet contribution in Li_2Pt_3B (3; 4), while others suggest both compounds to be BCS-type superconductors with an isotropic gap (2). Further evidence for s-wave superconductivity in Li_2Pd_3B stems from our previous studies (5). In order to elucidate this controversy, we investigated $Li_2Pd_{1.5}Pt_{1.5}B$ and completely Pt substituted Li_2Pt_3B by means of the transverse-field μSR technique.

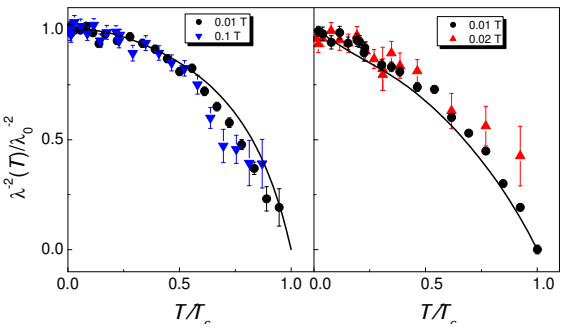

Figure 8.7: λ^{-2}(T)/λ^{-2}(0) versus reduced temperature T/T_c for $Li_2Pd_{1.5}Pt_{1.5}B$ (left panel) and Li_2Pt_3B (right panel) at different applied fields. The solid lines correspond to a theoretical fit as explained in the text.

Figure 8.7 shows the temperature dependence of the magnetic penetration depth λ normalized to the value at zero temperature λ(0), i.e. the quantity $\lambda^{-2}(T)/\lambda^{-2}(0)$, for the samples studied. $\lambda^{-2}(T)/\lambda^{-2}(0)$ saturates at low temperatures for $Li_2Pd_{1.5}Pt_{1.5}B$ (left panel), which is expected for an isotropic superconductor, whereas in Li_2Pt_3B (right panel) the slope of $\lambda^{-2}(T)/\lambda^{-2}(0)$ is nonzero in the low-temperature regime, probably suggesting the existence of nodes in the superconducting gap.

In general the lack of inversion symmetry induces an antisymmetric spin orbit coupling (ASOC), which is not destructive to special spin-triplet states. As a consequence an admixture of spin-singlet and spin-triplet states are allowed. The ASOC lifts the energy degeneracy of the spin states and results in a two-gap function where nodes may exist in one gap depending on the weight of the spin triplet contribution. We analyzed our μSR data based on these ideas (solid lines in Fig. 8.7) using the BCS expression for $\lambda^{-2}(T)/\lambda^{-2}(0)$ under the assumption of two anisotropic gaps

whose expression was elaborated in Ref. (3). We obtain a dominant spin triplet contribution in Li_2Pt_3B in agreement with Ref. (3), whereas $Li_2Pd_{1.5}Pt_{1.5}B$ seems to be a fully gapped superconductor like Li_2Pd_3B (5). These findings are also consistent with an increasing spin-orbit coupling with growing Pt content (6).

[1] K. Togano et al., Phys. Rev. Lett. **93**, 247004 (2004).

[2] H. Takeya et al., Phys. Rev. B **72**, 104506 (2005).

[3] H.Q. Yuan et al., Phys. Rev. Lett. **97**, 017006 (2006).

[4] M. Nishiyama et al., Phys. Rev. Lett. **98**, 047002 (2007).

[5] R. Khasanov et al., Phys. Rev. B **73**, 214528 (2006).

[6] K.-W. Lee and W.E. Pickett, Phys. Rev. B **72**, 174505 (2005).

8.3.6 Investigation of the two-gap behavior of $La_{2-x}Sr_xCuO_4$

It is mostly believed that the order parameter in cuprate HTS has pure $d-$wave symmetry, as indicated by e.g. tri-crystal experiments (1). There are, however, a wide variety of experimental data that support s or even more complicated types of symmetries ($d+s$, $d+is$, etc.) (2). In order to solve this controversy Müller suggested the presence of two superconducting condensates with different symmetries ($s-$ and $d-$wave) in HTS (3). This idea was generated partly because two gaps were observed in $n-$type $SrTiO_3$ (4), the first oxide in which superconductivity was detected. In addition, it is known that a two-order parameter scenario leads to a substantial increase of the superconducting transition temperature in comparison to a single-band model (5).

Important information on the symmetry of the order parameter can be obtained from magnetic field penetration depth λ measurements. Recently, we performed a study of the in-plane magnetic penetration depth (λ_{ab}) in slightly over-doped single-crystal $La_{1.83}Sr_{0.17}CuO_4$ by means of μSR (6). At low magnetic fields ($\mu_0 H < 0.3$ T), $\lambda_{ab}^{-2}(T)$ exhibits an inflection point at $T \approx$10-15 K (see Fig. 8.8). We interpret this feature as a consequence of the presence of two superconducting gaps, analogous to double-gap MgB_2 (7). It is suggested that the large gap (Δ_1^d=8.2(1) meV) has $d-$ and the small gap (Δ_2^s=1.57(8) meV) $s-$wave symmetry. With increasing magnetic field the contribution of Δ_2^s decreases substantially, in contrast to an almost constant contribution of Δ_1^d. Both the temperature and the field dependencies of λ_{ab}^{-2} were found to be similar to what was observed in double-gap MgB_2 (7; 8).

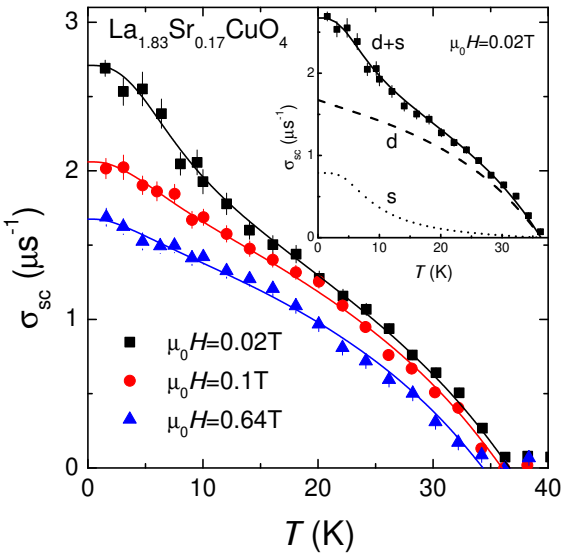

Figure 8.8: Temperature dependence of the μSR relaxation rate $\sigma_{sc} \propto \lambda^{-2}_{ab}$ of single-crystal $La_{1.83}Sr_{0.17}CuO_4$ measured at 0.02 T, 0.1 T, and 0.64 T (field-cooled). Lines in the main figure and in the inset represent the fit with the two-gap model [6]. In the inset the contributions from the large d-wave gap and the small s-wave gap at μ_0H=0.02 T are shown separately.

[1] C.C. Tsuei et al., Phys. Rev. Lett. **73**, 593 (1994).
[2] G. Deutscher, Rev. Mod. Phys. **77**, 109 (2005).
[3] K.A. Müller, Nature (London) **377**, 133 (1995).
[4] G. Binnig et al., Phys. Rev. Lett. **45**, 1352 (1980).
[5] A. Bussmann-Holder et al., Eur. Phys. J. B **37**, 1434 (2004).
[6] R. Khasanov et al., Phys. Rev. Lett **98**, 057007 (2007).
[7] A. Carrington and F. Manzano, Physica C **385**, 205 (2003).
[8] S. Serventi et al., Phys. Rev. Lett. **93**, 217003 (2004).

8.4 Magnetic properties of novel electronic materials

8.4.1 Study of the upper critical field anisotropy of $Al_{0.16}Mg_{0.84}B_2$

It is now well accepted that MgB_2 is a conventional phonon mediated superconductor, with the peculiarity to have two separate gaps, whose interplay strongly influences the physical properties of the material. The temperature dependence of the upper critical field anisotropy $\gamma_H = H_{c2}^{||ab}/H_{c2}^{||c}$, first observed by (1), can be understood as the changing interplay of the two bands by varying the temperature.

Recently, much progress in understanding the superconducting properties of this two-band superconductor was made by doping aluminum into MgB_2 single crystals. Whereas T_c decreases by replacing the Mg ions with aluminum, point-contact spectroscopy studies show that the two-gap behavior remains up to 20% doping (2).

By using the combination of a magnetic torque magnetometer with highly sensitive piezo-resistive sensors and a commercial SQUID (Quantum Design MPMS XL) we studied how the anisotropy evolves with temperature and heavy aluminum doping. In Fig. 8.9 the measured temperature behavior of γ_H and the upper critical field H_{c2}, which strongly depends on the direction of the field relative to the crystallographic axes, of $Al_{0.16}Mg_{0.84}B_2$ and pure MgB_2 is shown. While γ_H of MgB_2 is strongly temperature dependent, the anisotropy of $Al_{0.16}Mg_{0.84}B_2$ is much reduced compared to MgB_2 and is almost temperature independent. This suggests that the two-gap behavior becomes less important with higher Al doping.

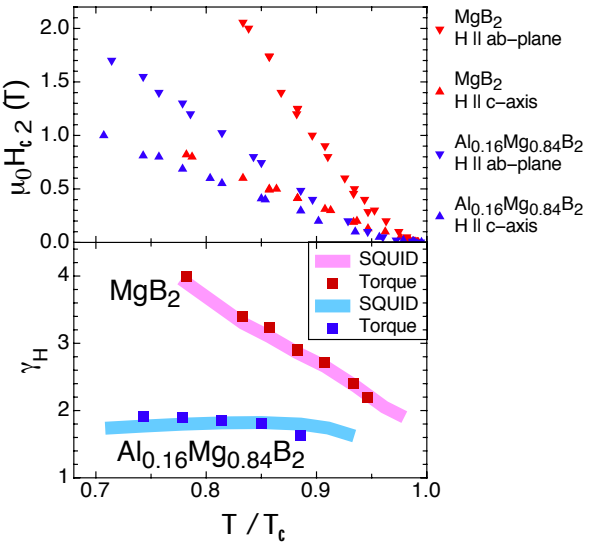

Figure 8.9: Upper graph: Temperature dependence of $H_{c2}^{||c}$ and $H_{c2}^{||ab}$ of MgB_2 and $Al_{0.16}Mg_{0.84}B_2$ measured by torque and SQUID magnetometry. Lower graph: Temperature dependence of upper critical field anisotropy γ_H of MgB_2 and $Al_{0.16}Mg_{0.84}B_2$. The anisotropy of $Al_{0.16}Mg_{0.84}B_2$ is clearly reduced and almost temperature independent.

[1] M. Angst et al., Phys. Rev. Lett. **88**, 167004 (2002).
[2] J. Karpinski et al., Phys. Rev. B **71**, 174506 (2005).

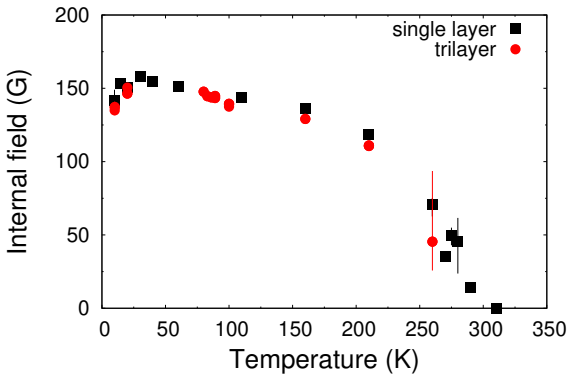

Figure 8.10: Spontaneous internal fields in PBCO (black squares: single layer 50 nm, red circles: trilayer) as a function of temperature.

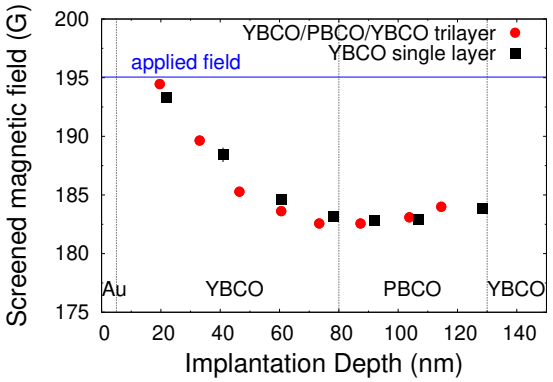

Figure 8.11: The diamagnetic field profile measured inside the tri-layer at T=25 K (circles) and the 200 nm YBCO single layer (squares).

8.4.2 Low-energy μSR experiments on multilayers

Proximity effects in multilayers have been subject of intense research in recent years due to the variety of phenomena resulting from the interplay (competition and coexistence) between the two orderings in hetero-structures. For instance in super-lattices consisting of one unit cell thick layers of $YBa_2Cu_3O_7$ (YBCO) separated by $PrBa_2Cu_3O_7$ (PBCO) layers of variable thickness, the critical temperature of the heterostructure has been found to continuously decrease as the PBCO thickness is increased, indicating that some sort of coupling persists over distances of $\sim$10 nm (1).

Polarized low energy muons implanted in a YBCO(75nm)/PBCO(50nm)/YBCO(75nm) trilayer were used to investigate the local superconducting and magnetic properties of this structure. For comparison we investigated also single layer films of the constituents. Figure 8.10 shows the internal field measured by zero-field μSR in the PBCO layer as single film (50nm) and embedded in the two YBCO layers. Both samples show similar internal field distributions. If an external magnetic field is applied parallel to the surface (and perpendicular to the c-axis), by scanning the implantation energy, one can probe the field distribution of the YBCO layers in the Meissner state and the local magnetic field inside the PBCO layer. Superconductivity of YBCO manifests itself in a screened diamagnetic signal. In PBCO, the microscopic field measurements show two components. The first component reflects the magnetic order and appears at fields corresponding to the superposition of the internal and external fields. The second component displays a sizeable diamagnetic shift below the critical temperature of YBCO. The depth profile of the diamagnetically shifted component exhibits a monotonic decay in the YBCO layer and reaches the maximum shift in the PBCO layer (Fig. 8.11). Moreover, it is close to the field profile inside the 200 nm YBCO single layer in the Meissner state plotted for comparison. This result may present the signature of a large proximity effect not expected in this material on the base of conventional proximity models.

[1] J.M. Triscone and Ø. Fischer, Rep. Prog. Phys. **60** 1673 (1997).

8.4.3 μSR study of magnetic semiconductors

Recently, high temperature ferromagnetism was observed in chalcopyrite semiconductors doped by Mn, namely in CdGeP2:Mn, ZnGeP2:Mn, ZnGeAs2:Mn, and CdGeAs2:Mn (1), where the record Curie temperature of 350 K was reported. These novel diluted ferromagnetic semiconductors (DMS) are believed to be promising for room temperature spintronics. Our first μSR measurements at PSI of $CdGeAs_2$ polycrystalline samples doped with Mn (2) confirmed that the ferromagnetism detected in these samples is a bulk phenomenon, and revealed a big shift of the magnetic field seen by the muon. To understand the nature of this shift one has to appreciate the origin of the net magnetic field seen by the muon in a ferromagnetic medium according to the concept of a Lorentz sphere (3):

$$B_\mu = B_{ext} - B_{dem} + B_L + B_c + B_{dip},$$

where B_{ext} is the external magnetic field; $B_{dem} = 4\pi N m$ (N - demagnetization factor of the sample, m - magnetization) and $B_L = \frac{4\pi}{3} m$ are demagnetization fields from the finite sample and the empty Lorentz sphere ($N_{sphere} = \frac{1}{3}$), respectively; B_c is the contact hyperfine field at the muon and B_{dip} is the net magnetic field from magnetic dipoles inside the Lorentz sphere. In the case of a rectangular sample (8x8 mm^2, thickness 0.82 mm) (2), the uncertainty of N introduced a large systematic error in the determination of the physical term $B_c + B_{dip}$.

To eliminate this uncertainty experiments must be performed with spherical samples ($N = \frac{1}{3}$), where the Lorentz field and demagnetization field cancel each other. This year we were able to get a big polycrystalline sample of $CdGeAs_2$:3%Mn and to machine it to an almost spherical shape (diameter 3.30(5) mm).

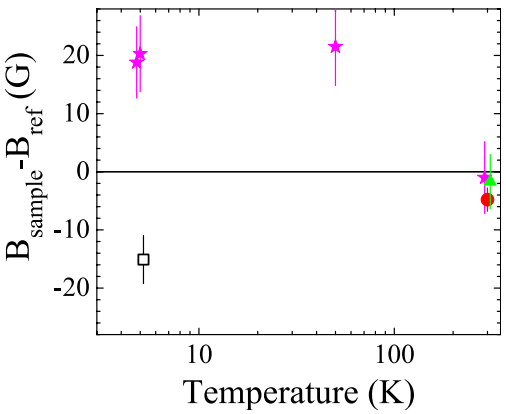

Figure 8.12: Temperature dependence of the field shift seen by the muon in $CdGeAs_2$ doped with 3% Mn. The applied field is H=6400 Oe. Different symbols correspond to the different orientations of the sample. Circle - original position; triangle - sample rotated 60°; square - sample rotated 180°; stars - sample rotated -60°.

Fig. 8.12 shows the difference between the field seen by the muon and the applied field of 6400 Oe as a function of temperature. To eliminate the systematic errors due to unideal shape, several measurements with different sample orientations have been conducted. At room temperature the data points are scattered with an average value dB =-1.6±1.5 G. The measured value of $B_c + B_{dip}$ is about 3-4 orders of magnitude less than that in ferromagnetic metals Fe, Co, Ni, Gd etc. (3). This value has to be set against theoretical estimates using recent calculations (4; 5; 6).

[1] V.M. Novotortsev et al., Rus. J. Inorg. Chem. **50**, 492 (2005).

[2] V.G. Storchak et al., Physica **B374-375**, 430 (2006).

[3] A. Schenck, Muon Spin Rotation: Principles and Applications in Solid State Physics, Adam Hilger, Bristol, 1986.

[4] S.C. Ervin and I. Zutic, Nature Materials **3**, 410 (2004).

[5] Y.-J. Zhao, W.T. Geng, A.J. Freeman, and T. Oguchi, Phys. Rev.**B63**, 201202 (2001).

[6] P. Mahadevan and A. Zanger, Phys. Rev. Lett. **88**, 047205 (2002).

8.5 Electric field effects in perovskites

8.5.1 Resistive memory effects in Cr-doped $SrTiO_3$

Resistive memory effect (resistive switching) in some selected perovskites are under intense investigation because of their potential technological applications for non-volatile memory devices. We report on a study of single crystals of Cr-doped $SrTiO_3$ as a model system (1). By comparing the EPR signal in the insulating state and the conducting state obtained after exposure to an electrical field (forming), a broadening of the lineshape of the Cr^{3+} signals was detected after the forming process. Such changes indicate that the forming procedure affects a volume fraction of $\leq 10\%$ of the entire bulk. By optical measurements during the forming process, while applying positive and negative voltage pulses, we were able to detect a luminescence band centered at 790nm. This luminescence is known as the Cr R-line (2) resulting from a recombination of electrons at the Cr^{4+} center, and is a clear signature of a charge transfer process involved during the insulator-to-metal transition. A broader band was detected at the same spectral region during the memory switching from the high to the low conductive state which indicates that a carrier recombination process occurs during the resistance increase. Additional investigations are required to assign the broad luminescence line to well defined energy level of the Cr-doped $SrTiO_3$.

[1] Y. Watanabe et al., Appl. Phys. Lett. **78**, 3738 (2001).

[2] T. Feng, Phys. Rev. B **25**, 627 (1982).

8.5.2 μSR study of conductive Cr-doped $SrTiO_3$

Knowledge about the role of oxygen vacancy doping in $SrTiO_3$ is essential in order to understand the physics of the insulator-to-metal transition in the material. Muon-spin rotation experiments (including μSR in electric fields) proved to be a powerful tool to study muonium (muon + electron) and other muon charge states in semiconductors and insulators. Usually muonium is detected in insulators or slightly doped semiconductors, whereas bare muons are observed in heavily doped semiconductors and metals. Monitoring the ratio muon to muonium signal intensity can yield an estimate of the metal to insulator volume ratio. Transverse magnetic field μSR measurements on a single crystal of Cr-doped $SrTiO_3$ shows a change in the muon signal (asymmetry) due to a different annealingprocedure of the virgin materials (Fig.8.13).

We found the largest muon signal in the virgin oxygen vacancy enriched sample (black).

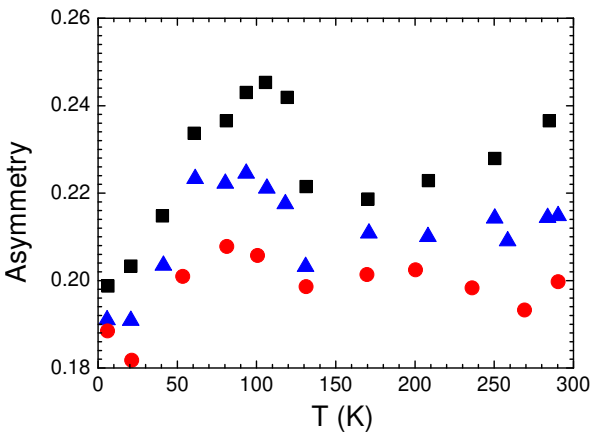

Figure 8.13: Temperature dependence of the asymmetry parameter of single crystal $SrTiO_3$:Cr0.2%.

black: **virgin reduced (annealed in H_2/Ar:5% at 1150°C for 8h)**

red: **virgin oxidized (annealed in O_2 at 1150 °C for 8h)**

blue: **reduced conductive**

The two annealing procedures affect both the Cr valence state and the oxygen vacancy content due to a charge compensation. By comparing the two virgin samples one can conclude that in the virgin oxygen vacancy enriched sample the larger muon signal reflects a larger metallic volume fraction. On the other hand, a decrease of the muon signal in the conducting state obtained after the electric field forming procedure is in contradiction to the idea of an increase of the fraction of metallic regions. This observation requires more experimental investigations.

8.6 New developments in instrumentation and data handling

8.6.1 Implementation of the flip-coil technique at the Avoided Level Crossing instrument at PSI

In avoided level crossing (ALC) experiments the integral muon decay asymmetry

$$Asy = (F - B)/(F + B)$$

(where F and B are the total number of positron events in the forward and backward counters, respectively) is measured as a function of applied magnetic field. One principal limitation of a standard ALC technique lies in the systematic fluctuations due to the various beam line instabilities (noise of the power supplies, fluctuation of the primary proton beam, small HV discharges in the separator). Typical clean and noisy raw ALC spectra are presented in Fig. 8.14. To average out systematic errors the so-called flip-coil technique was introduced at TRIUMF (1). A similar approach (Red-Green mode) is used at ISIS.

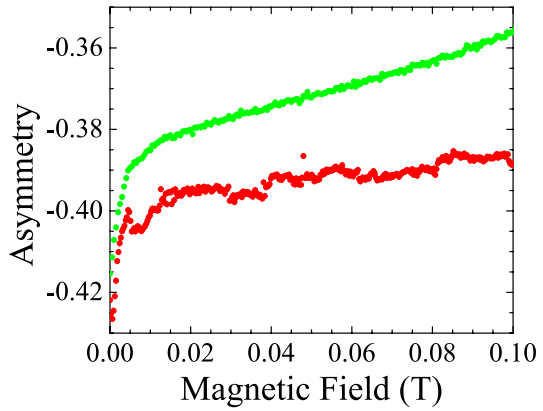

Figure 8.14: Typical examples of a clean (green) and a noisy (red) raw ALC spectrum.

Here we report the first implementation of the flip-coil technique at the ALC instrument at PSI. A small coil capable to produce a square-wave modulation field (amplitude up to $\Delta H \simeq 20$ Oe) was attached to the standard ALC cryostat and placed inside the warm bore of the superconducting magnet. The modulation field was alternated at a frequency of 1 Hz by an external generator and two separate ALC spectra were collected

$$Asy^{\pm} = (F^{\pm} - B^{\pm})/(F^{\pm} + B^{\pm}),$$

where $\pm$ refers to the direction of the modulation field. Finally, one can construct the differential asymmetry

$$Asy_{\rm diff} = Asy^{+} - Asy^{-}$$

or

$$Asy(H)_{\rm diff} = Asy(H + \Delta H/2) - Asy(H - \Delta H/2).$$

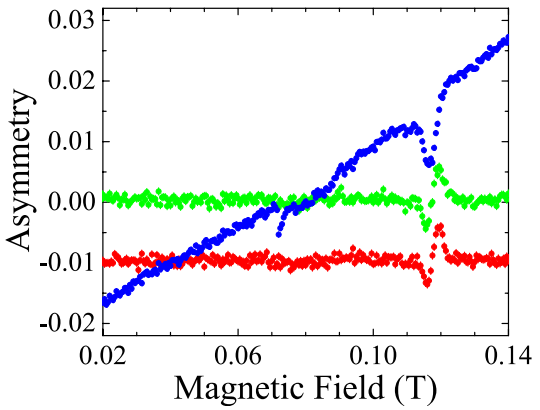

Figure 8.15: ALC spectra measured in Al_2O_3 at T=15 K in an electric field E=+11.32 kV/cm.
Red - Asy$_{diff}$ of "clean" data (shown shifted by -0.01 for clarity).
Blue - noisy original raw signal.
Green - Asy$_{diff}$ made of the original noisy signal.
One can see that the noise is absent in the flip-coil presentation.

For low frequency fluctuations ($f_{\rm noise} < 1$ Hz) the noise contribution to $Asy_{\rm diff}$ is subtracted. These features are illustrated in Fig 8.15. In conclusion, the flip-coil technique was implemented at the ALC instrument and is ready for further experiments.

[1] R.F. Kiefl et al., Phys. Rev. **A34**, 681 (1986).

8.6.2 Setup for simultaneous observation of EPR, luminescence and current-voltage measurements

In order to study changes in the valence states of transition metal ion dopants (Cr, Fe, Co, Mn) in $SrTiO_3$ during current voltage (I-V) measurements, a special sample holder and special electrodes were developed. Simultaneous measurements of EPR, I-V curves, and luminescence are now possible with a reproducibility of the EPR signal improved from 10% to 1%, which is an essential prerequisite to study small changes in the entire bulk. The new setup (Fig.8.16) consist of a special enlarged hole window in the wall of the EPR cavity which is aligned with a series of two optical lenses. The sample position coincides with the center of the cavity and the focal point of the first lense. With such a system it is possible to collect light emitted by the sample and couple it to an optical fiber connected to a Single Photon Counting Module (SPCM of Laser Components) with a dark count of 25 cps. The SPCM is then connected to a ratemeter (Canberra Lin-Log Ratemeter 1481LA). For the I-V in-situ measurement stripe-like electrodes of platinum are deposited on two opposite faces of the $SrTiO_3$ single crystal. Such stripe-like platinum layers being transparent to the EPR microwave allow to apply an electrical field and give access for the optical luminescence detection.

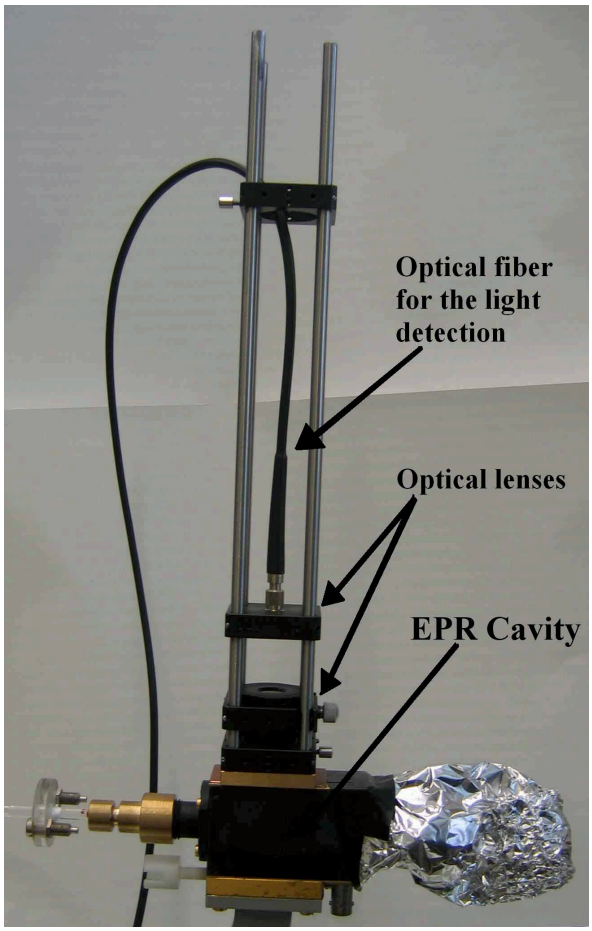

Figure 8.16: EPR cavity modified for optical luminescence detection.

8.6.3 Calculation of the magnetic field distribution in type-II superconductors

Analysis of μSR data for type-II superconductors with a high value of $\kappa = \lambda/\xi$, like cuprate HTS, is a demanding task. In this case the second moment of the magnetic field distribution in the mixed phase depends on several parameters: the penetration depth λ, the coherence length ξ, and the degree of the vortex lattice disorder (1). Several methods were proposed to calculate μSR spectra as a function of these parameters (see for example (2)). However, most of them fail to describe precisely experimental data

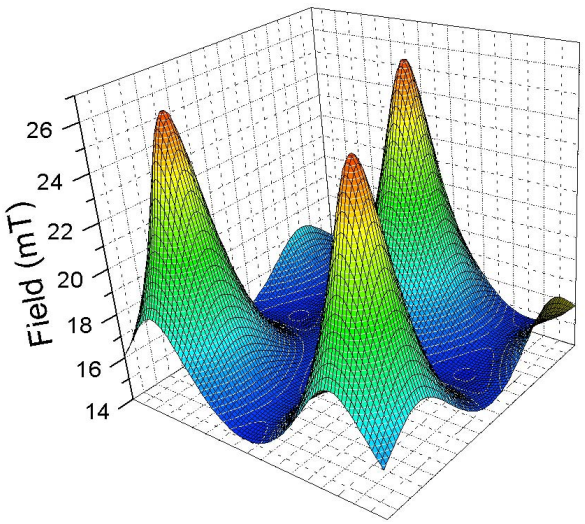

Figure 8.17: Spatial distribution of the magnetic field in a type-II superconductor calculated using the Ginzburg-Landau model for λ = 200 nm, ξ = 20 nm, average field 0.02 $\mu_0 H_{c2}$ = 16.45 mT, and inter-vortex distance 380.9 nm.

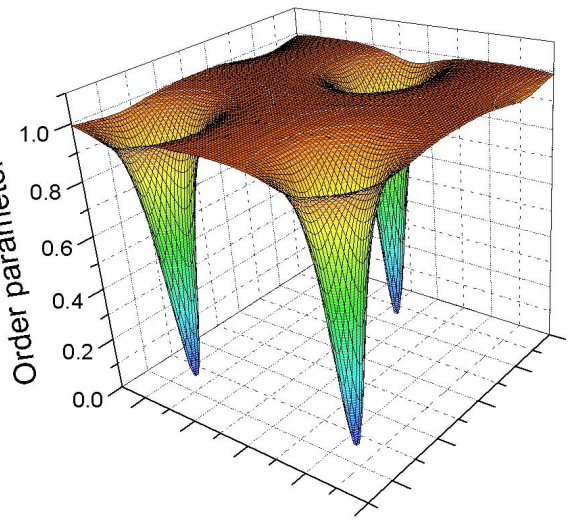

Figure 8.18: Spatial distribution of the normalized absolute value of the order parameter in a type-II superconductor calculated using the Ginzburg-Landau model for λ = 200 nm, ξ = 20 nm, average field 0.02 $\mu_0 H_{c2}$ = 16.45 mT, and inter-vortex distance 380.9 nm.

as the applied magnetic field approaches H_{c2}. The magnetic field distribution in a flux line lattice (FLL) can be calculated using the Ginzburg-Landau model. Brandt described an algorithm for numerical calculation of the magnetic field distribution in a type-II superconductor for hexagonal and rectangular geometries of the FLL by minimizing the Ginzburg-Landau free energy (3). Based on this algorithm we wrote a program in MATLAB to simulate and to fit the field and time domain μSR spectra.

As an example, Figs. 8.17 and 8.18 show the spatial distribution of the magnetic field and the order parameter of a type-II superconductor, calculated by our program. The corresponding field domain μSR spectrum is shown in Fig. 8.19. Compared to other models the program is able to analyze type-II superconductors with small values of κ and in fields close to H_{c2}. It also allows the exact calculation of the reversible magnetization in type-II superconductors.

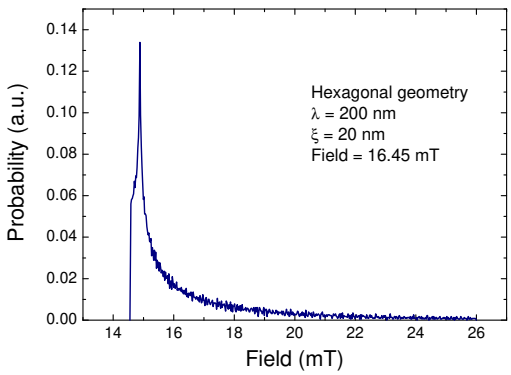

Figure 8.19: Field domain μSR spectrum corresponding to the spatial distribution of magnetic field shown in Fig. 8.17

[1] E.H. Brandt, Phys. Rev. B, **68**, 054506 (2003).

[2] J.E. Sonier, J.H. Brewer, and R.F. Kiefl, Rev. Mod. Phys., **72**, 769 (2000).

[3] E.H. Brandt, Phys. Rev. Lett., **78**, 2208 (1997).

9 Phase transitions, new materials and superconducting γ-detectors

M. Reibelt, R. Dell'Amore, H. Bartolf, S. Siegrist, A. Engel and A. Schilling

in collaboration with:
Paul Scherrer Institute (Ch. Rüegg, J. Mesot, M. Medarde, K. Pomjakushina, K. Conder), University of Bern (K. Krämer), Bhaba Atomic Research Center (G. Ravikumar), Forschungszentrum Karlsruhe (Th. Wolf, H. Küpfer), Universität Karlsruhe (K. Il'in), ETH Zürich (J. Karpinski), Deutsches Zentrum für Luft- und Raumfahrt (H.-W. Hübers), University of Wellington (B. Ruck), Istituto Nazionale di Ricerca Metrologica I.N.RI.M Torino (C. Portesi), CSEM Neuenburg, FIRST Lab ETH Zürich.

Last year we have continued our activities at the FIRST Center for Micro- and Nanoscience at the ETH Zürich where we have successfully implemented a lift-off technique as an alternative to etching processes in the electron-beam lithography for producing superconducting thin-film photon detectors (H. Bartolf and A. Engel). We have also discovered a first-order like feature in the specific heat of a V_3Si single crystal near the transition to superconductivity, and studied the effect of the thermal and the magnetic history on this feature in detail. We have built a high-frequency susceptometer working in the MHz range which is necessary to study possible resonance phenomena in an exotic magnetic state of $TlCuCl_3$ (R. Dell'Amore). Finally we have continued our synthesis experiments on $LaSrNiO_4$ and related compounds to study the influence of cation and anion substitution on its electronic properties.

9.1 Physics of superconducting thin-film nanostructures and possible applications as fast single-photon detectors

The detectors we want to study and advance rely on the combined effect of quasi-particle multiplication upon absorption of a photon and a high bias current, which is just below the critical current of the superconducting meander. In a superconductor an absorbed photon leads to the break-up of a Cooper-pair. Because the photon energy is in general much larger than the superconducting gap energy a cascading process sets in during which many more Cooper-pairs are broken up resulting a cloud of quasi-particles. This cloud of quasi-particles at the absorption site is equivalent to a local reduction of the current-carrying capacity of the superconducting strip line. Eventually the bias current exceeds the local critical current and a voltage pulse is generated that can be registered with standard electronics. The main advantages of these detectors compared to other technologies is the ultra-high speed, the accuracy to determine the arrival time of a photon and the very high sensitivity.

E-beam lithography

In order to get a good detector it is of paramount importance that the complete device is as homogeneous as possible. Already very small variations in T_c, I_c or the cross-sectional area of the strip line lead to a reduced performance or even a complete failure. This implies great demands on the production process of the device. During the last year, we developed a three step lift-off process that enables us to generate nanometer-sized devices structured from

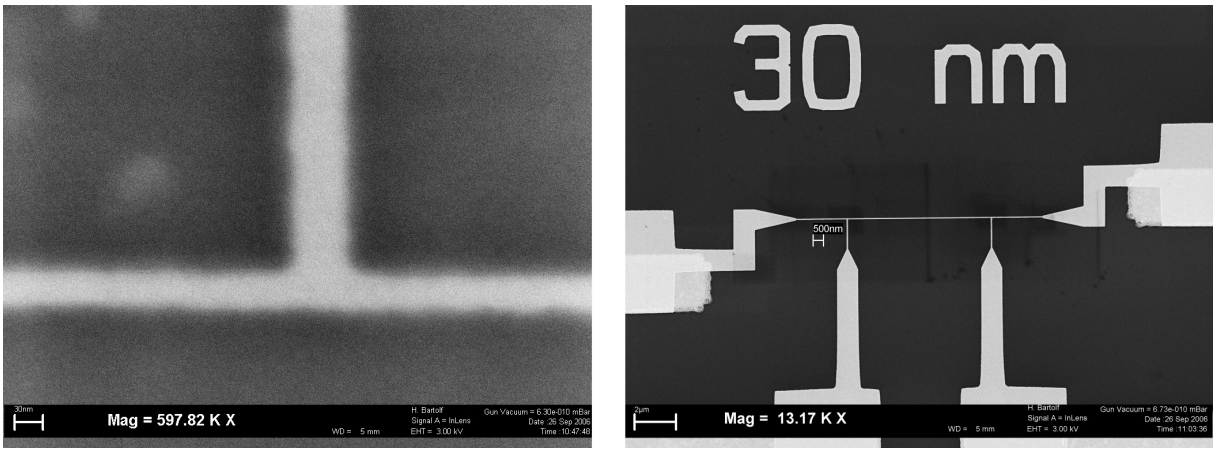

Figure 9.1: SEM pictures of a Au/Cr bridge with a width of 30 nm and thickness approximately 25 nm created with lift-off. The picture on the right shows the bridge and the connection pads that allow for 4-point resistance measurements. On the left we show a blow-up (rotated by 180°) of one of the voltage junctions at maximum resolution.

evaporated films, with thicknesses from only a few nanometers to some ten nanometers. The films are evaporated on a silicon substrate, and the layout is designed to allow for four point resistivity measurements on our devices. In the first step, bond pads, orientation marks (for the second optical lithography step and the third electron-beam lithographic step) are created by optical lithography, Cr/Au evaporation and a lift-off. We work with ma-N 405, a standard photolithographic resist, of 300 nm total thickness. The film thickness of the resulting structures is about 100 nm. In the second step connection pads are made by the same technique. The thickness of these pads is a fifth of that of the first structures, i.e. roughly 20 nm. Finally, electron-beam lithography and subsequent lift-off is used to define the nanostructures. In order to obtain very small feature sizes, we work with 1.6 nm step size, 30 kV acceleration voltage and a bilayer resist (PMMA 20 nm / copolymer 50 nm). Dose tests with thin resists show that we are able to achieve minimum feature sizes of about 10 nm (1). In Fig. 9.1 we show a SEM picture of a 30 nm wide bridge fabricated with the above described process. This bridge is made of approximately 25 nm thick Au on top of a roughly 1 nm thick Cr adhesion layer. For ease of use and to demonstrate the feasibility of our process most structures produced so far are made of similar Au films. In a next step we plan to use superconducting films.

Transition metal nitrides

Currently, NbN is used as the standard material for these kind of single-photon detectors. In many respects NbN is a very good material, not only because of its favorable superconducting properties, but also because it is well characterized and there is considerable experimental experience with it. However, it has a relatively high critical temperature limiting its useful spectral range to visible and near-infrared radiation. This is our motivation to explore other superconducting materials as possible alternatives to NbN. In 2006 we started to look at other transition metal nitrides. With the exception of Cr all neighboring elements to Nb in the periodic table also form superconducting nitrides with T_c values of several Kelvin. In a first attempt we tried to grow TaN films. Ta was evaporated by means of an e-gun in a N_2 atmosphere at about 9×10^{-5} mbar and a small flux of

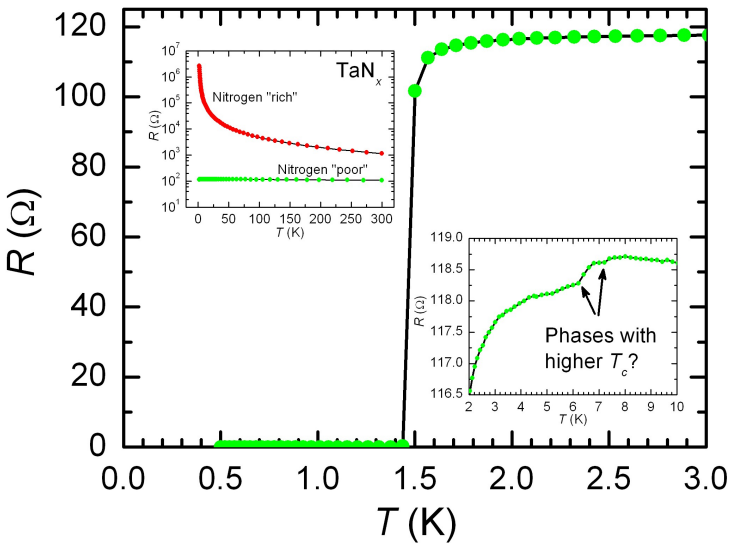

Figure 9.2: The upper left inset shows resistance v.s. temperature data for two TaN films with low and high N-content as indicated. As shown in the main graph the film with a reduced N-content becomes superconducting at $T_c \approx 1.45$ K. The blow-up of the temperature range from 2 to 10 K in the lower right inset reveals steps in the resistance data, which we attribute to superconducting transitions of small inclusions with higher T_c.

N_2^+-ions. Ta and N form various stable phases with different N-content. Adjusting the current density due to the flux of N_2-ions we could tailor the characteristics of the resulting films from semiconductor-like for those films with a high N-content to metallic for films with a reduced amount of N. To prevent oxidation, films with a reduced N-content were protected by a GaN capping layer. The films were deposited onto sapphire and Si substrates held at constant temperatures during evaporation ranging from $80°$C to about $120°$C. Based on previous experience with Ta evaporation in the same vacuum chamber, we expected highly disordered or even amorphous films.

This expectation was confirmed by x-ray analysis, which showed no sign of crystalline structure, and the temperature dependence of the resistance. In the upper left inset of Fig. 9.2 we show resistance data for two films from room temperature down to below 10 K. The nitrogen-rich film exhibits a clearly non-metallic behavior, whereas the nitrogen-poor has a small negative temperature coefficient, typical for strongly disordered or amorphous metals. The latter film does become superconducting at a $T_c \approx 1.45$ K, see the main graph of Fig. 9.2; considerably lower than for bulk crystalline TaN with a $T_c = 14$ K, but still higher than for amorphous Ta ($T_c = 0.9$ K). In the lower right inset of Fig. 9.2 we show a blow-up of the resistance data of the metallic TaN film between 2 and 10 K. Here we observe several small steps in the resistance curve. These steps shift and eventually vanish when we increased the measuring current. We interpret these steps as signs of small inclusions in our films with higher T_c. With further optimization of deposition parameters and additional annealing of the films at higher temperatures, we are hopeful to increase T_c into a range where the films might become useful for detector applications.

T-dependence of the critical current

One of the key operating parameters of the single-photon detectors is the bias current, which is adjusted to about 90% to 95% of the critical current. The ratio between bias current and critical current directly influences the sensitivity of the detectors. In addition there may be more subtle effects related to the absolute value of the bias current, e.g. caused by the interaction between bias current and vortices, which could be present in the strip line. Knowledge of the temperature-dependence of the critical current of the strip line is therefore necessary to choose the best possible

operating conditions. Within standard GL-theory one expects a smooth and continuous increase of the critical current with decreasing temperature. Preliminary measurements of the critical current on NbN bridges with widths ranging from 10 μm down to 300 nm showed various unexpected kinks and sometimes even steps in their temperature dependence. We have now started to systematically investigate these effects.

9.2 A history dependent first-order like phase transition feature near H_{c2} in V_3Si

V_3Si and Nb_3Sn share the same cubic "β-tungsten (A-15)" structure. Nb_3Sn is frequently used in technical applications, therefore the phase diagram of this class of materials is not only of academic interest. Besides the superconducting transition at the H_{c2}-line the rich phase diagram of V_3Si also features an irreversibility line, a peak-effect region, a low-field and a high-field phase-transition line which separates a quasi-ordered Bragg glass phase from a disordered phase of the vortex matter, a flux-line lattice reorientation line between a hexagonal and cubic symmetry, and in most crystals a structural phase transition can also be observed.

A15 compounds such as Nb_3Sn and V_3Si are well known to exhibit such a structural transition from a high-temperature cubic to a low-temperature tetragonal phase. This transformation is often called "martensitic transition" and is believed to be driven by a Peierls instability. Its origin is a band-type Jahn-Teller effect which leads to the formation of a Peierls like energy gap (2). Several experimental and theoretical studies (3; 4) have been carried out to clarify a correlation between the martensitic transition (in general the lattice instability) and the relatively high T_c in these conventional superconductors, because the A15 compounds showed the highest known T_c before the discovery of the high-T_c materials by Müller and Bednorz in 1986. It was found that the structural transition affects the superconducting transition in various ways which leads to a net decrease of the transition temperature T_c by approximately 0.3 K in the tetragonal phase. Superconductivity has, in turn, a more profound effect on the martensitic transition. It was predicted by theoretical models and also found in experiments that the developing tetragonality upon cooling is interrupted at the transition to superconductivity. If the superconducting transition occurs already in the cubic phase, the martensitic transition is completely suppressed and the crystal remains cubic.

We have observed a so far unreported first-order like phase transition feature in the specific heat of a single crystalline sphere of V_3Si that depends on the thermal history of the sample and that occurs very close to the H_{c2} line. The martensitic transition is very close to the transition to superconductivity in our crystal, and we assume that this proximity to H_{c2} is relevant for the occurrence of the observed effect.

Fig. 9.3 shows the specific heat of the V_3Si sample ($m = 11.1$ mg) measured in a commer-

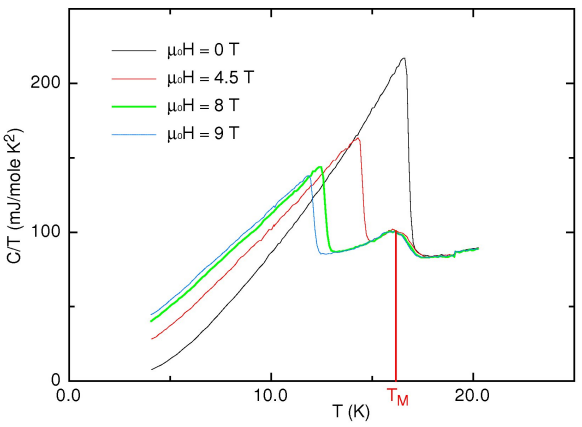

Figure 9.3: Specific heat of a V_3Si single crystal measured in a commercial PPMS by a conventional heat relaxation technique. The superconducting and the martensitic transition are clearly observable, but no first-order like peak can be resolved near H_{c2}.

cial PPMS system (Quantum Design) by a conventional heat-relaxation technique. Both the superconducting and the martensitic transitions are observable as continuous phase transitions. The estimated transition width ΔT_c from these data for $\mu_0 H = 0$ T is $\Delta T_c = 280$ mK, and the specific-heat discontinuity at T_c in zero field is $\Delta C/T = 143$ mJ/mol K^2. In zero magnetic field the martensitic transition (at T_M) is suppressed by the superconducting state. Since T_M decreases much less than the critical temperature T_c with increasing magnetic field, the martensitic transition is fully developed for $\mu_0 H = 1$ T (for lower magnetic fields only the onset of the martensitic transition is observable). No first-order like peak can be resolved near T_c in this type of experimental set up.

We have investigated the same sample with a DTA (differential-thermal analysis) method that is particularly well suited for the detection of sharp phase transitions in samples of milligram size (5; 6). We collected data in 18 different magnetic fields parallel to the $[100]$ direction of the crystal. In Fig. 9.4 we show some of these results (data for intermediate fields are not shown for clarity reasons), scaled with the PPMS data from Fig. 9.3. The estimated transition width ΔT_c for $\mu_0 H = 0$ T is only $\Delta T_c = 75$ mK, which is considerably less than the corresponding value obtained from the PPMS data. Our DTA method is indeed able to measure variations in entropy without being affected by any instrumental broadening of the data, in contrast to conventional methods to measure a specific heat, including the relaxation method used by the PPMS (5; 6).

Surprisingly, for all magnetic fields above $\mu_0 H = 1$ T a distinct first-order like peak can be resolved at a temperature T_p near T_c with a width of approximately $\Delta T_p = 36$ mK. Fig. 9.5 shows DTA data for $\mu_0 H = 7$ T on an expanded scale, and we have marked the relevant temperatures that we have used to draw the phase diagram shown in Fig. 9.6.

The absence of this sharp feature in corresponding literature data may be explained by a lower data-point density and/or a certain instrumental broadening of such data. Another possibility may be the fact that the occurrence of the observed feature turned out to strongly depend on the cooling history of the sample. The peak appears only for a fast cooling rate (i.e., of the order of 200 mK/sec) prior to a measurement, and disappears for a very slow cooling rate (0.2 mK/sec, data not shown).

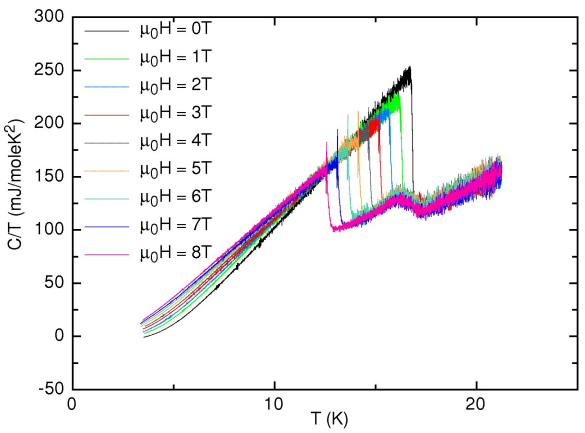

Figure 9.4: Field dependence of the specific heat measured in a DTA-cell and for magnetic fields parallel [100]. A first-order like peak appears for fields μ_0H≥1 T close to T_c.

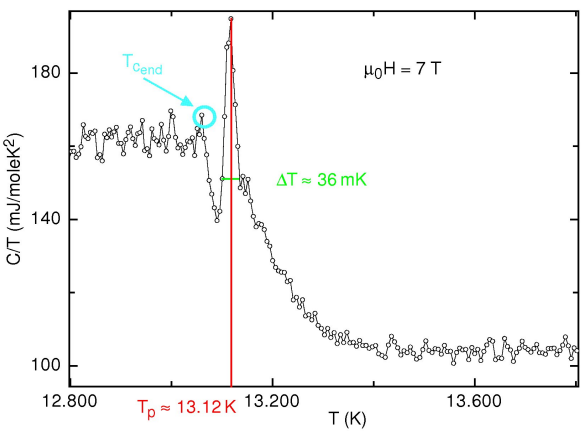

Figure 9.5: Representative specific-heat measurement for μ_0H = 7 T on an expanded scale.

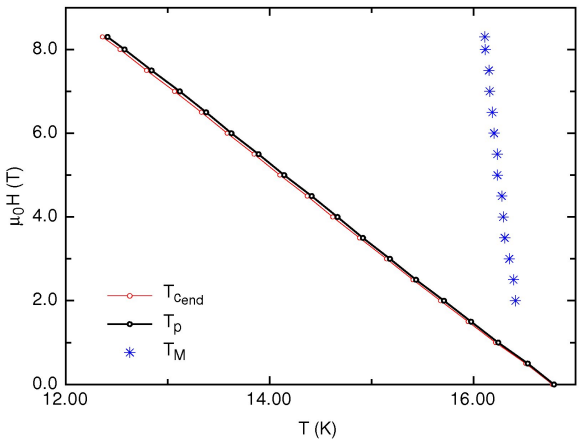

Figure 9.6: Phase diagram of the investigated V_3Si single crystal. T_c and T_p (see Fig. 9.5) are very close to each other, while T_M is almost field independent.

Interestingly the feature does not depend on the magnetic history, e.g., cooling in the magnetic field (FC) or zero-field cooling (ZFC). The use of external coils that produce a transverse ac "shaking" field also did not show any effect on the observed phenomenon. These facts, together with the observation that the entropy change associated with the first-order like peak does not scale with the external magnetic field, indicate that the peak in C/T is probably not related to a transition of vortex lattice. This conclusion is supported by the peculiar strong angular dependence of the feature when the magnetic field is rotated away from the $[100]$ direction, and by the results from SQUID magnetization measurements (by S. Weyeneth, group of Prof. Keller) that do not show any clear signature at the corresponding temperatures as we may expect for a vortex-related phase transition.

9.3 Search for resonance phenomena in $TlCuCl_3$ in the MHz range

Low dimensional quantum spin systems exhibit a variety of quantum phenomena that have gained much in interest in the last decade (7; 8; 9; 10). Our work is focused on $\mathrm{TlCuCl_3}$ for two particular reasons. This material was one of the first solids, in which experimental work indicated that the magnetic quasiparticles (magnons) form a Bose-Einstein condensate (BEC) above a critical field $\mu_0 H_c \approx 5.5\mathrm{T}$ at low temperatures (8; 11). Meanwhile several other materials have been found, that exhibit various features which can be explained within the framework of a condensation of quasiparticles with integer spin (9; 10; 12). Limitations of our cryo-system (such as the lowest reachable temperature and the highest applicable magnetic field) do not allow us to investigate this phenomenon in other materials than $\mathrm{TlCuCl_3}$, however.

The discovery of a BEC-like scenario of different types of quasiparticles in all these different materials raised various questions (13). In one case (14), the lifetime of the quasiparticles is very short (a few picoseconds). In other cases the number of quasiparticles is not conserved (15) or symmetry aspects are not entirely fulfilled (16). To what extent these unfavorable conditions affect the Bose-Einstein condensation is still an issue of debate. To prove that there is in fact a true condensate one has to show that the particles form a single coherent state, similar to the superfluid state as observed in liquid $^4\mathrm{He}$. A convincing method would therefore be to demonstrate the existence of such a superfluid component in the system. In analogy to $^4\mathrm{He}$, a second-sound mode in such a condensate phase would manifest itself as an oscillation of the density of the quasiparticles (superfluid and normalfluid component flow relative to one another) and accordingly of the entropy in the system. The detection of such a mode would therefore be a clear sign for the occurrence of a BEC.

Last year we have performed our measurements on $\mathrm{TlCuCl_3}$ at $\mathrm{T} = 2\mathrm{K}$ and $\mu_0\mathrm{H} = 9\mathrm{T}$ with a home-made AC driven Wheatstone-like bridge set-up. However, the resulting data have not revealed the distinct resonances that we have expected to occur due to

a "second-sound mode" of a possible BEC-state. The occurrence of many sharp resonances in the background signal made the detection of the expected small signals coming from the sample quite unreliable. Performing an immediate background subtraction, moving the sample in and out of the detection coil "in situ" in helium atmosphere has not resulted in a significant improvement. Therefore we decided to design a new detection coil set-up, in which no current is flowing through the coils in order to avoid undesired resonance phenomena resulting in a relatively large and arbitrary background signal.

We built a new AC susceptometer to perform high-frequency magnetic-susceptibility measurements from 200 kHz up to 2 MHz. The design is a standard 3-coil configuration with a primary coil and two secondary pick-up coils (see Fig. 9.7). A highly symmetric arrangement of the secondary coils with respect to each other and their immediate surroundings is necessary to avoid any unbalance of the induced voltage signal. Imperfections of the two pick-up coils or just a slight inhomogeneity of the AC magnetic field in the primary coil cause a non-zero induced voltage even in absence of any sample (see Fig. 9.8). A step motor enables us to move the sample in and out of the pick-up coils, or to move it from one secondary coil to the other one. Thus an immediate background subtraction is implemented. Any residual offset strongly increases with measuring frequency and amplitude of the AC magnetic field, however.

The impedance of the primary coil with inductance L, $Z = i\omega L$, also increases with frequency, which results in a limitation of the current passing through the coil and consequently of the amplitude of the generated AC magnetic field. A powerful high-frequency current source was therefore designed and built in collaboration with our domestic electronic work-shop. As a signal analyzer we use a standard lock-in amplifier (EG & G Instruments 7260 DSP lock-in amplifier) or a spectrum analyzer (Rohde & Schwarz FSL spectrum analyzer), which enables us to perform a larger frequency scan in a shorter time period limiting the resolution bandwidth to 10 Hz (every measured data point is averaged over 10 Hz). First measurements with this new set-up still revealed an insufficient sensitivity over the large studied frequency range due to remaining unbalance of the signal. Therefore an even more precise voltage compensation circuit is required, which is still under construction.

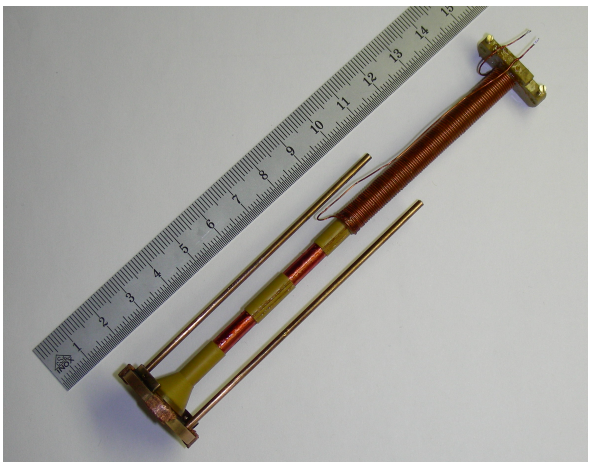

Figure 9.7: The disassembled coil system for measuring high-frequency AC susceptibility, showing both primary coil and the secondary pick-up coils.

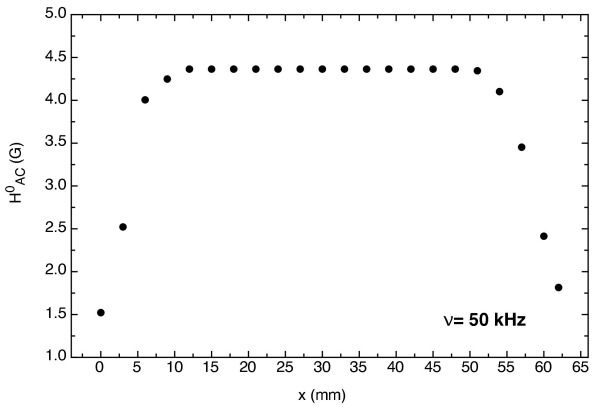

Figure 9.8: Magnetic-field profile of the primary coil.

9.4 Cation and anion substitution in $LaSrNiO_4$ and $LaBaNiO_{4-\delta}$

Last year we had reported that polycrystalline $LaBaNiO_{4-\delta}$ samples as-prepared by standard wet chemical procedures) are oxygen deficient ($\delta = 0.15$), which might explain the poor electrical conductivity as compared to metallic $LaSrNiO_4$, because also the planar oxygen atoms seem to be affected. We have hypothesized that fully oxygenated $LaBaNiO_{4-\delta}$ might behave in a very different way as soon as $\delta = 0$ is achieved. To verify this hypothesis we have prepared single phased $LaBaNiO_{4-\delta}$ and $LaSr_{0.5}Ba_{0.5}NiO_4$, and annealed the samples at $400°C$ at an O_2 pressure of 880 bar (in collaboration with J. Karpinksi, ETHZ).

Chemical analysis (done by K. Pomjakushina, LNS) revealed an oxygen content $4.03(1)$ confirming the desired oxygen stoichiometry. In Fig. 9.9 we show the electrical conductivity in comparison with corresponding data from metallic $LaSrNiO_4$. The electrical conductivity of $LaBaNiO_4$ still shows a pronounced variable-range hopping-type temperature dependence over a wide range of temperatures. Therefore it is clear that the electrical transport in $LaBaNiO_4$ is indeed intrinsically different from that in $LaSrNiO_4$.

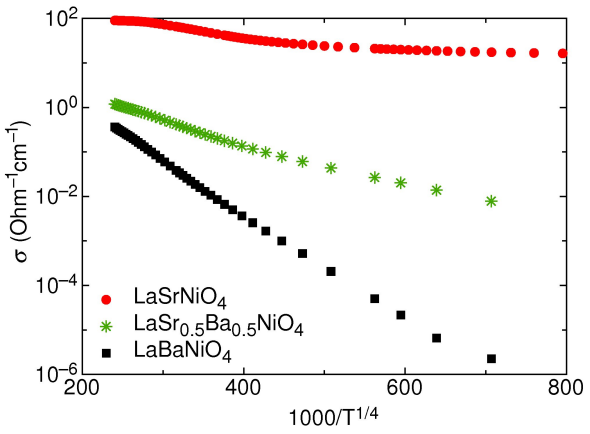

Figure 9.9: Electrical conductivity of $LaSrNiO_4$, $LaSr_{0.5}Ba_{0.5}NiO_4$, and $LaBaNiO_4$ after high oxygen-pressure annealing. $LaBaNiO_4$ exhibits an almost perfect variable-range hopping-type conductivity.

In an attempt to modify the physical properties of $LaSrNiO_4$ we made a number of substitution experiments, e.g., by replacing La or Sr with elements of smaller ionic radii, i.e., by the application of "chemical pressure". Up to now, only the stoichiometric compounds $RESrNiO_4$ with RE = La, Nd, Sm, Eu, and Gd have been reported to exist (all metallic) (17), while partial substitution has been achieved for $Dy_{1.5}Sr_{0.5}NiO_4$ (18), and $Nd_{1.4}Ca_{0.6}NiO_4$ (19). Our preparation under elevated oxygen pressure (1 kbar at $1000°C$) resulted in the formation of the new compounds $DySrNiO_4$, $HoSrNiO_4$, $NdCaNiO_4$ and $SmCaNiO_4$ (at present, no structural refinement has been made to ensure the exact cation stoichiometry).

Finally, a number of attempts have been made to change the electronic structure of $LaSrNiO_4$ by replacing the apical oxygen in the oxygen octahedra by halogen atoms. This substitution has been reported to be possible in transition-metal perovskites with the K_2NiF_4 structure for the case of Cu (substitution with F, Cl or Br (20; 21)), Fe (Cl or Br (22)), Co (Cl or Br (23)), and Mn (Cl (24)). In analogy to these structures we might expect the existence of compounds such as Sr_2NiO_3X or Ca_2NiO_3X with X = F, Cl or Br. Among the several possible synthesis techniques described in the literature we chose to fluorinate with NH_4F and to try a direct solid-state reaction using $NiCl_2$. In none of these experiments any compounds with the K_2NiF_4 structure and containing halogen atoms were formed.

[1] H. Bartolf, et al.,
in *Electron beam applications at ETH Zürich*, Raith Application Note 2006, Raith GmbH.

[2] G. Bilbro and W. L. McMillan,

Phys. Rev. B **14**, 1887 (1976).
[3] N. Toyota, T. Kobayashi et al., J. Phys. Soc. Jap. **57**, pp. 2089-3101 (1988).
[4] L. R. Testardi: Rev. Mod. Phys. **47**, 637 (1975).
[5] A. Schilling and O. Jeandupeux, Phys. Rev. B **52**, 9714 (1995).
[6] A. Schilling and M. Reibelt, Rev. Sci. Instrum. **78**, 033904 (2007).
[7] B.C. Watson et al., Phys. Rev. Lett. **86**, 5168 (2001).
[8] Ch. Rüegg et al., Nature **423**, 62 (2003).
[9] B. Grenier et al., Phys. Rev. Lett. **92**, 087203 (2004).
[10] V.S. Zapf et al., Phys. Rev. Lett. **96**, 077204 (2006).
[11] T. Nikuni et al., Phys.Rev. Lett. **84**, 5868 (2000).
[12] M. Jaime et al., Phys. Rev. Lett. **93**, 077204 (2004).
[13] D. Snoke et al., Nature **443**, 403 (2006).
[14] J. Kasparzak et al., Nature **443**, 409 (2006).
[15] S.O. Demokritov et al., Nature **443**, 430 (2006).
[16] V.N. Glazkov et al., Phys. Rev. B **69**, 184410 (2004).
[17] G. Demazeau et al., J. Solid State Chem. **18** (1976) 159, M. James and J. P. Attfield, J. Mater. Chem. **6** (1996) 57.
[18] G. L. Lu et al., Hua Hsueh Hsueh Pao **54** (1996) 667.
[19] Y. Takeda, et al., J. Solid State Chem. **96** (1992) 72.
[20] M. Al-Mamouri et al., Nature **369** (1994) 382.
[21] B. Grande and H. Müller-Buschbaum, Z. Anorgan. Allg. Chem. **429** (1977) 88.
[22] J. A. Ackerman, J. Solid State Chem. **92** (1991) 496.
[23] C. S. Knee and M. T. Weller, J. Solid State Chem. **168** (2004) 1.
[24] C. S. Knee and M. T. Weller, Chem. Commun. **3** (2002) 256.

10 Surface Physics

T. Greber, M. Hengsberger, J. Lobo, T. Okuda, R. Schillinger, S. Berner, C. Galli Marxer, J.-H. Dil, A. Dolocan, M. Corso, C. Cirelli, M. Morscher, T. Brugger, M. Allan, S. Berner, L. Brandenberger, D. Leuenberger, T. Wassmann, T. Mattle, M. Klöckner, J. Osterwalder

The surface physics group continues to study model systems of well defined surfaces and interfaces in order to address fundamental issues that are relevant for nanoscience and nanotechnology. Our laboratory is well equipped for the preparation and characterization of clean surfaces, metal and molecular monolayer films, as well as self-assembling nanostructures, all under ultra-high vacuum (UHV) conditions. Experimental techniques available to us include x-ray photoelectron spectroscopy (XPS) and diffraction (XPD), angle-resolved photoemission spectroscopy (ARPES), two-photon photoemission (2PPE) using femtosecond laser pulses, low-energy electron diffraction (LEED) and scanning tunneling microscopy (STM). At the nearby Swiss Light Source we have built up two more photoemission spectrometers, one for spin-resolved Fermi surface mapping and one for near-node photoelectron holography. A growing network of national and international collaborations expands this set of experimental techniques and provides us also with the necessary theoretical support.

The research carried out during the report period can be grouped into three topics:

- **Electronic states at metal surfaces**
  On well ordered metal surfaces new electronic states, deviant from the bulk electronic states, arise due to the abrupt termination of the crystal lattice at the surface. These states are confined to a few atomic surface layers, while the electrons can propagate along the surface. Therefore, they can be considered as model systems for a two-dimensional electron gas. Due to the absence of inversion symmetry at the surface, spin-orbit coupling can lead to a momentum dependent spin-splitting of these states, the so-called Rashba effect. In semiconductor heterostructures, this effect represents an interesting route to manipulate electron spins by means of electric fields, thus raising a lot of interest in the field of *spintronics*. Since the splitting is much larger on these metal surface states, they permit us to study systematically how this splitting and the associated spin structures are affected by steps, kinks or adsorbates, or by regular superstructures. This is the main aim of our spin-resolved photoemission experiment COPHEE (the COmplete PHotoEmission Experiment) at the Swiss Light Source.

  Over the last years we experienced serious problems with external magnetic fields from the highly non-uniform and time-dependent magnetic environment at the synchrotron beamline entering the trajectories of the photoelectrons, leading to spurious effects in the spin-polarization measurements. We therefore decided to build an external double-walled μ-metal shield around the electron analyzer and the spin polarimeter. Designing and building this shield around the existing, highly complex instrument, represented a formidable task for our group and for the mechanical workshop (see Sec. 12). It is now finished and currently being annealed in a hydrogen atmosphere for perfect magnetic conditioning. Nevertheless, some experiments not requiring spin-polarization analysis could be performed in the meantime. As described in Sec. 10.1, a new surface state was discovered on the Ni(111) surface, for which there were some theoretical hints but so far no experimental

evidence.

- **Monolayer films of hexagonal boron nitride on metal surfaces**
  Hexagonal boron nitride (h-BN) is a layered, wide gap insulator with very strong sp^2 bonds within graphene-like sheets. Perfect single monolayers can be grown on transition metal surfaces by simple thermal decomposition of borazine, which is the BN-analogon to benzene. The study of such films has represented a large activity of the group over the last years, funded both by the SNF as well as by an EU STREP project. An important development of last year was the solution of the atomic structure of the highly complex nanomesh structure formed by h-BN on Rh(111), which could be achieved by a close collaboration within the European consortium. Rather than being a double layer structure of two incomplete mesh layers, evidence could be gathered for it being a single and complete, but highly corrugated h-BN layer (Sec. 10.2). Nevertheless, the corrugation produces a regular array of potentials wells for trapping molecules (Sec. 10.3) and small metal clusters (Sec. 10.4).

  On Ni(111), the h-BN monolayer is well lattice matched and essentially flat. This system is therefore well suited for the study of the electronic structure of this single-layer variant of boron nitride. While the occupied electronic bands have been well characterized over the last years, we were now able to perform inverse photoemission experiments at the Universität Münster in Germany in order to study also the unoccupied conduction band (Sec. 10.5), and to compare these results to our previous 2PPE results. At the same time, we extended the 2PPE measurements to high temperatures, all the way through the Curie temperature of the Ni(111) substrate, in order to establish this spectroscopy as a probe for the magnetic state of the surface (Sec. 10.6). This will give us later the opportunity to use this probe for time-resolved studies of ultrafast demagnetization of nickel by intense laser pulses with femtosecond resolution.

- **Molecular monolayers**
  By immobilizing molecules on solid surfaces we can study two types of effects. Like in a molecular crystal, we have the possibility to determine the structure of the individual molecule, which is maybe different in the adsorbed state compared to the gas phase. On the other hand, we can study the arrangement of the molecules, their interactions and the resulting electronic properties. Over the last few years, monolayers of C_{60} fullerene molecules have been one of the main scientific topics in the group. Last year, we were able to obtain unique samples of $H_2@C_{60}$ endofullerenes from a group at Kyoto University, consisting of C_{60} buckyball cages filled with one H_2 molecule each. First photoemission experiments aiming at the electronic character of the encapsulated hydrogen molecule are presented in Sec. 10.7. Interestingly, no distinct signal due to the H_2 1σ molecular orbital is observed in the spectra.

  The electron spin is an important degree of freedom also in molecular adsorption, especially when ferromagnetic substrates are involved. The group is therefore trying to expand our instrumentation for spin polarization measurements also to the photoelectron spectrometer at the Zürich laboratory, which is equipped with excellent preparation and characterization facilities for the study of molecular layers. For this purpose, a new, simpler spin detection scheme (Sec. 10.8) is currently being evaluated.

10.1 A new surface state on Ni(111)

In collaboration with:
Peter Blaha, Institut für Materialchemie, Technische Universität Wien, A-1060 Vienna, Austria, and Luc Patthey, Surface and Interface Spectroscopy Beamline, Swiss Light Source, Paul-Scherrer-Institut, Villigen.

On Ni(111) two different surface states near normal emission are known (1; 2): an sp-band derived Shockley surface state very close to the Fermi energy with an electron-like (upward) dispersion, and a d-band derived Tamm surface state with a minimum binding energy of ∼250 meV and with a hole-like (downward) dispersion. A third surface state with Tamm character is predicted from density functional theory (DFT) calculations. It is located in the existing local d-band energy gap and originates from the deeper lying d-band. But, even though the electronic structure of Ni(111) has been studied in great detail by several groups and techniques over the last three decades, no experimental evidence for the existence of this new surface state has been produced.
To uncover this state we made use of the high sensitivity of surface states to the presence of adsorbates. Hydrogen adsorption is known to strongly affect the surface states on Ni(111), quenching them completely when the saturation coverage (∼ 0.5 ML at room temperature) is reached (3). The top graph of Fig. 10.1 shows the spectra from the clean and hydrogen saturated surface measured at normal emission with a photon energy of 35 eV. The clean surface shows a spectrum dominated by two peaks at binding energies of 0.54 eV and 1.37 eV which correspond to the bulk d-bands labeled Λ_1 and Λ_3. Two small shoulders with binding energies of 0.025 eV and 0.28 eV correspond to the Shockley and Tamm states, respectively. A first visual search for the theoretically expected new surface state is unsuccessful.

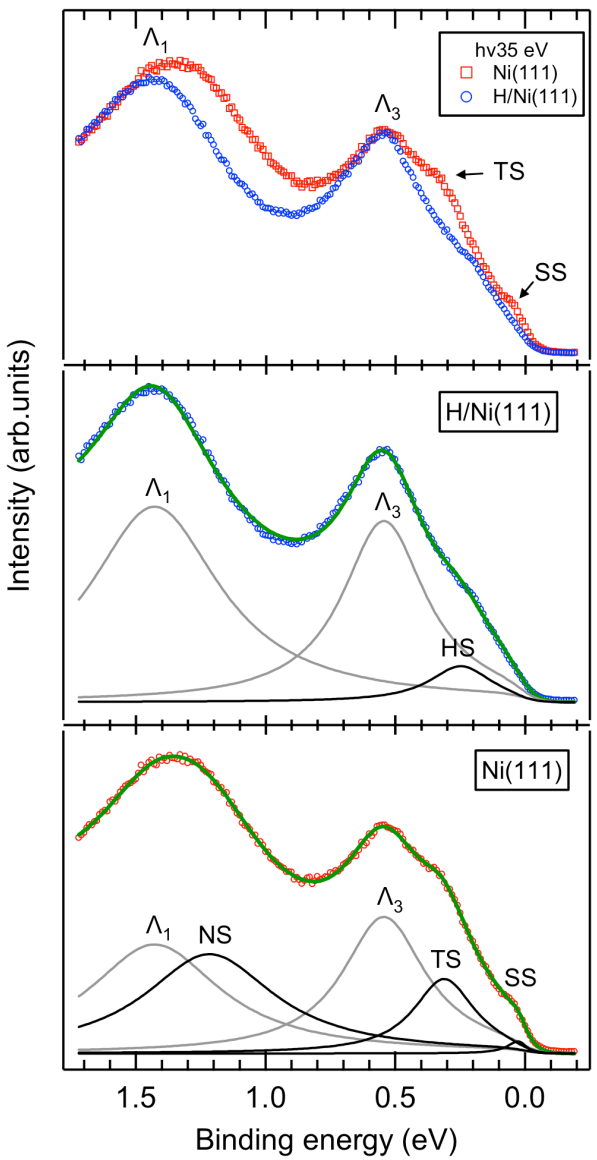

Figure 10.1: Top: Room temperature spectra measured on the clean (red squares) and hydrogen saturated (blue circles) Ni(111) surface measured at normal emission with a photon energy of 35 eV. The center and bottom panels display fits to the two spectra using a procedure described in the text. Notation: SS = Shockley state; TS = Tamm state; NS = new surface state; HS = hydrogen induced surface state; Λ_1 and Λ_3 = bulk d-bands.

The spectrum from the hydrogen saturated surface shows significant differences: the Shockley and the Tamm states have disappeared, while a new shoulder can be seen at a binding energy of 0.23 eV. Concerning the bulk states, the Λ_3 band remains basically unchanged, whereas the peak corresponding to Λ_1 experiences an ostentatious change in the peak width and an apparent binding energy shift of about 0.1 eV. This may be an indication that more than one component contribute to the Λ_1 peak. To verify this, we performed a least square fit for each spectrum assuming that both bulk bands maintain the same width and binding energy. For the clean surface spectrum, a superposition of five Lorentzian components was necessary, together with a linear background and multiplication with a Fermi-Dirac distribution. For the hydrogen-passivated surface only three Lorentzian components were needed to fit the spectrum. The overall agreement of these fits is very good. They are shown in the center and bottom graphs of Fig. 10.1. On the clean surface, the small component near the Fermi energy corresponds to the Shockley state (SS), the one found at 0.28 eV to the Tamm state (TS). The component located at 1.19 eV represents the expected new surface state (NS). It is located in the local d-band gap in between the Λ_3 and Λ_1 bulk bands, in close proximity to the latter. In this way, each of the bulk d-bands gives rise to its own Tamm surface state.

[1] F. J. Himpsel, D. E. Eastman, Phys. Rev. Lett. **41**, 507 (1978).

[2] G. Borstel, G. Thorner, M. Donath, V. Dose, A. Goldmann, Solid State Communications **55**, 469 (1985).

[3] F. J. Himpsel, J. A. Knapp, D. E. Eastman, Phys. Rev. B **19**, 2872 (1979).

10.2 Boron nitride nanomesh: a corrugated monolayer

In collaboration with:
R. Widmer and *O. Gröning*, EMPA Swiss Federal Laboratories for Materials Testing and Research, Feuerwerkerstrasse 39, CH-3602 Thun, and *R. Laskowski*, *P. Blaha* and *K. Schwarz*, Institut für Materialchemie, Technische Universität Wien, A-1060 Vienna, Austria.

Hexagonal boron nitride (*h*-BN) on the Rh(111) surface forms a highly regular hexagonal nanomesh of 2 nm pore size and a periodicity of 3.22 nm (1) which corresponds to a coincidence lattice of (13×13) *h*-BN units on (12×12) Rh lattice spacings (2). Based on STM and UPS data a first structure model was proposed, which consisted of two overlapping *h*-BN mesh layers. Further experimental studies on this peculiar material, which forms also on the Ru(0001) surface (3), and DFT calculations (4) support a new model where the nanomesh is a corrugated single *h*-BN layer. A conclusive evidence for this is given by low temperature (77 K) STM images which allow to resolve the atomic structure of the nanomesh in detail.

Fig. 10.2(a) shows a few nanomesh unit cells with a continuous hexagonal atomic lattice. The short range atomic periodicity inside the pores and on the wires has a value close to 2.5 Å (the N-N or B-B in-plane distance), and it is due to only one species within the *h*-BN layer (probably the nitrogen (5)). The large-scale nanomesh modulation appears in the rims around the mesh pores which are imaged bright even though they are topographically low, and in the inner part of the wires which are dark even though they represent the highest regions on the surface. Such electronic effects can be removed by filtering the image, thus obtaining a projection of the atomic arrangement on the surface plane (Fig. 10.2(c-d)). The nanomesh can now be viewed as formed by asymmetric hexagons,

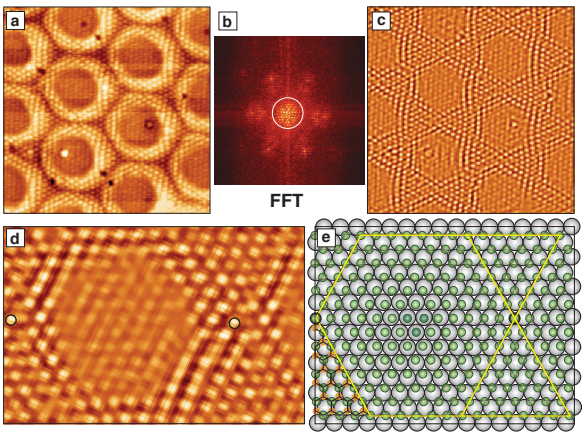

Figure 10.2:
(a) Constant current STM image (9.4×9.4 nm^2, I_t=1 nA) taken at 77 K at a sample bias voltage of V_s=-2 mV. These values are close to the Fermi level, which allows to resolve the atomic structure of the h-BN nanomesh on Rh(111). Only one atomic species is imaged. In (c), image (a) has been filtered in order to remove the 3.22 nm periodicity and to emphasize the atomic corrugation in the wires and pores. For this filtering the spots inside the white circle around the (0,0) spot in the fast Fourier transform (b) of image (a) have been removed. (d) is a zoom into (c), where a single nanomesh unit cell is enlarged permitting atom counting. In (e) a model for (d) is shown with the atomic assignment and registry given by the DFT calculations in [4]. The green atoms are nitrogen and the gray rhodium. On the bottom left of (d), some orange boron atoms are drawn to indicate the complete h-BN units. The three darker N atoms mark the center of the nanomesh pore.

the sides of which are due to alternating 6 or 7 N-N (B-B) spacings. The centers of the hexagons are represented by three atoms. Each hexagon is surrounded by six equilateral triangles with sizes defined by the corresponding side of the hexagon. Each pair of neighboring triangles shares an atom which identifies the center of the nanomesh wire. Within a single nanomesh unit cell 169 (N or B) atoms are imaged as expected for the (13×13) periodicity (Fig. 10.2(d)). The STM does not allow to make any assignment about the registry of the *h*-BN layer with respect to the substrate, since only one atomic species appears. From the DFT study by *Laskowski et al.* (4), the strongest bonding with the Rh substrate happens when the N and B atoms occupy *on-top* and *fcc* sites, respectively. In their theoretical model for the nanomesh unit cell, the pores are flat areas where the N atoms occupy nearly *on top* positions, and the BN is bonded strongly to the metal. The wires consists of two areas: in one the B atoms occupy *on-top* and the N atoms *hcp* sites, in the second one they occupy *hcp* and *fcc* sites, respectively. Since these are not optimal adsorption positions above the Rh lattice, the B and N atoms are pushed upwards by 0.55 Å, creating the topographic corrugation of the nanomesh layer. This model is in good agreement with the atomically resolved STM data (Fig. 10.2(e)), where the smaller and bigger triangles around the hexagons would correspond to the two types of wire areas. Surface x-ray diffraction experiments will be performed at the Swiss Light Source (SLS) to further refine the nanomesh unit cell structure.

[1] M. Corso, W. Auwärter, M. Muntwiler, A. Tamai, T. Greber and J. Osterwalder, Science, **303**, 217 (2004).

[2] O. Bunk, M. Corso, D. Martoccia, R. Herger, P. R. Willmott, B. D. Patterson and J. Osterwalder, J. F. van der Veen, Surf. Sci., **601**, L7 (2007).

[3] A. Goriachko, Y. He, M. Knapp, H. Over, M. Corso, T. Brugger, S. Berner, J. Osterwalder and T. Greber, Langmuir, **23**, 2928 (2007).

[4] R. Laskowski, P. Blaha, T. Gallauner and K. Schwarz, Phys. Rev. Lett., **98**, 106802 (2007).

[5] G. B. Grad, P. Blaha, K. Schwarz, W. Auwärter and T. Greber, Phys. Rev. B, **68**, 085404 (2003).

10.3 Trapping molecules in the nanomesh pores

The boron nitride nanomesh on Rh(111) (1) was used as a template to organize organic molecules on a surface. Naphthalocyanine (Nc) molecules were vapor-deposited onto the nanomesh kept at room temperature. These planar molecules have a conjugated π-electron system and their diameter of about 2 nm is comparable to the nanomesh pore size. They form a well-ordered array with the periodicity of the nanomesh (3.22 nm) as observed in the STM image shown in Fig. 10.3. High-resolution images reveal that individual Nc molecules are trapped inside the pores, indicating a highly site-selective adsorption.

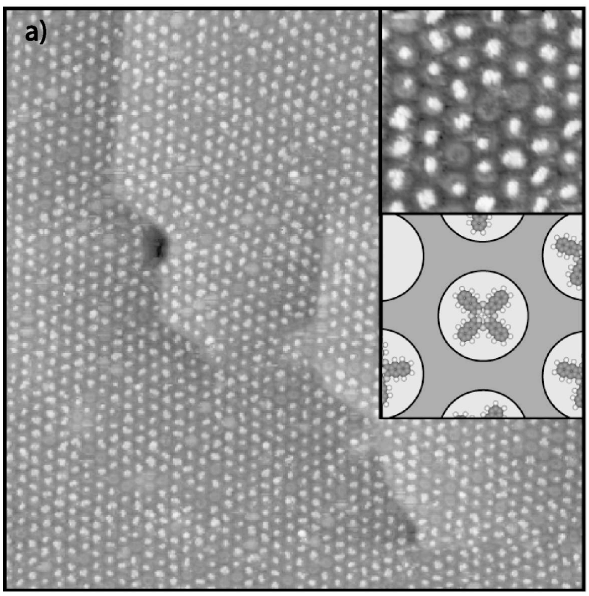

Figure 10.3: Site-selective adsorption of naphthalocyanine (Nc) molecules in the nanomesh pores. STM image (120 nm x 120 nm, I = 0.3 nA, U = 1.3 V) showing a nearly complete monolayer [3] of Nc molecules on the nanomesh. The inset on the top right shows an enlargement (19 nm x 19 nm) and gives a high-resolution view that shows the trapping of the Nc molecules inside the nanomesh pores. The inset on the right shows a schematic representation of the molecular structure of naphthalocyanine ($C_{48}H_{26}N_8$) plotted on top of a nanomesh pore.

Adding more and more molecules leads to the continuous filling of all the nanomesh pores. Molecule-substrate interactions are therefore dominating the adsorption behavior and intermolecular interactions are weak. This behavior is in contrast to Nc on flat graphite layers where the structure formation within the molecular layer is dominated by intermolecular interactions. A completely different molecular arrangement is observed in that case, with a much smaller periodicity of 1.7 nm (2).

The selective adsorption into the pores is also reflected in the normal emission UPS spectra (Fig. 10.4). The spectrum of the clean h-BN

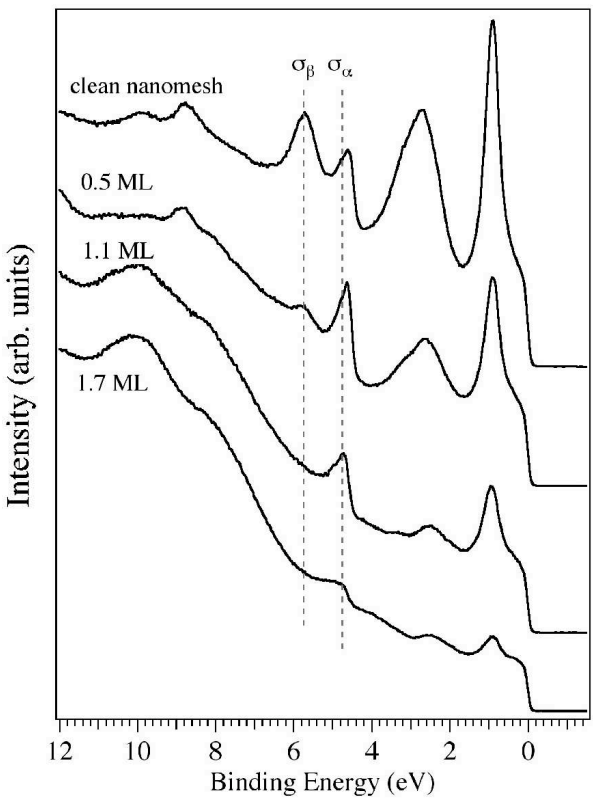

Figure 10.4: Normal emission UPS spectra for increasing Nc coverage on the nanomesh. The site-selective adsorption of the Nc is reflected in the selective attenuation up to the first monolayer of the σ_β component that is associated with the nanomesh pores. Further increasing the coverage leads also to attenuation of the σ_α component that is related to the mesh wires.

layer on Rh(111) shows the appearance of two pairs of BN-related peaks and indicates thus the presence of two species of h-BN that have their binding energies for the σ and π bands shifted by about 1 eV (1). Adsorption of the molecules onto the nanomesh leads to the attenuation of the intensity of the σ_β component, whereas the other one (σ_α) remains unchanged for coverages up to one monolayer (3) (Fig. 10.4. The σ_β component is associated with the nanomesh pores and the selective attenuation thus reflects the trapping of the Nc molecules in the pores. Further increasing the coverage leads also to attenuation of the σ_α component that is related to the mesh wires.

The strength of the trapping potential for Nc was studied in time-lapsed STM series for a partial coverage. At room temperature a very low mobility of the trapped molecules was observed with only rare hopping events. Annealing experiments confirmed the rather high diffusion barrier observed in STM. Annealing to 650 K does not lead to the desorption of the molecules from the pores. The Nc molecules thus form a robust array of equally spaced and well-separated individual molecules on the nanomesh. The present study exemplifies the potential of the nanomesh as a template for the growth of ordered molecular arrays. The large spacing between individual molecules and negligible intermolecular interactions are in many cases mandatory for preserved functionality of individual molecules on surfaces. Such arrays might be interesting for applications such as molecular electronics and storage, in photochemistry or in optical devices.

[1] M. Corso et al., Science, **303**, 217 (2004).

[2] M. Lackinger et al., J. Phys. Chem. B, **108**, 2279 (2004).

[3] The term monolayer refers in this case to one molecule per nanomesh pore.

10.4 Using the nanomesh as a template for magnetic cluster growth

In collaboration with: Philipp Buluschek and Harald Brune, Institut de Physique des Nanostructures, École Polytechnique Fédérale de Lausanne; Axel Enders and Klaus Kern, Max-Planck-Institut für Festkörperforschung, Stuttgart.

Arrays of nanometer-size particles can exhibit peculiar magnetic properties, quite different compared to the bulk properties of the same material (1). In order to investigate such differences, accurate control of the size and the arrangement of the magnetic particles is necessary. This can be achieved e.g. in metal cluster beams or through growth on supporting surfaces. We demonstrate that the h-BN nanomesh on Rh(111) (2) serves as a good template for controlled metal cluster growth.

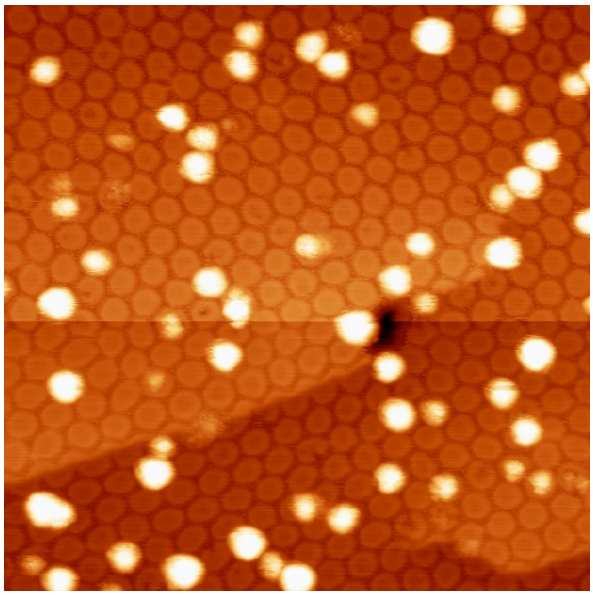

Figure 10.5: Constant current STM image of 0.1 ML Co on h-BN/Rh(111) evaporated at 300 K. Image size 50x50 nm^2, I=0.2 nA, V=0.8 V. The horizontal line near the center of the image is due to a spontaneous tip change and the associated change of tunnelling conditions. Two monatomic steps in the h-BN/Rh(111) substrate can be identified in the lower half of the image.

We evaporated cobalt (Co) onto the nanomesh at room temperature under ultra-high vacuum conditions. STM and photoemission experiments were performed to investigate the resulting morphologies and structures. STM images show that Co clusters form, with diameters comparable to the nanomesh pores. In Fig. 10.5 the result from a room temperature deposition of 0.1 ML Co, followed by a short annealing to 650 K, is imaged. At this low Co coverage the nanomesh, with its corrugation of 0.6 Å, is clearly resolved. Co clusters appear with typical heights of about 1 nm, spread randomly over the imaged area. The clusters have quite a narrow size distribution, and they are in their vast majority centered at the pores of the underlying nanomesh. This represents a first promising result regarding its functionality as a template for the growth of monodisperse metal cluster arrays.

[1] J. Shen and J. Kirschner, Surface Science **500**, 300 (2002).

[2] M. Corso et. al, Science **303**, 217 (2004).

10.5 The unoccupied band structure of h-BN on Ni(111).

in collaboration with: C. Eibl, K. Wulff, K. Zumbrägel, and M. Donath, Physikalisches Institut der Universität Münster, Germany.

In the past years, the electronic and atomic structure of a monolayer of hexonal boron nitride deposited on Ni(111) was studied in great detail with various methods (1). Some aspects, however, like the charge transfer through the boron nitride layer (2), or the reasons for the occurrence of spin-polarized photocurrents from this interface (3), strongly depend on the unoccupied band structure and cannot be studied by conventional photoemission. Two-photon-photoemission was successfully used to obtain first information about these states (4). Inverse photoemission, however, is by far the most direct way for accessing the unoccupied band structure, in particular for low photon energies (5). Briefly, a well collimated beam of monochromatic electrons is absorbed in the surface, occupying states with well defined energies and momenta. The electrons decay into states at lower energies under emission of radiation, creation of electron-hole pairs or heat dissipation. In inverse photoemission in isochromatic mode, the emission of photons within a narrow energy window (about 400 meV at 9.5 eV) is detected as a function of kinetic energy and direction of the incoming electrons. Since the photon energy and the initial electron energy are known, the final state energy inside the solid can be calculated as well as the corresponding crystal momentum. In addition, using spin-polarized electrons (6), the spin character of the bands can be extracted (7).

The measurements were carried out in the group of Prof. M. Donath at the University of Münster. The sample was a Ni(111) single crystal, which has a hexagonal frame shape such that the magnetic flux lines are closed inside the sample (7). The spectra were taken in remanence, obtained by magnetizing the sample with a current pulse through a coil wrapped around one leg of the hexagon. Spin-polarized electrons were produced using photoemission of electrons from a cesiated GaAs source using circularly polarized light (6). Some selected spectra taken from the pristine and boron nitride covered Ni(111) are displayed in Fig. 10.6. The features close to the Fermi level originate from bulk transitions (B_d) present on both samples and, in addition, from a mostly unoccupied surface state (SS) on the clean Ni(111) surface (see Ref. (7) and references therein). The image potential state (IS) found at higher energy is a bound state of an electron trapped

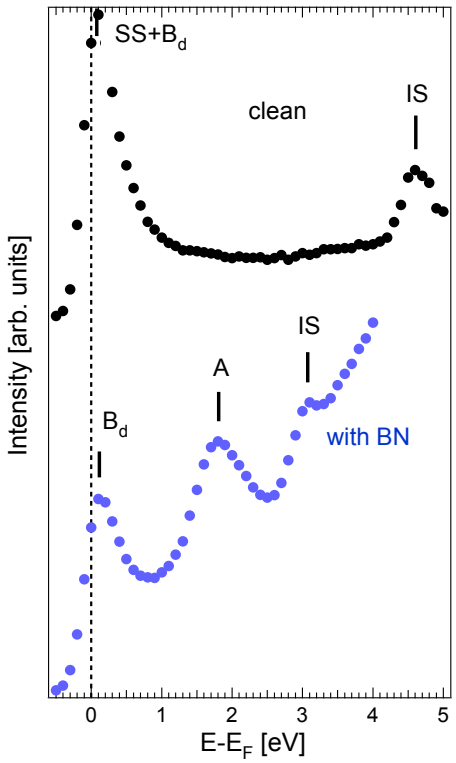

Figure 10.6: Spin-resolved inverse photoemission data from h-BN/Ni(111) in normal incidence (Θ=0°). Selected spectra from pristine and h-BN-covered Ni(111); B_d corresponds to Ni bulk states, SS to a surface transition; the interface state of boron nitride is denoted by A, the image potential states on both surfaces by IS.

between the crystal and the potential barrier of its own image potential. Its binding energy depends on the difference between Fermi and vacuum level, *i.e.* the work function. Upon adsorption of boron nitride, the work function changes dramatically by about 1.8 eV due to the modified surface dipole. Accordingly, the image state is shifted to lower binding energy by the same amount.

We focus now on the state found in normal incidence at 1.7 eV above the Fermi level, labeled A in Fig. 10.6. This state is attributed to the lowest unoccupied interface state in h-BN/Ni(111). Its energy position is in excellent agreement with density functional (DFT) calculations (1) and slightly higher than the corresponding value found in two-photon-photoemission (4). Its effective mass was found to be 1.1±0.2 in units of the free-electron rest mass (data not shown). More interestingly, theory predicts a substrate induced exchange splitting of the order of 100 meV (1). Using the asymmetry calculated from the experimental data for different directions of electron spin polarization and sample magnetization, and an instrumental spin resolution function P_{eff}, fully spin-resolved spectra can be retrieved. This is shown in Fig. 10.7 for an electron spin polarization of about 30% and a remanent sample magnetization of 70% at room temperature, as determined independently by temperature dependent measurements of the secondary electron spin polarization (8). This leads to an exchange splitting of the interface state of 150±50 meV (8), in good agreement with the DFT calculations (1). The sub-band corresponding to the spin magnetic moment aligned with the bulk magnetization direction (majority spin) is found at lower binding energy as expected from an exchange splitting

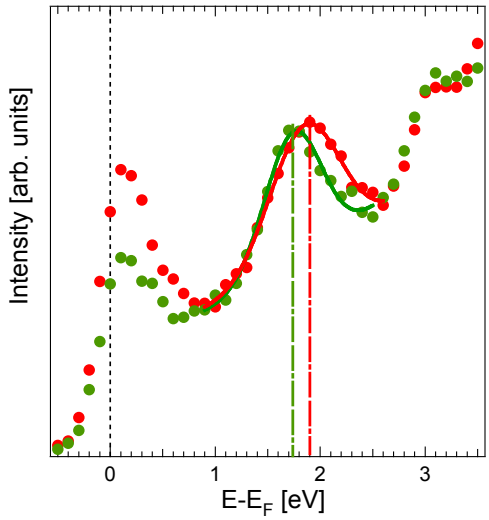

Figure 10.7:
Spin-resolved spectra, extracted from the raw data using an instrumental spin resolution function of P_{eff}≈0.2; green (red) symbols denote the spectra for spin magnetic moment pointing parallel (antiparallel) to the bulk magnetization direction; the exchange splitting obtained in this fashion for the interface state is indicated by vertical dashed-dotted lines.

induced by the substrate magnetization. These results will shed light on the mechanism behind the spin-polarized photocurrent in particular and on spin-polarized transport through this model interface in general.

[1] G.B. Grad, P. Blaha, K. Schwarz, W. Auwärter, and T. Greber, Phys. Rev. B **68**, 085404 (2003).

[2] M. Muntwiler, W. Auwärter, A.P. Seitsonen, J. Osterwalder, and T. Greber, Phys. Rev. B, **71**, 241401 (2005).

[3] M. Hengsberger, M. Muntwiler, T. Greber, and J. Lobo-Checa,
Source for spin-polarized electrons, US patent WO 2007/006168 (published 18th of January 2007).

[4] M. Muntwiler, M. Hengsberger, A. Dolocan, H.J. Neff, T. Greber, and J. Osterwalder,
Phys. Rev. B **75**, 075407 (2007).

[5] V. Dose, W. Altmann, A. Goldmann, U. Kolac, and J. Rogozik, Phys. Rev. Lett. **52**, 1919 (1984).

[6] D.T. Pierce and F.A. Meier, Phys. Rev. B **13**, 5484 (1976).

[7] M. Donath, Surf. Sci. Rep. **20**, 251 (1994).

[8] K. Zumbrägel, diploma thesis, University of Münster, 2007.

10.6 Two-photon photoemission from h-BN on Ni(111) across the ferromagnetic phase transition

Two-photon photoemission (2PPE) is an alternative method to study the unoccupied electronic structure of surfaces, at least for states between the Fermi level and the vacuum energy. In the pump-probe mode the lifetimes of electronic excitations into such states can be measured. The method has recently been applied to h-BN/Ni(111) by our group (1). Two distinct intermediate states were detected, both populated from initial *3d*-bands of Ni(111) and with remarkably long lifetimes between 100 and 270 fs .

Nickel is considered to be the textbook example for an itinerant ferromagnet. The non-localized magnetic moments in nickel are carried by electrons of the spin polarized *3d*-bands, situated close to the Fermi energy. Below the Curie temperature T_c, the electrons in the completely filled *majority* subband (magnetized parallel to an external field) and from the partially occupied *minority* subband (anti-parallel alignment) are energetically separated by an amount that is termed the *exchange splitting*. As the temperature is raised, the exchange splitting is reduced and collapses completely at T_c (2). The purpose of the present study was to see how this change in the electronic structure of the ferromagnetic substrate is reflected in the 2PPE spectra from h-BN/Ni(111), where electrons from exchange-split *3d*-bands of Ni(111) are excited into intermediate states within the h-BN film before photoemission occurs by a second photon.

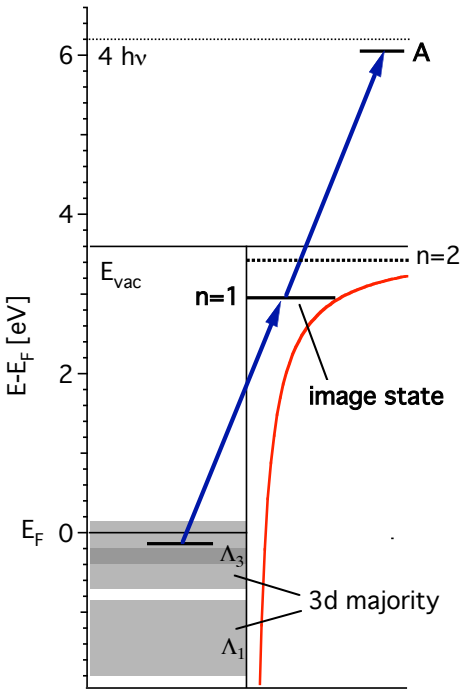

Figure 10.8: Level scheme of the blue-blue transition which is related to peak A. The red curve indicates the image potential at the Ni(111) metal surface.

Specifically, the focus was on a transition from the *3d*-bands of nickel as initial state to the unoccupied image potential state (n=1) as intermediate state, followed by a transition into a final free photoelectron state. Both transitions are induced by blue photons ($h\nu$ = 3.1 eV), provided by a femtosecond laser pulse (schematically drawn in Fig.10.8). With the aim of following the evolution of the 2PPE spectra across the magnetic phase transition of the substrate, series of 2PPE spectra were recorded while heating up and cooling down the sample surface through the critical temperature $T_c = 631$ K of nickel. The energy position as well as the width and intensity of the peak labeled A in Fig. 10.9 were monitored as a function of temperature. All of these features clearly reflect the temperature dependent magnetic phase transition of nickel at the Curie temperature.

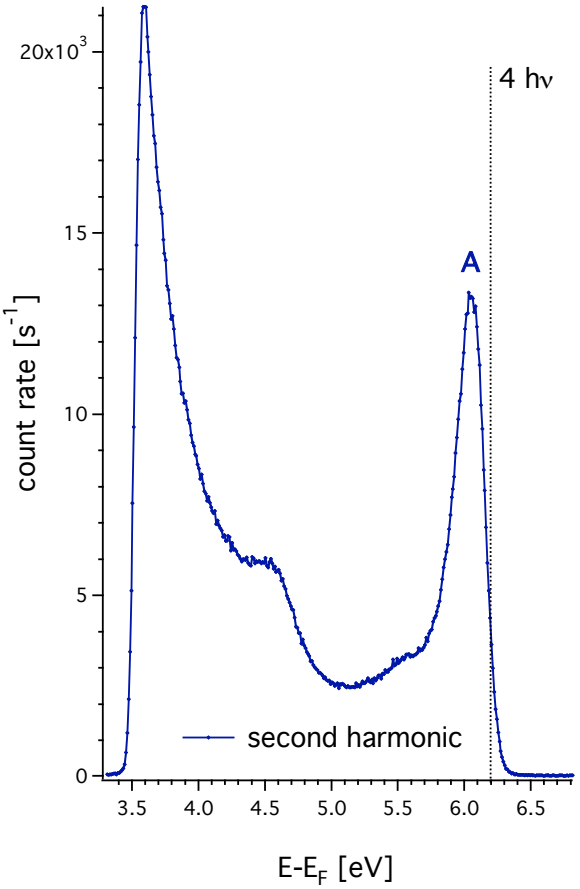

Figure 10.9: Monochromatic two-photon photoemission spectrum with blue light (hν = 3.1 eV) at normal emission and room temperature. The peak related to the image potential state is labeled with A.

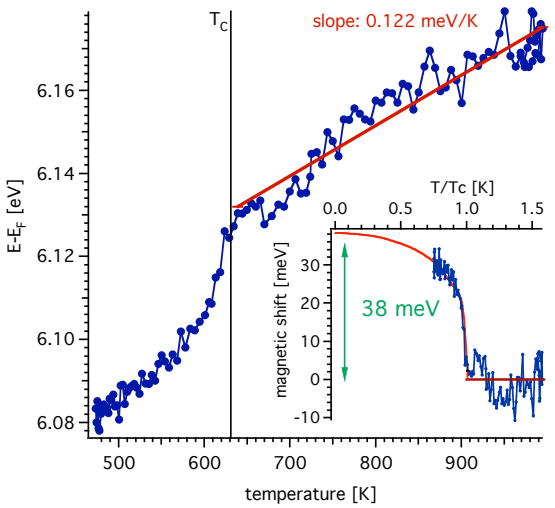

Figure 10.10: Image potential state peak position (peak A in Fig. 10.9), obtained from temperature dependent 2PPE spectra. Inset: Extracted magnetic shift of the image potential state position as a function of temperature.

Figure 10.10 shows the temperature behaviour of the peak position. Above T_c it increases linearly due to thermal lattice expansion. Below T_c, also the collapsing exchange splitting contributes to the change in peak position. Since the final photoelectron energy reflects directly the energy position of the intermediate image potential state, one can determine the exchange splitting of the (n=1) image potential state from the measured magnetic shift in Fig. 10.10. The latter can be extracted by subtracting the thermal shift from the total shift (inset of Fig. 10.10). Extrapolation to low temperatures produces a value of 38 meV which is in excellent agreement with the 2PPE study of Fischer *et al.* on clean Ni(111) that finds a value of $\Delta E_{ex} < 40$ meV at the $\bar{\Gamma}$ point in k-space (3). The investigated 2PPE image potential state transition is thereby shown to be sensitive to the ferromagnetic phase change of nickel and can thus be used e.g. to probe laser pulse induced ultrafast demagnetization.

[1] M. Muntwiler, M. Hengsberger, A. Dolocan, H. Neff, T. Greber, and J. Osterwalder,
Phys. Rev. B **75**, 07407 (2007).

[2] T. J. Kreutz, T. Greber, P. Aebi, J. Osterwalder,
Phys. Rev. B **58**, 1300 (1998).

[3] N. Fischer, S. Schuppler, Th. Fauster, and W. Steinmann,
Phys. Rev. B, **42**, 9717 (1990).

10.7 Hydrogen in C_{60}

in collaboration with: Ari P. Seitsonen, Institut de Minéralogie et de Physique des Milieux Condensés, Université Pierre et Marie Curie Paris 06, France, and Koichi Komatsu, Institute for Chemical Research, Kyoto University, Uji, Kyoto 611-0011, Japan.

Closed-cage fullerene molecules like C_{60} bear the possibility to house other atoms or molecules inside their cavity (1). This class of materials, called endofullerenes, opens many new aspects, such as the encapsulation of single atoms (1) or the chemical isolation of free electron spins (2; 3). Experiments with endofullerenes on surfaces are demanding since they ask for quantities of purified material in the micromol range, and a deposition procedure that does not affect the endohedral configuration. Recently, an organic reaction scheme, which involves the opening, filling and closing of the C_{60} cage by chemical means, was demonstrated for H_2 in C_{60}. Nuclear magnetic resonance showed H_2 to be inside the cage with a thermal stability up to 770 K (4). A hydrogen molecule inside C_{60} (Fig. 10.11) represents the simplest fullerene system housing a molecule. The volume available inside the cage corresponds to a nominal hydrogen pressure of about 1 kbar at room temperature. It is a relatively simple molecular system, though with some electronic overlap between the host and the guest molecule. Furthermore, little is known about how the peculiar spin statistics of the two protons, which dictates via the Pauli principle the population of the rotational states of H_2, is affected by the cage. Before all these interesting questions can be addressed, hydrogen represents a real challenge to be detected at all. If it can

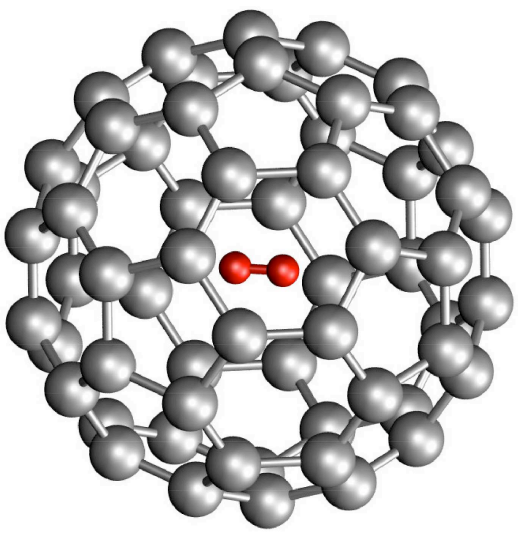

Figure 10.11:
Stick and ball model of H_2 in C_{60} (H_2@C_{60}).

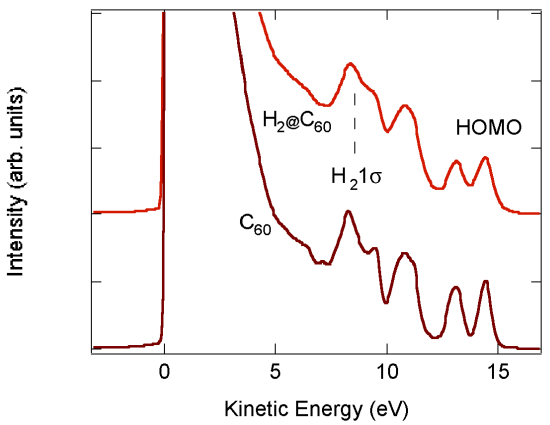

Figure 10.12: Comparison of He Iα normal emission spectra of multilayers of C_{60} and H_2@C_{60} on Al (111) recorded at room temperature. The position of the H_2 1σ molecular orbital as determined by DFT and aligned to the experimental highest occupied molecular orbital (HOMO) position is indicated as well.

be observed by photoemission, this system will give the opportunity to study issues like electron correlations and coherence in the photoemission process.

In Fig. 10.12 the photoemission spectra of multilayers of C_{60} and of $H_2@C_{60}$ are compared. The inclusion of hydrogen results in spectra similar to those of pristine C_{60}, though they are slightly less sharp. The position of the H_2 1σ molecular orbital as determined by density functional theory (DFT) for a $H_2@C_{60}$ is marked; it lies 2.76 eV above the H_2 ionisation threshold in the gas phase. This indicates that the C_{60} cage screens the H_2 1σ hole efficiently. In contrast to photoemission experiments on H_2 in the gas phase (5), no sharp H_2 1σ emission line is observed in the spectra from the endofullerenes.

[1] M. Saunders, R.J. Cross, H.A. JimŐnez-Vazquez, R. Shimshi, A. Khong, Science, **271**, 1693 (1996).

[2] T. Almeida Murphy, Th. Pawlik, A. Weidinger, M. Höhne, R. Alcala and J.-M. Spaeth, Phys. Rev. Lett. **77**, 1075 (1996).

[3] S. Yang, L. Dunsch, Chem. Eur. J. **12**, 413 (2006).

[4] K. Komatsu, M. Murata, Y. Murata, Science, **307**, 238 (2005).

[5] D.W. Turner, Phil. Trans. of the Royal Soc. of London, Series A, **268**, 7 (1970).

10.8 Test of a new electron detection scheme for Mott polarimeters

In collaboration with: Vladimir N. Petrov, St. Petersburg Technical University, Russia, and P. Robmann, Physik-Institut, Universität Zürich.

Mott polarimeters are the most widely used measurement devices to determine the electron spin polarization in photoemission experiments or in scanning electron microscopy with polarization analysis (SEMPA). These detectors exploit the left-right asymmetry in the backscattering of electrons due to spin-orbit interaction, typically from a gold foil target at electron energies of 20-100 keV. An example for an instrument using Mott detectors is COPHEE, the COmplete PHotoEmission Experiment, which has been designed and built by our group and which is now located at the Swiss Light Source. It combines angle-resolved photoemission and three-dimensional spin polarimetry by using two Mott detectors simultaneously in an orthogonal configuration (1).

The electron spin is an important but hitherto neglected degree of freedom also in molecular films on surfaces. With the purpose to implement spin resolution also in the photoelectron spectrometer in our Zürich laboratory, which offers a range of techniques for the preparation and for the characterization of molecular films, a new Mott polarimeter needs to be designed due to geometrical constraints in the existing electron analyzer. At the same time a considerable simplification of the traditional detection scheme in such detectors is attempted. The goal is to count the backscattered electrons via scintillation and to increase the maximum count rate (2). In our new design, the light pulses from the scintillators are guided through glass rods to photomultipliers outside the vacuum chamber. Therefore, the detection electronics do not need to be placed inside ultrahigh vacuum, and it can be operated at ground potential. The first tests of this detection scheme were successful. We have measured, via our light guide system, the light produced in scintillating crystals upon irradiation with electrons of energies ranging from 5 to 40 keV. A typical measurement is shown in Fig. 10.13. The resulting light yield is sufficient for a reasonable energy resolution and for noise separation at energies as low as 25 keV.

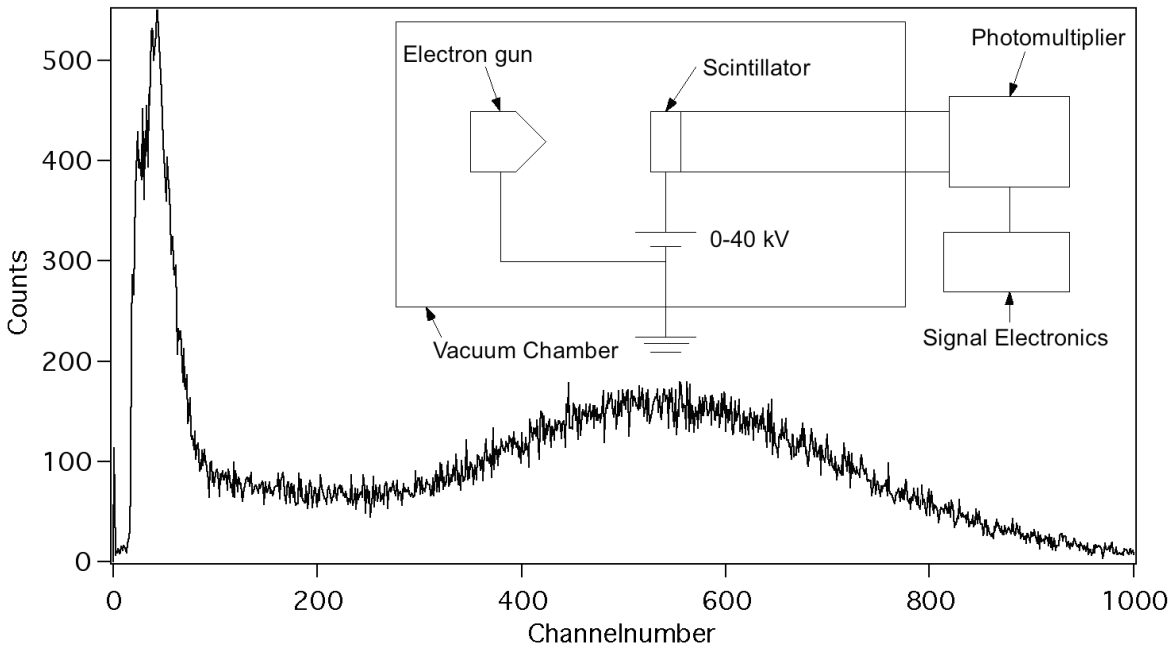

Figure 10.13: Pulse-height spectrum from the scintillator under excitation with 25 keV electrons measured with a photomultiplier. The signal due to the high-energy electrons peaks at channel 530 and is clearly separated from the contribution of single photons around channel 40. In the inset the measurement setup is shown schematically.

[1] Moritz Hoesch, PhD Thesis, Universität Zürich, 2002.

[2] V.N. Petrov, V.V. Grebenshikov, A.N. Andronov, P.G. Gabdullin, A.V. Maslevtcov, Rev. Sci. Instr. **78**, 025102 (2007).

11 Physics of Biological Systems

C. Andreoli, C. Escher, H.-W. Fink, M. Krüger (until October 06), Tatiana Latychevskaia, H. Okamoto (until October 06), Elvira Steinwand (since December 06), G. Stevens (until October 06)

in collaboration with: Jevgeni Ermantraut, Clondiag Chip Technologies (Germany); Dr. Pierre Sudraud, Orsay Physics (France); Prof. John Miao, University of California at Los Angeles (USA); Prof. Dieter Pohl, University of Basel; Prof. Andreas Plückthun, Dr. Peter Lindner, Biochemistry Institute, University of Zurich; Prof. Joachim M. Buhmann, Institute for Computational Science, ETH Zurich; Prof. Bettina Böttcher, European Institute of Molecular Biology (EMBL), Heidelberg; Prof. Andre Geim, Manchester Centre for Mesoscience & Nanotechnology, University of Manchester.

We intent to develop holography with low energy electrons into a tool for structural biology on the single molecule level. Last year we have been able to achieve some milestones towards this goal. One of the realized steps is finding of a solution to the twin image problem. Since the invention of holography by Denis Gabor more that 50 years ago, it has been the general believe that the twin image problem is an intrinsic limitation of Gabor holography. The apparently unavoidable presence of the conjugated image obscures the information extracted from a holographic record. Despite this general belive we invented a numerical algorithm to remove the effect of this conjugated image and are now able to generate twin-image free hologram reconstructions of both amplitude and phase objects. On the experimental side, an improved detector system for low energy electrons allows to record holograms of DNA molecules with total currents less than 1 nA from the point source and 20 ms acquisition time at the hologram detector. This leads to higher interference resolution in electron holograms. Some of our holography work, that of imaging single proteins, has now been embedded into a European NEST (*New Emerging Science and Technologies*) ADVENTURE European programme with our group being the leading partner within a European consortium. Our studies on the energetics of individual DNA molecules have been extended to the investigation of diffusion of individual molecules in the liquid. Temperature dependent experiments of DNA as well as of latex spheres of comparable mass reveal diffusion coefficients as well as activation barriers for diffusion. It turns out that the DNA diffusion coefficient is much less than that of a comparable stiff object of similar mass, while both objects exhibit similar values for the diffusion barrier.

11.1 Holography of single molecules

11.1.1 Solution to the twin image problem[1]

Holography, since its invention by Dennis Gabor (2), has been troubled by the so-called twin image problem limiting the information that can be obtained from a holographic record. Due to symmetry reasons there are always two images appearing in the reconstruction of a hologram and the unwanted out of focus twin image obscures the object. The problem of the twin images is especially pronounced for emission electron as well as for x- and gamma-ray holography, where the source-object distances are small, and the reconstructed images of atoms are very close to their twin images from which they can hardly be distinguished.

The most widely employed approach to address the twin image problem is to record a set of holograms at different wavelengths

(3; 4). However, this method only suppresses but does not eliminate the twin image and is experimentally difficult to implement in particular when it comes to record fragile biological molecules subject to radiation damage. Most of the known numerical reconstruction routines reconstruct either absorbing or phase shifting properties of the recorded objects (5; 6; 7; 8; 9; 10). We show how the two distributions can be reconstructed simultaneously. This is achieved by the presentation of the transmission function in the object plane as $(1 - a(r_{obj})) \exp(-i\varphi(r_{obj}))$, where $a(r_{obj})$ defines the absorbing properties of the object and $\varphi(r_{obj})$ the phase shift introduced by the object with respect to the incident wave. On the other hand, the transmission function in the object plane can be written as $1 + t(r_{obj})$, where 1 corresponds to the transmittance in the absence of the object, and $t(r_{obj})$ is a complex function describing the presence of the object, so:

$$(1 - a(r_{obj})) \exp(-i\varphi(r_{obj})) = 1 + t(r_{obj}) \ . \quad (11.5)$$

Writing the transmission function as $1 + t(r_{obj})$ helps to identify the part of the incident beam which passes the object un-scattered, thus forming the reference wave on the screen $R(r_s)$. The part of the beam scattered by the object gives rise to the object wave on the screen $O(r_s)$. The recorded hologram is reconstructed numerically by multiplication with the simulated reference wave and further backward propagation of the field to the object plane, where the absorption and phase parts can be separated from the transmission function.

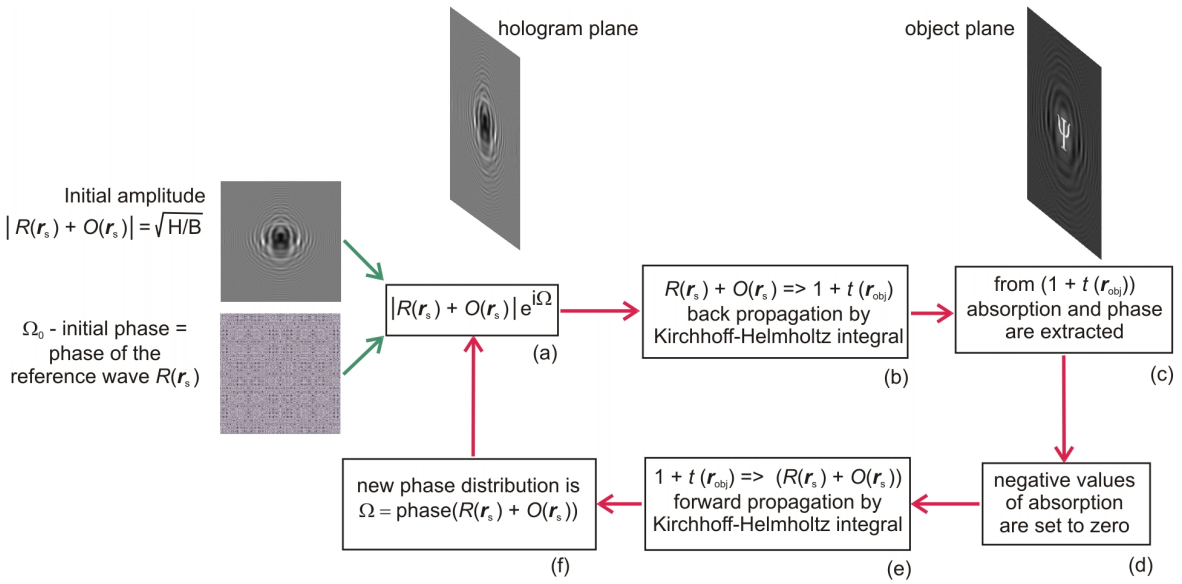

Figure 11.1: Iterative scheme of hologram reconstruction. The amplitude of the complex field in the screen plane is always set as magnitude of the hologram image H divided by the background image B; the initial phase is set to the phase of the reference wave and is iteratively retrieved.
(a) The Complex field in the screen plane is formed.
(b) The field is back propagated to the object plane.
(c) Absorption and phase properties of the object function are extracted.
(d) Negative values of absorption are set to zero.
(e) The field from the updated object function is forward propagated to the hologram plane.
(f) The phase of the propagated field is adopted for step (a) in the next iteration.

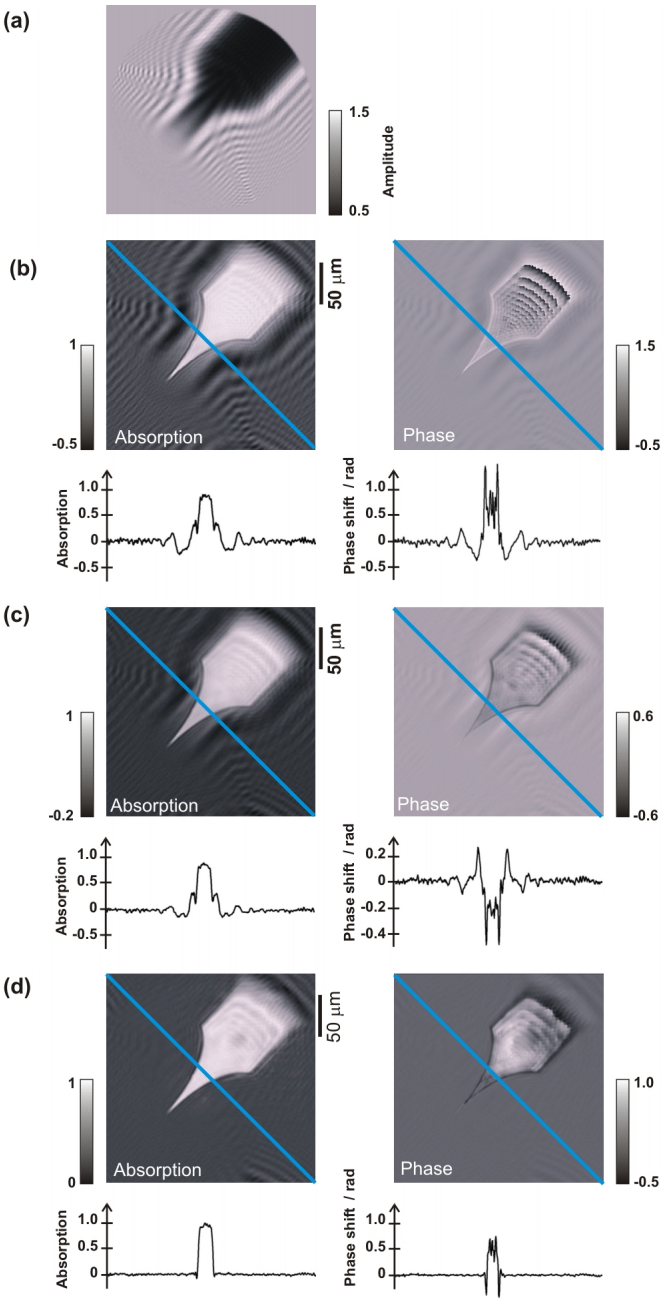

Moreover, we use a filter, which is applied to the reconstructed absorption distribution and sets all negative values to zero. The basic physical notion behind this is the principle of energy conservation. Since negative absorption values would correspond to increased amplitude following a scattering process, we suppress them by replacing them with zeros. Using this filter in an iterative process, shown in Fig. 11.1, the truthful amplitude and phase distributions of the object are retrieved, and the twin image disappears.

Twin-image free reconstructions of simulated and experimental holograms have been obtained for both, strongly absorbing objects, like a metal tip, see Fig. 11.2, as well as for weak scattering, mainly phase shifting objects, like micron sized latex spheres on a glass substrate, see Fig. 11.3.

Our algorithm of reconstructing a hologram completely free of the twin image disturbances is general; no assumptions about the object need to be imposed. Objects can be of arbitrary shape, exhibiting absorbing and/or phase shifting properties. Moreover, the method can be applied to any type of holography independent of the wavelength used and the nature of the wave, be it visible light, x-rays, electrons or any other coherent radiation.

Figure 11.2: Iteratively reconstructed experimental optical hologram of a tungsten tip etched from a 0.1 mm diameter wire.
(a) Normalized hologram.
(b) Reconstructed absorption and phase distributions by conventional reconstruction.
(c) Reconstructed absorption and phase distributions after the first iteration. The oscillations due to the twin image are apparent.
(d) Reconstructed amplitude and phase distributions after 500 iterations.
Below each reconstruction the intensity distributions along the blue lines are displayed. A round cosine window filter was applied to the hologram to avoid artefacts from edges while Fourier-transforming.

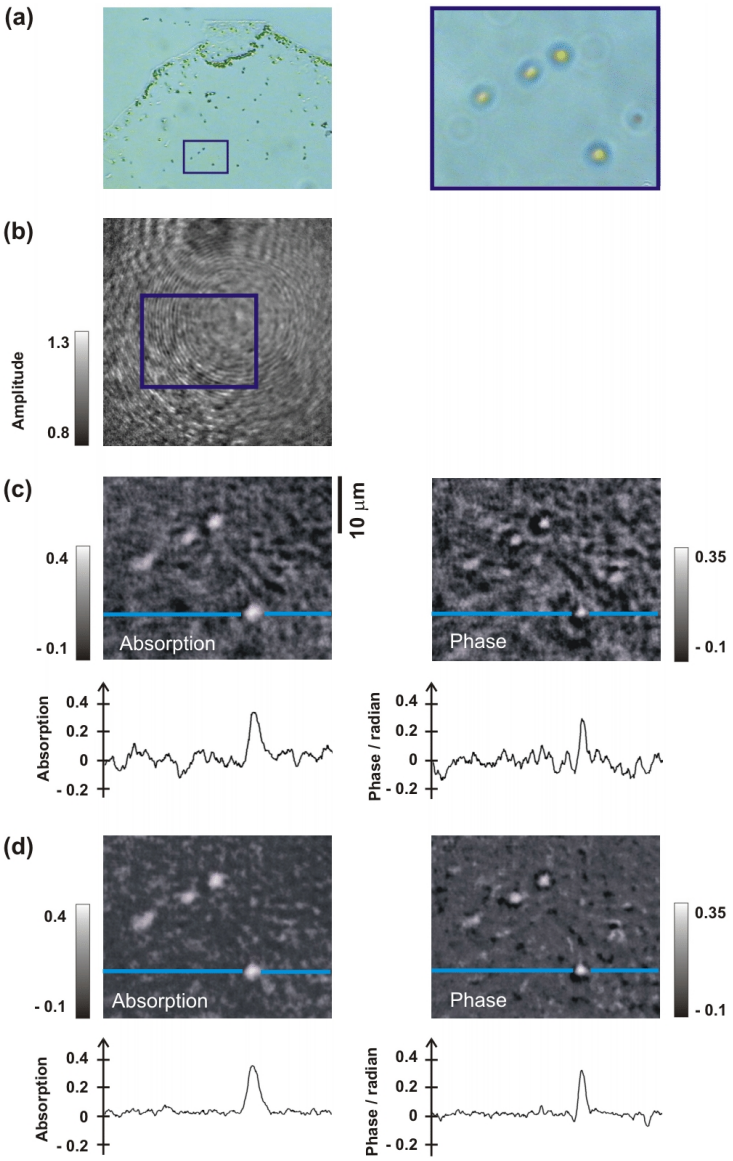

Figure 11.3: Iteratively reconstructed experimental optical hologram of latex spheres of 1 micrometer in diameter.
(a) Conventional optical micrograph of latex spheres deposited onto a glass coverslip. The area marked in blue and magnified at the right was subject to the divergent laser beam to generate the holograms.
(b) Normalized hologram.
(c) Reconstructed absorption and phase distributions by conventional reconstruction.
(d) Reconstructed amplitude and phase distributions after 500 iterations. The phase shifting properties of the spheres are recovered iteratively.
Below each reconstruction the intensity distributions along the blue lines are displayed.

[1] T. Latychevskaia and H.-W. Fink, Solution to the Twin Image Problem in Holography, Phys.Rev.Lett., in press.
[2] D. Gabor Nature, 161 (1948) 777-778.
[3] S. Y. Tong, H. Hua Li, and H. Huang, Phys.Rev.Lett.67, 3102 (1991).
[4] J. J. Barton, Phys.Rev.Lett.67, 3106 (1991).
[5] K. A. Nugent, Opt. Comm. 78, 293 (1990).
[6] G. Liu and P. D. Scott, J. Opt. Soc. Am. 4, 159 (1987).
[7] L. Onural and P. D. Scott, Opt. Eng. 28, 1124 (1987).
[8] X. M. H. Huang, J. M. Zuo, and J. C. H. Spence, Appl. Surf. Sci. 148, 229 (1999).
[9] J. F. Arocena, T. A. Rotwell, and M. R. A. Shegelski, Micron 36, 23 (2005).
[10] A. L. Bleloch, A. Howie, and E. M. James, Appl. Surf. Sci. 111, 180 (1997).

11.1.2 DNA holography, radiation damage

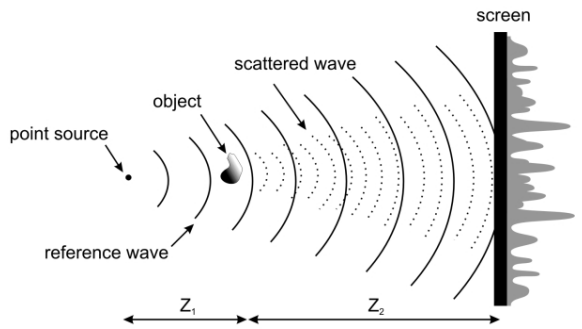

Figure 11.4: Schematic diagram of a LEEPS Microscope: A sharp W-tip acts as a field emitting electron point source of coherent spherical electron waves (20-300 eV). The sample is typically a few microns away from the point source. An electron hologram is formed on a screen located at a macroscopic distance from the specimen by the interference of a scattered electron wave (dotted line) and un-scattered reference electron wave.

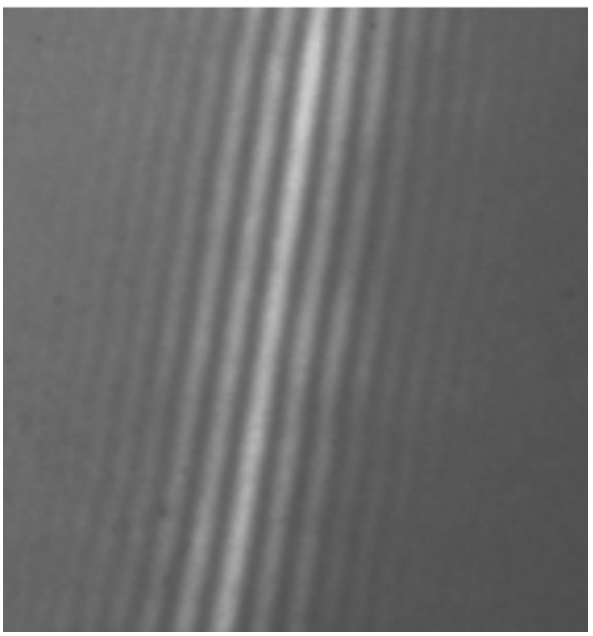

Figure 11.5: A hologram of a multi-walled carbon nanotube (MWNT) is shown at the right part. The MWNT is lying across a micron-sized hole so that the reference wave can pass by the specimen undisturbed.

The basic setup of a (LEEPS) microscope is shown schematically in Fig. 11.4. In this lens-less microscope, images of molecules are obtained by placing them near a point source of coherent electrons in vacuum so that a divergent beam passes by the molecule onto a detector screen located some distance away where a $10^5 - 10^6$ times magnified image is observed. This is precisely the set-up envisioned by Gabor, the inventor of the principle of holography. A hologram as shown in Fig. 11.5 is then created by the interference between object- and reference wave. In contrast to diffraction techniques, like x-ray crystallography in which the phase information is a priori unknown, holograms contain all the phase and amplitude information necessary to reconstruct the original object in three dimensions. Reconstructions are obtained by applying the Kirchhoff-Helmholtz transform to the hologram. Experimental holograms of filamentous macromolecules such as DNA (1) and phthalocyanine polysiloxane (PcPS) (2) have been obtained at electron energies of 50 eV and 70 eV respectively and images of single DNA and PcPS macromolecules were reconstructed from the holograms at a resolution of approximately 2 nm. No observable electron beam damage occurred to the molecules at these energies.

A vital aspect is the need to observe a single molecule for a sufficiently long time to acquire a high resolution hologram but without causing radiation damage. Preliminary experiments with single DNA molecules clearly indicate that there are energy ranges at which neither inelastic scattering nor radiation damage is detectable. Evidence for that is provided in Fig. 11.6 in which a DNA molecule is shown after continuous exposure to low energy electrons for more than 1 hour.

[1] H.-W. Fink, H. Schmid, E. Ermantraut, T. Schulz, J. Opt. Soc. Am. A, 14 (1997) 2168.

[2] A. Gölzhäuser et al., J. Vac. Sci. Technol. A, 16 (1998) 3025.

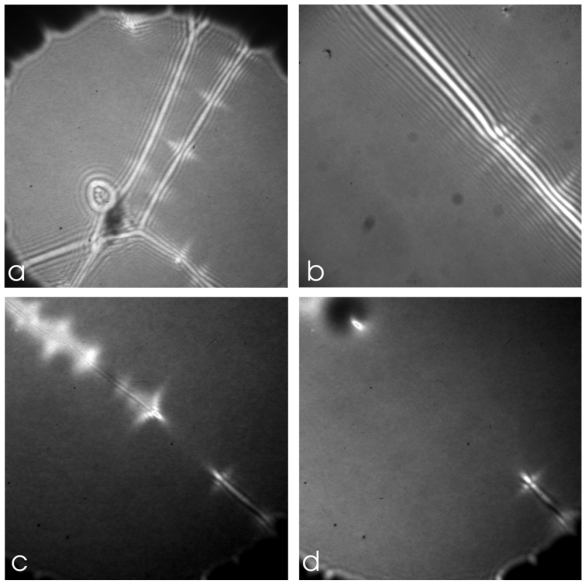

Figure 11.6:
a: Low energy electron hologram of DNA molecules stretched over holes in a thin carbon film.
b: This individual DNA molecule has been imaged and observed for more than one hour being subject to radiation with electrons of energies around 100 eV. No indication for radiation damage occurred.
c: At higher kinetic energies, above 250 eV, radiation damage is apparent.
d: After a few minutes of continuous observation with electrons above 260 eV energy, the DNA strand is found to be decomposed.

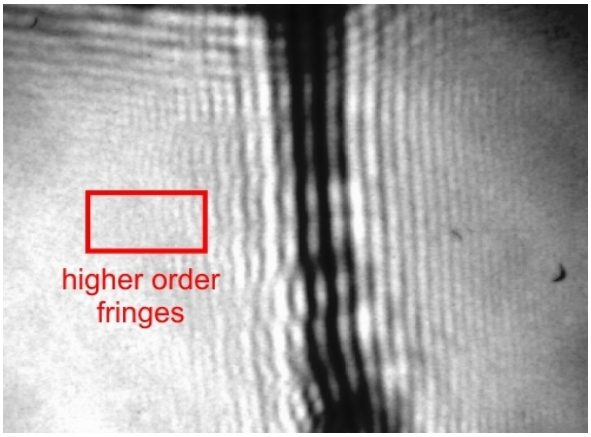

Figure 11.7: A typical noisy experimental electron hologram of a carbon nanotube.

[9]Diploma thesis of Igor Beati

11.1.3 Numerical de-noising of holograms[9]

in collaboration with:
Joachim M. Buhmann, Institute for Computational Science, ETH Zurich.

The holograms recorded with a CCD camera, can be reconstructed numerically by back propagation of the field distribution. The result is a three-dimensional structure monitored on a computer screen. The wavelength of the electron beam (0.1-1 Å) provides sub-nm resolution of the reconstructed objects. One of the problems of numerical reconstruction is associated with the elimination of statistical noise from the holograms. To achieve atomic resolution, higher order interference fringes in holography must be distinguished from noise, see Fig. 11.7. Therefore a numerical pattern recognition routine was developed.

Several de-noising filters were tested:

- Diffusion filter
- Wiener filter
- Median filter
- Wavelets-based filters
- Countourlets based filters
- Coefficients shrinkage-based filters
- Principal components analysis (PCA)-based filter

First, the filters were applied to simulated holograms with superimposed Gaussian noise. The filtered holograms were then compared to simulated noise-free holograms.

As a measure of quality, the peak signal-to-noise ratio (PSNR) has been taken into account. The PSNR is expressed in decibels and it is defined as follows:

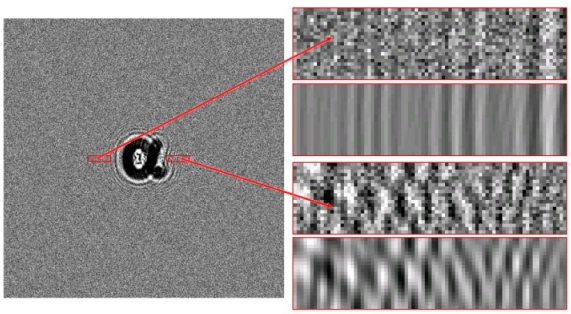

Figure 11.8: Simulated noisy holograms of the letter α (left). On the right side selected areas are shown with (red arrows) and without noise.

$$\mathrm{PSNR} \equiv 10 \times \log \frac{(max(H_0))^2}{MSE} \quad ,$$

where H_0 is the noise-free holographic image, $max(H_0)$ is the maximum pixel value of the image, MSE is the mean squared error of the image defined as

$$MSE \equiv \frac{1}{mn} \sum_{i=0}^{m-1} \sum_{j=0}^{n-1} \|H(i,j) - H_0(i,j)\|^2$$

where H is the noisy holographic image and H_0 is the noise-free holographic image.

Noise-free and noisy holograms of the letter α were simulated and two areas were selected for qualitative analysis, see Fig.11.8.

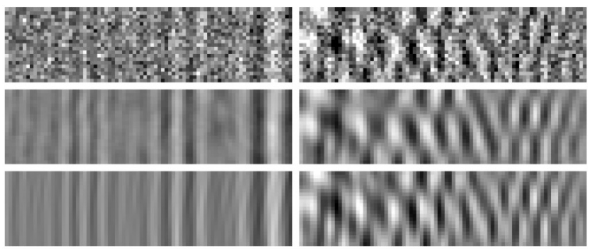

Figure 11.9:
Results of PCA filtering of a noisy hologram. From top to bottom: noisy, de-noised and noise-free.

The best results achieved with the PCA filter are shown in Fig.11.9.

Having defined the most appropriate filter, it was applied to an experimental optical hologram of a phase object, i.e. the letter Ψ engraved in a glass plate. The hologram before and after the de-noising procedure is shown in Fig. 11.10. A significant improvement in terms of identification of individual fringes can be seen on the detail of the hologram.

Fig. 11.11 shows the phase reconstruction. In some regions of the reconstruction of the non-filtered hologram it is impossible to distinguish signal from noise; e.g. regions marked with rectangles A and C. From the reconstruction of the filtered hologram it becomes obvious that the pattern in region A is to be associated with noise, whereas the pattern in region C is to be associated with signal (from the twin image).

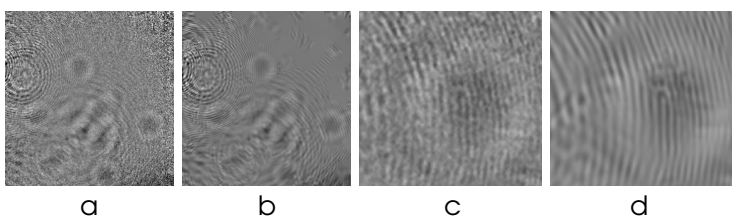

Figure 11.10: Experimental optical hologram of a phase object; a: non-filtered, b: after de-noising with the PCA filter, c and d: details of a and b, respectively.

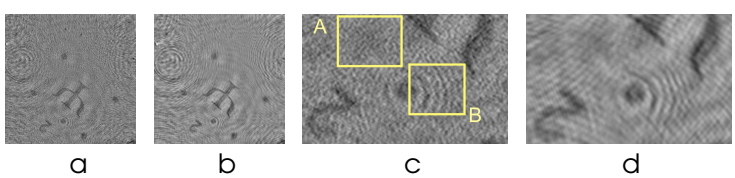

Figure 11.11: Reconstructed phase distributions of the optical hologram shown in Fig. 11.10; Labels defined as in Fig.11.10.

11.1.4 The SIBMAR project

in collaboration with: Gregory Stevens, Peter Lindner and Andreas Plückthun, Biochemistry Institute; Willem Tichelar and Bettina Böttcher, European Molecular Biology Laboratory, Heidelberg; Kostya Novoselov and Andre Geim, University of Manchester.

The main objective of the SIBMAR project is to obtain structural information about individual biological macromolecules at atomic resolution. A consortium with groups headed by Prof. Andre Geim of the University of Manchester and Dr. Bettina Böttcher of the EMBL in Heidelberg has been formed and is funded by the European commission since October 2006. The administrative lead of this project is with the Zurich Euresearch team, Jürg Brunnschweiler and Agate Keller in collaboration with Monika Röllin and Ruth Halter of the Physics Institute. Given the technological and possibly commercial interest, the founder of Clondiag Chip Technologies, Jevgeni Ermantraut, has agreed to assume the role of chairman of the scientific steering committee of SIBMAR. We envision tackling the following sub-objectives:

- An atomically thin carbon support substrate will be developed by the group of Andre Geim.
- The effects of low energy electrons on biological molecules will be studied by Bettina Böttcher's group.
- Andreas Plückthuns group will develop methodologies for preparing individual bio molecules.
- Tatiana Latychevskaia, of our group, will develop numerical reconstruction routines for recovering three-dimensional images from a set of holograms.
- Others in our group will develop a prototype LEEPS microscope for obtaining high resolution holograms.

11.2 Activation barrier for single DNA diffusion from direct measurements of the tracer diffusion coefficient[1]

Molecular transport of bio-molecules in the liquid represents a fundamental issue related to the physics of biological systems. Mobility is a pre-requisite for subsequent interaction such as recognition and binding. The quantity describing such transport in microscopic systems is the diffusion coefficient. Within the last decade, tracking the motion of single DNA molecules in the liquid has become feasible by employing fluorescence video microscopy. Here we present first direct measurements of the energetics involved in self diffusion of a single DNA molecule by observing the random motion of the molecule at different temperatures. Since a DNA molecule is a semi flexible biopolymer, it is not a priori clear how the displacement of the centre of mass actually proceeds. It seems however clear that the Brownian agitation of the solvent frequently leads to rearrangements of the molecules configuration without displacing its centre of mass significantly. For a quantitative evaluation, we have measured both, the diffusion of a stained DNA molecule as well as the diffusion of a rigid fluorescent sphere of 50 nm radius unable to undergo shape changes upon statistical collisions with the solvent. The concentrations are held sufficiently low to allow tracing an individual molecule or sphere reliably. As it turns out the DNA molecule diffuses much slower despite the fact that its mass is an order of magnitude lower than the mass of the rigid sphere; see Fig. 11.12.

According to $< x^2 >= 2Dt$, the mean square displacement reveals the diffusion coefficient. The experimental set up allows observation under thermo dynamical equilibrium conditions at different, well defined temperatures between freezing of the sample and denaturation of the DNA molecule. From the tem-

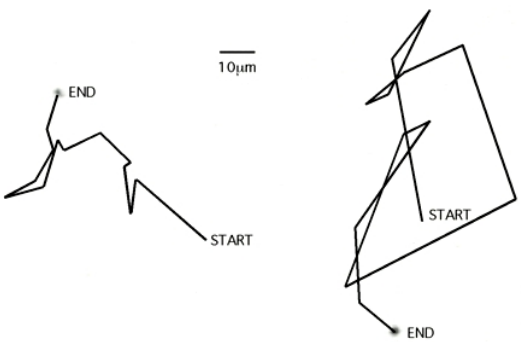

Figure 11.12: Random walk in a thin water film. Left: the displacement of the centre of mass of an individual DNA molecule is traced at time intervals of 30 s. The molecule is stained and embedded in a thin sealed water film. Only a partial sequence (13 out of 50 steps) is depicted here. Right: for comparison the displacement of a styrene sphere with a diameter of 100 nm is monitored under equal conditions.

perature dependence of the diffusion coefficient we compute the activation barrier for self diffusion for both, the DNA molecule and the styrene sphere respectively; see Fig.11.13.

At all measured temperatures we find the diffusion coefficient to be one order of magnitude bigger for the massive (but rigid) sphere than for the light (but filiform) DNA molecule.

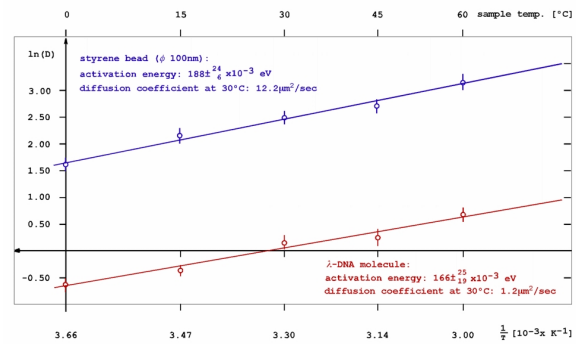

Figure 11.13: Arrhenius plot of the diffusion coefficient. In red: the diffusion coefficient of a single DNA molecule; in blue: the diffusion coefficient of a 50 nm radius styrene sphere at various temperatures. The activation energy for self diffusion is derived from the slope of the linear fit to the data.

However, the activation energy involved in self diffusion is - within the errors - found to be the same for the molecule and the sphere and therefore might have to be assigned solely to the characteristics of the embedding solvent.

[1] Zupfen am Lebensfaden: Experiment mit einzelnen DNS Molekülen, Conrad Escher und Hans-Werner Fink, Physik in unserer Zeit, Heft 4 (2007).

11.3 Coherent low-energy electron diffraction microscopy of single biomolecules

in collaboration with: John Miao, University of California at Los Angeles

This project started in October 2006. The objective is to demonstrate a technique for recording oversampled coherent low-energy electron diffraction patterns of individual biological molecules. From these, the three dimensional structure of the molecule can be recovered at a resolution of 2Å, which is sufficient to show the location of individual atoms in the molecule. The principle of phase retrieval by oversampling, pioneered by J. Miao, D. Sayre, and H.N. Chapman, in which unique phase information about the wave front is recovered from a diffraction pattern, has already been demonstrated experimentally using x-rays and high-energy electrons. However, even with the free electron lasers, currently under construction, averaging over 10^6 molecules is necessary due to the dominating inelastic scattering of x-rays.

The novel aspect of this project is to use low-energy electrons to obtain the diffraction pattern of a single molecule. In contrast to high-energy electrons and x-rays, electrons with energies below 200 eV do not appear to

damage individual biological molecules since elastic scattering dominates.

Experimentally, diffraction patterns will be obtained by using coherent low-energy electrons passing by a single freestanding biological molecule positioned across a hole of a few 10 nm in diameter. Therefore, a parallel coherent electron beam must be formed and directed towards the molecule. The fine structure of the resulting coherent diffraction pattern must be recorded with high detector resolution to fulfil the oversampling criteria. For recovering the 3-dimensional structure of the molecule at atomic resolution, rotation of the molecule needs to be implemented for recording 3-dimensional diffraction patterns.

The main goal of the project will be accomplished following a clearly laid out plan of experimental work. Specific tasks are:

- To develop an electrostatic micro-lens for creating a parallel electron beam and maintaining a high degree of coherence.
- To develop a methodology for preparing single bio molecules so that they extend out into holes exhibiting diameters of a few 10 nm.
- To design and build a diffraction microscope with a dedicated detector system optimised for obtaining oversampled diffraction patterns.

If successful, this technique has the potential to be used for obtaining structural information about all biological molecules, rather than a small subset that is currently accessible by x-ray crystallography or NMR spectroscopy.

11.3.1 The over sampling method

J. Miao, D. Sayre, and H.N. Chapman (1) have shown that, provided a diffraction pattern is sampled on a sufficiently fine grid and the surrounding of the molecule is known, an iterative procedure allows recovering the phase information and with this the structure of the molecule. Miao et al. demonstrated that the phase retrieval algorithm converges after a couple of thousand iterations. Below, some details of the method are given.

An object can be described by a three-dimensional complex electron density function. The amplitude of this function describes the object's absorption properties and the phase of this function expresses the phase shift introduced by the object due to elastic scattering of the incident wave. For a non-crystalline sample the diffraction intensity in the far-field forms a continuous pattern. If the pattern is sampled with the Nyquist frequency (inverse of the size of the specimen) N it can be expressed as the amplitude of the Fourier-transform of the object electron density function (2).

$$
\begin{aligned}
&\mid F(k_x, k_y, k_z) \mid = \\
&= \mid \sum_{x=0}^{N-1} \sum_{y=0}^{N-1} \sum_{z=0}^{N-1} \rho(x,y,z) e^{2\pi i (k_x + k_y + k_z)/N} \mid \\
&k_x, k_y, k_z = 0, \ldots, N-1 \; .
\end{aligned}
$$

Each pixel of the diffraction pattern is expressed by a Fourier transform through all the unknown values of the object electron density values, which gives rise to a set of equations. When the object electron density function $\rho(x,y,z)$ is complex, then the number of equations is N^3, while the number of unknowns is $2N^3$, for the real and the imaginary part. When $\rho(x,y,z)$ is real the number of equations is $N^3/2$, due to the symmetry of the diffraction pattern. For a unique solution, the number of equations should be equal to the number of unknowns which can be achieved by chosing the sampling number of pixels in the diffraction pattern M^3 with $M = \sqrt[3]{2}N$.

Sampling the diffraction pattern with a larger number of pixels ($M > \sqrt[3]{2}N$) is equivalent to surrounding the object function with zero values. The following parameter is introduced to characterize the degree of oversampling:

$$\sigma = 2\,\frac{\text{volume of } e^{-}\text{density} + \text{volume with } 0'\text{s}}{\text{volume of } e^{-}\text{density}}$$

The condition is than replaced by $M = \mathcal{O}\mathcal{N}$ where $\mathcal{O} = \sqrt[3]{\sigma}$ (3).

The iterative reconstruction procedure (4) includes the following steps, also illustrated in Fig. 11.14:

- The measured magnitude of the diffraction pattern and an arbitrary guessed phase set (random phase set for initial set $(-\pi;\pi)$) are combined.

- An inverse Fourier transform is applied to the combined set and a complex object electron density function is obtained.

- The value of pixels in the area that is expected to be occupied by the object electron density function (S), defined according to the value of σ, are adjusted so that the negative values of the real or imaginary part are set to zero. The values of pixels located outside this area (regions S_1 and S_2) where there should be no object electron density are gradually set to zero according to:

$$\begin{aligned}\rho_{j+1}(x) &= \rho_j(x) - \beta_1\rho'_j(x)\,, \quad x \in S_1\\ &= \rho_j(x) - \beta_2\rho'_j(x)\,, \quad x \in S_2\end{aligned}$$

  Such asymmetrical constraint speeds up the convergence of the algorithm. A forward Fourier transform is applied, and the phase distribution of the obtained result is set as an actualized phase set for step one of the procedure.

At the end of this procedure, two complex fields are obtained: an object electron density and the field distribution in the far-field, which are mutual Fourier transforms of each other. The higher the value of σ the faster the algorithm converges.

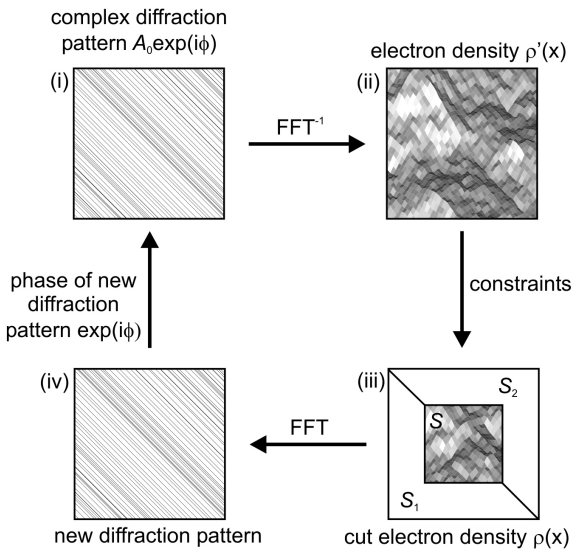

Figure 11.14: An illustration of the iterative reconstruction procedure.
(i) Complex diffraction pattern, where A_0 is the magnitude of the measured diffraction pattern. The phase for the initial phase is randomly distributed.
(ii) By FFT^{-1} the complex electron density is obtained.
(iii) The values surrounding the central part are set to zero.
(iv) FFT gives a new diffraction pattern, whose phase $\exp(i\phi)$ is set as new phase for step (i) [5].

[1] J. Miao, D. Sayre, and H.N. Chapman, J. Opt. Soc. Am. A 16(6) (1998) 1662.
[2] J. Miao, K.O. Hodgson, and D. Sayre, PNAS 98 (2001) 6641.
[3] J. Miao, T. Ishikawa, E.H. Anderson and K.O. Hodgson, Phys. Rev. B 67 (2003) 174104.
[4] J. Miao, D. Sayre, and H.N. Chapman, J. Opt. Soc. Am. A 16(6) (1998) 1662.
[5] J. Miao, D. Sayre, Acta Cryst. A. 56 (2000) 596.

11.3.2 Micro-Lens

An essential experimental aspect is to develop an electrostatic micro lens for generating a parallel electron beam that preserves the spatial coherence of the electron point source beam. A micro lens is required for use with low-energy electrons since the lens aberrations scale with the dimensions of the lens. To maintain coherence, lens aberrations should be several orders of magnitude less than for conventional macroscopic lens. The specifications of the beam are mentioned below. Initial testing of the lens will be done in a LEEPS microscope so that this work can begin while a purpose built low-energy electron microscope is being designed.

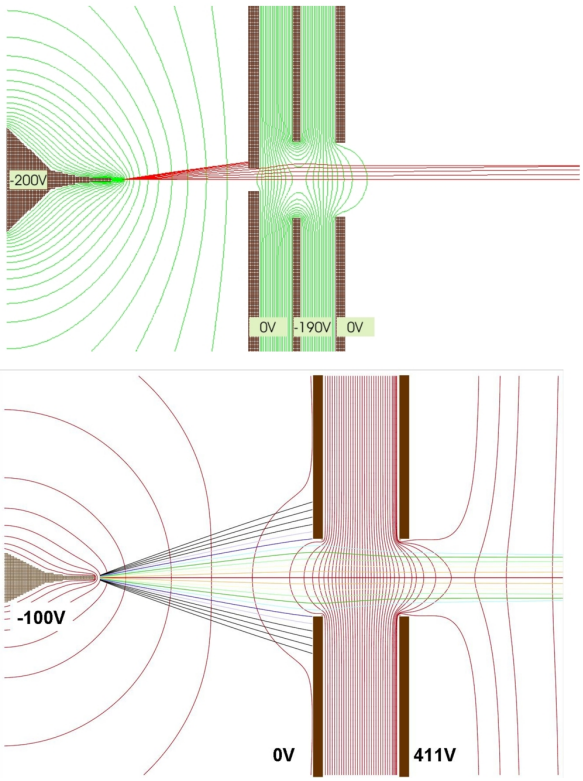

Figure 11.15: SIMION simulation of electron trajectories for an electrostatic lens used to form a parallel beam out of the coherent spherical wave originating from an atomic point source. Top: Einzel lens. Bottom: Two-electrode lens.

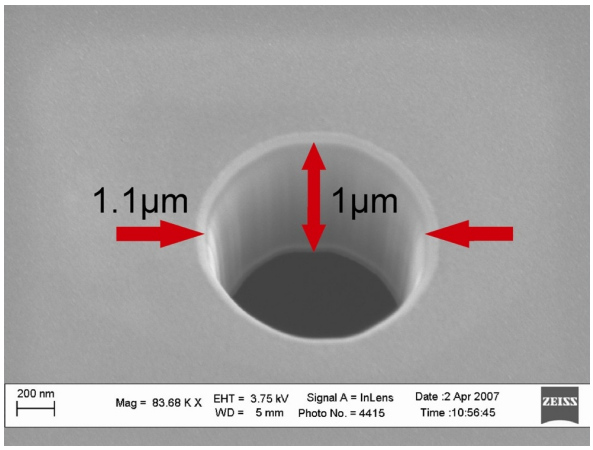

Figure 11.16: SEM image of a micrometer hole in a silicon nitride membrane of 1 μm thickness milled with the FIB. The membrane is covered with Pt layers on both sides.

The lens will be designed with the aid of the ray-tracing software SIMION, which will be used for simulating trajectories of electrons within the microscope. An example of such a simulation for a preliminary lens design is shown in Fig.11.15.

To simplify matters a first lens design is based on a two-electrode architecture as shown in Fig. 11.15 (on the botom). It can be made out of a commercially available silicon-nitride membrane, which constitutes an insulating layer. Two conducting layers evaporated on both sides of the membrane form the electrodes. The aperture in the center of the membrane can be structured using a FIB instrument. Figure 11.16 shows such a micrometer hole in a silicon-nitride membrane covered with a platinum layer of about 30 nm on both sides.

11.3.3 Overall system design

The overall system consist of a fixed mounted micro-lens while the electron point source as well as the sample can be manipulated with nm precision to align the three optical elements. The detector consists of a channel

plate - fibre optic plate assembly to transfers the image directly to a high resolution CCD chip. The system shall also be equipped with a secondary electron detector, both for initial alignment of the source with the micron sized first lens aperture and for testing the optical properties of the lens by scanning the focussed beam over a test structure.

11.3.4 Numerical recovery of the molecular structure from diffraction data

Initially, a 2-dimensional image of a bio molecule will be recovered from a single 2-dimensional diffraction pattern. This will be done in collaboration with Prof. J. Miao at the UCLA who will be in Zurich for regular meetings and updates. Dr. Tatiana Latychevskaia, who is responsible in our group for developing the numerical reconstruction software for LEEPS microscopy will also be involved with this aspect of the work. The quality of the reconstructed images will provide feedback about the experimental conditions used to obtain the diffraction pattern and show how the quality of the patterns might be improved.

Ultimately, a set of 2-dimensional diffraction patterns of a molecule will be obtained from a range of angles. This set will then be assembled into a single 3-dimensional diffraction pattern from which the 3-dimensional electron density map of the molecule will be recovered.

11.4 Bachelor studies

Alice Kohli, under the supervision of Gregory Stevens, Conrad Escher and Hans-Werner Fink, has studied in her Bachelor thesis the influence of various environmental conditions on the light emission of the Green Fluorescent Protein (GFP). It has turned out that GFP emits photons even under vacuum conditions provided the molecules are cooled down to liquid nitrogen temperatures.

In relation to our recent invention of a solid electrolyte ion source (1) Matthias Germann, under the supervision of Conrad Escher, Cornel Andreoli and Hans-Werner Fink, has studied the silver ion transport in thin wires of amorphous (AgI)(AgPO3) which is a solid electrolyte. It has been possible to fabricate and electrically characterize thin electrolyte wires. Observations in the Scanning Electron Microscope have also been carried out and showed the formation of bulk silver at the negative pole at which the wire has been contacted by a carbon electrode.

[1] C. Escher, S. Thomann, C. Andreoli, H.-W. Fink, J. Toquant and D.W. Pohl,
Appl. Phys. Lett. 89, 053513 (2006).

11.5 Education

Two physics laboratory assistant apprentices (from ETHZ) spent part of their practical education course in our lab under the guidance of Cornel Andreoli. Apart from a crucible control for the electron beam evaporator that allows automatic selection of the target material, a valve control for the SEM was built to reduce nitrogen gas wastage.

12 Mechanical Workshop

K. Bösiger, B. Lussi, R. Maier, M. Schaffner, S. Scherr, O. Fardin (apprentice) and R. Reichen (apprentice)

The modern equipment of the institute's mechanical workshop allows to fulfill almost every wish from the researchers. The numerically controlled tools are also used to produce parts for other institutes of the university. The metal and technical material store, maintained by the workshop, is used by more than 30 institutes [10]. We also give advise in technical problems, like the choice of the appropriate materials, etc. For outside companies we do construction and modification work. We also design and build prototypes and limited-lot productions. The resulting income is available for new tooling and the education and advanced training of the apprentices and the staff members.

Figure 12.1: Installation of the new milling machine.

In December 2006 we installed a milling machine with 5 axes. Three of them are simultaneously computer controlled whereas the other two are positioned at fixed values. The powerful tool changer with 16 pockets allows the automatic production of complex workpieces. The design offers a perfect solution for manufacturing almost anything from single parts to small series. The compact design with a walled enclosure and the modern ergonomics emphasize the universality of the machine which replaces a 22 years old machine.

Besides educating two apprentices the workshop staff organizes and teaches also two basic courses for the bachelor students in physics. In the first part the students learn how to use all kinds of measuring tools and how to read and produce technical drawings. They also accomplish simple work on drilling and milling machines as well as on the lathe. The course finishes with an introduction in the technique of hard soldering. In the second part more demanding machining techniques are trained. Different materials are handled and an introduction into various welding processes is given. In autumn 2006 and spring 2007 four courses of 35 hours each were arranged.

Below we list some of our main projects and activities during 2006.

[10] For a catalogue see http://www.physik.unizh.ch/groups/werkstatt/dienstleistung.html

LHCb inner tracking detector (Group Straumann, see Sec. 6)

The main part of the workshop workload was related to this project. The complete detector housings including the adjustable suspension were produced. In the middle of 2006 we produced all the custom-built electronic crates with the integrated water cooling. The complete system with the rails and the detector housings including the cooling circuits was then assembled in the institute's assembly hall. Cooling tests under realistic conditions were performed successfully. By the end of 2006 the complete system was moved to CERN and installed in the LHCb experimental hall.

Figure 12.2: Crate-cooling elements.

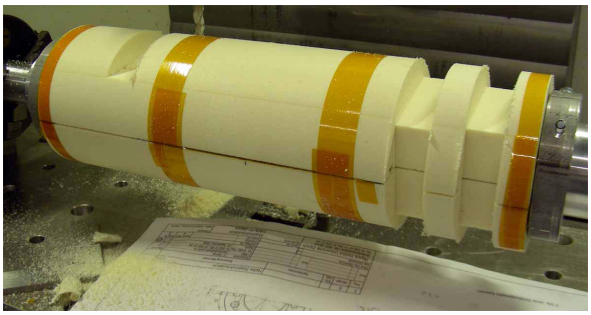

Figure 12.3: Thermal beam-pipe shielding.

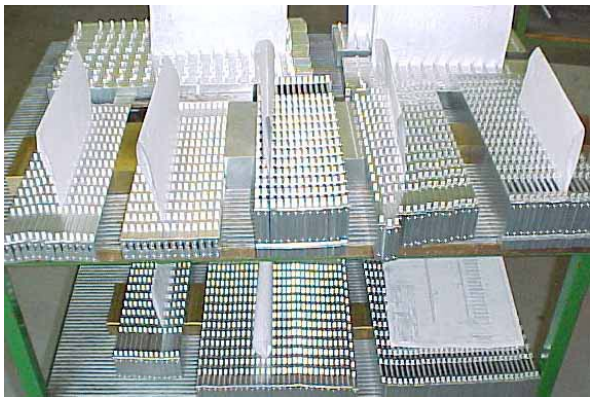

Figure 12.4: Parts of the electronic crates.

Figure 12.5: Inner tracking detector for LHCb with partially-installed silicon sensors.

CMS pixel detector
(Group Amsler, see Sec. 7)

In close collaboration with industry the laser welding process was optimized. The quality of this manufacturing process is crucial to guarantee the tightness of the detector cooling system. Missing tooling for the third detector layer was produced. At the beginning of 2007 the production of the first supply tube started. The modern milling machine installed last year was used to produce cooling fluid distributors with a complex shape made out of stainless steel.

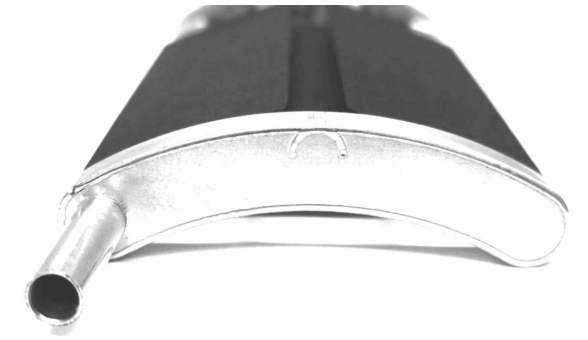

Figure 12.6: Test segment.

Figure 12.7: Mounting tool for the third detector layer.

DIRAC II
(Group Amsler, see Sec. 4)

For the DIRAC II experiment at the CERN-PS we built the housings for the Čerenkov detector.

Figure 12.8: Čerenkov-detector housings.

Surface Physics
(Group Osterwalder, see Sec. 10)

The frame for the μ-metal shielding for the COPHEE experiment installed at the swiss light source (SLS) in Villigen was designed and manufactured. A series of probe- and vacuum-deposition-holders were produced. Some apparatus were upgraded, in addition we performed maintenance and repair work.

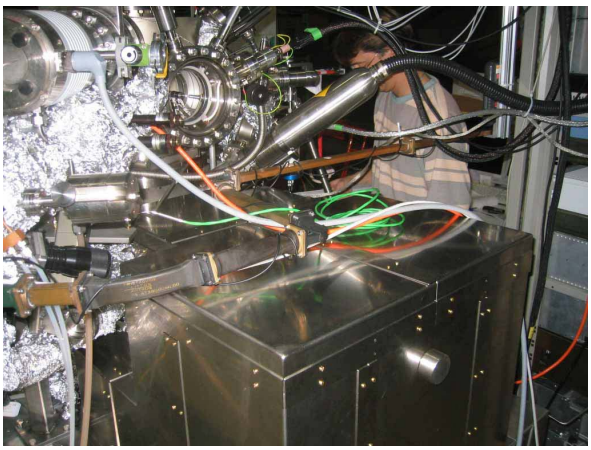

Figure 12.9: Picture of the COPHEE experiment showing the newly installed μ-metal shielding for the Mott detectors.

Figure 12.10: Probe holders made out of Molybdenum.

Physics of Biological Systems
(Group Fink, see Sec. 11)

Different mechanical infrastructure was manufactured and some test setups were built. We produced also a high temperature oven made out of ceramic material.

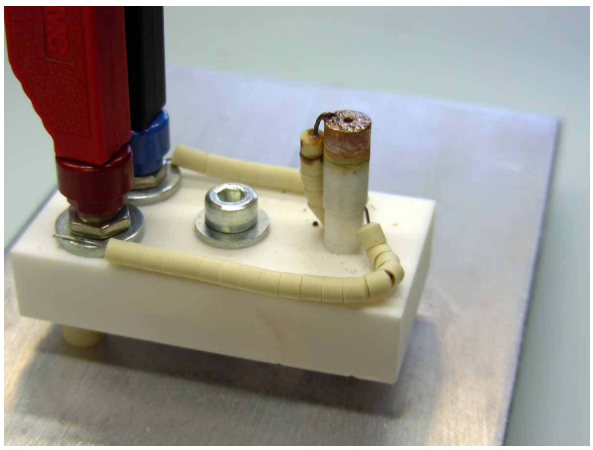

Figure 12.11: The new oven in operation.

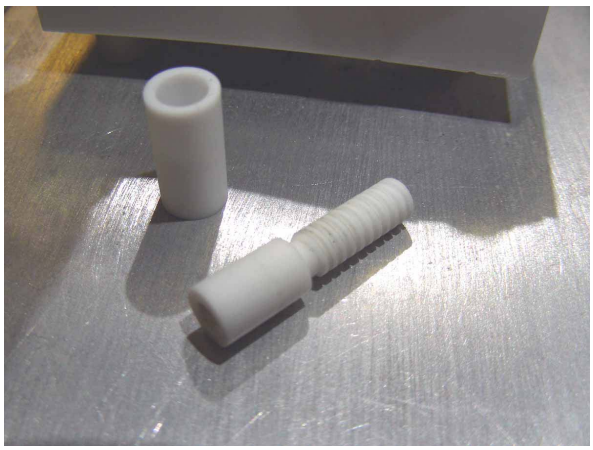

Figure 12.12: Coil bobin and outer shell.

Projects of other institutes and outside companies

We completed various projects of other institutes of the university as well as outside companies. For the zoological institute we carried out a major welding task for a touring exposition.

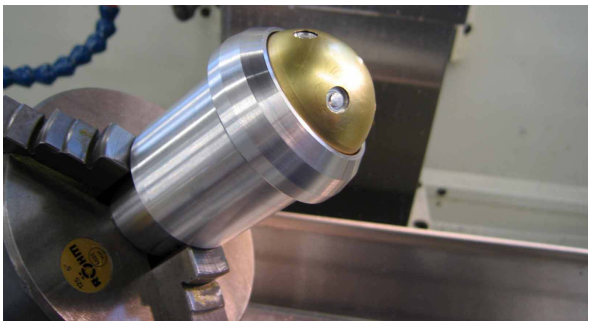

Figure 12.13: Special light source.

Figure 12.14: Replacement wheel housing for a racing car.

Figure 12.15: Feeding trays for the animal hospital.

Continuing education of the workshop staff

On the sixth of February we visited Deckel Maho Gildenmeister in Pfronten (Germany). An overview was given of the latest milling machines and state-of-the-art milling techniques. We also attended seminars and training courses for the CAM software used in the workshop, new welding procedures and machining techniques.

Figure 12.16: Here we are watching a huge milling machine.

Education of the apprentices

Besides the mandatory courses the apprentices attend they also completed advanced education in computer controlled machine (CNC) programming, pneumatics and electronics. The apprentices also carried out by themselves a project for the animal hospital of the university. The intermediate and final examinations will take place in May 2007.

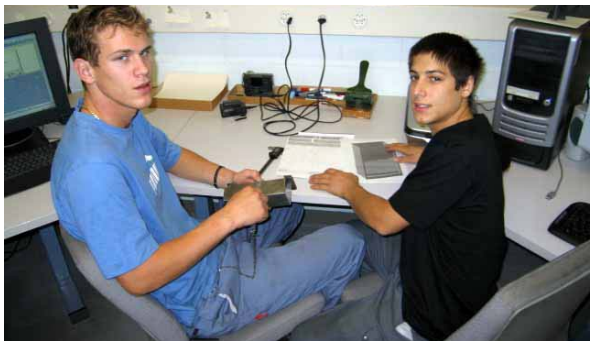

Figure 12.17: The apprentices discussing their project.

13 Electronics Workshop

W. Fässler, Hp. Meyer, P. Soland and K. Szeker

The electronics workshop supports all research groups in maintaining and repairing the existing devices. We also help to evaluate and procure new equipment. In collaboration with L. Pauli and J. Seiler, who are responsible for the preparation of the experiments, we constantly improve and renew the demonstration experiments in the lecturer hall. In connection with the electronics laboratory courses for the bachelor students we procured a set of micro-controllers and prepared some tutorial lab sessions. Different seminars, courses and exhibitions were attended to remain up-to-date in this fast-developing field. Besides many small modifications of modules, repair work and design and construction of simple circuits and prototypes for the laboratories, the main effort went into the following projects:

- For the LHCb inner tracking detector (Group Straumann, see Section 6) we assembled the complete set of detector high voltage and slow control cables. Here we also redesigned the special jumper cables, which connect the detectors through the walls of the detector housings to the readout electronics, for the final series production. These cables with a very small pitch and tiny tracks consist of flexible printed circuit boards.

- For the CMS Barrel Pixel detector (Group Amsler, see Section 7) a series of printed circuit boards for the detector readout and control electronics were designed. A complete prototype system was assembled and tested. We also designed the Barrel Pixel detector front-end control system with the associated communication and control unit boards (CCU boards). A section of such board installed in the test setup is shown in Fig. 13.1. The corresponding electronics connect the detector system to the front end controller module (FEC), which is the master of the network and uses two optical fibres to send the timing and data signals to a number of slave CCU nodes, and another two fibres to receive return communication traffic. The two receiver channels on the digital opto-hybrid (DOH) transmit the 40 MHz clock and control data at 40 Mbit/s from the FEC to the ring of communication and control units (CCUs). The two transmitter channels send clock and data back to the FEC from the ring of CCUs. The CCU chip is the core component developed for the slow control, monitoring and clock distribution in the CMS tracking system. Each chip contains various types of peripheral controllers and has dual network input and output ports allowing the cabling of a redundant network. Inside the chip, critical circuitry is tripled and a majority-voting scheme is used to cope with errors caused by single event radiation effects. The design was fabricated with a library in rad-tolerant 0.25 μm CMOS developed at CERN. Each board carries nine of these chips packed in a 196 pin ball grid array. The whole system had to undergo also a high voltage test because it

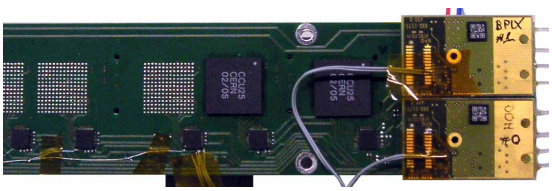

Figure 13.1:
Section of the CCU board with the two installed digital opto-hybrids. Note that the test setup board is equipped with only two CCU chips.

provides in addition the detector bias voltage of 600 V at maximum.

- For the SCOPES project we built a second unit of a 70 MHz NMR spectrometer consisting of the high frequency part and the corresponding power supply. Figure 13.2 shows an insight of the high frequency part.
- In collaboration with the Glaciology and Geomorphodynamics Group from the Department of Geography of the University we designed the printed circuit board for a dedicated sensor. The sensors are used to measure the heat flux and phase change processes in porous fractured rock. These measurements are needed in order to develop theoretical models for hazard assessment and the support of infrastructure maintenance. The sensors are mounted in a fiberglass rod and measure temperature and electrical conductivity between electrodes with high accuracy at four depths inside the 95 cm deep drill hole. The direct current conductivity of the rock depends on its pore water content and the phase state of this water. The resistance of dry rock is orders of magnitudes higher compared to saturated but frozen rock and if this water thaws the resistance decreases again by about two orders of magnitudes. Measurement electronics are kept inside the rod to minimize the effect of temperature fluctuations. As drilling effort should be minimized, the diameter of the drilling hole is only 14 mm. Hence the wiring and mounting of the electronics became a challenge. We designed the special printed circuit board for the sensor with a width of only 9.7 mm and a length of 185.2 mm (see Fig. 13.3). We also helped the colleagues in putting the electronics into operation and in improving the electronics circuits.

Figure 13.2: The SCOPES 70 MHz NMR-spectrometer high frequency device.

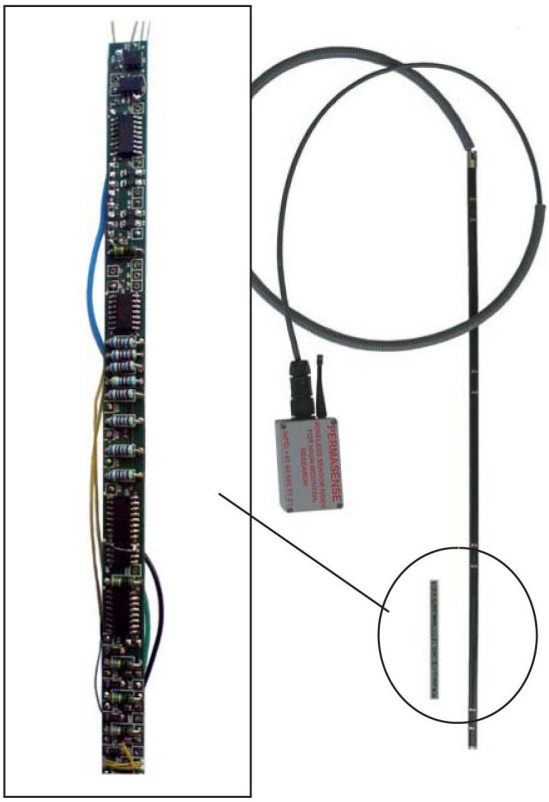

Figure 13.3: Complete PERMASENS sensor with the enlarged printed circuit board.

14 Publications

Research group of Prof. C. Amsler

Articles

- **Study of $K\bar{K}$ resonances in $\bar{p}p \to K^+K^-\pi^0$ at 900 and 1640 MeV/c**
  C. Amsler et al. (CRYSTAL BARREL Collaboration), Phys. Lett. **B 639** (2006) 165.
- **Search for Laser-Induced Formation of Antihydrogen Atoms**
  M. Amoretti et al. (ATHENA Collaboration), Phys. Rev. Lett. **97** (2006) 213401.
- **Evidence For The Production Of Slow Antiprotonic Hydrogen In Vacuum**
  N. Zurlo et al. (ATHENA Collaboration), Phys. Rev. Lett. **97** (2006) 153401.
- **Progress with cold antihydrogen**
  M. Amoretti et al. (ATHENA Collaboration),
  Nucl. Instr. Meth. in Phys. Research **247** (2006) 133.
- **Review of Particle Physics**
  W.-M. Yao et al. (Particle Data Group), J. Phys. G : Nucl. and Part. Phys. **33** (2006) 1.
- **Particle Physics Booklet**
  W.-M. Yao et al. (Particle Data Group), Institute of Physics Publishing (2006).
- **Quark Model**
  C. Amsler, T. DeGrand and B. Krusche, J. Phys. G : Nucl. and Part. Phys. **33** (2006) 165.
- **The η (1405), η (1475), $f_1(1420)$, and $f_1(1510)$**
  C. Amsler and A. Masoni, J. Phys. G : Nucl. and Part. Phys. **33** (2006) 591.
- **Non $q\bar{q}$-Mesons**
  C. Amsler, J. Phys. G : Nucl. and Part. Phys. **33** (2006) 949.
- **The CMS high level trigger**
  W. Adam et al. (CMS Collaboration), Eur. Phys. J. **C 46** (2006) 605.
- **A Gaussian sum - Filter for vertex reconstruction**
  T. Speer, R. Frühwirth, Comp. Phys. Comm. **174** (2006) 935.
- **Track reconstruction in the CMS tracker**
  T. Speer et al., Nucl. Instr. Meth. in Phys. Research **A 559** (2006) 143.
- **Robust vertex fitters**
  T. Speer et al., Nucl. Instr. Meth. in Phys. Research **A 566** (2006) 149.
- **A double junction model of irradiated silicon pixel sensors for LHC**
  V. Chiochia et al., Nucl. Instr. Meth. in Phys. Research **A 568** (2006) 51.
- **Simulation and hit reconstruction of irradiated pixel sensors for the CMS experiment**
  E. Alagöz, V. Chiochia, M. Swartz, Nucl. Instr. Meth. in Phys. Research **A 566** (2006) 40.

- **Sensor simulation and position calibration for the CMS pixel detector**
  V. Chiochia, E. Alagöz, M. Swartz, Nucl. Instr. Meth. in Phys. Research **A 569** (2006) 132.

- **Extraction of electric field in heavily irradiated silicon pixel sensors**
  A. Dorokhov et al., Nucl. Instr. Meth. in Phys. Research **A 560** (2006) 112.

- **Observation, modeling and temperature dependence of doubly peaked electric fields in irradiated silicon pixel sensors**
  M. Swartz et al., Nucl. Instr. Meth. in Phys. Research **A 565** (2006) 212.

- **The control and readout systems of the CMS pixel barrel detector**
  D. Kotlinski et al., Nucl. Instr. Meth. in Phys. Research **A 565** (2006) 73.

- **Assembly of the CMS pixel barrel modules**
  S. König et al., Nucl. Instr. Meth. in Phys. Research **A 565** (2006) 62.

- **Design and performance of the CMS pixel detector readout chip**
  H. Chr. Kästli et al., Nucl. Instr. Meth. in Phys. Research **A 565** (2006) 188.

- **Impact of CMS silicon tracker misalignment on track and vertex reconstruction**
  L. Barbone et al., Nucl. Instr. Meth. in Phys. Research **A 566** (2006) 45.

- **CMS Physics technical design report, Volume I : Detector Performance and Software**
  CMS Collaboration, CMS - TDR - 8.1 CERN/LHCC-2006-001
  http://cmsdoc.cern.ch/cms/cpt/tdr/ .

- **CMS Physics technical Design Report, Volume II : Physics Performance**
  CMS Collaboration , CMS-TDR-8.2, CERN/LHCC 2006-021
  http://cmsdoc.cern.ch/cms/cpt/tdr/ .

- **Prospects for B physics at CMS**
  T. Speer, Nucl. Phys. **B (Proc. Suppl.) 163** (2007) 159.

- **Study of the $B_s \to J/\psi\,\phi\,\mu^+\mu^-K^+K^-$ channel with CMS**
  V. Ciulli et al., Nucl. Phys. **B (Proc. Suppl.) 156** (2006) 109.

Thesis

- **Design and Performance of the Silicon Pixel Detector Modules for the CMS Experiment**
  C. Hörmann, PhD Thesis, Universität Zürich, 2006.

Book

- **Kern-und Teichenphysik**
  C. Amsler, UTB, Uni-Taschenbücher, Stuttgart, vdf Hochschulverlag AG, ETHZ.

Articles in press

- **Partial wave analysis of $\bar{p}p$ annihilation at rest into $2\pi^+2\pi^-\eta$**
  C. Amsler et al. (Crystal Barrel Collaboration), Eur. J. Phys.
- **Design and performatnce of silicon sensors for the CMS barrel pixel detector**
  Y. Allkofer et al., Nucl. Instr. Meth. in Phys. Research **A**.
- **A new aerogel Čerenkov detector with wavelength shifter**
  Y. Allkofer et al., Nucl. Instr. Meth. in Phys. Research **A**.
- **The ATLAS and CMS Detectors and Triggers for B-Physics**
  T. Speer, Nucl. Phys. **B**.
- **Protonium production in ATHENA at CERN**
  L. Venturelli et al., Nucl. Instr. Meth. in Phys. Research **B**.
- **Detection VUV scintillation light in one ton of liquid argon**
  C. Regenfus, World Scientific.

Invited Lectures

- C. Amsler: **Status of the DIRAC experiment**
  CHIPP plenary meeting, PSI, 2 October 2006.
- V. Boccone: **Light readout for the ArDM WIMP-detector**
  Swiss Physical Society, Zürich, 21 February 2006.
- V. Chiochia: **Sensor simulation and position calibration for the CMS pixel detector**
  8th RD50 Workshop on Radiation Hard Semiconductor Devices for Very High Luminosity Colliders, 25 June 2006.
- C. Regenfus: **Detecting light from WIMPS in 1 ton liquid argon (ArDM)**
  6th Int. Workshop on the Identification of Dark Matter, IDM06, Rhode Island , 13 September 2006.
- C. Regenfus: **The ArDM experiment**
  CHIPP Workshop on Neutrino Physics, Bern, 20 October 2006.
- T. Speer: **B-Physics at CMS**
  First Workshop on Theory, Phenomenology and Experiments in Heavy Flavour Physics, Capri, 31 May 2006.
- T. Speer: **The ATLAS and CMS Detectors and Triggers for B Physics**
  7th Int. Conf. on Hyperons, Charm and Beauty Hadrons (BEACH 2006), Lancaster 7 July 2006.
- L. Wilke: **Extracting $\Delta\Gamma$ in the B_s-system from angular distributions of the $B_s \to (J/\psi)\phi$ decay with the CMS detector**
  Swiss Physical Society, Zürich, 21 February 2006.

- L. Wilke: **Study of the Decay $B_s \to (J/\psi)\phi$ with the CMS Detector**
  Flavor Workshop in the Era of the LHC, 10 October 2006.

ATHENA Collaboration (2006):

M. Amoretti, C. Amsler, G. Bonomi, P. Bowe, C. Canali, C. Carraro, C. L. Cesar, M. Charlton, M. Doser, A. Fontana, M. C. Fujiwara, R. Funakoshi, P. Genova, J. S. Hangst, R. S. Hayano, L. V. Joergensen, I. Johnson, A. Kellerbauer, V. Lagomarsino, R. Landua, E. Lodi Rizzini, M. Macri, N. Madsen, G. Manuzio, D. Mitchard, P. Montagna, H. Pruys, C. Regenfus, J. Rochet, A. Rotondi, G. Testera, A. Variola, L. Venturelli, D. P. van der Werf, Y. Yamazaki, N. Zurlo

CRYSTAL BARREL Collaboration (2006):

C. Amsler, C. A. Baker, B. M. Barnett, C. J. Batty, M. Benayoun, P. Blüm, K. Braune, V. Credé, K. M. Crowe, M. Doser, W. Dünnweber, D. Engelhardt, M. A. Faessler, R. P. Haddock, F. H. Heinsius, N. P. Hessey, P. Hidas, D. Jamnik, H. Kalinowsky, P. Kammel, J. Kisiel, E. Klempt, H. Koch, M. Kunze, U. Kurilla, R. Landua, H. Matthäy, C. A. Meyer, F. Meyer-Wildhagen, R. Ouared, K. Peters, B. Pick, M. Ratajczak, C. Regenfus, U. Strohbusch, M. Suffert, U. Thoma, I. Uman, S. Wallis-Plachner, D. Walther, U. Wiedner, B. S. Zou, Č. Zupančič

PARTICLE DATA Group (2006):

W.-M. Yao, C. Amsler, D. Asner, K.S. Babu, R.M. Barnett, J. Beringer, P.R. Burchat, C.D. Carone, C. Caso, O. Dahl, G. D'Ambrosio, A.D. Gouvea, M. Doser, S. Eidelman, J.L. Feng, T. Gherghetta, M. Goodman, C. Grab, D.E. Groom, A. Gurtu, K. Hagiwara, K.G. Hayes, J.J. Hernandez-Rey, K. Hikasa, H. Jawahery, C. Kolda, Y. Kwon, M.L. Mangano, A.V. Manohar, A. Masoni, R. Miquel, K. Mönig, H. Murayama, K. Nakamura, S. Navas, K.A. Olive, L. Pape, C. Patrignani, A. Piepke, G. Punzi, G. Raffelt, J.G. Smith, M. Tanabashi, J. Terning, N.A. Törnqvist, T.G. Trippe, P. Vogel, T. Watari C.G. Wohl, R.L. Workman, P.A. Zyla

DIRAC Collaboration (2006):

B. Adeva, L. Afanas'ev, Y. Allkofer, C. Amsler, D. Bartos, A. Benelli, V. Brekhovskikh, A. Caragheorgheopol, T. Cechak, M. Chiba, S. Constantinescu, C.O. Curceanu, C. Detraz, D. Dreossi, D. Drijard, A. Dudarev, I. Evangelou, J. L. Fungueirino Pazos, J. Gerndt, P. Gianotti, G. Giolu, O. Gorchakov, K. Gritsay, C. Guaraldo, M. Hansroul, S. Horikawa, M. Iliescu, V. Karpukhin, J. Kluson, M. Kobayashi, P. Kokkas, V. Komarov, L. Kruglova, V. Kruglov, A. Kulikov, A. Kuptsov, K. I. Kuroda, A. Lamberto, A. Lanaro, V. Lapchine, R. Lednicky, P. Levi Sandri, L. Lopez Aguera, V. Lucherini, N. Manthos, C. Marinas Pardo, L. Nemenov, M. Nikitin, K. Okada, V. Ol'shevskiy, M. Pentia, A. Penzo, M. Plo, T.C. Ponta, Z. Pustylnik, G.F. Rappazzo, J. Rochet, A. Romero Vidal, J. J. Saborido Silva, J. Schacher, F. Takeutchi, A. Tarasov, L. Tauscher, F. A. Triantis, T. Trojek, S. Trusov, J. Smolik, S. Sugimoto, A. Ryazantsev, V. Rykalin, O. Vazquez Doce, T. Vrba, V. Yaz'kov, M. Zhabitskiy, P. Zrelov

Research group of Prof. H.-W. Fink

Articles

- **Vacuum Ion Emission from Solid Electrolytes**
  C. Escher, S. Thomann, C. Andreoli, H.-W. Fink, J. Toquant and D. Pohl,
  Applied Physics Letters 89, 053513 (2006).

- **Direct Evidence for Conduction Pathways in Solid Electrolytes**
  C. Escher, T. Latychevskaia, H.-W. Fink and D. Pohl, Phys.Rev.Lett.97, 136601 (2006).

- **Zupfen am Lebensfaden: Experimente mit einzelnen DNA Molekülen**
  C. Escher und H.-W. Fink, Physik in unserer Zeit, Wiley-VCH Verlag, Heft 4 (2007).

Article in print

- **Solution of the Twin Image Problem in Holography**
  T. Latychevskaia and H.-W. Fink, Phys.Rev.Lett.

Invited talks

- H.-W. Fink: **From Field Ion Microscopy to Holography of Individual Bio-Molecules**
  Gert Ehrlich Symposium, University of Illinois at Urbana Champaign, May 31, 2006.

- C. Escher: **Direct Microscopic Insight into the Conduction Mechanism of a Solid Electrolyte**
  International Conference on Nanoscience and Technology (ICN+T), 30.07 - 4.08.2006, Basel

- T. Latychevskaia: **Electron Holography of an Individual Virus**
  International Conference on Nanoscience and Technology (ICN+T), 30.07 - 4.08.2006, Basel

- T. Latychevskaia and C. Escher: **Conformational and Structural Studies on Single Bio-Molecules**
  Swiss Physical Society Meeting 2007, 20-21.02.2007, University Zürich.

Research group of Prof. H. Keller

Articles

- **Effect of Pressure on the Ginzburg-Landau Parameter $\kappa = \lambda/\xi$ in YB_6**
  R. Khasanov, P.S. Häfliger, N. Shitsevalova, A. Dukhnenko, and H. Keller,
  Phys. Rev. Lett. **97**, 157002-1-4 (2006).

- **Muonium in InSb: Shallow acceptor versus deep trap or recombination center**
  V.G. Storchak, D.G. Eshchenko, J.H. Brewer, S.P. Cottrell, and R L. Lichti,
  Phys. Rev. B **73**, 081203-1-4 (2006).

- **Pseudogap of the high-temperature superconductor $La_{1.96-x}Sr_xHo_{0.04}CuO_4$ as observed by neutron crystal-field spectroscopy**
  Petra S. Häfliger, A. Podlesnyak, K. Conder, E. Pomjakushina, and A. Furrer,
  Phys. Rev. B **74**, 184520-1-13 (2006).

- **Muon-spin-rotation measurements of the penetration depth in Li_2Pd_3B**
  R. Khasanov, I.L. Landau, C. Baines, F. La Mattina, A. Maisuradze, K. Togano, and H. Keller,
  Phys. Rev. B **73**, 214528-1-6 (2006).

- **Quantum diffusion of muonium atoms in solids: Localization vs. band-like propagation**
  V.G. Storchak, D.G. Eshchenko, and J.H. Brewer, Physica B **374-375**, 347-350 (2006).

- **Formation and dynamics of muonium centers in semiconductors**
  V.G. Storchak, D.G. Eshchenko, J.H. Brewer, and S.P. Cottrel,
  Physica B **374-375**, 398-401 (2006).

- **Room temperature ferromagnetism in III-V and II-IV-V2 dilute magnetic semiconductors**
  V.G. Storchak, D.G. Eshchenko, H. Luetkens, E. Morenzoni, R.L. Lichti, S.F. Marenkin, O.N. Pashkova, and J.H. Brewer, Physica B **374-375**, 430-432 (2006).

- **Correlation between oxygen isotope effects on transition temperature and magnetic penetration depth in high-temperature superconductors close to optimal doping**
  R. Khasanov, A. Shengelaya, K. Conder, E. Morenzoni, I.M. Savić, J. Karpinski, and H. Keller,
  Phys. Rev. B **74**, 064504-1-6 (2006).

- **Nonlocal Meissner screening**
  A. Suter, E. Morenzoni, N. Garifianov, R. Khasanov, E. Kirk, H. Luetkens, T. Prokscha, and M. Horisberger, Physica B **374-375**, 243-246 (2006).

- **The oxygen isotope effect on the infrared photo-induced absorption spectra of La_2SrCuO_4**
  R.V. Yusupov, K. Conder, T. Mertelj, D. Mihailovic, K.A. Müller, and H. Keller,
  Eur. Phys. J. B **54** 465-469 (2006).

- **Mixed order parameter symmetries in cuprate superconductors**
  A. Bussmann-Holder, R. Khasanov, A. Shengelaya, A. Maisuradze, F. La Mattina, H. Keller, and K.A. Müller, Europhys. Lett. **77**, 27002-p1-p4 (2007).

- **Temperature dependences of the upper critical field and the Ginzburg-Landau parameter of Li_2Pd_3B from magnetization measurements**
  I.L. Landau, R. Khasanov, K. Togano, and H. Keller, Physica C **451**, 134-138 (2007).

- **Experimental evidence for two gaps in the high-temperature $La_{1.83}Sr_{0.17}CuO_4$ superconductor**
  R. Khasanov, A. Shengelaya, A. Maisuradze, F. La Mattina, A. Bussmann-Holder, H. Keller, and K.A. Müller, Phys. Rev. Lett. **98**, 057007-1-4 (2007).

- **Magnetic field dependence of the oxygen isotope effect on the magnetic penetration depth in hole-doped cuprate superconductors**

R. Khasanov, A. Shengelaya, D. Di Castro, D.G. Eshchenko, I.M. Savić, K. Conder, E. Pomjakushina, J. Karpinski, S. Kazakov, and H. Keller,
Phys. Rev. B (Rapid Communication) **75**, 060505-1-4 (2007).

- **Electric-field-effect modulation of the transition temperature, mobile carrier density, and in-plane penetration depth of $NdBa_2Cu_3O_7$ thin films**
D. Matthey, N. Reyren, and J.-M. Triscone, and T. Schneider,
Phys. Rev. Lett. **98**, 057002-1-4 (2007).

- **Novel sensor design for torque magnetometry**
S. Kohout, J. Roos, and H. Keller, Rev. Sci. Instrum. **78**, 013903-1-5 (2007).

Articles in press

- **Influence of Ti^{4+} on the magnetic state of $CaRu_{1-x}Ti_xO_3$**
A. Zorkovská, A. Baran, I. Bradarić, I. Savić, J. Šebek, E. Šantavá, D. Marinčev, S. Kohout, H. Keller, and A. Feher, Journal of Magnetism and Magnetic Materials.

- **Polaron Effects in High-Temperature Cuprate Superconductors**
A. Bussmann-Holder and H. Keller, in *Polarons in Advanced Materials*, ed. A.S. Alexandrov, Canopus Publishing Bristol (2007).

- **Real and marginal isotope effects in cuprate superconductors**
A.R. Bishop, A. Bussmann-Holder, O.V. Dolgov, A. Furrer, H. Kamimura, H. Keller, R. Khasanov, R.K. Kremer, D. Manske, K.A. Müller, and A. Simon, Journal of Superconductivity (2007).

- **High T_c Superconductors and Related Transition Metal Oxides**
A. Bussmann-Holder and H. Keller, editors (Springer, Berlin, 2007).

- **Two-gap superconductivity in the cuprate superconductor $La_{1.83}Sr_{0.17}CuO_4$**
R. Khasanov, A. Shengelaya, A. Bussmann-Holder, and H. Keller,
in *High T_c Superconductors and Related Transition Metal Oxides*, eds. A. Bussmann-Holder and H. Keller (Springer, Berlin, 2007).

- **Electronic phase separation and unusual isotope effects in $La_{2-x}Sr_xCuO_4$ observed by electron paramagnetic resonance**
A. Shengelaya, B.I. Kochelaev, K. Conder, and H. Keller, in *High T_c Superconductors and Related Transition Metal Oxides*, eds. A. Bussmann-Holder and H. Keller (Springer, Berlin, 2007).

- **^{139}La NMR and NQR investigations of the superconductor $LaBa_2Cu_3O_{7-\delta}$**
S. Strässle, J. Roos, M. Mali, K. Conder, E. Pomjakushina, and H. Keller, Physica C.

- **Dual character of the electronic structure in $YBa_2Cu_4O_8$: conduction bands of CuO_2 planes and CuO chains**
T. Kondo, R. Khasanov, J. Karpinski, S.M. Kazakov, N.D. Zhigadlo, T. Ohta, H.M. Fretwell, A.D. Palczewski, J.D. Koll, J. Mesot, E. Rotenberg, H. Keller, and A. Kaminski, Phys. Rev. Lett.

- **View point: On the superconductivity in hole doped cuprates**
K.A. Müller, J. Phys.: Condens. Matter.

PhD thesis

- **Torque Magnetometry in Novel Superconductors: I Torque Apparatus Developments II Correlation Lengths and Anisotropy**
  St. Kohout, PhD Thesis, Universität Zürich, 2005/2006.

Master thesis

- **Untersuchungen von $YBa_2(Cu_{1-x}Fe_x)_4O_{8+\delta}$**
  R. Kuhn, Master Thesis, Universität Zürich, 2007.

Conference reports

- **^{139}La NMR investigations of the superconductor $LaBa_2Cu_3O_{7-\delta}$**
  S. Strässle, J. Roos, M. Mali, K. Conder, E. Pomjakushina, and H. Keller,
  M2S-HTSC VIII, Dresden, 9-14 July, 2006.

- **EPR study of the spin-lattice relaxation of Yb^{3+} doped YBCO**
  A. Maisuradze, A. Shengelaya, K. Pomjakushina, K. Conder, K. A. Müller, and H. Keller,
  M2S-HTSC VIII, Dresden, 9-14 July, 2006.

- **On the Nature of the Insulator-to-Metal Transition in reduced Cr-doped $SrTiO_3$.**
  F. La Mattina, S. Alvarado, J.G. Bednorz, A. Shengelaya, and H. Keller,
  XIII International Workshop on Oxide Electronics, Ischia (Italy), October 8-11, 2006.

- **EPR and Optical investigation on charge transfer processes in Cr-doped $SrTiO_3$**
  F. La Mattina, S. Alvarado, J.G. Bednorz, A. Shengelaya, and H. Keller,
  Annual meeting of the Swiss Physical Society, Zürich, 20-21 February, 2007.

- **Upper critical field anisotropy of MgB_2 and $Al_{0.16}Mg_{0.84}B_2$**
  S. Weyeneth, C. Duttwyler, R. Puzniak, S. Kohout, N.D. Zhigadlo, J. Karpinski, and H. Keller,
  Annual meeting of the Swiss Physical Society, Zürich, 20-21 February, 2007.

- **Torque magnetometry with highly sensitive piezoresistive sensors**
  S. Weyeneth, C. Duttwyler, S. Kohout, J. Roos, and H. Keller,
  Annual meeting of the Swiss Physical Society, Zürich, 20-21 February, 2007.

- **^{139}La NMR study of the cuprate superconductor $LaBa_2Cu_3O_{7-\delta}$**
  S. Strässle, J. Roos, M. Mali, K. Conder, E. Pomjakushina, and H. Keller,
  Annual meeting of the Swiss Physical Society, Zürich, 20-21 February, 2007.

- **EPR study of Oxygen Isotope Effect on spin lattice relaxation rate of Yb^{3+} in YBCO**
  A. Maisuradze, A. Shengelaya, B Kochelaev, K. Pomjakushina, K. Conder, K.A. Müller, and H. Keller, Annual meeting of the Swiss Physical Society, Zürich, 20-21 February, 2007.

- **^{63,65}Cu Nuclear quadrupole resonance (NQR) study of $YBa_2(Cu_{1-x}Fe_x)_4O_{8+\delta}$**
  R. Kuhn, S. Strässle, A. Maisuradze, B. Graneli, J. Roos, and H. Keller,
  Annual meeting of the Swiss Physical Society, Zürich, 20-21 February, 2007.

Invited lectures/talks

- Petra S. Häfliger: **Muon-Spin Rotation Measurements of the Penetration Depth in the Noncentrosymmetric Superconductors $Li_2(Pd/Pt)_3B$**
  Condensed Matter Physics Seminar, Institute for Theoretical Physics, ETH Zürich, Zürich, Switzerland, September 27, 2006.

- Petra S. Häfliger: **Aspects of Unconventional Superconductivity: (A) The Pseudogap in LSCO-Type High-Temperature Superconductors (B) Possible Occurrence of Spin-Triplet States in $Li_2(Pd/Pt)_3B$**
  Seminar at FRM-II, Neutrons and their Use in Science and Industry, Technische Universität München, München, Germany, December 4, 2006.

- H. Keller: **Unconventional isotope effects in cuprate superconductors - what can we learn from them?**
  Conference on *Lattice Effects in Superconductors*, Santa Fe, USA, April 17-20, 2006.

- H. Keller: **Unconventional isotope effects in cuprate superconductors**
  Third Meeting of CoMePhS, Paris, France, June 17-19, 2006.

- H. Keller: **Wie entsteht ein Ton?**
  Kinderuniversität, Universität Zürich, Zürich, Switzerland, May 10, 2006.

- H. Keller: **Unconventional isotope effects in cuprate high-temperature superconductors**
  8th International Conference on Materials and Mechanisms of Superconductivity and High Temperature Superconductors (M2S 2006 Dresden), Dresden, Germany, July 9-14, 2006.

- H. Keller: **Vortex matter and unconventional isotope effects in cuprate superconductors**
  First Swiss-Japanese workshop on the applications and on new developments in muon spectroscopy on novel materials, KEK, Tsukuba, Japan, September 28-30, 2006.

- H. Keller: **Unconventional isotope effects in cuprate high-temperature superconductors**
  Miniworkshop on Isotope Effect in HTSC Cuprates: Experiment vs. Theory, National Institute of Advanced Industrial Science and Technology (AIST), Tsukuba, Japan September 29, 2006.

- H. Keller: **Unconventional isotope effects in cuprate high-temperature superconductors**
  The Hong Kong University of Science and Technology, Hong Kong, China, October 4, 2006.

- H. Keller: **Grundlagenforschung, wozu? - Bildung und Wissenschaft, kostbare "Rohstoffe" der Schweiz**
  Kiwanis Klub Rapperswil-Jona, Rapperswil-Jona, Switzerland, November 23, 2006.

- H. Keller: **Experimental evidence for two gaps in cuprate high-temeprature superconductors**
  Sixth International Conference on New Theories, Discoveries, and Applications of Superconductors and Related Materials, Sydney, Australia, January 9-11, 2007.

Research group of Prof. J. Osterwalder

Articles

- **Single layer hexagonal boron nitride films on Ni(110)**
  T. Greber, L. Brandenberger, M. Corso, A. Tamai, J. Osterwalder,
  e-J. Surf. Sci. Nanotech., 4, 410-413 (2006).

- **Spin-polarized photoemission**
  J. Osterwalder, in *Magnetism: Synchrotron Radiation Approach*, chapter 5, Lecture Notes in Physics, Volume 697, E. Beaurepaire, H. Bulou, F. Scheurer, J.-P. Kappler, eds. (Springer, Berlin, Heidelberg, New York 2006) 95-120.

- **Observation of a Mott insulating ground state for Sn/Ge(111) at low temperature**
  R. Cortés, A. Tejeda, J. Lobo, C. Didiot, B. Kierren, D. Malterre, E. G. Michel, A. Mascaraque, Phys. Rev. Lett. 96, 126103-1-4 (2006).

- **Matrix element effects in angle-resolved valence band photoemission with polarized light from the Ni(111) surface**
  M. Mulazzi, M. Hochstrasser, M. Corso, I. Vobornik, J. Fujii, J. Osterwalder, J. Henk, G. Rossi, Phys. Rev. B 74, 035118-1-8 (2006).

- **Large dispersion of incoherent spectral features in highly ordered C_{60} chains**
  A. Tamai, A. P. Seitsonen, T. Greber, J. Osterwalder, Phys. Rev. B 74, 085407-1-5 (2006).

- **Electronic structure of C_{60} on Au(887)**
  F. Schiller, M. Ruiz-Osés, J. E. Ortega, P. Segovia, J. Martínez-Blanco, B. Doyle, V. Pérez-Dieste, J. Lobo, N. Néel, R. Berndt, J. Kröger, J. Chem. Phys. 125, 144719-1-6 (2006).

- **Formation of single-layer h-BN on Pd(111)**
  M. Morscher, M. Corso, T. Greber, J. Osterwalder, Surf. Sci. 600, 3280-3284 (2006).

- **Photoelectron diffraction for a look inside nanostructures**
  J. Osterwalder, A. Tamai, W. Auwärter, M. P. Allan, T. Greber, Chimia 60, 795-799 (2006).

- **Energetics and dynamics of unoccupied electronic states at the h-BN/Ni(111) interface**
  M. Muntwiler, M. Hengsberger, A. Dolocan, H. Neff, T. Greber, J. Osterwalder,
  Phys. Rev. B 75, 075407-1-7 (2007).

- **Surface x-ray diffraction study of boron-nitride nanomesh in air**
  O. Bunk, M. Corso, D. Martoccia, R. Herger, P. R. Willmott, B. D. Patterson, J. Osterwalder, J. F. van der Veen, T. Greber, Surf. Sci. 601, L7-L10 (2007).

- **Tunable self-assembly of one-dimensional nanostructures with orthogonal directions**
  M. P. Allan, S. Berner, M. Corso, T. Greber, J. Osterwalder, Nanoscale Res. Lett. 2, 94-99 (2007).

- **Self-assembly of a hexagonal boron nitride nanomesh on Ru(0001)**
  A. Goriachko, Y. He, M. Knapp, H. Over, M. Corso, T. Brugger, S. Berner, J. Osterwalder, T. Greber, Langmuir 23, 2928-2931 (2007).

- **Probing enantioselectivity with x-ray photoelectron spectroscopy and density functional theory**
  R. Schillinger, Z. Sljivancanin, B. Hammer, T. Greber, Phys. Rev. Lett. 98, 136102-1-4 (2007).

Article in press

- **Boron nitride nanomesh: functionality from a corrugated monolayer**
  S. Berner, M. Corso, R. Widmer, O. Groening, R. Laskowski, P. Blaha, K. Schwarz, A. Goriachko, H. Over, S. Gsell, M. Schreck, H. Sachdev, T. Greber, J. Osterwalder, Angew. Chem. Int. Ed.

Theses

- **Tilting corannulene molecules on surfaces**
  Louis Brandenberger, Diploma Thesis, Physik-Institut, Universität Zürich, 2006.
- **Time-resolved low-energy electron diffraction and photoemission pump-probe experiments**
  Andrei D. Dolocan, Ph. D. Thesis, Physik-Institut, Universität Zürich, 2006.
- **Dynamics of space-charge and molecules on surfaces investigated by means of picosecond low-energy electron diffraction**
  Claudio Cirelli, Ph. D. Thesis, Physik-Institut, Universität Zürich, 2006.
- **Boron-nitride nanostructures on transition metals: flat layers and nanomesh**
  Martina Corso, Ph. D. Thesis, Physik-Institut, Universität Zürich, 2006.
- **Time-resolved photoemission from h-BN/Ni(111) across the ferromagnetic transition**
  Dominik Leuenberger, Master Thesis, Physik-Institut, Universität Zürich, 2007.
- **Nanomesh on Rh(111) thin films on Si(111) and its possible technical applications**
  Thomas Mattle, Bachelor Thesis, Physik-Institut, Universität Zürich, 2007.

Contributed conference presentations

- **Time-resolved two-photon photoemission experiments on the boron nitride nanomesh**
  A. Dolocan, 5th Symposium on Ultra-Fast Surface Dynamics, Abashiri, Japan, 22.5.06.
- **Detecting enantiomers by x-ray photoemission spectroscopy: cysteine on Au(17 11 9)^S**
  R. Schillinger, International Conference on Nano-Structures Self-Assembling, Aix-en-Provence, France, 4.7.06.
- **Co clusters on h-BN/Rh(111) (Poster)**
  T. Brugger, Summer School on Metal Clusters on Surfaces, Pisa, Italia, 6.7.06.
- **Activity boost of a biomimetic oxidation catalyst by immobilisation onto a gold surface**
  S. Berner, International Conference on Nanoscience and Technology, Basel, 31.7.06.
- **Trapping single molecules in boron nitride nanomesh pores**
  S. Berner, International Conference on Nanoscience and Technology, Basel, 4.8.06.
- **Is short-range order detrimental to long-range order in large-scale self assembly ?**
  M. Corso, International Conference on Nanoscience and Technology, Basel, 4.8.06.

- **Co clusters on h-BN/Rh(111) (Poster)**
  T. Brugger, NanoMesh Workshop, Braunwald, 18.9.06

- **Nanomesh on Rh(111) thin films on Si(111) (Poster)**
  T. Mattle, NanoMesh Workshop, Braunwald, 18.9.06.

- **Formation of single-layer h-BN on Pd(111) (Poster)**
  M. Morscher, NanoMesh Workshop, Braunwald, 18.9.06.

- **Is short-range order detrimental to long-range order in large-scale self assembly ?**
  M. Corso, NanoMesh Workshop, Braunwald, 18.9.06.

- **One-dimensional boron and boron-nitride nanostructures on the (110) surface of molybdenum (Poster)**
  M. P. Allan, NanoMesh Workshop, Braunwald, 18.9.06.

- **Trapping single molecules in boron nitride nanomesh pores**
  S. Berner, NanoMesh Workshop, Braunwald, 19.9.06.

- **Growth of molecular arrays by trapping single molecules in boron nitride nanomesh pores**
  S. Berner, Jahrestreffen der Schweizerischen Arbeitsgemeinschaft für Oberflächen und Grenzflächen (SAOG), Universität Fribourg, 26.1.07.

- **Hidden surface states on pristine and hydrogen-passivated Ni(111)**
  J. Lobo-Checa, Swiss Physical Society Meeting, Zürich, 20.2.07.

- **Boron-nitride nanomesh: a peculiar structure with functionality**
  S. Berner, Swiss Physical Society Meeting, Zürich, 20.2.07.

- **Cobalt clusters on h-BN/Rh(111) (Poster)**
  T. Brugger, Swiss Physical Society Meeting, Zürich, 20.2.07.

- **Temperature-dependent and time-resolved photoemission on a ferromagnetic surface**
  D. Leuenberger, Swiss Physical Society Meeting, Zürich, 21.2.07.

- **Dynamics of space-charge and molecules on surfaces investigated by means of picosecond low-energy electron diffraction**
  C. Cirelli, Swiss Physical Society Meeting, Zürich, 21.2.07.

- **Self-assembled thiol-functionalized cobalt porphyrines: boosted catalytic activity by immobilization onto a gold surface**
  S. Berner, Swiss Physical Society Meeting, Zürich, 21.2.07.

- **Hydrogen in C_{60} (Poster)**
  T. Greber, Symposium on Surface Science (3S), Les Arcs, France, 13.3.07.

- **Co clusters on the boron nitride nanomesh**
  T. Brugger, Frühjahrstagung der Deutschen Physikalischen Gesellschaft, Regensburg, 27.3.07.

Invited lectures

- J. Lobo-Checa: **Estructura electronica en superficies metálicas vecinales**
  Consejo nacional de investigaciones cientificas y técnicas, Santa Fe, Argentina, 12.4.06.
- J. Osterwalder: **Hexagonal boron nitride layers as nanotemplates**
  Seminar, Max-Planck-Institut für Festkörperforschung, Stuttgart, 26.4.06.
- J. Osterwalder: **Valence band photoemission (6 hours of lectures)**
  School on Synchrotron Radiation, International Centre for Theoretical Physics, Trieste, 18.-22.5.06.
- A. Dolocan: **Time-resolved low-energy electron diffraction and photoemission pump-probe experiments**
  Seminar, Physics Department, University of Tsukuba, Japan, 26.5.06.
- M. Hengsberger: **Zwei-Photonen-Photoemissionsexperimente auf Bornitridfilmen**
  Seminar, Physikalisches Institut der Universität Würzburg, 4.7.06.
- T. Greber: **Monolayers of boron nitride with and without holes**
  International Conference on Nano-Structures Self-Assembling, Aix-en-Provence, France, 4.7.06.
- T. Greber: **The near-node photoelectron holography endstation at the Swiss Light Source**
  1st MolCH-Surf Discussion Meeting, Schweizerischer Nationalfonds, Bern, 12.7.06.
- J. Lobo-Checa: **Electronic structure of vicinal noble-metal surfaces**
  Seminar, ALBA CELLS (Barcelona Synchrotron), Bellaterra, Spain, 18.7.06.
- J. Osterwalder: **Hexagonal boron-nitride monolayers: a versatile skin for metal surfaces**
  Condensed Matter Colloquium, Paul-Scherrer-Institut, 8.9.06.
- T. Greber: **Assembling boron-nitride nanostructures**
  NanoMesh Workshop, Braunwald, 18.9.06.
- J. Lobo-Checa: **Electronic and magnetic properties of surface states**
  Seminar, Physikalisches Institut, Universität Basel, 21.9.06.
- J. Osterwalder: **Photoemission from valence bands: band mapping and Fermi surface mapping**
  Mainz-MATCOR Summer School on Photoemission, Mainz, 25.-29.9.06.
- T. Greber: **Flat and textured boron nitride layers on transition metals: new materials at the nanometer scale**
  Workshop of the INTERREG IIIA Slowenian-Italian Project, Trieste, 23.9.06.
- J. Osterwalder: **Hexagonal boron-nitride layers on transition metal surfaces**
  13th International Conference on Solid Films and Surfaces, San Carlo de Bariloche, Argentina, 8.11.06.
- C. Cirelli:
  Dynamics of space-charge and molecules on surfaces investigated by means of picosecond LEED
  Group-Seminar, Swiss Light Source, Paul-Scherrer-Institut, 13.11.06.
- C. Cirelli:
  Dynamics of space-charge and molecules on surfaces investigated by means of picosecond LEED
  Group-Seminar, Ultrafast Laser Group, ETH Zürich, 1.12.06.

- C. Cirelli:
  Dynamics of space-charge and molecules on surfaces investigated by means of picosecond LEED
  Seminar, Center of Applied Photonics, Universität Konstanz, 6.12.06.

- A. Dolocan: **Time-resolved low-energy electron diffraction and photoemission pump-probe experiments**
  Seminar, Physics Department, University of Stony Brook, USA, 9.1.07.

- J. Lobo-Checa: **Surface states of Ni(111) and H/Ni(111)**
  SLS/SIS Spectroscopy on Novel Materials Workshop, Rigi, 11.1.07.

- J. H. Dil: **Electron localization in thin metal films: structure, morphology and interactions**
  SLS/SIS Spectroscopy on Novel Materials Workshop, Rigi, 11.1.07.

- A. Dolocan: **Time-resolved low-energy electron diffraction and photoemission pump-probe experiments**
  Seminar, Brookhaven National Laboratory, USA, 11.1.07.

- T. Greber: **PEARL: a new beamline**
  SLS/SIM Workshop, Unterwasser, 12.1.07.

- A. Dolocan: **Time-resolved low-energy electron diffraction and photoemission pump-probe experiments**
  Seminar, Physics Department, Columbia University, New York City, USA, 17.1.07.

- J. Osterwalder:
  Hexagonal boron-nitride monolayers on metal surfaces: growth, properties and applications
  Festkörper-Kolloquium, Universität Erlangen, 25.1.07.

- A. Dolocan: **Time-resolved low-energy electron diffraction and photoemission pump-probe experiments**
  Seminar, Physics Department, City College of New York, USA, 25.1.07.

- T. Greber: **Monolayers of boron nitride on transition metals with and without misfit dislocations: from flat layers to nanomesh**
  22nd Workshop on Novel Materials and Superconductivity, Planneralm, Österreich, 15.2.07.

- T. Greber: **Do dipole rings explain the bonding in nanomesh ?**
  NanoMesh Steering Committee Meeting, Wien, 23.3.07.

- J. Osterwalder: **The electronic structure of a liquid Pb film**
  March Meeting of the American Physical Society, Invited Session on *Exotic electronic structures of complex materials and phases*, Denver, Colorado, 9.3.07.

- J. Osterwalder: **Surface science: application of synchrotron radiation techniques (4 hours of lectures)**
  HERCULES School at SOLEIL, St. Aubin, France, 19./20.3.07

Research group of Prof. A. Schilling

Articles

- **Fluctuation effects in superconducting nanostrips**
  A. Engel, A. Semenov, H.-W. Hübers, K. Il'in, M. Siegel, Physica C, **444**, (2006) 12-18.

- **Superconducting Single Photon Detectors**
  H. Bartolf, A. Engel, A. Schilling, in Electron beam applications at ETH Zürich, F. Robin, Raith Application Note 2006, Raith GmbH (2006).
- **Electric noise and local photon-induced nonequilibrium states in a current-carrying nanostructured superconductor**
  A. Engel, A. Semenov, H.-W. Hübers, K. Il'in, and M. Siegel, in Progress in Superconductivity Research, edited by B. P. Martins, Nova Science Publishers, Inc., (2006) 153-189.
- **Low-temperature differential-thermal analysis to measure variations in entropy**
  A. Schilling and M. Reibelt, Rev. Sci. Instrum. **78**, 033904 (2007).

Articles in press

- **Spectral Sensitivity and Spectral Resolution of Superconducting Single-Photon Detectors**
  P. Haas, A. Semenov, H.-W. Hübers, J. Beyer, A. Kirste, T. Schurig, K. Ilin, M. Siegel, A. Engel, A. Smirnov, IEEE Trans. Supercond.

Diploma thesis

- **Construction of NMR equipment to be used in the Physical Properties Measurement System (PPMS, Quantum Design)**
  Alexander Gafner, Diplomarbeit, Physik-Institut, Universität Zürich, 2006.

Contributed Conference Presentations

- **Lift-off technique for the fabrication of superconducting nanostructures (poster)**
  H. Bartolf, A. Engel, A. Schilling, Kryoelektronische Bauelemente 2006, Ilmenau, Germany, 3.-5.10.2006.
- **Lift-off technique for the fabrication of nanostructures**
  H. Bartolf, SPS Jahrestagung 2007, Zürich, 20.-21.2.2007.
- **Exploration of new materials for superconducting single-photon detectors (poster)**
  A. Engel, H. Bartolf, A. Schilling, B. J. Ruck, C. Portesi, SPS Jahrestagung 2007, Zürich, 20.-21.2.2007.

Invited Lectures

- A. Engel: **Superconducting Single Photon Detectors – Chances & Challenges**
  Istituto Nazionale di Ricerca Metrologica I.N.RI.M, Torino, Italy, 20.6.2006.

- A. Engel: **Superconducting Single-Photon Detectors**
  Victoria University, Wellington, New Zealand, 22.8.2006.
- A. Engel: **Superconducting Nanostructures – Single-Photon Detector**
  Manep Project 5 Internal Workshop 2007, Neuchâtel, Switzerland, 17.1.2007.

Research group Prof. U. Straumann (for H1 publications see further below)

Articles

- **A measurement of Newton's gravitational constant**
  S. Schlamminger, E. Holzschuh, W. Kundig, F. Nolting, R. E. Pixley, J. Schurr and U. Straumann, Phys. Rev. D **74**, 082001 (2006).
- **Storage of ultracold neutrons in a volume coated with diamondlike carbon**
  F. Atchison et al., Phys. Rev. C **74**, 055501 (2006).
- **Structural characterization of diamond-like carbon coatings for ultracold neutron applications**
  F. Atchison, T. Brys, M. Daum, P. Fierlinger, A. Foelske, M. Gupta, R. Henneck, S. Heule, M. Kasprzak, K. Kirch et al., Diamond and Related Materials 16 (2007) 334.
- **Performance of long ladders for the LHCb silicon tracker**
  O. Steinkamp, Nucl. Instr. Meth. A 569 (2006) 84-87.
- **Silicon sensor probing and radiation studies for the LHCb silicon tracker**
  C.Lois, Nucl. Instr. Meth. A 568 (2006) 277-283.
- **Design and performance of the LHCb silicon tracker**
  K. Vervink, on behalf of the LHCb Silicon Tracker group, Nucl. Instr. Meth. A 566 (2006) 170-173.
- **Long term performance studies of the silicon strip detectors of the LHCb Silicon Tracker**
  S.Köstner and H.Voss, Nucl. Instr. Meth. A 563 (2006) 259-262.
- **Tracking in high multiplicity environments**
  J. Gassner, F. Lehner, M. Needham, O. Steinkamp, U. Straumann and A. Vollhardt, Proceedings of the 1st Workshop TIME 2005, Zuerich, Switzerland, October 3-7, 2005, Nucl. Instr. Meth. A 566 (2006).
- **The LHCb silicon tracker project**
  M. Agari et al., Nucl. Phys. Proc. Suppl. **150**, 114 (2006).
- **Storage of ultracold neutrons in a volume coated with diamondlike carbon**
  F. Atchison, B. Blau, M. Daum, P. Fierlinger, A. Foelske, P. Geltenbort, R. Henneck, S. Heule, M. Kasprzak et al., Phys. Rev. C74 (2006), 055501.
- **LHCb silicon tracker performance studies**
  S. Köstner et al., IEEE Trans. Nucl. Sci. **53**, 2440 (2006).
- **Design and performance of the LHCb silicon tracker**
  K. Vervink et al., Nucl. Instrum. Meth. A **566**, 170 (2006).

- **Measurement of the $t\bar{t}$ production cross section in $p\bar{p}$ collisions at $\sqrt{s}$=1.96 TeV using secondary vertex b tagging**
  V. M. Abazov et al. (D0 Collaboration), Phys. Rev. D **74**, 112004 (2006).

- **Measurement of the CP-violation parameter of B0 mixing and decay with p $\bar{p} \to \mu\mu X$ data**
  V. M. Abazov et al. (D0 Collaboration), Phys. Rev. D **74**, 092001 (2006).

- **Measurement of the W boson helicity in top quark decay at D0**
  V. M. Abazov et al. (D0 Collaboration), Phys. Rev. D **75**, 031102 (2007).

- **Measurement of the top quark mass in the lepton + jets final state with the matrix element method**
  V. M. Abazov et al. (D0 Collaboration), Phys. Rev. D **74**, 092005 (2006).

- **Limits on anomalous trilinear gauge couplings from $WW \to e^+e^-$, $WW \to e^\pm\mu^\mp$, and $WW \to \mu^+\mu^-$ events from $p\bar{p}$ collisions at $\sqrt{s}$ = 1.96-TeV**
  V. M. Abazov et al. (D0 Collaboration), Phys. Rev. D **74**, 057101 (2006).

- **Search for pair production of scalar bottom quarks in $p\bar{p}$ collisions at $\sqrt{s} =$ 1.96-TeV**
  V. M. Abazov et al. (D0 Collaboration), Phys. Rev. Lett. **97**, 171806 (2006).

- **Experimental discrimination between charge $2e/3$ top quark and charge 4e/3 exotic quark production scenarios**
  V. M. Abazov et al. (D0 Collaboration), Phys. Rev. Lett. **98**, 041801 (2007).

- **Search for scalar leptoquarks in the acoplanar jet topology in $p\bar{p}$ collisions at $\sqrt{s}$=1.96 TeV**
  V. M. Abazov et al. (D0 Collaboration), Phys. Lett. B **640**, 230 (2006).

- **Search for the standard model Higgs boson in the $p\bar{p} \to$Z H$\to \nu\bar{\nu}b\bar{b}$ channel**
  V. M. Abazov et al. (D0 Collaboration), Phys. Rev. Lett. **97**, 161803 (2006).

- **Search for neutral, long-lived particles decaying into two muons in $p\bar{p}$ collisions at $\sqrt{s}$=1.96 TeV**
  V. M. Abazov et al. (D0 Collaboration), Phys. Rev. Lett. **97**, 161802 (2006).

- **Search for associated Higgs boson production W H$\to$ W W W* $\to l^\pm\nu l'^\pm\nu' + X$ in $p\bar{p}$ collisions at $\sqrt{s}$=1.96 TeV**
  V. M. Abazov et al. (D0 Collaboration), Phys. Rev. Lett. **97**, 151804 (2006).

- **Search for W' boson production in the top quark decay channel**
  V. M. Abazov et al. (D0 Collaboration), Phys. Lett. B **641**, 423 (2006).

- **Search for a heavy resonance decaying into a Z + jet final state in $p\bar{p}$ collisions at $\sqrt{s}$=1.96 TeV using the D0 detector**
  V. M. Abazov et al. (D0 Collaboration), Phys. Rev. D **74**, 011104 (2006).

- **Search for R-parity violating supersymmetry via the LLE couplings Λ_{121}, Λ_{122} or Λ_{133} in $p\bar{p}$ collisions at $\sqrt{s}$=1.96 TeV**
  V. M. Abazov et al. (D0 Collaboration), Phys. Lett. B **638**, 441 (2006).

- **Search for neutral Higgs bosons decaying to tau pairs in $p\bar{p}$ collisions at $\sqrt{s}$=1.96 TeV**
  V. M. Abazov et al. (D0 Collaboration), Phys. Rev. Lett. **97**, 121802 (2006).

- **Search for resonant second generation slepton production at the Tevatron**
  V. M. Abazov et al. (D0 Collaboration), Phys. Rev. Lett. **97**, 111801 (2006).

- **Search for particles decaying into a Z boson and a photon in $p\overline{p}$ collisions at $\sqrt{s}$=1.96 TeV**
  V. M. Abazov et al. (D0 Collaboration), Phys. Lett. B $\mathbf{641}$, 415 (2006).

- **Search for the rare decay $B_s^0 \to \Phi\mu + \mu-$ with the D0 detector**
  V. M. Abazov et al. (D0 Collaboration), Phys. Rev. D $\mathbf{74}$, 031107 (2006).

- **Search for squarks and gluinos in events with jets and missing transverse energy in $p\overline{p}$ collisions at $\sqrt{s}$=1.96 TeV**
  V. M. Abazov et al. (D0 Collaboration), Phys. Lett. B $\mathbf{638}$, 119 (2006).

- **Search for excited muons in $p\overline{p}$ collisions at $\sqrt{s}$=1.96 TeV**
  V. M. Abazov et al. (D0 Collaboration), Phys. Rev. D $\mathbf{73}$, 111102 (2006).

- **A precise measurement of the B_s^0 lifetime**
  V. M. Abazov et al. (D0 Collaboration), Phys. Rev. Lett. $\mathbf{97}$, 241801 (2006).

- **Measurement of $B(t \to Wb)/B(t \to Wq)$ at $\sqrt{s} =$ 1.96-TeV**
  V. M. Abazov et al. (D0 Collaboration), Phys. Lett. B $\mathbf{639}$, 616 (2006).

- **First direct two-sided bound on the B_s^0 oscillation frequency**
  V. M. Abazov et al. (D0 Collaboration), Phys. Rev. Lett. $\mathbf{97}$, 021802 (2006).

- **Search for pair production of second generation scalar leptoquarks in $p\overline{p}$ collisions at $\sqrt{s} =$ 1.96-TeV**
  V. M. Abazov et al. (D0 Collaboration), Phys. Lett. B $\mathbf{636}$, 183 (2006).

Article in press

- **Diamond-like carbon coatings for Ultracold neutron guides**
  F. Atchison, M. Daum, A. Foelske, R. Henneck, S. Heule, M. Kasprzak et al.,
  Symposium H of the E-MRS 2006 conference, Applied Surface Science.

Theses

- **Flavor-Changing Neutral Currents at Hadron Colliders**
  F. Lehner, Habilitation, Universität Zürich, Mai 2006.

- **Search for Lepton Flavour Violation with the H1 Experiment at HERA**
  L. Lindfeld, Dissertation, Universität Zürich, August 2006.

- **Thermal and Mechanical Characterization of the TT Detector for the LHCb Experiment**
  A. Büchler, Master Thesis, Universität Zürich, March 2007.

- **Observation for the $B_s^0 \to \psi(2S)\phi$ decay with the D0 Experiment**
  Christophe Salzmann, Master Thesis, Universität Zürich, December 2006.

- **LHCb TT Module Properties**
  V. Hangartner, Bachelor Thesis, Universität Zürich, March 2007.

- **The LHCb TT production database and an overview of quality characteristics of the detector modules**
  N. Chiapolini, Bachelor Thesis, Universität Zürich, March 2007.

Conference contributions and invited seminars

- J. van Tilburg: **γ determination from tree decays ($B \to DK$) with LHCb**
  Lake Louise Winter Institute 2007, 19-24 February 2007, Alberta, Canada.

- D. Volyanskyy: **Selection of the decay $B_s^0 \to J/\psi\, \eta'$ at LHCb and its sensitivity to B_s^0 mixing parameters**
  Annual meeting of the Swiss Physical Society, 21. February 2007.

- C. Salzmann: **Observation of the decay $B_s^0 \to \psi(2S)\phi$**
  Annual meeting of the Swiss Physical Society, 21. February 2007.

- F. Lehner: **Semileptonic B decays at Tevatron**
  4th International Workshop on the CKM Unitarity Triangle, December 12 - 16, 2006, Nagoya, Japan.

- R. P. Bernhard: **Search for rare decays of the B_s meson at the Tevatron**
  41st Rencontres de Moriond: QCD and Hadronic Interactions, La Thuile, Italy, 18-25 Mar 2006, arXiv:hep-ex/0605065, to appear in the proceedings.

- A. Büchler: **Construction of the LHCb Trigger Tracker station**
  Annual meeting of the Swiss Physical Society, 21. February 2007.

- S. Heule: **Storage and guide materials for PSI ultracold neutron source**
  Annual meeting of the Swiss Physical Society, 21. February 2007.

- A. Knecht: **Systematic Effects in the Neutron EDM Experiment**
  Annual meeting of the Swiss Physical Society, 21. February 2007.

- U. Straumann: **Status and prospects of the LHCb Experiment**
  Colloquium, PSI, Villigen, Switzerland, 4. Januar 2007.

- O. Steinkamp: **Design and Production of the LHCb Silicon Tracker**
  11th Vienna Conference on Instrumentation (VCI 2007) Vienna, Austria, February 19-24, 2007.

- O. Steinkamp: **Design and Production of the LHCb Silicon Tracker**
  6th International "Hiroshima" Symposium on the Development and Application of Semiconductor Tracking Detectors (STD6), Carmel, California, USA, September 11-15, 2006.

- O. Steinkamp: **Tracking In High Multiplicity Environments**
  Colloquium, NIKHEF, Amsterdam, The Netherlands, April 5, 2006.

- U. Straumann: **Forces: Fundamental Interactions in Particle Physics**
  Vortrag für die Swiss Physics Olympiad Teilnehmer, Aarau, 25. March 2006.

Collaboration notes for LHCb[11]

- **Selection of the $B_s^0 \to J/\psi(\mu^+\mu^-)\,\eta'(\rho^0\gamma)$ decay at LHCb and its sensitivity to the B_s^0 mixing phase ϕ_s**
  D. Volyanskyy and J. van Tilburg, LHCb-2007-027.
- **Performance of the track matching**
  M. Needham and J. van Tilburg, LHCb-2007-020.
- **Design and Production of Detector Modules for the LHCb Silicon Tracker**
  Proceedings VCI 2007, Vienna, Sep 18-24, 2007 O. Steinkamp et al., LHCb-2007-009.
- **Design and Production of Detector Modules for the LHCb Silicon Tracker**
  Proceedings STD6, Carmel, Sep 11-15, 2006 O. Steinkamp et al., LHCb-2006-063.
- **Updated geometry description for the LHCb Trigger Tracker**
  M. Needham, D. Volyanskyy, LHCb-2006-032.
- **Radiation tests of the VELO ECS and analogue repeater mezzanines**
  L. Eklund, R. Frei, A. Vollhardt and A. van der Gracht, CERN-LHCB-2006-001.
- **Der Bachelor- und Masterstudiengang in Physik an der Universität Zürich**
  U. Straumann, Bulletin der Vereinigung Schweizerischer Hochschuldozenten, 32. Jahrgang, Heft Nr. 4, November 2006, 15.

H1 Publications by the groups of Straumann and Truöl

Articles

- **Forward Jet-Production in Deep Inelastic Scattering at HERA**
  H1-Collaboration**, A. Aktas *et al.*,
  DESY 05 – 135, hep-ex/0508055, Eur.Phys.J.**C46** (2006), 27 - 42.
- **Elastic J/ψ Production at HERA**
  H1-Collaboration**, A. Aktas *et al.*,
  DESY 05 – 161, hep-ex/0510016, Eur.Phys.J.**C46** (2006), 585 - 603.
- **Measurement of Event Shape Variables in Deep Inelastic Scattering**
  H1-Collaboration**, A. Aktas *et al.*,
  DESY 05 – 225, hep-ex/0512014, Eur.Phys.J.**C46** (2006), 343 - 356.
- **Photoproduction of Dijets with High Tansverse Momenta at HERA**
  H1-Collaboration**, A. Aktas *et al.*,
  DESY 06 – 020, hep-ex/0603014, Phys.Lett.**B639** (2006), 21 - 31.
- **Diffractive Photoproduction of ρ Mesons with Large Momentum Transfer at HERA**
  H1-Collaboration**, A. Aktas *et al.*,
  DESY 06 – 023, hep-ex/0603038, Phys.Lett.**B638** (2006), 422 - 431.

[11] LHCb notes can be accessed through the CERN document server on http://cdsweb.cern.ch/

- **Tau Lepton Production in ep Collisions at HERA**
  H1-Collaboration**, A. Aktas *et al.*,
  DESY 06 – 029, hep-ex/060422, Eur.Phys.J.**C48** (2006), 699 - 714.

- **Search for Doubly-Charged Higgs Boson Production at HERA**
  H1-Collaboration**, A. Aktas *et al.*,
  DESY 06 – 038, hep-ex/0604027, Phys.Lett.**B638** (2006), 432 - 440.

- **Measurement of Charm and Beauty Dijet Cross Sections in Photoproduction using the H1 Vertex Detector at HERA**
  H1-Collaboration**, A. Aktas *et al.*,
  DESY 06 –039, hep-ex/0605016, Eur.Phys.J.**C47** (2006), 597 - 610.

- **Search for a Narrow Baryonic Resonance in Decaying in $K_s^0 p$ or $K_s^0 \bar{p}$ in Deep Inelastic Scattering at HERA**
  H1-Collaboration**, A. Aktas *et al.*,
  DESY 06 – 044, hep-ex/060456, Phys.Lett.**B639** (2006), 202 - 209.

- **Diffractive Deep Inelastic Scattering with a Leading Proton at HERA**
  H1-Collaboration**, A. Aktas *et al.*,
  DESY 06 – 048, hep-ex/0606003, Eur.Phys.J.**C48** (2006), 749 - 766.

- **Measurement and QCD Analysis of the Diffractive Deep Inelastic Scattering Cross Section at HERA**
  H1-Collaboration**, A. Aktas *et al.*,
  DESY 06 – 049, hep-ex/0606004, Eur.Phys.J.**C48** (2006), 715 - 748.

- **Diffractive Open Charm Production in Deep Inelastic Scattering and Photoproduction at HERA**
  H1-Collaboration**, A. Aktas *et al.*,
  DESY 06 – 164, hep-ex/0610076, Eur.Phys.J.**C50** (2007), 1 - 20.

- **Inclusive $D^{*\pm}$-Meson and $D^{*\pm}$-Jet Correlations in Photoproduction at HERA**
  H1-Collaboration**, A. Aktas *et al.*,
  DESY 06 – 110, hep-ex/0608042, Eur.Phys.J.**C50** (2007), 251 - 267.

Conference contributions and invited seminars

- Stefania Xella: **Search for Single Top Production in ep Collisions at HERA**
  Proc. Int. Workshop on Top Quark Physics (TOP2006), Coimbra, Portugal, January 12 - 15, 2006; Proc. of Science **TOP 2006** (2006), 030.

- C. Schmitz: **Hadronic final states and spectroscopy in ep collisions at HERA**
  42nd Rencontres de Moriond on QCD and High Energy Hadronic Interactions, March 17-24 2007, La Thuile, Aosta Valley, Italy.

- K. Nowak: **Prompt Photons in Photoproduction**
  Spring conference of the German Physical Society, 7. March 2007.

- K. Nowak: **Prompt Photons in Photoproduction**
  Annual meeting of the Swiss Physical Society, 21. February 2007.

- L. Lindfeld: **Exotic (non-SUSY) Searches at HERA**
  SUSY06, 14th International Conference on Supersymmetry and the Unification of Fundamental Interactions, 12-17 June 2006, Irvine, USA.

- C. Schmitz: **Prompt Photons in DIS**
  DIS 2006, XIV. International Workshop on Deep Inelastic Scattering, April 20-24 2006, Tsukuba, Japan, arXiv:hep-ex/060793, to appear in the proceedings.

- Stefania Xella Hansen: **Tau Production at HERA**
  DIS 2006, XIV International Workshop on Deep Inelastic Scattering, April 20-24 2006, Tsukuba, Japan

** H1-collaboration (2006)

A. Aktas, V. Andreev, T. Anthonis, B. Antunovic, S. Aplin, A. Asmone, A. Astvatsatourov, A. Babaev, S. Backovic, A. Baghdasaryan, P. Baranov, E. Barrelet, W. Bartel, S. Baudrand, S. Baumgartner, J. Becker†, M. Beckingham, O. Behnke, O. Behrendt, A. Belousov, Ch. Berger, N. Berger, J.C. Bizot, M.-O. Boenig, V. Boudry, J. Bracinik, G. Brandt, V. Brisson, D. Bruncko, F.W. Büsser, A. Bunyatyan, G. Buschhorn, L. Bystritskaya, A.J. Campbell, F. Cassol-Brunner, K. Cerny, V. Cerny, V. Chekelian, J.G. Contreras, J.A. Coughlan, B.E. Cox, G. Cozzika, J. Cvach, J.B. Dainton, W.D. Dau, K. Daum, Y. de Boer, B. Delcourt, M. Del Degan, A. De Roeck, E.A. De Wolf, C. Diaconu, V. Dodonov, A. Dubak, G. Eckerlin, V. Efremenko, S. Egli, R. Eichler, F. Eisele, A. Eliseev, E. Elsen, S. Essenov,A, Falkewicz, P.J.W. Faulkner, L. Favart, A. Fedotov, R. Felst, J. Feltesse, J. Ferencei, L. Finke, M. Fleischer, G. Flucke, A. Fomenko, G. Franke, T. Frisson, E. Gabathuler, E. Garutti, J. Gayler, C. Gerlich, S. Ghazaryan, S. Ginzburgskaya, A. Glazov,I. Glushkov, L. Goerlich, M. Goettlich, N. Gogitidze, S. Gorbounov, C. Grab, T. Greenshaw, M. Gregori, B.R. Grell, G. Grindhammer, C. Gwilliam, D. Haidt, L. Hajduk, J. Haller, M. Hansson, G. Heinzelmann, R.C.W. Henderson, H. Henschel, G. Herrera, M. Hildebrandt, K.H. Hiller, D. Hoffmann, R. Horisberger, A. Hovhannisyan, T. Hreus,S. Hussain, M. Ibbotson, M. Ismail, M. Jacquet, L. Janauschek, X. Janssen, V. Jemanov, L. Jönsson, D.P. Johnson, A.W. Jung, H. Jung, M. Kapichine, J. Katzy, I.R. Kenyon, C. Kiesling, M. Klein, C. Kleinwort, T. Klimkovich, T. Kluge, G. Knies, A. Knutsson, V. Korbel, P. Kostka, K. Krastev, J. Kretzschmar, A. Kropivnitskaya, K. Krüger, M.P.J. Landon, W. Lange, G. Laštovička-Medin, P. Laycock, A. Lebedev, G. Leibenguth, V. Lendermann, S. Levonian, L. Lindfeld†, K. Lipka, A. Liptaj, B. List, J. List, E. Lobodzinska, N. Loktionova, R. Lopez-Fernandez, V. Lubimov, A.-I. Lucaci-Timoce, H. Lueders, D. Lüke, T. Lux, L. Lytkin, A. Makankine, N. Malden, E. Malinovski, S. Mangano, P. Marage, R. Marshall, L. Marti, M. Martisikova, H.-U. Martyn, S.J. Maxfield, A. Mehta, K. Meier, A.B. Meyer, H. Meyer, J. Meyer, V. Michels, S. Mikocki, I. Milcewicz-Mika, D. Milstead, D. Mladenov, A. Mohamed, F. Moreau, A. Morozov, J.V. Morris, M.U. Mozer, K. Müller†, P. Murín, K. Nankov, B. Naroska, Th. Naumann, P.R. Newman, C. Niebuhr, A. Nikiforov, G. Nowak, K. Nowak†, M. Nozicka, R. Oganezov, B. Olivier, J.E. Olsson, S. Osman, D. Ozerov, V. Palichik, I. Panagoulias, T. Papadopolou, C. Pascaud, G.D. Patel, H. Peng, E. Perez, D. Perez-Astudillo, A. Perieanu, A. Petrukhin, D. Pitzl, R. Plačakytė, B. Portheault, B. Povh, P. Prideaux, A.J. Rahmat, N. Raicevic, P. Reimer, A. Rimmer, C. Risler, E. Rizvi, P. Robmann†, B. Roland, R. Roosen, A. Rostovtsev, Z. Rurikova, S. Rusakov, F. Salvaire, D.P.C. Sankey, E. Sauvan, S. Schätzel, S. Schmidt, S. Schmitt, C. Schmitz†, L. Schoeffel, A. Schöning, H.-C. Schultz-Coulon, F. Sefkow, R.N. Shaw-West, I. Sheviakov, L.N. Shtarkov, T. Sloan, P. Smirnov,

Y. Soloviev, D. South, V. Spaskov, A. Specka, M. Steder, B. Stella, J. Stiewe, A. Stoilov, U. Straumann†, D. Sunar, V. Tchoulakov, G. Thompson, P.D. Thompson, T. Toll, F. Tomasz, D. Traynor, P. Truöl†, I. Tsakov, G. Tsipolitis, I. Tsurin, J. Turnau, E. Tzamariudaki, K. Urban, M. Urban†, A. Usik, D. Utkin, A. Valkárová, C. Vallée, P. Van Mechelen, A. Vargas Trevino, Y. Vazdik, C. Veelken, S. Vinokurova, V. Volchinski, K. Wacker, J. Wagner, G. Weber, R. Weber, D. Wegener, C. Werner, M. Wessels, B. Wessling, Ch. Wissing, R. Wolf, E. Wünsch, S. Xella†, W. Yan, V. Yeganov, J. Žáček, J. Zálešák, Z. Zhang, A. Zhelezov, A. Zhokin, Y.C. Zhu, J. Zimmermann, T. Zimmermann, H. Zohrabyan, and F. Zomer† Physik-Institut, Universität Zürich

Research group of Prof. P. Truöl (for H1 publications see above)

Articles

- **A Search for $\mu - e$ Conversion in Muonic Gold**
  W. Bertl, R. Engfer, E.A. Hermes, G. Kurz, T. Kozlowski, J. Kuth, G. Otter, F. Rosenbaum, N.M. Ryskulov, A. van der Schaaf, P. Wintz, and I. Zychor, Eur.Phys.J.**C47** (2006), 337 - 346.

- **Measurement of the J/Ψ Production Cross Section in 920 GeV/c Fixed-Target Proton-Nucleus Interactions**
  HERA-B-Collaboration*, I. Abt *et al.*,
  DESY-05-232, hep-ex/0512029, Phys.Lett.**B638** (2006), 407 - 414.

- **Polarization of Λ and $\bar{\Lambda}$ in 920 GeV Fixed-Target Proton-Nucleus Interactions**
  HERA-B-Collaboration*, I. Abt *et al.*,
  DESY 06 – 027, hep-ex/0603047, Phys.Lett.**B638** (2006), 415 - 421.

- **Measurement of the Upsilon Production Cross Section in 920 GeV Fixed-Target Proton-Nucleus Collisions**
  HERA-B-Collaboration*, I. Abt *et al.*,
  DESY-05-253, hep-ex/0603015, Phys.Lett.**638** (2006), 13 - 21.

- **A Measurement of the ψ' to J/ψ Production Ratio in 920-GeV Proton-Nucleus Interactions**
  HERA-B Collaboration*, I. Abt *et al.*,
  DESY-06-117, hep-ex/0607046, Eur.Phys.J.**C49** (2007), 545 - 558.

- **K_0^* and ϕ Meson Production in Proton-Nucleus Interactions at $s^{1/2}$ = 41.6 GeV**
  HERA-B Collaboration*, I. Abt *et al.*,
  DESY-06-096, hep-ex/0606049, Eur.Phys.J.**C50** (2007), 315 - 328.

Articles in print

- **Bottom Production Cross Section from Double Muonic Decays of b-Hadrons in 920 GeV Proton-Nucleus Collision**
  HERA-B Collaboration*, I. Abt *et al.*, DESY-06-214, hep-ex/0612024, Phys.Lett.**B** (2007).

Published conference contributions

- **High Intensity K Experiments**
  A. van der Schaaf, Proc. High Intensity Frontier Workshop (HIF05), La Biodola, Isola d'Elba, Italy, May 28 - Jun 1, 2005; Nucl.Phys.Proc.Suppl. **154** (2006), 12 - 19.
- **Studies on Wrapping Materials and Light Collection Geometries in Plastic Scintillators**
  S. Scheu, H. Kaspar, P. Robmann, A. van der Schaaf, and P. Truöl,
  Proc. 4^{th} Int. Conf. on New Developments in Photodetection (BEAUNE 2005): From Infra Red to Gamma Rays, Beaune, France, June 19 - 24, 2005; Nucl.Instr.Meth. A**567** (2006), 345 - 349.

Invited Lectures

- A. van der Schaaf: **Two new $\pi \to e\nu$ experiments**
  Workshop on Flavour in the era of the LHC, 3rd meeting, CERN, May 15-17 2006.
- A. van der Schaaf: **LFV experiments and lepton universality**
  Workshop on Flavour in the era of the LHC, 4th meeting, CERN, March 26-28 2007.

* HERA-B Collaboration (2006)

I. Abt, M. Adams, M. Agari, H. Albrecht, A. Aleksandrov, V. Amaral, A. Amorim, S.J. Aplin, V. Aushev, Y. Bagaturia, V. Balagura, M. Bargiotti, O. Barsukova, J. Bastos, J. Batista, C. Bauer, Th.S. Bauer, A. Belkov, Ar. Belkov, I. Belotelov, A. Bertin, B. Bobchenko, M. Böcker, A. Bogatyrev, G. Bohm, M. Brauer, M. Bruinsma, M. Bruschi, P. Buchholz, T. Buran, J. Carvalho, P. Conde, C. Cruse, M. Dam, K.M. Danielsen, M. Danilov, S. De Castro, H. Deppe, X. Dong, H.B. Dreis, V. Egorytchev, K. Ehret, F. Eisele, D. Emeliyanov, S. Essenov, L. Fabbri, P. Faccioli, M. Feuerstack-Raible, J. Flammer, B. Fominykh, M. Funcke, Ll. Garrido, A. gellrich, B. Giacobbe, J. Gläß, D. Goloubkov, Y. Golubkov, A. Golutvin, I. Golutvin, I. Gorbounov, A. Gorisek, O. Gouchtchine, D.C. Goulart, S. Gradl, W. Gradl, F. Grimaldi, J. Groth-Jensen, J.D. Hansen, J.M. Hernandez, W. Hofmann, M. Hohlmann, T. Hott, W. Hulsbergen, U. Husemann, O. Igonkina, M. Ispiryan, T. Jagla, C. Jiang, H. Kapitza, S. Karabekyan, N. Karpenko, N. Karpenko, S. Keller, J. Kessler, F. Khasanov, Yu. Kiryushin, K.T. Knöpfle, H. Kolanoski, S. Korpar, C. Krauss, P. Kreuzer, P. Križan, D. Krücker, S. Kupper, T. Kvaratskheliia, A. Lanyov, K. Lau, B. Lewendel, T. Lohse, B. Lomonosov, R. Männer, R. Mankel, S. Masciocchi, I. Massa, I. Matchikhilian, G. Medin, M. Medinnis, M. Mevius, A. Michetti, Yu. Mikhailov, R. Mizuk, R. Muresan, M. zur Nedden, M. Negodaev, M. Nörenberg, S. Nowak, M.T. Nunez Pardo de Vera, M. Ouchrif, F. Ould-Saada, C. Padilla, D. Peralta, R. Pernack, R. Pestotnik, M.-A. Pleier, M. Poli, V. Popov, D. Pose, S. Prystupa, V.M. Pugatch, Y. Pylypchenko, J. Pyrlik, K. Reeves, D. Reßing, H. Rick, I. Riu, P. Robmann†, I. Rostotseva, V. Rybnikov, F. Sánchez, A. Sbrizzi, M. Schmelling, B. Schmidt, A. Schreiner, H. Schröder, A.-J. Schwartz, A.-S. Schwarz, B. Schwenninger, B. Schwingenheuer, F. Sciacca, N. Semprini-Cesari, S. Shuvalov, L. Silva, K. Smirnov, L. Sözüer, S. Solunin, A. Somov, S. Somov, J. Spengler, R. Spighi, A. Spiridonov, A. Stanovnik, M. Starič, C. Stegmann, H.S. Subramania, M. Symalla, I. Tikhomirov, M. Titov, I. Tsakov, U. Uwer, C. van Eldik, Yu. Vassiliev, M. Villa, A. Vitale, I. Vukotic,

H. Wahlberg, A.H. Walenta, M. Walter, J.J. Wang, D. Wegener, U. Werthenbach, H. Wolters, R. Wurth, A. Wurz, Yu. Zaitsev, M. Zavertyaev, T. Zeuner, A. Zhelezov, Z. Zheng, R. Zimmermann, T. Zivko and A. Zoccoli† Physik-Institut, Universität Zürich